On the way to the determination of the Neutrino Mass Hierarchy with JUNO

Qinhua Huang

université PARIS-SACLAY

ÉCOLE POLYTECHNIQUE
UNIVERSITÉ PARIS-SACLAY

On the way to the determination of the neutrino mass hierarchy with JUNO

Thèse de doctorat de l'Université Paris-Saclay
préparée à l'Ecole Polytechnique

École doctorale n°576 Particules, Hadrons, Énergie, Noyau, Instrumentation, Imagerie, Cosmos et Simulation (PHENIICS)
Spécialité de doctorat : Physique des particules

Thèse présentée et soutenue à Palaiseau, le 6 novembre 2019, par

QINHUA HUANG

Composition du Jury :

M. Yves Sirois
Directeur de recherche, CNRS (LLR)   Président

Mme. Heide Costantini
Maître de conférences, Université Aix-Marseille (CPPM)   Rapporteur

M. Claudio Giganti
Chargé de recherche, CNRS (LPNHE)   Rapporteur

Mme. Sandrine Emery
Ingénieure chercheuse, CEA (Irfu/DPhP)   Examinatrice

M. Olivier Drapier
Directeur de recherche, CNRS (LLR)   Directeur de thèse

M. Marcos Dracos
Directeur de recherche, CNRS (IPHC)   Co-directeur de thèse

Thèse de doctorat

Abstract

The JUNO experiment is a multi-purpose liquid scintillator neutrino experiment with the main objective of determining the neutrino mass hierarchy (νMH) with a significance better than 3σ. To achieve this goal, it is crucial that JUNO has an unprecedented energy resolution of 3% at 1 MeV. Therefore, the JUNO Central Detector (CD) will be built with 20 000 ton high transparency liquid scintillator and high photomultiplier tube (PMT) photocathode coverage of 78%, which is provided by 18 000 20"-PMTs (LPMTs) and 25 000 3"-PMTs (SPMTs). At the same time, the background induced by atmospheric muons should be vetoed by using reconstructed muon tracks. The Top Tracker (TT) is a muon tracker installed on top of the CD for precise muon tracking.

This thesis details firstly the optimisation of the LPMT and the SPMT systems, which are directly related to the antineutrino calorimetry. New designs of light concentrator tailored for the JUNO LPMT are studied in order to verify their performance on increasing the JUNO photoelectron yield. By comparing different configurations, the relation between the SPMT system performance and the non-uniform distribution of the SPMT emplacements is studied, and the scheme used for cabling between SPMTs and their Under Water Boxes (UWBs) is studied to ensure a minimal performance degradation in case of UWB failure.

Afterwards, this thesis reports on the design and optimisation of the TT trigger algorithms. Due to the background induced by natural radioactivity in the JUNO cavern, the TT cannot work correctly without a trigger system. The results show that a 2-level trigger with the optimised trigger algorithm is effective for the background suppression and thus a muon detection efficiency of 93% can be achieved.

A discussion about the TT contribution to the suppression and the measurement of the atmospheric muon-induced background, is also included.

Résumé

L'expérience JUNO est une expérience basée sur un détecteur à scintillateur liquide ayant pour objectif principal de déterminer la hiérarchie de masse des neutrinos. JUNO atteindra une sensibilité de trois écarts standards en 6 ans, avec une résolution en énergie sans précédent, meilleure que 3% à 1 MeV. Le détecteur central de JUNO est un détecteur à scintillateur liquide de 20 kilotonnes, construit avec une couverture de photocathode élevée (78%) et une bonne transparence. La couverture de photocathode est assurée par 18 000 photomultiplicateurs de 20 pouces et 25 000 de 3 pouces, ce qui permet d'atteindre un rendement d'environ 1200 photoélectrons par MeV. Malgré les 700 m d'épaisseur de roche protégeant le détecteur des rayonnements cosmiques, le bruit de fond induit par les muons atmosphériques est toujours considéré comme non négligeable par rapport au signal attendu pour la détermination de la hiérarchie de masse. Pour faire face à ce bruit de fond, un détecteur appelé « Top Tracker » permet d'améliorer la détection de ces muons. Cette thèse concerne les travaux d'optimisation pour cette expérience actuellement en cours de construction, et dont les prises de données commenceront en 2021.

Pour les photomultiplicateurs de 20 pouces, deux nouvelles géométries de concentrateurs de lumière sont étudiées afin de vérifier leurs performances pour augmenter le rendement photoélectronique et donc la résolution en énergie de JUNO. La distribution spatiale et le schéma de câblage des photomultiplicateurs de 3 pouces font aussi l'objet d'études pour assurer une performance optimale du système.

Cette thèse aborde ensuite la conception du système de déclenchement du Top Tracker. En effet, ce détecteur doit posséder un tel système pour rejeter les signaux produits par la radioactivité naturelle dans la caverne. Les résultats montrent qu'un système à 2 niveaux doté d'algorithmes optimisés est efficace pour la suppression de ces signaux et qu'il est ainsi possible d'obtenir une efficacité de détection des muons de 93%. Une discussion sur la contribution du Top Tracker à la suppression et à la mesure du bruit de fond induit par les muons atmosphériques est également incluse.

Acknowledgements

in particle physics. Michel, as the group leader, though he is not directly involved in my thesis, I would like to thank him for the understanding and support allowing me to achieve this doctorate. I wish to acknowledge many useful discussions with Thomas MUELLER, who has always explained me my questions in neutrino physics in a very pedagogical way and in extensive detail. I would like to thank Alberto, Alice, Guillermo, Matthieu, Olivier V., Sonia, Stephan, for being always available to discuss about physics and beyond. Equally, I wish to thank Eric and Leonidas, my colleagues at IPHC, for giving me many useful suggestions and pertinent comments on the manuscript and the defence presentation.

Besides the physicists, I would like to thank Jacques WURTZ and Michal SZELEZNIAK, electronics engineers at IPHC, for their collaboration and excellent advice on my FPGA design based on their expertise. At the same time, Franck GASTALDI, electronics engineer at LLR, deserves a mention for his direct contribution to my test bench.

Outside the scope of this thesis, I would like to thank Frédéric, Émilie, Felipe. Although they do not work in neutrino physics, they offered me an opportunity to learn some knowledge in other fields of particle physics through many interesting conversations. It is this experience that encourages me to step in a physics topic other than neutrino physics in my post-doc research. It must be mentioned that, Émilie and Felipe are not only excellent office mates but also very nice friends. I enjoyed so much chatting with them, and I am thankful for their friendship.

JUNO is an international collaboration that was initiated by IHEP, Beijing, China. Naturally, my work makes use of the combined work of many colleagues in IHEP. I would like to express my appreciation for their excellent work and their timely assistance whenever I incurred problems. Especially, I am greatly indebted to Jilei XU (徐吉磊), Haoqi LU (路浩奇), Tao LIN (林韬), and Wenjie WU (吴文杰). I thank also Professor Miao HE (何苗) individually for organising me a one-week lab work in IHEP, which I have much enjoyed.

Last, but certainly not least, I wish to acknowledge the support, help, encouragement, and great love of my family. Such an emotion can only be passed to them in Chinese, as I write below:

谢谢爸爸妈妈对我一直以来的悉心照顾，和对我从事科研工作的鼎力支持。在我最失落的时候，是你们给我以最大的信心来勇敢地做出新的选择，并且走出低谷。在论文的最后阶段，宝贝儿子多多出生了，开心之余，工作生活也多了许多挑战。你们千里迢迢来到法国，只为我能心无旁骛地完成论文的写作。这篇博士论文的完成离不开你们对我们这个小家庭无所保留的爱。这篇致谢的最后一个感谢毫不意外地给我的妻子，多多的妈妈，黄珅。从同学到爱人再到夫妻，这十年间，你对我的帮助和支持自不必赘述，你的大度和包容也常常让我自惭形秽。为了完成论文，我难以全身心做好一个父亲的角色，而你虽怨言不断，却也理解我的处境承担了所有照顾多多的责任。论文的压力让我辗转反侧，又是你轻声哼唱的摇篮曲，在安抚多多的同时，也带着我跨过黎明前的黑暗。

Contents

Introduction

Neutrinos are elementary particles of the fermion family. They exist in three flavours, namely electron neutrinos ν_e, muon neutrinos ν_μ, and tau neutrinos ν_τ. For a long time, they had been considered to be massless particles. In 1998, neutrino oscillations between flavours were discovered for the first time using atmospheric neutrinos. The neutrino oscillations describe a phenomenon in which neutrinos change flavours during their propagation. This phenomenon can only be explained if neutrinos have mass. Therefore, neutrinos have three mass eigenstates, commonly denoted ν_1, ν_2, and ν_3 with the corresponding masses m_1, m_2, and m_3. Although neutrinos have been proven to be massive, their masses should still be very small. Even compared with electrons, the lightest elementary particle that constitutes ordinary matter, neutrinos are lighter by 6 orders of magnitude.

Physicists describe phenomenologically oscillations through a neutrino flavour mixing matrix which contains mixing angles, and mass squared differences between mass eigenstates (e.g., $\Delta m_{21}^2 = m_2^2 - m_1^2$). Many experiments have been performed to measure the mixing angles and the mass squared differences. However, the mass hierarchy of the three mass eigenstates is not yet clearly known with the current experimental data. Two schemes are possible, namely $m_3 > m_2 > m_1$ and $m_2 > m_1 > m_3$, and we expect that the true scheme can be determined by next-generation neutrino experiments.

In Chapter 1, theories concerning neutrino masses and neutrino oscillations are summarised, after which the current experimental status of oscillation parameter measurements is detailed. At the end of the chapter, a few open questions in the neutrino physics sector are also briefly discussed.

The Jiangmen Underground Neutrino Observatory (JUNO) is a multi-purpose liquid scintillator neutrino experiment that will perform a precise measurement for the energy spectra of antineutrinos emitted from mainly two nuclear power plants. The design energy resolution is 3% at $1\,\mathrm{MeV}$, being better than any established neutrino detectors with similar technologies. As a next generation neutrino experiment, JUNO will determine the neutrino mass hierarchy with a significance better than 3σ in 6 years. So far, the development of most critical systems in JUNO have been finished, and the civil construction is ongoing. Data taking should start in 2021. A detailed description of the JUNO experiment and its physics program can be found in Chapter 2.

The photoelectron yield is one of the key parameters that determine the detector's energy resolution. The light concentrators, also known as Winston cones, are a device widely employed to take the light on a relatively large entrance aperture onto a smaller exit aperture. By placing a light concentrator on a photomultiplier tube (PMT), the effective photosensitive area is therefore enlarged. Such an enlargement has been proven helpful in increasing the photoelectron yield of the detector in various neutrino experiments. Chapter 3 presents a Monte-Carlo study on the design of light concentrators for the JUNO 20"-PMT (LPMT), in order to estimate the benefit that can be obtained

from employing such devices in JUNO.

As mentioned before, one of the critical requirements in JUNO is the 3% energy resolution. To achieve this goal, several calibration systems are needed. The system of 3"-PMTs (SPMTs), as one of these systems, helps the LPMT system to control the non-linearity. Due to mechanical constraints, some potential SPMT emplacements are not usable. The removal of the corresponding SPMTs from the system leaves a non-uniform distribution, which could degrade the system's light detection performance. In the baseline design, 128 SPMTs share the same electronics, stored in an Under Water Box (UWB). The failure of these UWBs can lead to loss of SPMTs, which will also disturb the light detection performance. We expect to reduce this impact by optimising the scheme of SPMT-UWB cabling. In Chapter 4, studies on different situations will try to address clearer answers to the problems related to both the non-uniform distribution and the cabling scheme.

Despite the $\sim 700\,\mathrm{m}$ rock overburden, a few atmospheric muons per second can still enter the detector and produce fake antineutrino signals. The number of muon-induced background events in the neutrino mass hierarchy analysis is estimated to be 71 per day, while the antineutrino event rate is 73 per day. This background can be reduced to an acceptable level of 1.6 events per day, only when the muons are tracked and the vicinity of the muons tracks is vetoed for a sufficiently long period.

The Top Tracker is part of the muon veto system in JUNO and it gives precise muon tracking information to other detectors. It is composed of 63 walls, with each wall having a $6.7 \times 6.7\,\mathrm{m}^2$ sensitive area. These walls are arranged in a 3 layer tracker, covering about 60% of the top area of the JUNO detector. The Top Tracker readout system is designed to handle a high background rate of the order of 10^6 events per second due to natural radioactivity in the JUNO cavern, with the help of a 2-level trigger. While the electronics design is almost finished, the trigger algorithms used to suppress the radioactive background have not yet been finalised. Chapter 5 is therefore devoted to the studies on the optimisation of the trigger algorithms.

Finally, Chapter 6 shows that the Top Tracker can not only assist directly the muon-induced background veto, but it will also serve to measure and to study this background thanks to its good muon reconstruction accuracy. Furthermore, the Top Tracker is able to tag some muons that do not cross the Central Detector or the Water Cherenkov Detector in JUNO, but generate background events after interacting with the surrounding rock. In this case, the Top Tracker is the unique tool to narrow the systematic uncertainty related to this kind of muons.

Chapter 1

Introduction to neutrino physics

Neutrinos are elementary particles with $1/2$ spin, no electric charge, and nearly zero mass. They are very commonly found in the Universe. For example, the Sun is one powerful astronomical neutrino source providing 6.6×10^{10} neutrinos per square centimetre per second at the Earth surface [1]. Besides, the Earth itself due to the decays of radioactive elements in the interior, generates a neutrino flux of about $10^6 \, \text{cm}^{-2} \, \text{s}^{-1}$ [2]. Some mankind facilities can also be regarded as important sources of neutrinos, such as particle accelerators and nuclear reactors. A typical commercial reactor power plant radiates $2 \times 10^{20} \, \bar{\nu}_e$ per gigawatt (GW) of thermal power [3].

Despite the fact that neutrinos are not rare, it is extremely difficult to detect them. The existence of neutrinos was firstly postulated by Wolfgang Pauli in 1930 as "ein verzwelfelter Ausweg" (a desperate remedy) to restore energy conservation in β-decays, and he acknowledged the issue of proposing an "undetectable" particle [4]. He was finally proven right: neutrinos are the missing particles in β-decays that carry away part of the electron kinetic energy, and they are only sensitive to the weak interaction and gravity, which leads to a very difficult detection. The first neutrino detection in history was done in 1956, 26 years after Pauli's prediction, by Clyde Cowan and Frederick Reines [5], which let the latter win the Nobel Prize in 1995.

Since then, people have made much progress in neutrino physics, both theoretically and experimentally. One of the great achievements is the discovery of neutrino oscillations in Super-Kamiokande [6] and in SNO [7]. Neutrinos exist in 3 generations corresponding to charged leptons [8], electron neutrino ν_e [5], muon neutrino ν_μ [9], and tau neutrino ν_τ [10], each is a composite quantum state of 3 mass eigenstates, ν_1, ν_2, and ν_3. In order to oscillate, the mass differences between two mass eigenstates should not vanish, therefore, neutrinos must be massive. Although experiments have measured the absolute values of differences between all mass eigenstates [11], the mass ordering of the 3 mass eigenstates, also known as the neutrino mass hierarchy, has not yet been determined.

This chapter will present the theoretical framework of neutrinos. Section 1.1 is an overview of the Standard Model (SM) of particle physics, while massive neutrinos and neutrino oscillations are formalised in Section 1.2 and Section 1.3, respectively. Finally, Section 1.4 will show the current status of neutrino experiments, including some of them seeking answers to open questions.

1.1 Overview of the Standard Model

The Standard Model of particle physics is a quantum field theory unifying the electromagnetism, the weak force, and the strong force. It describes particles that constitute matter as spin-1/2 particles, namely fermions, and the interactions between them are carried by spin-1 particles, namely bosons. The only spin-0 particle in the model is the Higgs boson, which is responsible for the mass generation.

The theory has been extensively used to explain innumerable data taken from particle physics experiments in the past several decades, including the data from the Large Hardon Collider (LHC) that led to the discovery of the Higgs boson [12, 13].

1.1.1 Particles of the Standard Model

The Standard Model has 12 fermions and same amount of antifermions. Fermions can be further categorised as either quarks or leptons, due to the fact that quarks are involved in the strong interaction, whereas leptons are not. Six quarks and their antiparticles exist in the SM. The six quarks are named up (u), down (d), charm (c), strange (s), top (t), and bottom (b). The model contains same amount of leptons and antileptons, where the leptons are electron (e), muon (μ), tau (τ), electron neutrino (ν_e), muon neutrino (ν_μ), and tau neutrino (ν_τ). The quarks, the leptons, and their antiparticles are considered to be building blocks of regular matter in the Universe. For example, hydrogen gas is composed of hydrogen molecule, the molecule is a bound system of 2 hydrogen atoms, each atom consists of one proton and one electron, and finally, the proton is built from 3 quarks. The fermions are summarised in Figure 1.1, together with their quantum numbers.
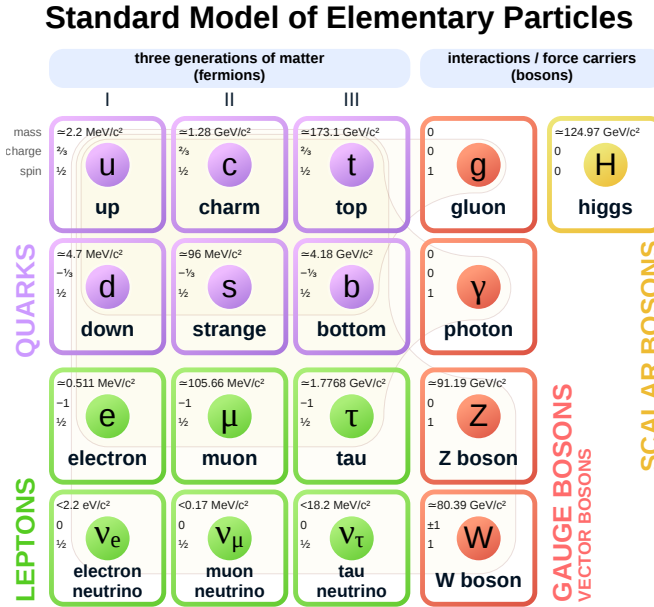
Figure 1.1 − The particle content of the Standard Model.

The fermions can also be organised as three generations, each generation has two quarks and two leptons (I, II, III in Figure 1.1). Apart from their flavour quantum numbers and masses, particles of higher generation are just like copies of those of the previous generation, such as $u \rightarrow c \rightarrow t$. Besides, for all charged fermions, the masses increase as the generation becomes higher, for example, τ is almost 3500 times heavier

than e. For neutrinos, their masses are very small compared to other fermions, which should be below a few eV [14]. Lacking of the naturalness, the absolute neutrino mass is one of the key issues within modern particle physics [15]. Additionally, as we will see later in Section 1.3, it exists an ambiguity about the neutrino mass hierarchy.

The interactions between fermions are realised by exchanging gauge bosons, which are introduced to maintain the local gauge symmetry, a fundamental symmetry of the Universe that will be talked about later in Section 1.1.2. The 12 gauge bosons of the Standard Model are the photon (γ), the 8 gluons (g), the Z-boson (Z^0), the W-bosons ($W^\pm$). In the theory, it is considered that the photon carries the electromagnetic force, the gluons carry the strong force, the Z-boson and the W-bosons carry the weak force.

The Standard Model introduces a quantum field called Higgs field, aiming to explain the mass generation for all SM particles except neutrinos: a massive particle obtains its mass through the Brout-Englert-Higgs mechanism, which will be detailed in Section 1.1.4. Higgs boson is a particle produced by the quantum excitation of the Higgs field, and it was discovered for the first time in 2012 by the LHC experiments. This discovery confirms the existence of the Higgs field as well as the theory of the mass generation.

1.1.2 The priciples of quantum field theories

Quantum electrodynamics (QED) is the first well-established quantum field theory describing the electromagnetism, and is famous for the extremely precise prediction of the fine-structure constant [16]. The quantum field theories including QED are all gauge theories, based on local gauge symmetry, where Lagrangian[1] is required to be invariant under the local gauge transformation. The Lagrangian of a free fermion can be written as

$$\mathcal{L} = \bar{\psi}(x)(i\partial\!\!\!/ - m)\psi(x), \tag{1.1}$$

where $\psi(x)$ is the Dirac spinor representing the field, $\partial\!\!\!/ \equiv \gamma^\mu \partial_\mu$ is defined as a product of Dirac matrices γ^μ and the covariant derivative ∂_μ [17], and m denotes the electron mass. Take QED as an example of gauge theory, it requires the local gauge symmetry under the $U(1)$ transformation

$$\psi(x) \to \psi'(x) = e^{-iq_e \alpha(x)} \psi(x), \tag{1.2}$$

where $\alpha(x)$ is the phase depending on the spacetime coordinates, and q_e is the electric charge. To preserve the local symmetry, a new covariant derivative is defined as

$$\partial_\mu \to D_\mu \equiv \partial_\mu - iq_e A_\mu(x), \tag{1.3}$$

where $A_\mu(x)$ is a four-vector gauge field. The invariance can be explicitly written as

$$D_\mu \psi(x) \to D'_\mu \psi'(x) = \left(\partial_\mu - iq_e A'_\mu(x)\right) e^{-iq_e \alpha(x)} \psi(x) = e^{-iq_e \alpha(x)} D_\mu \psi(x), \tag{1.4}$$

which gives rise to

$$A_\mu(x) \to A'_\mu(x) = A_\mu(x) - \partial_\mu \alpha(x). \tag{1.5}$$

Therefore, the QED Lagrangian describing both photons and fermions is written as

$$\mathcal{L}_{\text{QED}} = -\frac{1}{4} F^{\mu\nu} F_{\mu\nu} + \bar{\psi}(x)(i D\!\!\!\!/ - m)\psi(x), \tag{1.6}$$

---

[1]Technically speaking, $\mathcal{L}$ is the Lagrangian density.

Table 1.1 – The three quantum numbers used in Glashow-Salam-Weinberg model for electroweak unification of quarks and leptons in the SM.

Particle content	I^3	Y	q
$Q_L \equiv \begin{pmatrix} u_L \\ d_L \end{pmatrix}, \begin{pmatrix} c_L \\ s_L \end{pmatrix}, \begin{pmatrix} t_L \\ b_L \end{pmatrix}$	$\begin{pmatrix} +\frac{1}{2} \\ -\frac{1}{2} \end{pmatrix}$	$+\frac{1}{3}$	$\begin{pmatrix} +\frac{2}{3} \\ -\frac{1}{3} \end{pmatrix}$
$\ell_L \equiv \begin{pmatrix} \nu_{eL} \\ e_L \end{pmatrix}, \begin{pmatrix} \nu_{\mu L} \\ \mu_L \end{pmatrix}, \begin{pmatrix} \nu_{\tau L} \\ \tau_L \end{pmatrix}$	$\begin{pmatrix} +\frac{1}{2} \\ -\frac{1}{2} \end{pmatrix}$	-1	$\begin{pmatrix} 0 \\ -1 \end{pmatrix}$
$U_R \equiv u_R, c_R, t_R$	0	$+\frac{4}{3}$	$+\frac{2}{3}$
$D_R \equiv d_R, s_R, b_R$	0	$-\frac{2}{3}$	$-\frac{1}{3}$
$E_R \equiv e_R, \mu_R, \tau_R$	0	-2	-1

where the strength tensor $F_{\mu\nu} \equiv \partial_\mu A_\nu(x) - \partial_\nu A_\mu(x)$. It is to be noticed that a coupling between photons and fermions with a coupling constant equal to q_e is encoded in the second term of Equation (1.6).

Quantum chromodynamics (QCD) describes the strong force, which binds quarks together inside the hadrons. Having a formalism similar to QED, QCD is based on the $SU(3)$ local gauge symmetry, and its mechanism of the interaction is explained by the gluons carrying different charge colours (red, blue, green, antired, antiblue, antigreen) exchanged between quarks.

Neutrinos are sensitive to neither QED nor QCD. The only interaction in which neutrinos take part is the weak interaction, the fundamental interaction that is responsible for the radioactive β-decay of nuclei. The modern picture of the weak interaction is understood in terms of the electroweak theory (EW), developed by Glashow, Salam and Weinberg (GSW).

In the 1950s, people learned that the parity is not conserved in the weak interaction [18, 19], the behaviour of particles in weak processes depends on their chiralities. The chirality is an intrinsic property of particles, it can be either left-handed (L) or right-handed (R). Although the chirality is equal to the helicity for massless particles, the chirality is a Lorentz invariant, while the helicity is not. To unify the electromagnetism and the weak interaction, EW introduces the weak isospin (I^3), the weak hypercharge (Y), and expresses the electric charge (q) in terms of linear combination of both

$$q = I^3 + \frac{Y}{2}. \tag{1.7}$$

EW is then established with $SU(2)_L \times U(1)_Y$ gauge symmetry, where the $SU(2)_L$ gauge transformation is associated with the weak isospin while the $U(1)_Y$ gauge transformation is associated with the hypercharge. The left handed fermion fields are formalised as $SU(2)_L$ doublets and the right handed fermion fields as $SU(2)_L$ singlets. They are listed in the first column of Table 1.1, in which the subscript L denotes left-handed fermion fields, and R denotes right-handed.

It must be noticed that Table 1.1 does not have a $SU(2)_L$ singlet for right-handed neutrinos ν_R. Let us assume that such a singlet exists, by definition, its weak isospin is 0. Neutrinos are electrically neutral ($q = 0$), so according to Equation (1.7), Y must be 0, too. Therefore, EW does not need to include this singlet, since right-handed neutrinos would be one kind of particles not sensitive to the EW force. Experimentally,

right-handed active neutrinos are not observed in β-decays [20]. Nevertheless, ν_R may still exist in the Nature as sterile neutrinos.

With separated left-handed and right-handed components, the kinetic terms of fermion fields in GSW can be written as

$$\mathcal{L} = \overline{Q_L}i\slashed{D}Q_L + \overline{\ell_L}i\slashed{D}\ell_L + \overline{U_R}i\slashed{\partial}'U_R + \overline{D_R}i\slashed{\partial}'D_R + \overline{E_R}i\slashed{\partial}'E_R. \tag{1.8}$$

The gauge fields W_μ^k (for $k = 1, 2, 3$) and B_μ are introduced through the covariant derivatives:

$$D_\mu \equiv \partial_\mu - ig\frac{\sigma^k}{2}W_\mu^k - ig'\frac{Y}{2}B_\mu, \tag{1.9}$$

$$\partial_\mu' \equiv \partial_\mu - ig'\frac{Y}{2}B_\mu, \tag{1.10}$$

where σ^k (for $k = 1, 2, 3$) are the Pauli sigma matrices [17], g and g' represent the coupling constants of the two different gauge fields. The gauge invariant kinetic terms of the fields is described by Lagrangian

$$\mathcal{L}_G = -\frac{1}{4}W^{i\mu\nu}W_{\mu\nu}^i - \frac{1}{4}B^{\mu\nu}B_{\mu\nu}, \tag{1.11}$$

with

$$W_{\mu\nu}^i \equiv \partial_\mu W_\nu^i - \partial_\nu W_\mu^i + gf^{ijk}W_\mu^j W_\nu^k, \tag{1.12}$$

$$B_{\mu\nu} \equiv \partial_\mu B_\nu - \partial_\nu B_\mu, \tag{1.13}$$

where f^{ijk} are the structure constants [17]. W_μ^k and B_μ are nevertheless not physical particles. To end with physical bosons, a diagonalisation of the fields is needed by the transformations:

$$W_\mu^\pm \equiv \frac{1}{\sqrt{2}}\left(W_\mu^1 \mp iW_\mu^2\right), \tag{1.14}$$

$$\begin{pmatrix} Z_\mu \\ A_\mu \end{pmatrix} = \begin{pmatrix} \cos\theta_{\mathrm{w}} & -\sin\theta_{\mathrm{w}} \\ \sin\theta_{\mathrm{w}} & \cos\theta_{\mathrm{w}} \end{pmatrix} \begin{pmatrix} W_\mu^3 \\ B_\mu \end{pmatrix}, \tag{1.15}$$

where θ_{w} is the Weinberg angle and it is defined as $\tan\theta_{\mathrm{w}} = \frac{g'}{g}$. The physical fields $W_\mu^\pm$, Z_μ, A_μ are then associated with W-bosons, Z-bosons, and photons, respectively.

1.1.3 Standard neutrino interactions

Neutrinos can only weakly interact with other fermions via exchange of the W and Z bosons. The interaction with W-boson is called charged-current interaction (CC), described by the Lagrangian

$$\mathcal{L}_{\mathrm{cc}} = -\frac{g}{\sqrt{2}}\sum_{\ell=e,\mu,\tau}\bar{\ell}\gamma^\mu\frac{1-\gamma_5}{2}\nu_\ell W_\mu^- + \text{hermitian-conjugate (h.c.)}, \tag{1.16}$$

The Feynman diagrams of the neutrino CC interactions are shown in Figure 1.2.

Similarly, the Lagrangian coupling neutrinos and Z-boson can be written as

$$\mathcal{L}_{\mathrm{nc}} = -\frac{g}{\cos\theta_{\mathrm{w}}}\sum_{\ell=e,\mu,\tau}\bar{\nu}_\ell\gamma^\mu\frac{1-\gamma_5}{2}\nu_\ell Z_\mu, \tag{1.17}$$
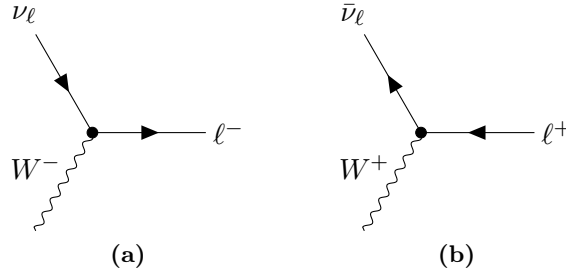
Figure 1.2 – Charged-current interactions between W-boson and (a) neutrino and (b) anti-neutrino.
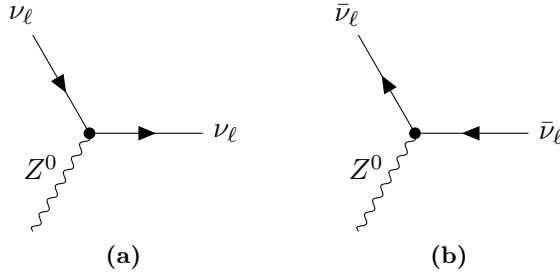
Figure 1.3 – Neutral-current interactions between Z-boson and (a) neutrino and (b) antineutrino.

giving two Feynman diagrams for neutrinos and antineutrinos shown in Figure 1.3. The Z-boson has no electric charge, so this interaction is named neutral-current interaction (NC).

The Lagrangian of both interactions include a factor $\frac{1-\gamma_5}{2}$, which is the left-handed projector that can be used to obtain the left-handed component of a spinor. That is to say, for both interactions, only the left handed chirality fields are involved.

1.1.4 The Brout–Englert–Higgs mechanism

Equation (1.8) does not include fermion mass terms like $m\bar{\psi}\psi$ in Equation (1.1). A mass terms can be decomposed as

$$m\bar{\psi}\psi = m\bar{\psi}(P_L + P_R)(P_L + P_R)\psi = m(\overline{\psi_R}\psi_L + \overline{\psi_L}\psi_R), \qquad (1.18)$$

where P_L and P_R are the chirality projectors [17]. Due to the gauge transformations which are not identical for left-handed and right-handed fields, the mass term combining directly fields with different chiralities spoils immediately the EW gauge symmetry. Consequently, they should not be included in GSW. However, fermions are certainly massive, so there must be a mechanism whereby masses can be generated while preserving the gauge invariance. In 1964, three independent groups, Robert Brout and François Englert [21], Peter Higgs [22], and Gerald Guralnik, C. R. Hagen, and Tom Kibble [23], proposed a mechanism that can fix the problem.

Given a scalar field $H \equiv (\phi^+, \phi^0)^T$, the gauge invariant Lagrangian reads

$$\mathcal{L}_\mathrm{H} = (D^\mu H)^\dagger (D_\mu H) - \mu^2 H^\dagger H - \lambda (H^\dagger H)^2, \qquad (1.19)$$

where μ^2 is a real number and λ is a positive real number. The particle spectrum described by the Lagrangian (1.19) depends on the choice of the value μ^2. If $\mu^2 > 0$,

the vacuum expectation value (VEV) of H is 0, since it gives zero potential. In this case the vacuum state is $SU(2)_L \times U(1)_Y$ gauge invariant and the gauge symmetry is preserved. If $\mu^2 < 0$, the minima should be fixed by

$$|\langle H \rangle|^2 = \frac{1}{2}v^2, \tag{1.20}$$

where $v = \sqrt{-\frac{\mu^2}{\lambda}}$ and $\langle H \rangle = \langle 0|H|0 \rangle$ denotes the VEV of field H.

As nature must have a well defined vacuum state for any field, one of the possible vacuum states is chosen

$$\langle H \rangle = \frac{1}{\sqrt{2}} \begin{pmatrix} 0 \\ v \end{pmatrix}. \tag{1.21}$$

This choice agrees with our observation that the vacuum is always electrically neutral. The consequence of this choice is that the vacuum state is no longer the $SU(2)_L \times U(1)_Y$ gauge invariant, which is termed spontaneous symmetry breaking. However, the vacuum state is still gauge invariant under the global gauge transformation $e^{i\alpha(\sigma^3 + \frac{Y}{2})}$, which simply refers to the $U(1)$ symmetry of QED.

In order to describe the excitations from the vacuum, we can parametrise the field H in vicinity of the chosen minimum as

$$H = e^{i\sigma^k \xi_k(x)} \frac{1}{\sqrt{2}} \begin{pmatrix} 0 \\ v + h(x) \end{pmatrix}, \tag{1.22}$$

where ξ^k $(k = 1, 2, 3)$ and $h(x)$ stand for the four real scalar fields. The $SU(2)_L$ gauge transformation of H is then written as

$$H(x) \rightarrow H'(x) = e^{-i\sigma^k \alpha_k(x)} H(x) = e^{i(\xi_k(x) - \alpha_k(x))\sigma^k} \begin{pmatrix} 0 \\ \frac{1}{\sqrt{2}}(v + h(x)) \end{pmatrix}. \tag{1.23}$$

Let $\xi_k(x) = \alpha_k(x)$, the transformed field becomes

$$H(x) = \frac{1}{\sqrt{2}} \begin{pmatrix} 0 \\ v + h(x) \end{pmatrix}. \tag{1.24}$$

With the covariant derivative (1.9) and the field (1.24), the Lagrangian (1.19) leads to the generation of boson masses and fermion masses. We firstly take a look on boson masses. The dynamic term $(D^\mu H)^\dagger (D_\mu H)$ reads

$$
\begin{aligned}
(D^\mu H)^\dagger (D_\mu H) =& \frac{v^2}{8} \begin{pmatrix} 0 & 1 \end{pmatrix} \left(g\sigma^k W_\mu^k + g'B_\mu \right) \left(g\sigma^k W_\mu^k + g'B_\mu \right) \begin{pmatrix} 0 \\ 1 \end{pmatrix} \\
&+ \frac{1}{2}\partial_\mu h \partial^\mu h + \text{interactions} \\
=& \frac{v^2}{8} \begin{pmatrix} W_\mu^1 & W_\mu^2 & W_\mu^3 & B_\mu \end{pmatrix} \begin{pmatrix} g^2 & 0 & 0 & 0 \\ 0 & g^2 & 0 & 0 \\ 0 & 0 & g^2 & -gg' \\ 0 & 0 & -gg' & g^2 \end{pmatrix} \begin{pmatrix} W_\mu^1 \\ W_\mu^2 \\ W_\mu^3 \\ B_\mu \end{pmatrix} \\
&+ \frac{1}{2}\partial_\mu h \partial^\mu h + \text{interactions}.
\end{aligned} \tag{1.25}
$$

After diagonalising the matrix so that the eigenstates are physical fields $W_\mu^\pm$, Z_μ^0 and A_μ, their masses are expressed as

$$m_{W^\pm} = \frac{1}{2}gv, \quad m_{Z^0} = \frac{1}{2}\sqrt{g^2 + g'^2}\,v = \frac{gv}{2\cos\theta_\text{w}}, \quad m_\gamma = 0. \tag{1.26}$$

The masses of fermions should stem from a new Lagrangian describing the Yukawa interactions between Higgs bosons and fermions:

$$\mathcal{L}_{\text{Yukawa}} = -\overline{Q_L}Y_u\tilde{H}U_R - \overline{Q_L}Y_dHD_R - \overline{\ell_L}Y_\ell HE_R + \text{h.c.}, \qquad (1.27)$$

where $\tilde{H} \equiv i\sigma^2 H^*$ is the charge conjugate of H, and Y_u, Y_d, Y_l are the 3×3 Yukawa coupling matrices. Note that neutrino masses cannot be generated by the coupling, because right-handed neutrinos do not exist in the SM. Models for neutrino masses will be discussed later in Section 1.2. By injecting Equation (1.24) in Equation (1.27), the mass terms emerge and assign the following masses to the weak eigenstates of quarks and charged leptons:

$$M_u = \frac{1}{\sqrt{2}}vY_u, \quad M_d = \frac{1}{\sqrt{2}}vY_d, \quad M_l = \frac{1}{\sqrt{2}}vY_l. \qquad (1.28)$$

In fact, the flavour eigenstates are mixtures of mass eigenstates, whose eigenvalues are the particle masses [24–26]. To obtain the masses, we further diagonalise the Yukawa coupling matrices by means of the bi-unitary transformations,

$$\begin{aligned} U_u^\dagger M_u U_u' &= \text{Diag}\{m_u, m_c, m_t\}, \\ U_d^\dagger M_d U_d' &= \text{Diag}\{m_d, m_s, m_b\}, \\ U_l^\dagger M_l U_l' &= \text{Diag}\{m_e, m_\mu, m_\tau\}, \end{aligned} \qquad (1.29)$$

where m_i denotes the mass of quarks and charged leptons i.

1.2 Massive neutrinos

As above mentioned, neutrino masses cannot be obtained through the spontaneous symmetry breaking of the Higgs field in the SM. However, neutrino oscillations have been observed, which proves that neutrinos are massive. Therefore, models are needed to complete the SM with massive neutrinos.

1.2.1 Dirac neutrinos

The first possible extension of the SM is the Dirac neutrino mass model, where neutrinos are considered to be massive Dirac fermions. Three right-handed neutrinos N_{1R}, N_{2R}, N_{3R} are then introduced in the SM, and they must be sterile, i.e., only sensitive to the gravity but not to other forces. Consequently, analogous to the other fermions in Equation (1.27), the Yukawa interaction between the lepton doublet and the singlet of right-handed neutrinos reads

$$-\mathcal{L}_{\text{Dirac}} = \overline{\ell_L}Y_\nu\tilde{H}N_R + \text{h.c.}, \qquad (1.30)$$

where $N_R \equiv (N_{1R}, N_{2R}, N_{3R})^T$. The spontaneous breaking of local $SU(2)_L \times U(1)_Y$ symmetry gives rise to the neutrino mass term in the Lagrangian:

$$\begin{aligned} -\mathcal{L}'_{\text{Dirac}} &= \overline{\nu_L}M_D N_R + \text{h.c.} \\ &= \overline{\nu_L'}\widehat{M_\nu}N_R' + \text{h.c.}, \end{aligned} \qquad (1.31)$$

where $M_D = Y_\nu \langle H \rangle$. M_D can be diagonalised by

$$V^\dagger M_D U = \text{Diag}\{m_1, m_2, m_3\} \equiv \widehat{M_\nu},$$

with V and U being two unitary matrices. U and V later can be absorbed by the neutrino fields via $\nu_L' = V^\dagger \nu_L$, and $N_R' = U^\dagger N_R$. Define the Dirac spinor of neutrinos by combining left-handed and right-handed components

$$\nu' = \nu_L' + N_R' = \begin{pmatrix} \nu_1 \\ \nu_2 \\ \nu_3 \end{pmatrix}, \tag{1.32}$$

we rewrite Equation (1.31) in terms of neutrino mass eigenstates:

$$-\mathcal{L}_{\text{Dirac}}' = \overline{\nu'} \widehat{M_\nu} \nu' = \sum_{i=1}^{3} m_i \overline{\nu_i} \nu_i. \tag{1.33}$$

In the Dirac picture, the neutrinos are Dirac particles, of which the masses are generated exactly in the same way as other fermions in the SM, and the total lepton number is therefore conserved.

1.2.2 Majorana neutrinos

Particles such as electron, muon, quarks, are Dirac particles, as their antiparticles are not identical to themselves. Since neutrinos are electrically neutral, the $U(1)_{\text{QED}}$ symmetry does not impose neutrinos to be Dirac. Theoretically, neutrinos can possibly be Majorana particles, and in this picture, antineutrinos and neutrinos are identical. With the Majorana property, the Majorana mass term of a left-handed neutrino field ν_L can be written as

$$-\mathcal{L}_{\text{Majorana}} = \frac{1}{2} \overline{\nu_L} M_L (\nu_L)^{\text{c}} + \text{h.c.}, \tag{1.34}$$

where $(\nu_L)^{\text{c}}$ denotes its right-handed charge-conjugate. The mass matrix M_L must be symmetric, i.e., $M_L^T = M_L$. Therefore, the mass matrix is diagonalised by $V^\dagger M_L V^* = \widehat{M_\nu} \equiv \text{Diag}\{m_1, m_2, m_3\}$ with a unitary matrix V and Equation (1.34) becomes

$$-\mathcal{L}_{\text{Majorana}} = \frac{1}{2} \overline{\nu_L'} \widehat{M_\nu} (\nu_L')^{\text{c}} + \text{h.c.}, \tag{1.35}$$

where $\nu_L' = V^\dagger \nu_L$ and $(\nu_L')^{\text{c}} = \mathcal{C} \overline{\nu_L'}^T$, $\mathcal{C}$ is the charge conjugation operator. Given the Majorana spinor of neutrinos is

$$\nu' = \nu_L' + (\nu_L')^{\text{c}} = \begin{pmatrix} \nu_1 \\ \nu_2 \\ \nu_3 \end{pmatrix}, \tag{1.36}$$

the mass terms can be further simplified as

$$-\mathcal{L}_{\text{Majorana}} = \frac{1}{2} \overline{\nu'} \widehat{M_\nu} \nu' = \frac{1}{2} \sum_{i=1}^{3} m_i \overline{\nu_i} \nu_i. \tag{1.37}$$

In Majorana picture, neutrinos require no right-handed neutrinos for the mass generation. Neutrinos and antineutrinos are the same particles, so the total lepton number is not conserved. In this case, it should be possible to observe the neutrino-less double β-decay, a rare process that two β-decays happen at the same time without emitting neutrinos. Currently, many experiments are actively searching for this process, and we will mention some of them in Section 1.4.2.

1.2.3 Seesaw paradigm

The unexpected small neutrino masses can be explained with the "Seesaw" mechanism. By introducing hybrid mass terms with new right-handed fermions N_R and its charge-conjugates $(N_R)^c$, the Lagrangian for mass generation can be written as

$$-\mathcal{L}_{\text{hybrid}} = \overline{\nu_L} M_D N_R + \frac{1}{2}\overline{\nu_L} M_L (\nu_L)^c + \frac{1}{2}\overline{(N_R)^c} M_R N_R + \text{h.c.}$$

$$= \frac{1}{2} \begin{bmatrix} \overline{\nu_L} & \overline{(N_R)^c} \end{bmatrix} \begin{pmatrix} M_L & M_D \\ M_D^T & M_R \end{pmatrix} \begin{bmatrix} (\nu_L)^c \\ N_R \end{bmatrix} + \text{h.c.}, \tag{1.38}$$

where M_D, M_L and M_R are mass matrices, among them, M_L and M_R are symmetric matrices. The larger matrix in Equation (1.38) combining M_D, M_L and M_R is then also symmetric, and can be diagonalised through the following transformation

$$\begin{pmatrix} V & R \\ S & U \end{pmatrix}^{\dagger} \begin{pmatrix} M_L & M_D \\ M_D^T & M_R \end{pmatrix} \begin{pmatrix} V & R \\ S & U \end{pmatrix}^{*} = \begin{pmatrix} \widehat{M}_\nu & \mathbf{0} \\ \mathbf{0} & \widehat{M}_N \end{pmatrix}, \tag{1.39}$$

where $\widehat{M}_\nu \equiv \text{Diag}\{m_1, m_2, m_3\}$, $\widehat{M}_N \equiv \text{Diag}\{M_1, M_2, M_3\}$ and the 3×3 sub-matrices V, R, S, U satisfy the following conditions:

$$VV^{\dagger} + RR^{\dagger} = SS^{\dagger} + UU^{\dagger} = \mathbf{1},$$
$$V^{\dagger}V + S^{\dagger}S = R^{\dagger}R + U^{\dagger}U = \mathbf{1},$$
$$VS^{\dagger} + RU^{\dagger} = V^{\dagger}R + S^{\dagger}U = \mathbf{0}. \tag{1.40}$$

So Equation (1.38) is further simplified as

$$-\mathcal{L}_{\text{hybrid}} = \frac{1}{2} \begin{bmatrix} \overline{\nu'_L} & \overline{(N'_R)^c} \end{bmatrix} \begin{pmatrix} \widehat{M}_\nu & \mathbf{0} \\ \mathbf{0} & \widehat{M}_N \end{pmatrix} \begin{bmatrix} (\nu'_L)^c \\ N'_R \end{bmatrix} + \text{h.c.}, \tag{1.41}$$

where we define $\nu'_L \equiv V^{\dagger}\nu_L + S^{\dagger}(N_R)^c$ and $N'_R = R^T(\nu_L)^c + U^T N_R$. The charge-conjugations are defined as $(\nu'_L)^c \equiv \mathcal{C}\overline{\nu'_L}^T$ and $(N'_R)^c = \mathcal{C}\overline{N'_R}^T$, respectively. The spinor in Seesaw mechanism is described by combining left-handed ν'_L, right-handed N'_R, and their charge-conjugates:

$$\nu' = \begin{bmatrix} \nu'_L \\ (N'_R)^c \end{bmatrix} + \begin{bmatrix} (\nu'_L)^c \\ N'_R \end{bmatrix} = \begin{pmatrix} \nu_1 \\ \nu_2 \\ \nu_3 \\ N_1 \\ N_2 \\ N_3 \end{pmatrix}. \tag{1.42}$$

The relation $\nu' = (\nu')^c$ is valid, so neutrinos are Majorana fermions in Seesaw mechanism. Thus, neutrino masses as eigenvalues of ν' emerge from Lagrangian 1.41:

$$-\mathcal{L}_{\text{hybrid}} = \frac{1}{2}\overline{\nu'} \begin{pmatrix} \widehat{M}_\nu & \mathbf{0} \\ \mathbf{0} & \widehat{M}_N \end{pmatrix} \nu' = \frac{1}{2} \sum_{i=1}^{3} \left(m_i \overline{\nu_i}\nu_i + M_i \overline{N_i}N_i \right). \tag{1.43}$$

The ansatz of Seesaw mechanism is $M_R \gg M_D \gg M_L$ and it leads to an approximation $R \sim S \sim \mathcal{O}(M_D/M_R)$. From the relation in Equation (1.40), we calculate

$$U\widehat{M}_N U^T = M_R(UU^{\dagger})^T + M_D^T(R^* U^T) \approx M_R,$$
$$V\widehat{M}_\nu V^T = M_L(VV^{\dagger})^T + M_D(S^* V^T) \approx M_L + M_D(S^* V^T)$$
$$\approx M_L - M_D M_R^{-1} M_D^T, \tag{1.44}$$

where $V \widehat{M_\nu} V^T$ is defined as the effective mass matrix of light neutrinos M_ν. This result is termed type-(I+II) Seesaw relation. If M_L is absent, the result becomes type-I Seesaw relation [27] and we have the effective mass matrix

$$M_\nu \approx -M_D M_R^{-1} M_D^T. \tag{1.45}$$

Equation (1.45) suggests that the small mass scale of M_ν is caused by the large mass scale of M_R, even though M_D is of the same order of magnitude as other fermions.

Seesaw mechanism predicts the non-unitarity of matrix V, which is interpreted as the leptonic flavour mixing matrix. The matrix plays an essential role in neutrino oscillations that will be talked about later in Section 1.3. The sub-percent precision measurements of oscillation parameters are expected to be a test of the matrix unitarity, providing a hint for the validity of Seesaw mechanism.

1.3 Neutrino oscillations in vacuum

As mentioned previously, flavour eigenstates of quarks are mixtures of mass eigenstates, which are the particle propagation eigenstates. The flavour mixing results in the so-called neutral particle oscillations in the hadronic sector, such as $K^0 \leftrightarrow \overline{K}^0$ oscillation. Inspired by the phenomenon, Pontecorvo proposed in 1957 oscillations between neutrinos and antineutrinos [28]. Although such oscillations have never been found, he pointed out the first time that neutrinos may oscillate, and if they oscillate, they should be massive. Later in 1960s', the theory was modernised by interpreting neutrino oscillations as a quantum phenomenon whereby a massive neutrino produced in one specific flavour (ν_e, ν_μ, ν_τ) is detected to have different flavour after propagating a certain distance, also known as the baseline [26, 29, 30].

Given the neutrino flavour eigenstates $|\nu_\alpha\rangle = (|\nu_e\rangle, |\nu_\mu\rangle, |\nu_\tau\rangle)^T$, and the neutrino mass eigenstates $|\nu_i\rangle = (|\nu_1\rangle, |\nu_2\rangle, |\nu_3\rangle)^T$, analogous to CKM matrix for quarks [24, 25], we have

$$|\nu_\alpha\rangle = \sum_{i=1}^{3} U_{\alpha i}^* |\nu_i\rangle, \tag{1.46}$$

where U is a matrix describing leptonic flavour mixing, which is commonly referred to as Pontecorvo-Maki-Nakagawa-Sakata (PMNS) matrix [26].

Only considering the known active flavours of neutrinos, the matrix then must be unitary, and its most common parametrisation can be written as

$$U = \begin{pmatrix} 1 & & \\ & c_{23} & s_{23} \\ & -s_{23} & c_{23} \end{pmatrix} \begin{pmatrix} c_{13} & & s_{13}e^{-i\delta} \\ & 1 & \\ -s_{13}e^{i\delta} & & c_{13} \end{pmatrix} \begin{pmatrix} c_{12} & s_{12} & \\ -s_{12} & c_{12} & \\ & & 1 \end{pmatrix} \times \mathrm{Diag}\{e^{i\rho}, e^{i\sigma}, 1\}$$

$$\tag{1.47}$$

where $c_{ij} \equiv \cos\theta_{ij}$, $s_{ij} \equiv \sin\theta_{ij}$ (for $ij = 12, 13, 23$). In terms of unitary matrix, PMNS should have had 9 free parameters, namely 3 mixing angles ($\theta_{12}, \theta_{13}, \theta_{23}$) and 6 phases. However, all phases are not physical [31]. Rephasing both charged leptons and neutrinos can eliminate some of them. If neutrinos are Dirac, then 5 phases are cancelled by this means, only the Dirac CP-violating phase (δ) is left. Otherwise, if neutrinos are Majorana, only 3 phases can be cancelled by rephasing the charged leptons, therefore, three phases (δ, ρ, σ) are left free, and the last two are termed Majorana CP-violating phases. But the Majorana phases do not contribute to oscillations since the its probability depends on UU^*, where the phases cancel.

Assuming that the mass eigenstates $|\nu_k\rangle$ propagate in vacuum as plane waves:

$$|\nu_k(x,t)\rangle = e^{-i(E_k t - \mathbf{px})}|\nu_k\rangle, \tag{1.48}$$

where $k = 1, 2, 3$, the wave function of the flavour eigenstates with a baseline L can be given by

$$|\nu_\alpha(L,t)\rangle = \sum_k U_{\alpha k}^* e^{-i(E_k t - \mathbf{p}L)}|\nu_k\rangle \tag{1.49}$$

$$= \sum_\beta \sum_k U_{\alpha k}^* e^{-i(E_k t - \mathbf{p}L)} U_{\beta k}|\nu_\beta\rangle. \tag{1.50}$$

The probability to observe the oscillation from flavour α to flavour β is therefore given by

$$P(\nu_\alpha \to \nu_\beta, L, t) = |\langle \nu_\beta |\nu_\alpha(L,t)\rangle|^2$$
$$= \sum_{k,l} U_{\alpha k}^* U_{\beta k} U_{\alpha l} U_{\beta l}^* e^{-i(E_k t - p_k L)} e^{i(E_l t - p_l L)}. \tag{1.51}$$

For ultra-relativistic neutrinos, namely the neutrino energy E is much larger than the neutrino mass, $t \approx L$ and $E_k \approx E_l = E$, therefore we have

$$E_k t - p_k L = \frac{E_k^2 - p_k^2}{E_k + p_k} L = \frac{m_k^2}{2E} L. \tag{1.52}$$

Similar result can be obtained for $E_l t - p_l L$, so Equation (1.51) can be simplified as

$$P(\nu_\alpha \to \nu_\beta, L) = \sum_k |U_{\alpha k}|^2 |U_{\beta k}|^2 + 2\mathfrak{Re} \sum_{k>l} U_{\alpha k}^* U_{\beta k} U_{\alpha l} U_{\beta l}^* e^{-i\frac{\Delta m_{kl}^2}{2E}L}, \tag{1.53}$$

where $\Delta m_{kl}^2 \equiv m_k^2 - m_l^2$. A similar formula can be constructed for antineutrinos by interchanging U and U^*:

$$P(\bar\nu_\alpha \to \bar\nu_\beta, L) = \sum_k |U_{\alpha k}|^2 |U_{\beta k}|^2 + 2\mathfrak{Re} \sum_{k>l} U_{\alpha k} U_{\beta k}^* U_{\alpha l}^* U_{\beta l} e^{-i\frac{\Delta m_{kl}^2}{2E}L}. \tag{1.54}$$

If neutrinos oscillate, two conditions have to be fulfilled: firstly, the corresponding PMNS matrix elements must not be diagonal; secondly, neutrinos must have non-vanishing masses and all masses must not be degenerated. One can notice also that both Equations (1.53) and (1.54) give $\delta_{\alpha\beta}$ when $L = 0$, which is as we expect.

Dirac CP-violating phase δ is related to the different oscillation probability of neutrinos and antineutrinos. The difference can be written as [14]

$$\Delta P_{\alpha\beta}(L) \equiv P(\nu_\alpha \to \nu_\beta, L) - P(\bar\nu_\alpha \to \bar\nu_\beta, L)$$
$$= 4\mathfrak{Im} \sum_{k>l} U_{\alpha k}^* U_{\beta k} U_{\alpha l} U_{\beta l}^* e^{-i\frac{\Delta m_{kl}^2}{2E}L}. \tag{1.55}$$

By requiring $\alpha \neq \beta$, we define

$$J_{\alpha\beta}^{kl} \equiv \mathfrak{Im}\left(U_{\alpha k}^* U_{k\beta} U_{\alpha l} U_{l\beta}^*\right) = \pm J, \tag{1.56}$$

where $J = c_{12} s_{12} c_{23} s_{23} c_{13}^2 s_{13} \sin\delta$ is *Jarlskog invariant*. If $\alpha = \beta$, $\Delta P_{\alpha\beta}(L)$ becomes 0. This implies that neutrino disappearance experiments, where the survival probabilities of neutrinos are measured, are not sensitive to the CP-violation.

Specially, the survival probability of electron antineutrinos is commonly measured in reactor neutrino experiments. When neutrinos propagates in matter (e.g. the Earth), they can interact with particles in matter via weak interaction, which alters the oscillation probabilities. Such an effect has been formalised by Stanislav Mikheyev, Alexei Smirnov [32], and Lincoln Wolfenstein [33, 34]. The effect is now referred to as Mikheyev–Smirnov–Wolfenstein (MSW) effect. In a typical reactor neutrino experiment, where neutrino energy is only a few MeV and the baseline is less than $100\,\mathrm{km}$, neutrino propagation can nevertheless be considered to be in vacuum, and the terrestrial matter effects are safely neglected [35]. By substituting both α and β in Equation (1.54) with e, the probability can be written as

$$P(\bar{\nu}_e \rightarrow \bar{\nu}_e, L) = 1 - 4 \sum_{k>l} \left(|U_{ek}|^2 |U_{el}|^2 \sin^2 \frac{\Delta m_{kl}^2 L}{4E} \right). \tag{1.57}$$

It can be further expressed in terms of mixing parameters defined in Equation (1.47):

$$\begin{aligned} P(\bar{\nu}_e \rightarrow \bar{\nu}_e, L) = 1 &- \sin^2 2\theta_{12} \cos^4 \theta_{13} \sin^2 \Delta_{21} \\ &- \sin^2 2\theta_{13} \left(\cos^2 \theta_{12} \sin^2 \Delta_{31} + \sin^2 \theta_{12} \sin^2 \Delta_{32} \right), \end{aligned} \tag{1.58}$$

with $\Delta_{kl} \equiv \Delta m_{kl}^2 L/4E$.

The mass squared differences Δm_{21}^2, Δm_{32}^2, and Δm_{31}^2 are observables in neutrino oscillations, and only two of them are independent. Δm_{21}^2 is measured to be very small with respect to Δm_{31}^2 or Δm_{32}^2 [14], therefore, $\left| \Delta m_{31}^2 \right| \approx \left| \Delta m_{32}^2 \right|$. The sign of Δm_{21}^2 is also known through observations of solar neutrinos, which can only be explained by ν_e MSW effect in the Sun [32].

It is challenging to determine experimentally the neutrino mass hierarchy (νMH) between two possible schemes: the normal hierarchy (NH) where $m_1 < m_2 < m_3$, and the inverted hierarchy (IH) where $m_3 < m_1 < m_2$. In Figure 1.4, both are graphically represented together with percentages of flavour eigenstates in each mass eigenstate labelled.

Figure 1.5 depicts electron antineutrino survival probabilities with different νMHs as a function of L/E. The left plot shows 3 consecutive oscillation periods from $L/E = 0$, whilst right plot zooms in the vicinity corresponding to the first valley of θ_{12}-driven oscillations in the left plot. We observe a slow oscillation from the first negative term in Equation (1.58) of Δm_{21}^2, and a fast oscillation from the last two terms in the same equation of Δm_{31}^2 and Δm_{32}^2. To see more clearly these two oscillations, Equation (1.58) can be transformed into [36–38]

$$\begin{aligned} P(\bar{\nu}_e \rightarrow \bar{\nu}_e, L) = 1 &- \frac{1}{2} \sin^2 2\theta_{13} \left[1 - \sqrt{1 - \sin^2 2\theta_{12} \sin^2 \Delta_{21}} \cos(2|\Delta_{ee}|\pm\phi) \right] \\ &- \cos^4 \theta_{13} \sin^2 2\theta_{12} \sin^2 \Delta_{21}, \end{aligned} \tag{1.59}$$

with $\Delta_{ee} \equiv \Delta m_{ee}^2 L/4E$. Here, the mass squared difference Δm_{ee}^2 and the phase ϕ are defined by [39, 40]

$$\Delta m_{ee}^2 = \cos^2 \theta_{12} \Delta m_{31}^2 + \sin^2 \theta_{12} \Delta m_{32}^2, \tag{1.60}$$

$$\sin \phi = \frac{c_{12}^2 \sin(2s_{12}^2 \Delta_{21}) - s_{12}^2 \sin(2c_{12}^2 \Delta_{21})}{\sqrt{1 - \sin^2 2\theta_{12} \sin^2 \Delta_{21}}}. \tag{1.61}$$

The new form gives rise to an analytical explanation of two oscillations: the slow one is controlled by Δ_{21}, and the fast one is controlled by Δ_{ee}. More important, it exists a

Normal hierarchy

m_3^2
2%   42%   56%

$2.54 \times 10^{-3} \, \text{eV}^2$

29%   34%   37%
m_2^2

$7.37 \times 10^{-5} \, \text{eV}^2$

m_1^2
69%   24%   7%

(a)

Inverted hierarchy

29%   23%   48%
m_2^2

$7.37 \times 10^{-5} \, \text{eV}^2$

m_1^2
69%   20%   11%

$2.56 \times 10^{-3} \, \text{eV}^2$

m_3^2
2%   58%   40%

(b)
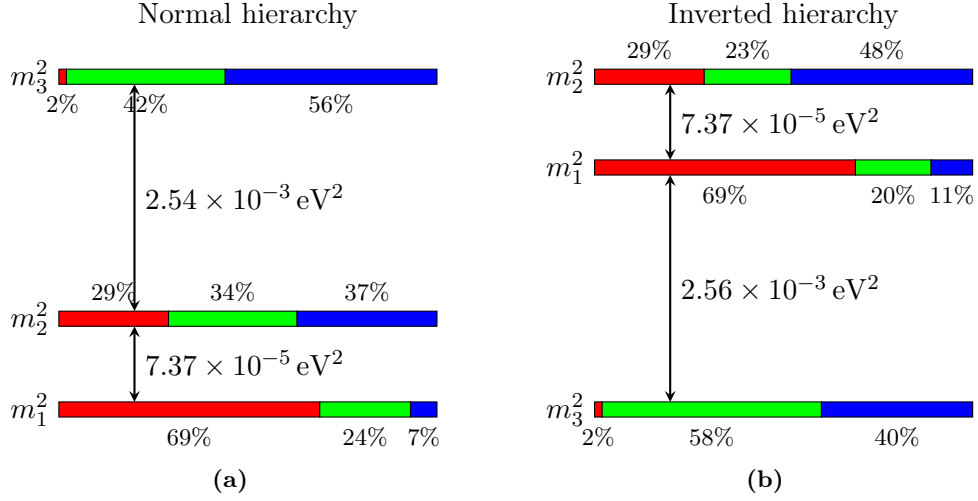
Figure 1.4 – (a) Normal hierarchy (NH). (b) Inverted hierarchy (IH). The red part represents flavour eigenstate ν_e, the green part represents flavour eigenstate ν_μ, and the blue part represents flavour eigenstate ν_τ. The percentages are calculated with best fit values of PMNS parameters in [14].
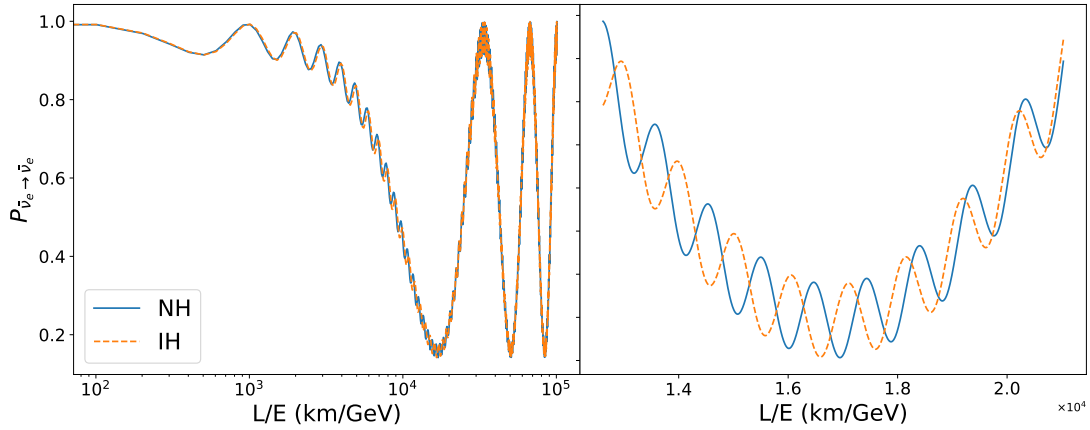
Figure 1.5 – Both plots show electron antineutrino survival probability with different νMHs as a function of L/E. Values are calculated with PMNS parameters in [14]. The left plot shows oscillations for a large range covering 3 oscillation periods, whilst the right plot shows only the vicinity of the first valley of θ_{12}-driven oscillations in the left plot. In the right plot, the phase difference ϕ between NH and IH is clearly displayed.

phase, depending on the νMH, it can be either positive $(+\phi)$ for NH, or negative $(-\phi)$ for IH. Indeed, in the right plot of Figure 1.5, we notice that the probability of different νMHs differs by a phase. Therefore, by measuring precisely the oscillation, we can confirm whether the phase is positive or negative, whereby the νMH is unambiguously determined. This method can be carried out by a reactor neutrino experiment.

1.4 Current status of neutrino experiments

In this section, we will outline the current status of neutrino experiments, and show the most recent results of the oscillation parameters. The neutrino experiments that have different objectives than measuring the oscillation parameters are also mentioned in this section.

1.4.1 Oscillation experiments

Let us review the parametrisation of PMNS matrix in Equation (1.47), ignoring the last diagonal matrix containing the Majorana phases, it factorises the PMNS matrix into three unitary matrices. Due to the historical reason, these three matrices are named in some references "atmospheric sector", "reactor sector", and "solar sector".

The first unitary matrix contains θ_{23}, which was first studied with atmospheric neutrinos produced by high energy cosmic ray in the Earth's atmosphere. For atmospheric neutrinos, the oscillations $\overset{(-)}{\nu}_\mu \to \overset{(-)}{\nu}_\mu$ are dominated by the parameters θ_{23} and Δm^2_{31}, so they are also referred to as atmospheric parameters, denoted by θ_atm and Δm^2_atm. Due to the small Δm^2_{21}, $\Delta m^2_{31} \approx \Delta m^2_{32}$. In some context, Δm^2_{32} can be regarded as Δm^2_atm.

θ_{13} in the second unitary matrix can be accessed via the oscillation $\bar{\nu}_e \to \bar{\nu}_e$, which was initially sought by reactor neutrino experiments.

θ_{12} in the last unitary matrix is related to the oscillation $\nu_e \to \nu_e$, which was found the first time in the solar neutrino experiment Homestake [41]. θ_{12} and Δm^2_{21} can be measured through this oscillation. They are also famous as $\theta_\odot$ and $\Delta m^2_\odot$, or solar parameters.

It is good to notice that nowadays people use different sources of neutrinos to measure the parameters, but the jargon "atmospheric parameters" and "solar parameters" are still widely used.

θ_{12} and Δm^2_{21} measurements

These two parameters are in the so-called solar sector. As neutrinos are only sensitive to weak interaction, they can travel a long distance to reach our detectors, even if there is a lot of matter in the way. People then realised that we can use neutrinos to study the physics in some places from where other particles cannot reach the detectors, for example, the solar core.

Homestake was the first solar neutrino detector, detecting neutrinos via the radiochemical reaction $\nu_e + {}^{37}\mathrm{Cl} \to e^- + {}^{37}\mathrm{Ar}$. Despite the successful detection of solar neutrinos, it reported a large deficit of neutrino flux as compared with the prediction of the Standard Solar Models (SSM) [42], as shown in Figure 1.6. SAGE [44] and GALLEX [45] using the reaction $\nu_e + {}^{71}\mathrm{Ga} \to e^- + {}^{71}\mathrm{Ge}$, and Kamiokande [46] and Super-Kamiokande [47] using the elastic scattering (ES) $\nu_x + e^- \to \nu_x + e^-$ subsequently confirmed the existence of such a deficit.
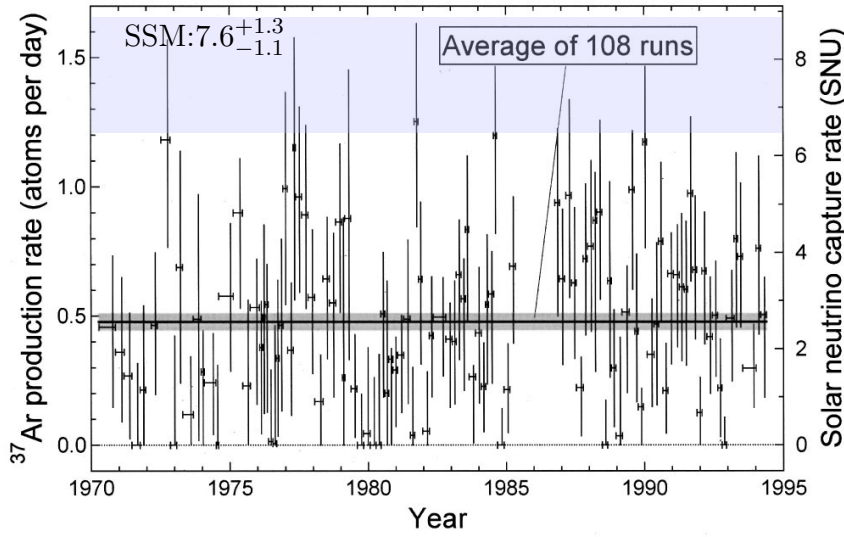
Figure 1.6 – A summary of runs made at Homestake over a period of 25 years, giving an average solar neutrino flux of 2.56 ± 0.16(statistical error)± 0.16(systematic error) SNU. The average is about $1/3$ as large as the flux predicted by the SSM [43].

The debate about whether the deficit is caused by neutrino oscillations continued until the SNO experiment [48] solved unambiguously the "solar neutrino puzzle" [49]. SNO was a 100-ton heavy water (D_2O) Cherenkov detector, it measured the total flux of all neutrino flavours from the Sun using three processes, the elastic scattering (ES) between all neutrinos and electrons, the charge current (CC) interaction between electron neutrinos and deuterium, and neutral current (NC) interaction between all neutrinos and deuterium. Figure 1.7 demonstrates that the measured flux of all neutrino flavours from the NC channel was consistent with the prediction of SSM, while the measured ν_e flux from the CC channel is 30% as large as the prediction [50], which shows that the same level of ν_e deficit was also observed in SNO as in the other solar neutrino experiments.

The KamLAND experiment [52], a reactor neutrino experiment with an average baseline equal to 180 km, observed at first the reactor neutrino oscillation, and measured precisely Δm_{21}^2. It used a kiloton-liquid-scintillator detector to detect neutrinos from all Japanese nuclear power plants. Figure 1.8 shows the survival probability measured by KamLAND, from which the dependency of the probability to L/E is demonstrated. The solutions of θ_{12} and Δm_{21}^2 from KamLAND data and the combined analysis of solar neutrino experiments is shown in Figure 1.9.

In 2019, the current best result obtained from the global fit [55] with 1σ of θ_{12} is $33.82_{-0.76}^{+0.78}$ degree, and Δm_{21}^2 is $7.39_{-0.20}^{+0.21} \times 10^{-5}\,\mathrm{eV}^2$.

θ_{23} and Δm_{32}^2 measurements

The first observations of atmospheric neutrinos were done in the 1960s' by two experiments in India [56] and South Africa [57]. However, they did not report any anomaly of the atmospheric neutrino flux. In 1986, IMB [58] and Kamiokande [59] found a deficit in their measured data with respect to the Monte-Carlo (MC) data. In 1992, things became clearer with more statistics in both IMB [60] and Kamiokande [61], by showing that the deficit was statistically significant, and the latter even gave an analysis with the assumptive $\nu_\mu \to \nu_\tau$ oscillations. Despite the objection of some experiments [62, 63],
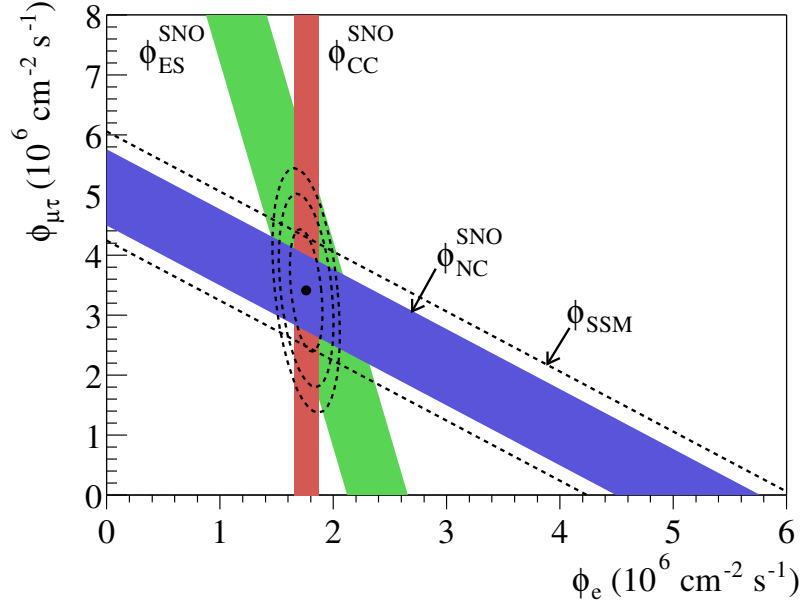
Figure 1.7 – Flux of ^{8}B solar neutrinos which are μ or τ flavour vs flux of electron neutrinos deduced from the three neutrino reactions in SNO. The diagonal bands show the total ^{8}B flux as predicted by the SSM [51] (dashed lines) and that measured with the NC reaction in SNO (solid band), the measured and predicted flux are consistent [50].
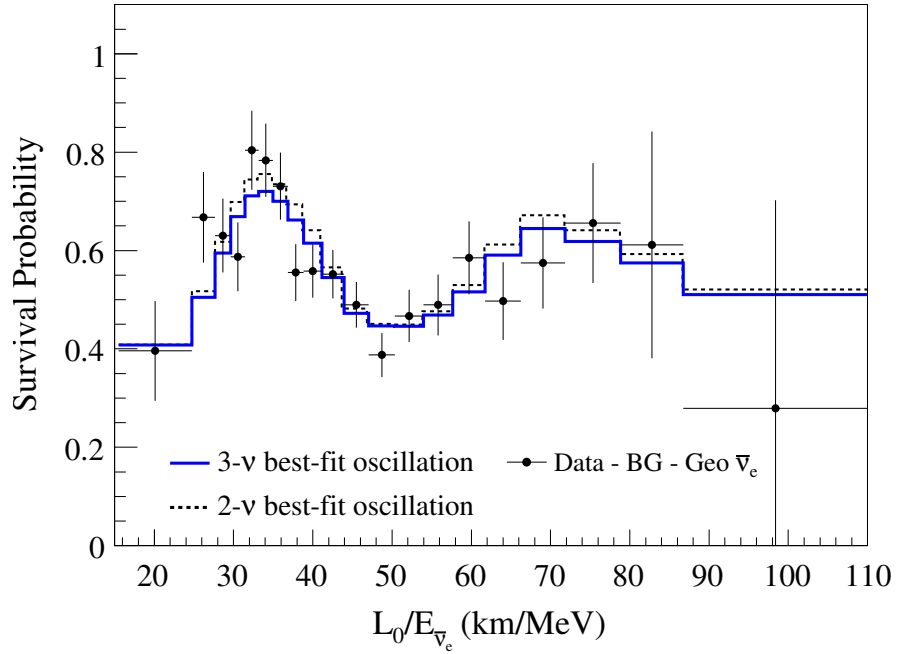
Figure 1.8 – The survival probability of reactor neutrino $\bar{\nu}_e$ measured in KamLAND [53]. L_0 is the effective baseline equal to 180 km.
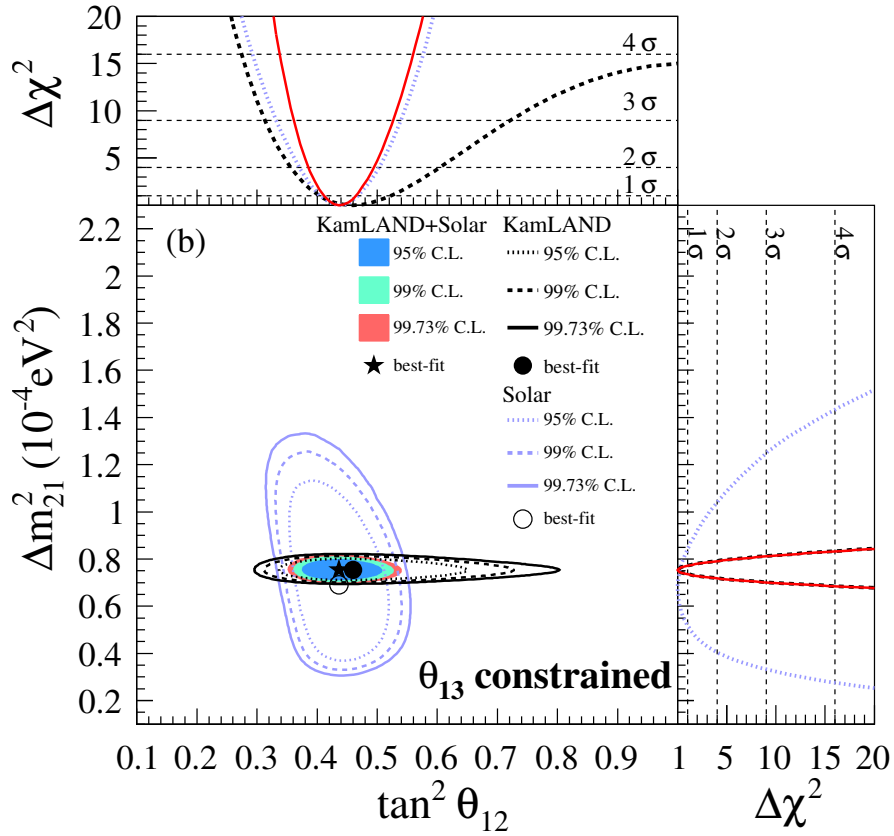
Figure 1.9 – Allowed regions projected in the $(\tan^2 \theta_{12}, \Delta m_{21}^2)$ plane, for solar and KamLAND data from a 3-flavor oscillation analysis. The coloured regions are from a combined analysis of the solar and KamLAND data. The side panels show the $\Delta \chi^2$-profiles projected onto the $\tan^2 \theta_{12}$ and Δm_{21}^2 axes. For this result, the value of θ_{13} is constrained by the results from reactor experiments with $\sim$km baselines [54].
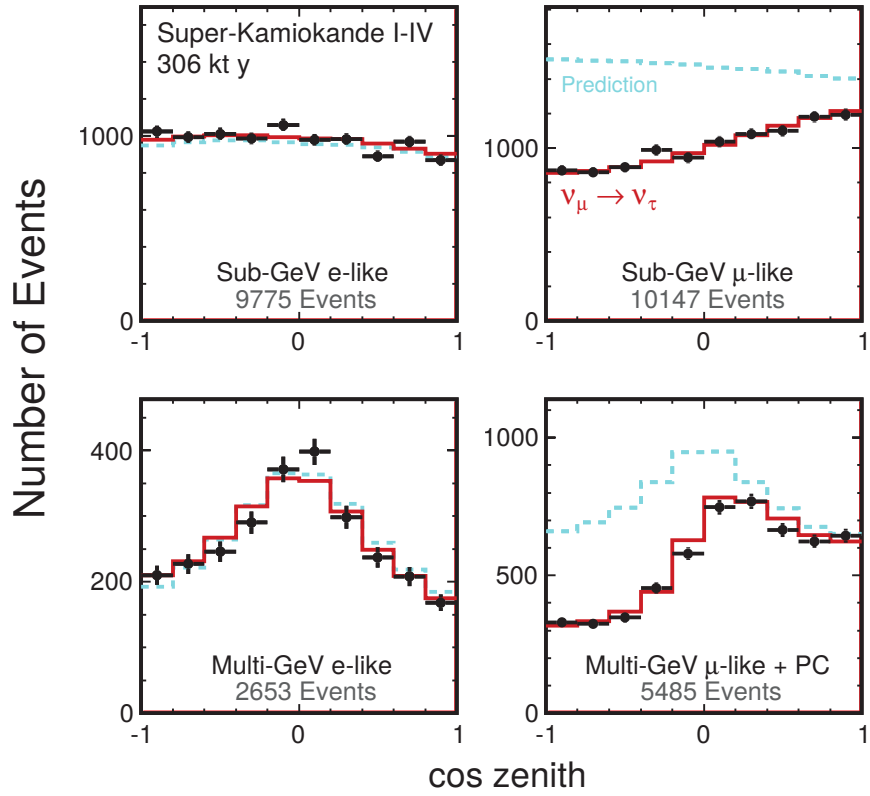
Figure 1.10 – Comparisons of different sub-samples of Super-Kamiokande data with the corresponding MC prediction. Upward-going particles have $\cos\theta < 0$ and downward-going particles have $\cos\theta > 0$. Sub-GeV and multi-GeV denotes samples with visible energy $< 1.33\,\mathrm{GeV}$ and $> 1.33\,\mathrm{GeV}$, respectively. The blue dashed lines show the non-oscillated distribution, and the solid histograms show the best-fit expectations for $\nu_\mu \rightarrow \nu_\tau$ oscillations [14].
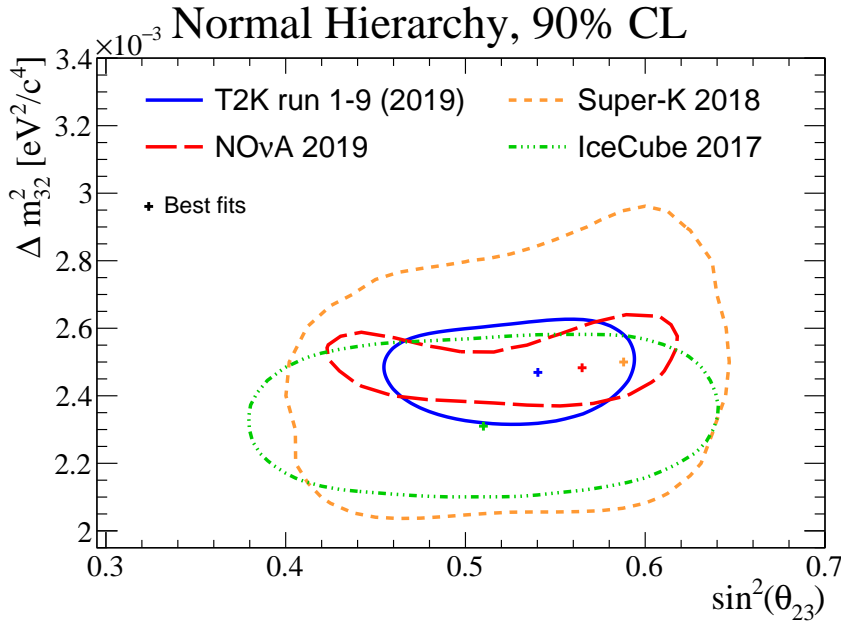
Figure 1.11 – Constraints on neutrino oscillation contours at the 90% C.L. from analyses of T2K, Super-Kamiokande [69], IceCube-DeepCore [70], and NOνA [71] by assuming the normal mass hierarchy. Plot is taken from [72].

in 1994, Kamiokande showed a zenith-angle dependent[2] deficit of muon-neutrino events with 2.8σ statistical significance [64].

In 1998, its successor experiment, the Super-Kamiokande gave a solid evidence of atmospheric neutrino oscillations by showing a 6σ deviation of measured ν_μ events from prediction without oscillations [6]. Figure 1.10 compares the zenith angle distributions of Super-Kamiokande e-like and μ-like events (black dots), with the blue dashed lines giving the prediction for each distributions. The deficit of μ-like events is significant, whilst the number of e-like events is consistent with the prediction. Together with SNO, the theory of neutrino oscillations was indisputably confirmed. From ν_μ disappearance, the Super-Kamiokande results required θ_{23} to be nearly maximal mixing, i.e., $\sim 45°$ [6].

On the other hand, muon neutrinos can also be obtained from particle accelerators. By dumping high energy proton beam on a graphite target, kaons and pions are produced. Then during their flight, they decay mainly into muon neutrinos. Compared with atmospheric experiments, the experiments using artificial neutrino beams know better the neutrino beam properties, such as the luminosity, the direction, the energy. Besides, the facilities usually allow to select either neutrinos or antineutrinos. T2K [65] and NOνA [66] have measured the two parameters and put constraints, as shown in Figure 1.11, where results of atmospheric neutrino experiments, Super-Kamiokande [67] and IceCube-DeepCore [68], are overlapped.

In 2019, by assuming NH is true, the current best result obtained from the global fit [55] with 1σ of θ_{23} is $49.7^{+0.9}_{-1.1}$ degree, and $\Delta m^2_{32/31}$ is $2.525^{+0.033}_{-0.031} \times 10^{-3}\,\mathrm{eV}^2$.

θ_{13} measurements

θ_{13} can be accessed with at least two oscillation channels: $\bar{\nu}_e \to \bar{\nu}_e$, and $\overset{(-)}{\nu}_\mu \to \overset{(-)}{\nu}_e$. The first channel is usually studied by reactor neutrino experiments. While the CHOOZ [73]

---

[2]Equivalent to changing the baseline, from $\sim 10\,\mathrm{km}$ (down-going) to $\sim 1.2 \times 10^4\,\mathrm{km}$ (up-going).
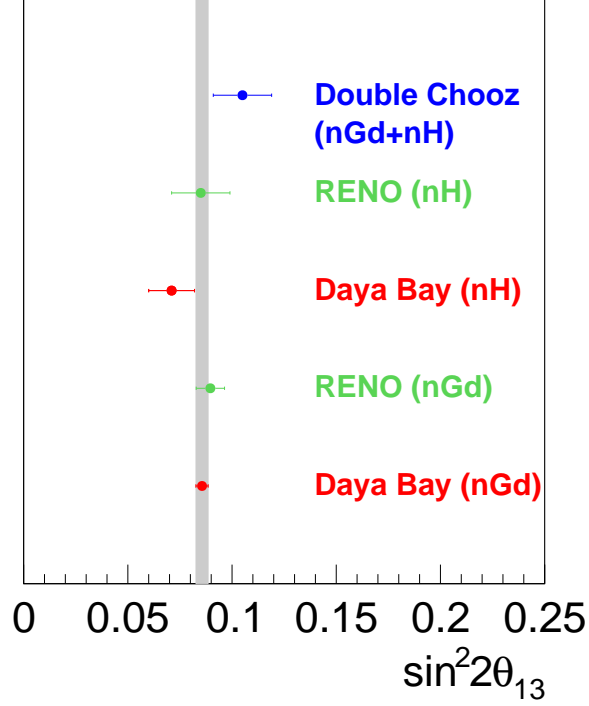
Figure 1.12 – Recent results of Double Chooz, Daya Bay, and RENO on θ_{13}. Figure extracted from [78]. The grey band shows 1σ-range of Daya Bay result.

and Palo Verde [74] experiments gave only upper limits in the late 1990s', the new generation of reactor neutrino experiments, Double Chooz [75], Daya Bay [76], and RENO [77], excluded zero-θ_{13} hypothesis in 2012, with an improvement of experimental method using near and far detectors. Subsequently, they contributed to the precise measurements of the mixing angle with more statistics. Their most recent results are summarised in Figure 1.12, as we can see, the results from reactor neutrino experiments are consistent.

Accelerator neutrino experiments are able to measure θ_{13} via ν_e appearance, however, the results are influenced by θ_{23} and δ_{CP}. K2K [79] was the first accelerator neutrino experiment that set an upper limit for the angle. As early as in 2011, T2K [80] and MINOS [81] reported hints for non-zero θ_{13}, which was confirmed later by the reactor neutrino experiments. The published result of T2K θ_{13} measurement [82] is compatible with those of reactor neutrino experiments.

In 2019, by assuming NH is true, the current best result obtained from the global fit [55] with 1σ of θ_{13} is $8.61^{+0.12}_{-0.13}$ degree.

δ_{CP} measurements

The observed rate of electron neutrino appearance in an accelerator neutrino experiment depends on θ_{13}, θ_{23} and δ_{CP}. Measuring precisely these three parameters in one experiment is not easy. If the mixing angles are constrained by the data of other types of experiments, then accelerator neutrino experiments can measure the last parameter with a better precision. The recent results of the T2K experiment presented the first indication of neutrino CP violation, by excluding 0 and π of δ_{CP} at 90% confidence

level [83]. The oscillation probability $\overset{\scriptscriptstyle(-)}{\nu}_\mu \to \overset{\scriptscriptstyle(-)}{\nu}_e$ often observed in an accelerator neutrino experiment is correlated simultaneously with the νMH and δ_{CP}, also known as the degeneracy of the νMH and δ_{CP}. Consequently, a precise measurement of δ_{CP} can help in the νMH determination. Such a measurement requires high statistics and small matter effects. A new accelerator neutrino experiment T2HK [84], as a natural extension of the operative T2K experiment, is designed to fulfil these requirements and thus to accomplish the measurement.

νMH determination

Due to the degeneracy, precise measurements of δ_{CP} improve the νMH sensitivity and vice versa. More specifically, the νMH provides strong constraints on parameter space for the CP violation measurement in accelerator neutrino experiments, such as T2K and T2HK. There are two methods to determine the νMH:

- Precise measurement of the oscillation probability to determine via the sign of the phase in Equation (1.59);

- Observation of resonant matter effects (i.e. MSW effects [85]) on ν or $\bar\nu$, depending on the νMH.

The first method can be realised with reactor antineutrino disappearance experiments. In order to obtain the best sensitivity, the baseline should be around the first valley of θ_{12}-driven oscillations in Figure 1.5. The observation of reactor antineutrino provides an unambiguous determination, as the result depends only on θ_{13}, which has been measured precisely. The unexpectedly large value of θ_{13} lowers the technical barrier for the experiments [36]. JUNO adopts this method, therefore, all related discussion will be left in Chapter 2.

Long-baseline accelerator neutrino experiments take the second path. However, results from such experiments are entangled with δ_{CP}. On one hand, to enhance the perturbation caused by MSW effects and to resolve the degeneracy of the νMH and δ_{CP}, the energy of the neutrino beam must be increased; on the other hand, the oscillation observables can be accessed more easily if $\Delta m^2_{32} L/(4E) \approx \pi/2$ [86], which requires that the baseline is enlarged proportionally to the beam energy. As shown in Figure 1.13, a longer baseline can make MSW effects more significant, whereby two scenarios are completely disentangled. That is how we can get rid of the impacts from other oscillation parameters and improve the νMH sensitivity. The established accelerator neutrino experiment NOνA and the planned DUNE experiment [87], will contribute to the νMH determination. Especially, DUNE, with 1300 km baseline, claims its capability to determine the νMH with a sensitivity better than 5σ. Japanese-Korean accelerator neutrino experiment T2HKK [88] is also proposed and aims to solve the νMH problem.

Finally, atmospheric neutrino detectors can also be used to determine the νMH via matter effect of upward-going neutrinos, which cross the entire Earth diameter to reach the detectors. Similar reasoning to long-baseline accelerator neutrino experiments, the terrestrial matter effect will enhance oscillations of $\nu(\bar\nu)$ and suppress oscillations of $\bar\nu(\nu)$. By assuming true NH, the matter effect enhancement will be seen in $P(\nu_\mu \to \nu_\mu)$ but be absent in $P(\bar\nu_\mu \to \bar\nu_\mu)$ [86]. The reversed situation is required by the true IH. Atmospheric neutrino experiments, such as PINGU [89], ORCA [90], Hyper-Kamiokande [84], INO [91], are proposed to use terrestrial matter effect for νMH determination with high sensitivity.
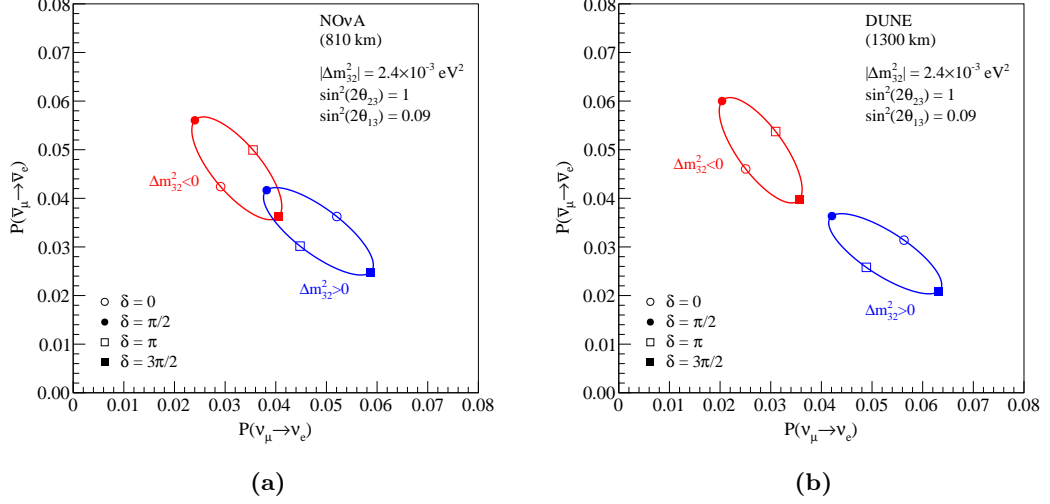
(a)   **(b)**

Figure 1.13 – $P(\nu_\mu \to \nu_e)$ vs $P(\nu_\mu \to \nu_e)$ for both NH (blue) and IH (red). The ellipses are given by accounting different δ_{CP} with a representative L/E at $0.4\,\text{km/MeV}$. (a) is for NOνA at $810\,\text{km}$. (b) is For DUNE at $1300\,\text{km}$. Plots are taken from [86].

In fact, JUNO is not expected to obtain the best νMH sensitivity among all aforementioned experiments, but it will still have its special contribution to the νMH determination, as the only experiment measuring the reactor antineutrino disappearance. A measurement of $\bar{\nu}_e$ disappearance at intermediate baseline endows JUNO with two advantages over the others: first, the determination is unambiguous, since the $\bar{\nu}_e$ survival probability does not depend on θ_{23} or δ_{CP}, especially when the latter has not yet been precisely measured; and second, terrestrial matter effects in such an experiment are very small [35], therefore, the JUNO results can be considered as measured in vacuum.

1.4.2 Majorana neutrinos

As we have discussed in Section 1.2.2, neutrinos may be modelled as Majorana particles because they have no electric charge. The Majorana property stipulates that a particle is its own antiparticle, this can be used to explain why only left-handed neutrinos exist—building a Majorana mass term does not require the existence of the right-handed counterpart (see Equations (1.36) and (1.37)). If neutrinos are Majorana particles, the lepton number conservation is then violated, and therefore neutrino-less double β-decay ($0\nu2\beta$) [93] can happen. Two Feynman diagrams are illustrated in Figure 1.14: (a) is for two normal β-decay and (b) is for a $0\nu2\beta$, where a vertex of ν "annihilation" is found. The detection of such a hypothesised process allows a determination of neutrino nature, whether they are Majorana or otherwise Dirac particles. Experiments, such as KamLAND-Zen [94], EXO-200 [95]/nEXO [96], NEXT [97], using ^{136}Xe, SNO+ [98] using ^{130}Te, GERDA [99] using ^{76}Ge, and SuperNEMO [100] using ^{82}Se,[3] are searching actively for this process. The current lower limits on the half-life of $0\nu2\beta$ exceed 10^{25}-10^{26} years [102].

Another parameter of interest in the $0\nu2\beta$ decay search is the effective Majorana

---

[3]Only for initial run, the design allows SuperNEMO to switch to other materials in future [101].

(a) **(b)**
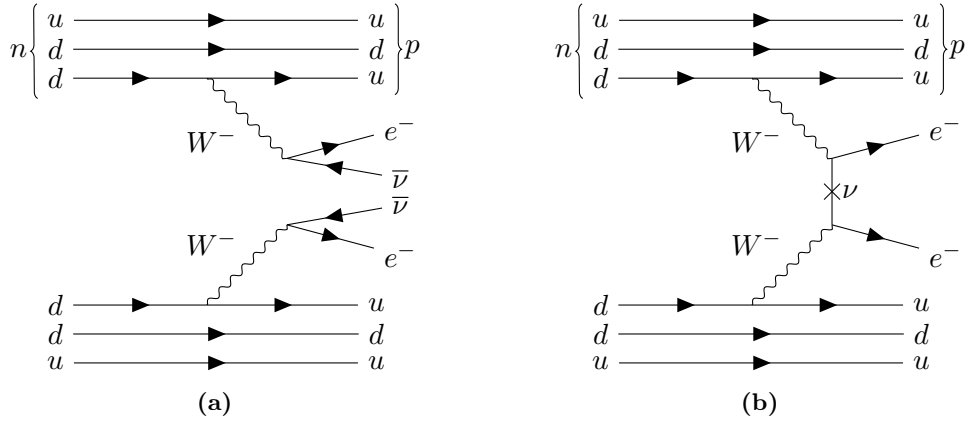
Figure 1.14 – (a) Feynmann diagram of two normal β-decay and the neutrinos are Dirac fermions, so the lepton number is conserved in the diagram. (b) Feynmann diagram of the $0\nu2\beta$ decay via the exchange of a virtual Majorana neutrino between two β-decays and leave only two electrons. The lepton number is thus no more conserved.
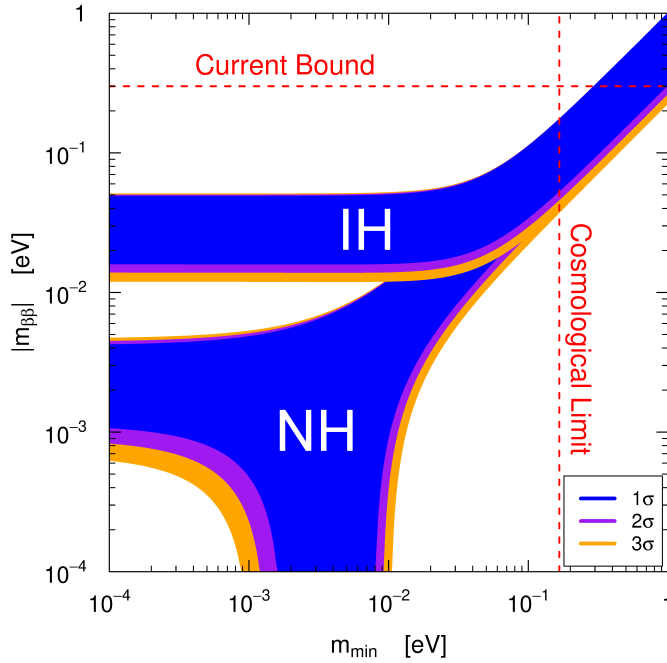
Figure 1.15 – Effective Majorana mass as a function of the lightest neutrino mass [92]. The top band correspond to the IH regime, the bottom to NH.

mass, which is defined as [103]

$$|m_{\beta\beta}| = \left| m_1 c_{12}^2 c_{13}^2 + m_2 s_{12}^2 c_{13}^2 e^{i\alpha} + m_3 s_{13}^2 e^{i\beta} \right|, \tag{1.62}$$

using the same notations in Equation (1.47), and α and β are two Majorana phases absorbing the CP-violating phase. The mass can be expressed in terms of lightest neutrino mass $m_{\min}$ [104], and depending on the true νMH, the allowed zones in $(m_{\min}, |m_{\beta\beta}|)$ parameter space are different, as shown in Figure 1.15. The $0\nu2\beta$ experimental results and cosmological observations set the upper limits on both $m_{\min}$ and $|m_{\beta\beta}|$, which are annotated in the figure. The constraint between the effective mass and νMH allows the determination of νMH by pushing down the effective mass upper limit below the IH allowed zone. On the other way around, if the true νMH is determined, it helps to define the goal of $0\nu2\beta$ search experiments. In particular, by assuming neutrinos are Majorana particles, the chance to observe $0\nu2\beta$ decays in the next-generation experiments is greatly enhanced for the IH, as suggested by Figure 1.15.

1.4.3 Reactor antineutrino anomaly

A global fit of ratios of measured reactor antineutrino fluxes over the predicted fluxes by Huber+Mueller [105, 106], including the results of ~km baseline experiments, such as CHOOZ, Palo Verde, Double Chooz, Daya Bay, RENO, and the past short-baseline ($<$ 100 m) measurements, demonstrates a deficit of measured antineutrino flux with respect to the theoretical prediction [107]. This deficit is referred to as reactor antineutrino anomaly. As shown in Figure 1.16, the global average ratio is $0.943 \pm 0.008(\text{exp.}) \pm 0.025(\text{model})$, it excludes the unitary at 1σ. The deficit cannot be explained with the estimated model uncertainty, so it is possible that either the model itself has a larger uncertainty [109], or there is a hint for new physics.

The deficit can be imputed to the ignorance of additional contribution from some isotopes. Double Chooz [110], Daya Bay [108], RENO [111], and NEOS [112] unanimously confirm the observation of an excess between the 4 MeV and 6 MeV prompt energy. Figure 1.17 shows the Daya Bay measured prompt energy spectrum, and a bump around 5 MeV can be clearly seen. The discrepancy gives support to the first explanation that larger uncertainty should be added to the model, and thus the deficit would be included in the error band.

Alternatively, some physicists suspect that the deficit is a hint of oscillations between $\bar{\nu}_e$ and the neutrinos of the fourth generation [113], which is an hypothesis also supported from other data. The current status of the researches in this direction shows still a huge ambiguity. To address a clear answer to this question, further investigations and measurements are necessary.

1.4.4 Absolute neutrino mass scale

Neutrino oscillation experiments have explored many features of neutrinos. What oscillation experiments cannot offer is the absolute neutrino mass scale, so the absolute neutrino masses must be measured by other methods. One of the methods to obtain electron neutrino mass is to measure with extreme high-precision the electron spectrum of tritium β decay near its endpoint. As the most sensitive direct measurement for the electron neutrino mass up to now, initiated by Troitsk Neutrino Mass Experiment [114] and Mainz Neutrino Mass Experiment [115], KATRIN [116], an experiment with the
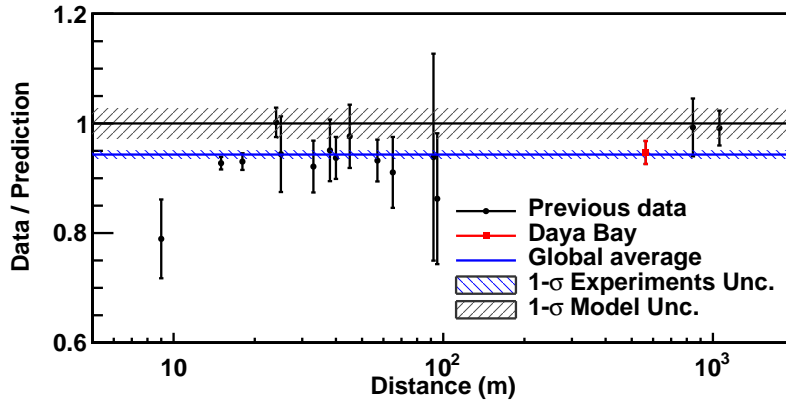
Figure 1.16 – The measured reactor $\bar{\nu}_e$ rate as a function of the distance from the reactor, normalised to the theoretical prediction with the Huber+Mueller model, whose uncertainty is believed to be 2.7% and is shown as band around unity. The blue shaded region represents the global average and the 1σ range [108].
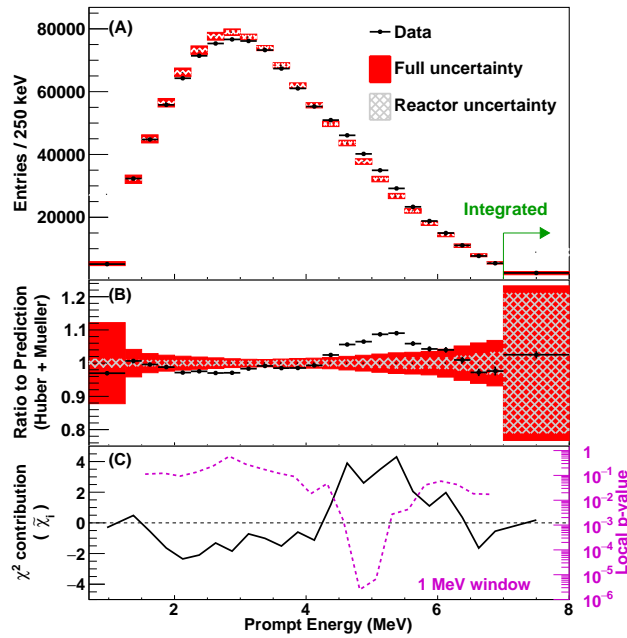
Figure 1.17 – Predicted and measured prompt-energy spectra in Daya Bay. The prediction is based on the Huber+Mueller model and normalised to the number of measured events [108].

same measurement technique and started in 2016, intends to continue pushing the upper limit of electron antineutrino mass to $0.2\,\text{eV}$, one order of magnitude smaller than its predecessors.

We foresee that, by combining the forecast results from direct measurements of electron antineutrino mass, cosmological constraints, and the νMH determination, the absolute neutrino mass scale will be much better constrained, and even be measured if the true νMH is IH [117, 118].

1.5   Summary

The chapter tries to address a basic introduction to the neutrino physics, including all necessary concepts for future discussions in this thesis. Particularly, we have recapitulated the principles of neutrino oscillations, which is the iconic phenomenon of massive neutrinos. This phenomenon opens a gateway for all interesting researches about the nature of neutrinos, therefore, we have shown the current experimental status of oscillation experiments and the current measurement results. Some other experiments, instead of focusing on oscillation parameters, are interested in other features or new physics about neutrinos. These experiments are also mentioned in this chapter.

Chapter 2

The JUNO experiment

The JUNO (Jiangmen Underground Neutrino Observatory) experiment is a multi-purpose neutrino experiment, near Jiangmen city, Guangdong province, China. The primary goal of JUNO is to perform an unambiguous determination of neutrino mass hierarchy (νMH) at 3σ sensitivity and a sub-percent measurement of the neutrino oscillation parameters θ_{12}, Δm_{21}^2, and $\Delta m_{31/32}^2$ with reactor $\bar{\nu}_e$. To achieve such a compelling determination and measurement, JUNO will have an unprecedented energy resolution of 3% at $1\,\mathrm{MeV}$ on the $\bar{\nu}_e$ energy spectra mainly contributed by two nuclear power plants (NPPs) located $53\,\mathrm{km}$ away, i.e. the Yangjiang and the Taishan NPPs. The location of JUNO is marked in Figure 2.1, together with the NPPs at a distance less than $500\,\mathrm{km}$, and the metropolises nearby.

Figure 2.1 − Location of the JUNO site.

This chapter serves as a general introduction of JUNO, helping the readers to understand its physics and apparatus. In Section 2.1, we will show how to obtain the expected energy spectrum of reactor $\bar{\nu}_e$ in JUNO without taking into account oscillation effects. Following this, Section 2.2 will introduce the JUNO detector, and the components related to this thesis will be presented with more details, as the extra information is useful for understanding the following chapters. In Section 2.3, the experimental method used in JUNO for νMH determination is explained in detail. Finally, as one of the best neutrino detectors in the next decade, JUNO has a rich physics program other than the νMH determination, to which Section 2.4 is dedicated.

2.1 Reactor antineutrino detection

The determination of νMH in JUNO will be done by measuring the energy spectrum of reactor antineutrinos. In order to understand the antineutrino signals in the detector, we need to know how antineutrinos are produced in reactors, and how to calculate the expected energy spectrum without neutrino oscillation.

2.1.1 Reactor neutrino flux

In a commercial reactor, the thermal energy is mostly produced by four fissile isotopes ^{235}U, ^{238}U, ^{239}Pu, and ^{241}Pu. After fissions, the unstable fission fragments of these isotopes will undergo β-decays, and emit $\bar{\nu}_e$. Statistically, one fission releases about 200 MeV of thermal energy, and emits 6 antineutrinos [119]. However, for a reactor $\bar{\nu}_e$ experiment, more details about the neutrino yield are needed. In particular, the neutrino yield as a function of neutrino energy is an import input for understanding the oscillation effects.

More precisely, the reactor neutrino flux can be calculated by

$$
\begin{aligned}
\Phi(E_\nu) &= \sum_i F_i S_i(E_\nu) \\
&= \frac{W_{\text{th}}}{\sum_i f_i e_i} \cdot \sum_i f_i S_i(E_\nu),
\end{aligned}
\tag{2.1}
$$

where F_i is the fission rate of isotope i and $S_i(E_\nu)$ is the neutrino flux per fission of isotope i. Here i represents the four major fissile isotopes ^{235}U, ^{238}U, ^{239}Pu, and ^{241}Pu. In the second line of Equation (2.1), F_i is written as a function of the thermal power W_{th}, fission fractions of four main isotopes f_i, and the thermal energy released in each fission e_i. For commercial reactors, such as those producing JUNO's $\bar{\nu}_e$ flux, parameters e_i, f_i, and S_i can be found in Table 2.1.

Table 2.1 – Parameters e_i, f_i, and S_i used in Equation (2.1) for different isotopes. Values are found in [120–122].

Isotopes	e_i (MeV)	f_i	S_i
^{235}U	201.92	0.58	$\exp(0.870 - 0.160E_\nu - 0.091E_\nu^2)$
^{238}U	205.52	0.07	$\exp(0.976 - 0.162E_\nu - 0.0790E_\nu^2)$
^{239}Pu	209.99	0.30	$\exp(0.896 - 0.239E_\nu - 0.0981E_\nu^2)$
^{241}Pu	213.60	0.05	$\exp(0.793 - 0.080E_\nu - 0.1085E_\nu^2)$

Table 2.2 summarises the thermal power W_{th} of all cores in Yangjiang (YJ) and Taishan (TS) and their baselines. The remote NPPs, Daya bay (DYB) and Huizhou (HZ) are also included in the table, but their thermal powers are given as the sum of all cores, as the baseline differences between cores are not important for JUNO. With these elements, the flux of antineutrinos from the cores can be calculated.

2.1.2 Inverse beta decay

The inverse beta decay (IBD) is a reaction between an electron antineutrino and a proton, producing in the final state a positron and a neutron. Its Feynman diagram in Figure 2.2 shows that IBD is a CC interaction.

Table 2.2 – Thermal power and baseline to the JUNO site for Yangjiang (YJ) and Taishan (TS) reactor cores. For the remote NPPs, Daya Bay (DYB) and Huizhou (HZ), the informations are also provided.

Cores	YJ-C1	YJ-C2	YJ-C3	YJ-C4	YJ-C5	YJ-C6
Power (GW)	2.9	2.9	2.9	2.9	2.9	2.9
Baseline (km)	52.75	52.84	52.42	52.51	52.12	52.21

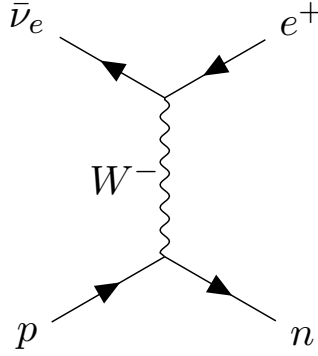| Cores	TS-C1	TS-C2	TS-C3	TS-C4	DYB	HZ
Power (GW)	4.6	4.6	4.6	4.6	17.4	17.4
Baseline (km)	52.76	52.63	52.32	52.20	215	265

Figure 2.2 – Feynman diagram of the inverse beta decay (IBD).

Reactor antineutrino experiments mainly detect antineutrinos by observing the IBD events. The most important reason for doing this is that, an IBD event generates a prompt-delayed signature, which helps much in background suppression by requiring time and space coincidence. Figure 2.3 illustrates how the prompt and delayed signals are created in an IBD event. In an IBD, the positron carries most of the neutrino energy, due to the large mass difference of positron and neutron. The positron deposits all kinetic energy quickly in the detector and annihilates with an electron, giving two back-to-back photons at 511 keV. This process is detected first in the detector, so it is called *prompt signal*. On the other hand, the neutron takes a much longer time to be thermalised, and is then captured by a nucleus in the detector. The signal created by the recoil neutron is called *delayed signal*. The time difference between prompt and delayed signals depends on the neutron capturing nucleus, for example, hydrogen (H) has an average time difference of 210 µs, while for gadolinium (Gd), the time difference is 30 µs [124]. The number of emitted photons in the neutron capture and their total energy are also related to the nucleus, for example, neutron capture by H gives a single photon of 2.2 MeV, whereas Gd gives a few photons with a total energy around 8 MeV. Figure 2.4 shows the distribution of prompt versus delayed energy in IBD events [125], where we can find the n-H capture and n-Gd capture signals having different delayed energies. It must be noticed that, in JUNO, the liquid scintillator is not doped with Gd, so the JUNO detector will only have n-H capture signals.

IBD has an energy threshold of 1.8 MeV due to the mass difference between the reactants ($\bar{\nu}_e$ and p) and the products (e^+ and n). The expression for IBD cross section
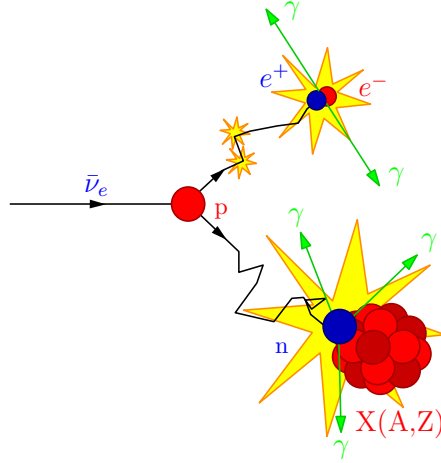
Figure 2.3 – Creation of prompt and delayed signals in an IBD event [123].

σ is given approximately by [121, 126]

$$\sigma = 0.0952 \times 10^{-42} \, \text{cm}^2 (E_e p_e / 1 \, \text{MeV}^2),\tag{2.2}$$

where $E_e = E_\nu - (M_n - M_p)$ is the positron energy when neutron recoil energy is neglected, and p_e is the positron momentum. Figure 2.5 shows the IBD cross section, the $\bar{\nu}_e$ yields per fission of four major fissile isotopes weighted by their corresponding fission fractions, and the total flux adding up all contributions given by Equation (2.1).

Taking into account the baseline and the IBD detection efficiency, we obtain the expected antineutrino spectrum in the detector without oscillation effects as

$$S(E_\nu) = \frac{1}{4\pi L^2} \cdot \Phi(E_\nu) \cdot \epsilon \cdot N_p \cdot \sigma(E_\nu),\tag{2.3}$$

where L is the baseline, ϵ is the detection efficiency, N_p is the target proton number. $\Phi(E_\nu)$ and $\sigma(E_\nu)$ are given by Equation (2.1) and (2.2), respectively. An observable IBD spectrum arbitrarily normalised is shown in Figure 2.5.

2.2 The JUNO detector

In order to achieve 3σ sensitivity of νMH with 6-year of reactor antineutrino energy spectrum measurement, it is critical to optimise the detector design such that the JUNO energy resolution is better than $3\%/\sqrt{E(\text{MeV})}$.

The JUNO Central Detector (CD) is a 20 kt liquid scintillator (LS) detector. 18 000 20"-PMTs and 25 000 3"-PMTs are commissioned for scintillation light detection with a photocathode coverage of 78%. Consequently, JUNO is able to detect at least 1200 photoelectrons (p.e.) per MeV of deposited energy. Such an ambitious design makes JUNO the largest LS detector currently being built, as well as the LS detector having the highest photoelectron yield amid all established experiments with similar technology. JUNO has chosen to use a 12 cm thick Acrylic Sphere (AS) to contain the LS, as the material has been proven to be reliable for a long-term usage [127, 128]. The AS is supported by the stainless steel truss (CD truss), and it is also the supporting structure for the PMT installation.
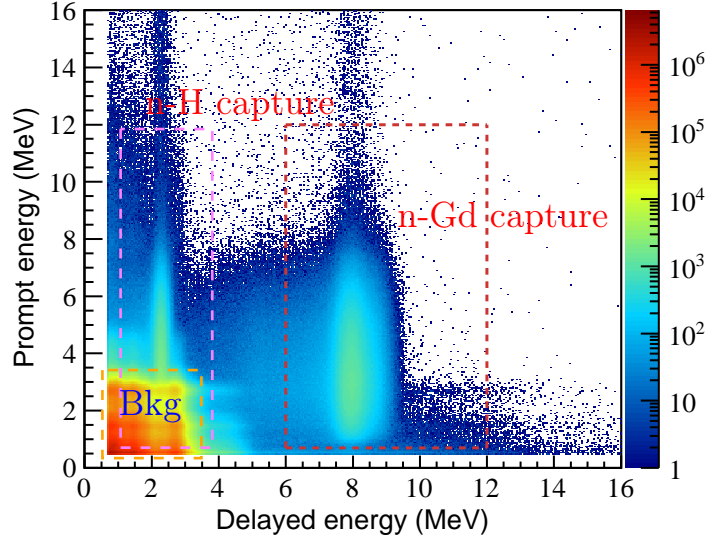
Figure 2.4 – Distribution of prompt versus delayed energy in IBD events measured by Daya Bay [125]. The data in the pink box are from n-H capture events, and in the red box are from n-Gd capture events. The background is framed by the orange box, it can be separated easily from n-Gd capture data by a delayed energy cut.

A calibration system is deployed in JUNO to ensure the non-linearity of the PMT calorimetry to be less than 1%. At the north pole of the CD, the CD chimney allows the system to lower the calibration sources into the CD. The system consists of various units, namely the Automatic Calibration Unit (ACU), Cable Loop System (CLS), Guide Tube Calibration System (GTCS), and Remotely Operated under-liquid-scintillator Vehicles (ROV) [129]. While the ACU scans the CD central axis regularly, the other units are to be used more sporadically for meticulous calibration in any given 3D position inside the CD.

JUNO will detect $\bar{\nu}_e$ by looking for the IBD prompt-delayed coincidences. However, atmospheric muons entering the detector may produce spallation isotopes, and the $\beta^- n$ decays of these isotopes form the most important IBD background. To reduce the atmospheric muon-induced background, the most effective approach is to shield the detector from muons with sufficient overburden. JUNO is being built at $-450\,\mathrm{m}$ depth under a 286 m high mountain, in order to have about 700 m rock overburden, that is ~1800 meter water equivalent (m.w.e.). Atmospheric muon flux is thus reduced to $0.0037\,\mathrm{Hz/m^2}$, 5.6×10^4 times smaller than the flux at sea level.

Despite the overburden, some muons can still enter the CD and induce a considerable number of IBD background events. To further suppress the background to an acceptable level, JUNO's main veto strategy is to reject all events inside a cylindrical detector volume along the muon tracks, where most fake IBDs should be found. More details about this strategy can be found in Section 2.3.1.

The key of this veto strategy is to reconstruct the muon tracks precisely. The Top Tracker (TT) will be built above the CD, covering about 60% of its top area, and aiming to provide the muon tracks that are measured precisely with a spatial resolution of $2.6\,\mathrm{cm} \times 2.6\,\mathrm{cm} \times 1\,\mathrm{cm}$. According to the MC simulation, about 40% of muons crossing the CD can be tracked by the TT. The remaining muons will then be reconstructed by the CD itself, for which the reconstruction methods should be calibrated with the muon tracks provided by the TT [130, 131].
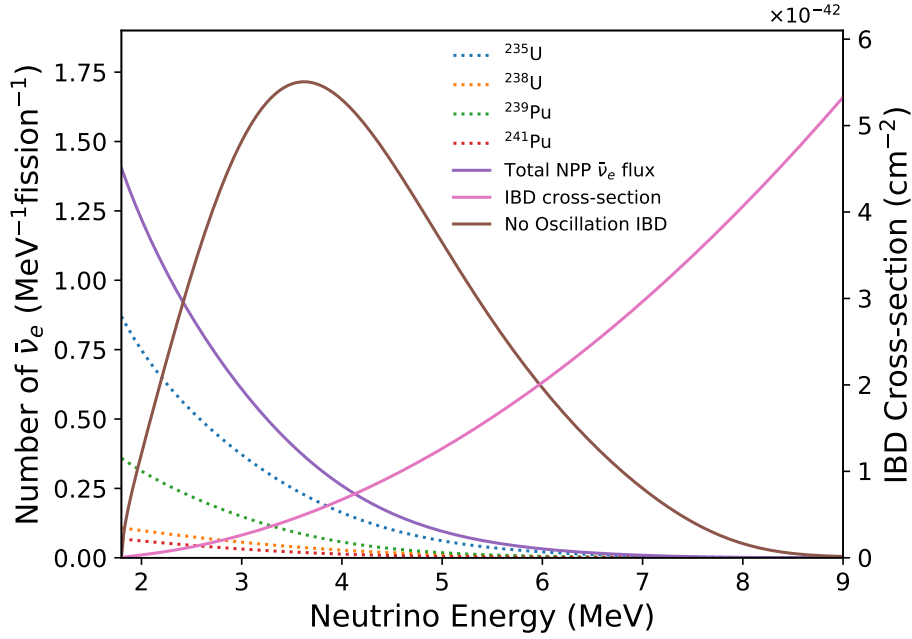
Figure 2.5 – The interaction cross section of the IBD from Equation (2.2) (axis on right side); neutrino yields per fission of four major fissile isotopes ^{235}U, ^{238}U, ^{239}Pu, and ^{241}Pu weighted by their corresponding fission fraction, and the total NPP $\bar{\nu}_e$ flux, as described by Equation (2.1) (axis on left side). The observable IBD spectrum in a JUNO-like detector assuming no oscillation effects is also shown. The observable IBD spectrum is arbitrarily normalised.

The Water Pool (WP) will be constructed to host the CD, and it will impede the radiation of the surrounding rock from entering the CD, which would cause accidental IBD-like coincidences. In JUNO, most radioactivity is coming from the rock, as the radiopurity of materials used for the detector is well controlled. With a minimum water buffer of 4 m at the CD equator, the radioactivity in rock (mainly ^{238}U, ^{232}Th and ^{40}K) is greatly reduced by the WP. The radioactivity rate is estimated to be 7.6 Hz in the CD fiducial volume, which has a radius of 17 m. On the CD truss, 2400 20"-PMTs will be installed facing outward, together with the WP, composing the Water Cherenkov Detector (WCD). The WCD will be used for muon tagging and tracking with a muon detection efficiency better than 99%.

Finally, because the decrease of 20"-PMT detection efficiency due to the Earth's magnetic field (EMF) is not negligible, JUNO decided to build global EMF shielding coils containing the whole CD, to neutralise the effect.

The global schematic of the JUNO detector is shown in Figure 2.6. The JUNO civil construction is ongoing. Currently, the underground complex of JUNO is being constructed, including the experimental hall. A vertical shaft and a slope tunnel for experimental hall access are already finished. Due to underground water, the civil construction was delayed. A new schedule aiming to complete all civil construction by the end of 2019 has been proposed, and so far the progress is well aligned with the new schedule. The data taking is to start end of 2021.

In the following, we will emphasise the components that will be needed for understanding the work presented in this thesis.
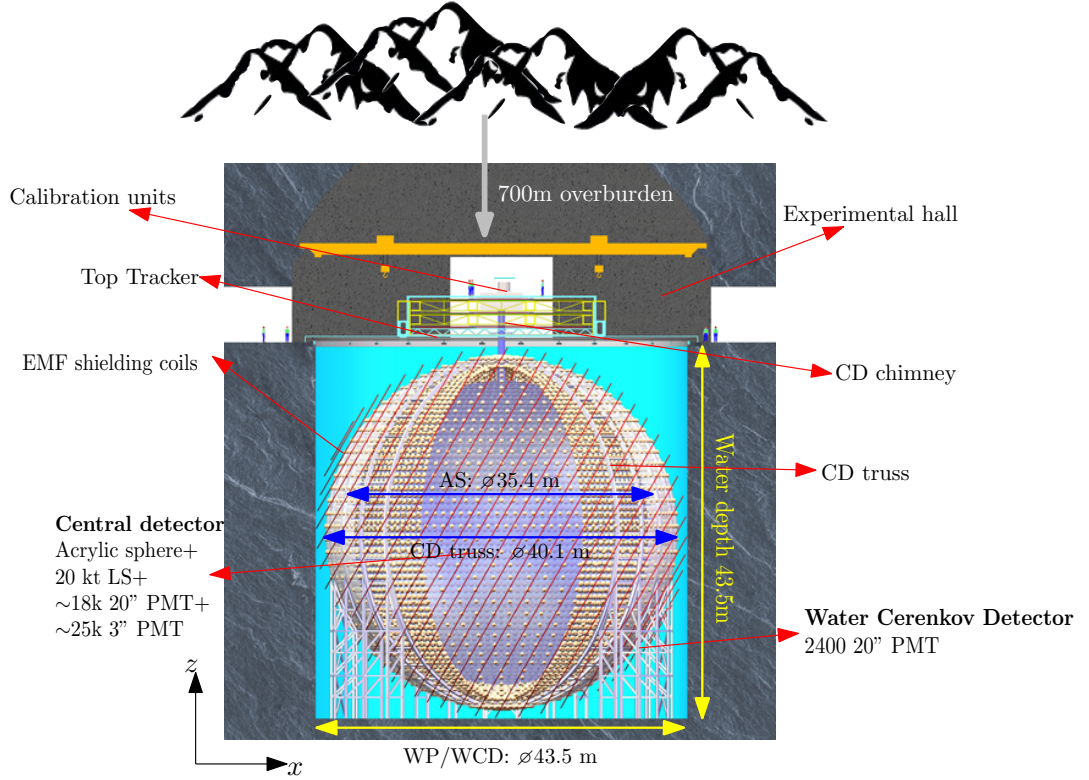
Figure 2.6 − Schematic view of the JUNO detector.

2.2.1 Liquid scintillator

The solvent liquid of the liquid scintillator (LS) is the linear alkyl benzene (LAB), which forms the bulk of IBD target material. The primary fluor (PPO) and the wavelength-shifter (Bis-MSB) is added to avoid the spectral self-absorption by the LAB. Figure 2.7 illustrates the process of scintillation light emission in the LS. The scintillation light wavelength is centred at 430 nm, and the decay time is 4.4 ns.

JUNO requires that the LS must have high light yield, long attenuation length, and low radio-impurity.

Daya Bay has provided an Antineutrino Detector for the JUNO LS study. The current status shows that the LS light yield is $\sim 10^4$ photons per MeV. Given that the JUNO photocathode coverage is 78% and the photon detection efficiency is about 30%, this light yield should result in a final photoelectron yield higher than 1200 p.e./MeV. The measured attenuation length of the LS is 23 m, being comparable with the CD radius. Measurements reveal that the length is a priori governed by the Rayleigh scattering between the photons and the solvent molecules [132].

A purification system will improve the radiopurity of the LS. It will guarantee that the concentrations of ^{238}U and ^{232}Th to be smaller than 10^{-15} g/g, and the concentration of ^{40}K to be smaller than 10^{-16} g/g. To rule out a re-contamination of the purified LS due to potential air leaks in the on-site purification and filling chain, the Online Scintillator Internal Radioactivity Investigation System (OSIRIS) [133] is being developed as a fail-safe monitor of the LS quality before filling it into the CD. The OSIRIS design sensitivity is better than 10^{-16} g/g in 24 hours for ^{238}U.
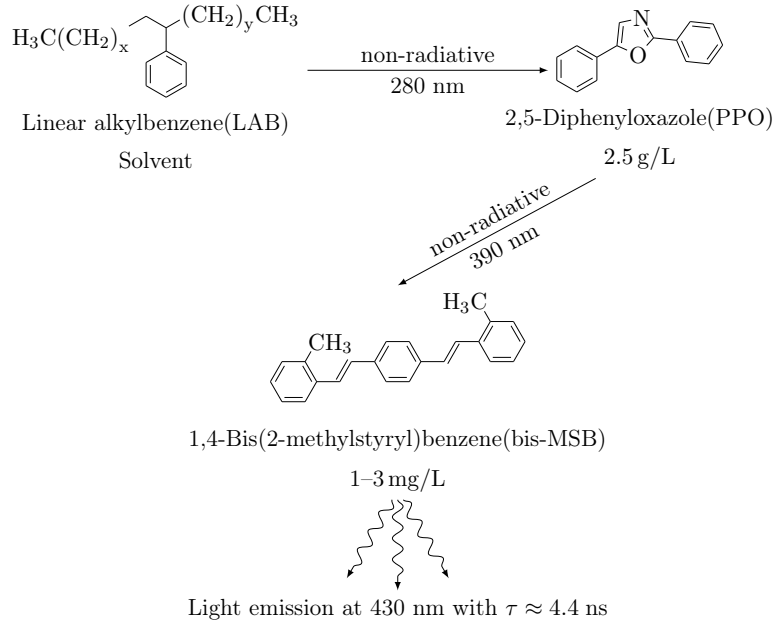
Figure 2.7 – Process that JUNO LS produces scintillation photons.

2.2.2   20" photomultiplier tube system

The energy resolution of a homogeneous electromagnetic calorimetry can be decomposed into a stochastic term, a noise term, and a constant term as [134]

$$\frac{\sigma_E}{E} = \sqrt{\left(\frac{a}{\sqrt{E}}\right)^2 + \left(\frac{b}{E}\right)^2 + c^2},\tag{2.4}$$

where a, b, c are to be determined empirically in the experiment. The stochastic term proportional to $1/\sqrt{E}$ is associated with fluctuations in the number of signal generating processes, such as the number of photoelectrons (number of photoelectrons (N_{pe})) generated. The noise term proportional to $1/E$ arises from noise in readout electronics and "pile-up" of simultaneous events. The last term is a constant, which is related to imperfections in calorimeter construction, non-uniformities in signal collection, channel-to-channel calibration errors, fluctuation in longitudinal energy containment, and fluctuations in energy lost in dead material.

In JUNO, the stochastic term is uniquely determined by the photoelectron yield, while the non-stochastic terms receive the contributions from the dark noise of the PMTs and electronics, the detector non-uniformity and vertex resolution, and the PMT charge resolution.

To guarantee the 3% energy resolution, the stochastic term must be controlled below 3%, such that a sufficient room for systematic uncertainty can be left. Figure 2.8 shows the evolution of the stochastic term of energy resolution as a function of photoelectron yield in JUNO, where we have found that it is critical to have a photoelectron yield higher than 1200 p.e./MeV. In this case, JUNO ought to achieve an energy scale uncertainty[1] less than 1%. This level of accuracy has been proven achievable in other LS-based

---

[1]Energy scale is defined as the non-linearity of the detector responses in N_{pe} (or reconstructed energies) to the deposited energies.
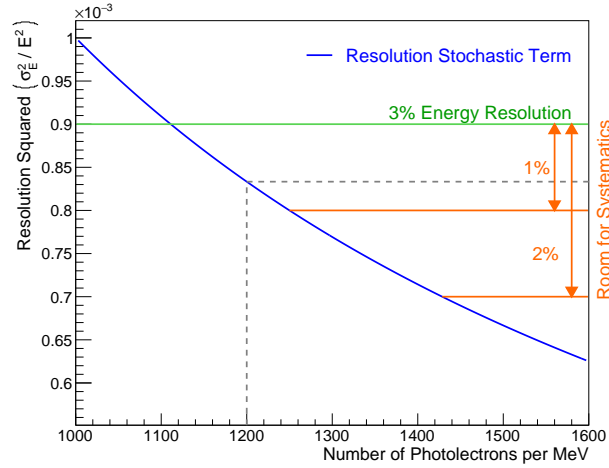
Figure 2.8 – Stochastic term of energy resolution as a function of light yield in JUNO.

(a)	**(b)**
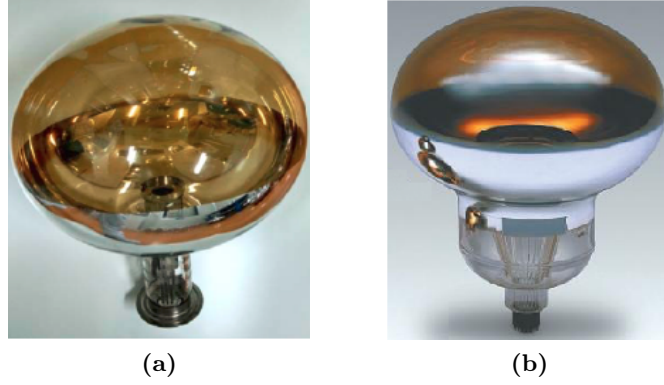
Figure 2.9 – Photos of (a) NNVT MCP-PMT and (b) Hamamatsu dynode-PMT.

neutrino experiments, e.g., Daya Bay at 0.5% [125], Double Chooz at 0.74% [135], and Borexino at 1% [136].

Although the LS provides a large amount of scintillation light, JUNO still requires a high photocathode coverage and a good detection efficiency (DE) of the PMTs, such that the final photoelectron yield is high. The 20"-PMTs, also known as Large PMTs (LP-MTs), are the major photodetectors in JUNO. 18 000 LPMTs together provide JUNO with a photocathode coverage of 75%.

Among 18 000 LPMTs, 13 500 of them are the model developed in a collaboration between Institute of High Energy Physics (IHEP) and North Night Vision Technology (NNVT), using the Micro-Channel-Plates (MCP) technology. The remaining 4 500 LPMTs will be manufactured by Hamamatsu[2] with the conventional dynode technology. They are referred to as MCP-PMT and dynode-PMT in this thesis, respectively. Figure 2.9 shows photos of both models.

Both models have a very similar average DE equal to 27%. A new model of HQE[3] MCP-PMT has been developed, and its DE is improved to 30%. Although the final decision has not yet been made, it is planned that a large portion of LPMTs in the CD

---

[2]Model number: Hamamatsu R12860

[3]High Quantum Efficiency
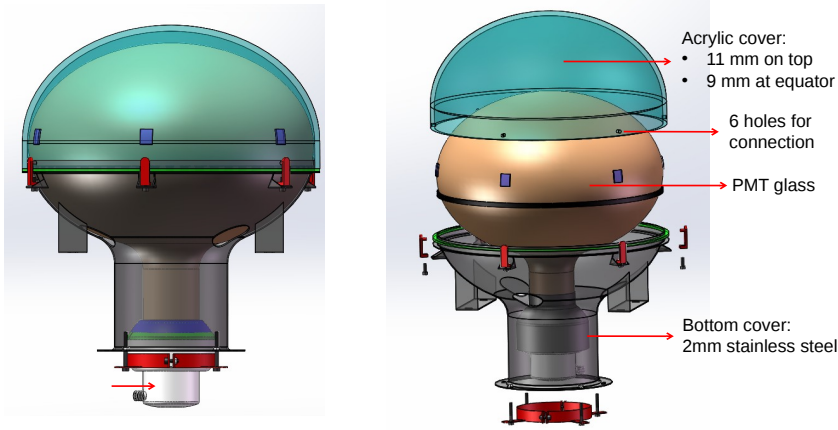
Figure 2.10 – Schematic design of the complete LPMT assembly, including its acrylic cover for shockwave protection.

will be the new HQE model.

There are two important differences between the MCP-PMT and the dynode-PMT. The dynode-PMTs have a better performance on the transit time spread (TTS), which is 2.7 ns for dynode-PMTs, and 12 ns for MCP-PMTs. The accuracy of vertex and energy reconstruction can be affected by the TTS performance. On the other hand, MCP-PMTs have been made with glass bulbs much less radioactive than dynode-PMTs', which is an essential requirement from the JUNO background control.

The LPMT protection covers have been developed to avoid chain reaction of PMT implosion like the accident that happened in the Super-Kamiokande detector [137]. Figure 2.10 shows the illustration of the complete LPMT assembly, including the acrylic cover (AC) for shockwave protection. The AC has a variant thickness from 9 mm at equator to 11 mm on top, and it has been proven to be endurable up to 30 MPa shockwave in the implosion test. Given that the clearance[4] has been set to 25 mm for 75% photocathode coverage, there is only a 3 mm gap left between two LPMT ACs after installation. Such a small mechanical margin is problematic if the deformation and the installation precision cannot be well controlled. In this case, the deformation and the installation precision must be less than 3 mm and 5 mm, respectively.

The data acquisition system (DAQ) of the LPMT system is triggered by the energy threshold. Actually, the threshold should be sufficiently small, as JUNO wants to have a high IBD efficiency as well as a good sensitivity to low energy neutrinos, typically in the solar and supernova neutrino studies. On the other hand, a low energy threshold will saturate the DAQ mainly due to the PMT dark noise. To solve this dilemma, JUNO will be equipped with a low-level trigger system, which can quickly reconstruct the event vertex and reject the non-reconstructible events. As described in [138], by dividing the CD into ∼180 cubic blocks, the trigger system tries to reconstruct the event vertex by simply searching for any cube that has a time-of-flight (TOF) distribution similar to the measured one. If the trigger system finds more than one cubic block, the event is reconstructed successfully; otherwise, the event will be rejected. With the help of the trigger system, the LPMT system is able to reduce the energy threshold to as low as 0.2 MeV.

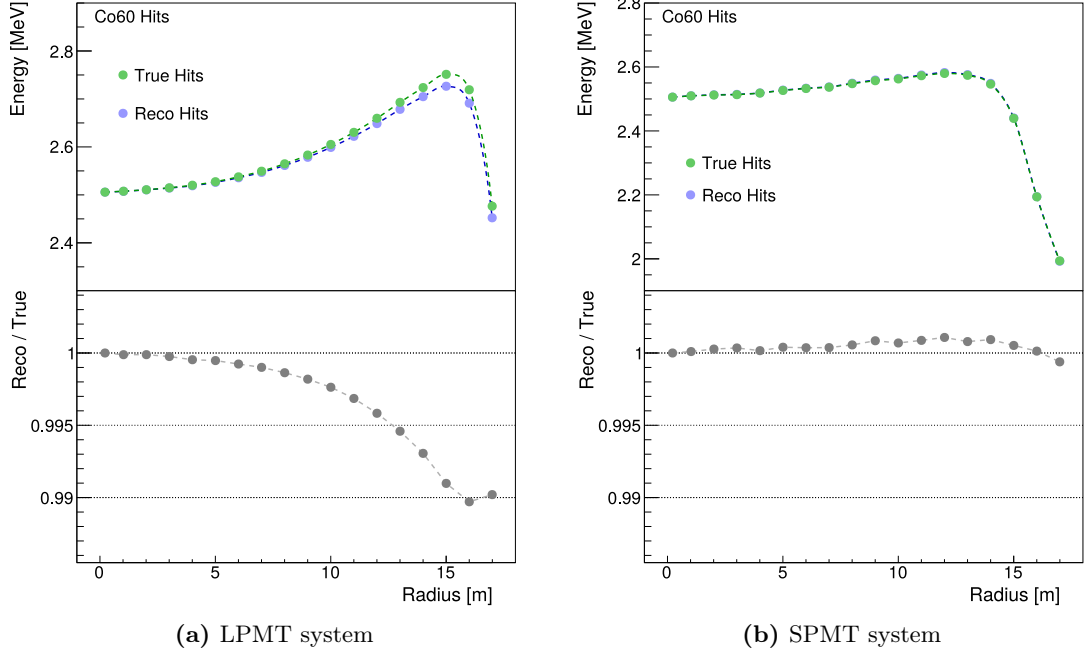[4]Shortest distance between two LPMT photocathodes

(a) LPMT system

(b) SPMT system

Figure 2.11 – Upper panels show visible energies of ^{60}Co source obtained from MC true ("true hits") and reconstructed ("reco hits") N_{pe} by using (a) the LPMT system and (b) the SPMT system, as a function of the radius at which the source is positioned. For every position, lower panels show the corresponding ratios between the visible energies of reco hits and true hits. Plots are taken from [140].

2.2.3   3" photomultiplier tube system

The 25 000 3"-PMTs, or Small PMTs (SPMTs) in JUNO's lexicon, add about 3% photocathode coverage, and the system provides an additional photoelectron yield of ~40 p.e./MeV. Despite the relatively small contribution to the calorimetry, the SPMT system is important for JUNO to ensure non-biased energy reconstruction.

   Due to the large photocathode area, a LPMT can receives multiple scintillation photons, especially when the energy deposit positions are close to the LPMT, and the N_{pe} detected by the LPMT system must be reconstructed via charge measurement. However, the charge reconstruction can introduce additional systematic uncertainty via the PMT gain non-linearity, and the sub-percent accuracy of the non-linearity calibration is very challenging [125, 139]. On the other hand, in the reactor antineutrino energy range, more than 98% of SPMT only detect one single photoelectron because of the small photocathode area, according to the MC simulation [139]. Such a feature allows us to reconstruct the detected N_{pe} of the SPMT system via "photon-counting" technique, namely, we regard directly the total number of fired SPMT as detected N_{pe} without using the charge information. This binary discrimination avoids bringing the PMT gain non-linearity to the systematic uncertainty, and it improves the detector non-uniformity.

   Figure 2.11 shows the simulation results of both the LPMT system and the SPMT system in a ^{60}Co calibration, where the source is moved along the CD z-axis from the centre to the north pole. The upper panels give the curves of visible energies with MC true N_{pe} ("true hits"), and with reconstructed N_{pe} ("reconstructed hits") for different source positions. The visible energies in MeV are obtained by normalising the N_{pe} of

Figure 2.12 – Photo of a JUNO SPMT.

events at the CD centre to 2.5 MeV, which is the total energy of ^{60}Co γ radiation. The reconstruction method for obtaining the N_{pe} in the LPMT system is the charge reconstruction, whilst for the SPMT system, the photo-counting technique is applied.

The lower panels of Figure 2.11 shows the ratios between the visible energies of reconstructed hits and true hits. From the upper panels, we notice that, compared with the LPMT system, the SPMT system presents only very small effect of non-uniformity up to 13 m, before that, the visible energy is almost independent of the source position. Moreover, the lower panel of Figure 2.11(a) reveal that, by using the LPMT system, the reconstructed N_{pe} is underestimated, and the difference between the true N_{pe} and the reconstructed N_{pe} becomes more important for larger radius.

In contrast to the LPMT system, as shown in the lower panel of Figure 2.11(b), the SPMT system has an almost-zero discrepancy between the true and the reconstructed N_{pe} throughout the CD radius, which proves that photo-counting is an effective approach for SPMT energy reconstruction, whereby the PMT non-linearity is excluded from the SPMT systematic uncertainty.

The JUNO calibration system can perform a uniformity calibration, and provide a correction function between measured N_{pe} and the radius. Nevertheless, the source calibration has two limitations: first, it is very difficult to scan thoroughly the entire CD with different sources; and second, the calibration is not real-time. The SPMT system is therefore the unique reference system in JUNO to improve the energy scale precision of the LPMT system during the data taking. Combining the LPMT and the SPMT system constitutes a stereo-calorimetry, which can serve to control both stochastic and non-stochastic effects.

Finally, SPMTs naturally extend the dynamic range of the energy measurement, which is much valued in the studies on the high-energy particles in JUNO, such as cosmic muons and atmospheric neutrinos.

Figure 2.12 shows the photo of a SPMT[5] used in JUNO. The SPMTs have a DE of 24%, and a TTS smaller than 5 ns. The relative small TTS with respect to the MCP-PMTs will help in the vertex reconstruction. The glass bulb has a radiopurity similar to the dynode-PMT's. In the installation, the SPMTs will be inserted into the gaps between the LPMTs as depicted in Figure 2.13.

The SPMT readout electronics is independent of the LPMT system. 128 SPMTs will be grouped to share one readout unit and one high voltage (HV), which will be placed all together in one Under Water Box (UWB), as shown in Figure 2.14. The UWBs will be sunk in the Water Pool, attached to the CD truss. In total, about 200

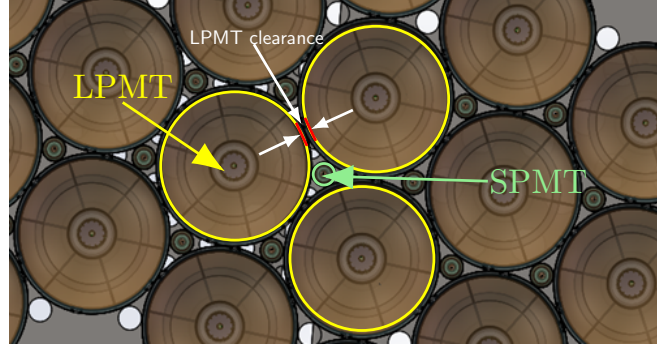[5]Model number: HZC (Hainan Zhanchuang Photonics) XP72B22

Figure 2.13 – Arrangement of LPMTs and SPMTs in JUNO. The LPMT clearance is also labelled.
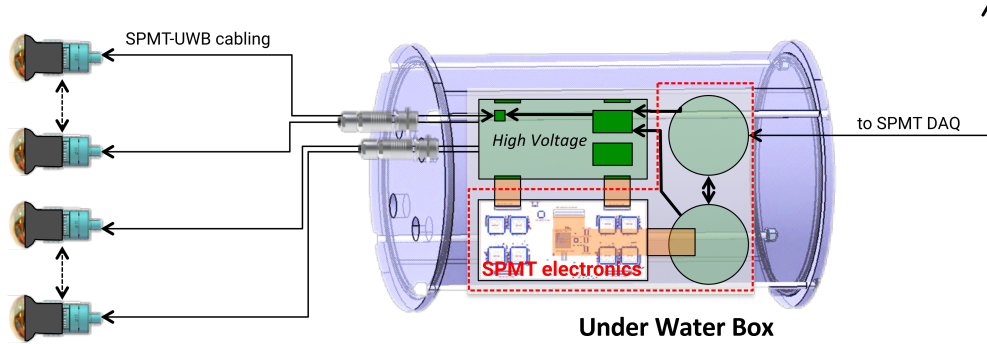
Figure 2.14 – Schematic design of the SPMT system.

UWBs will be deployed to connect all SPMTs. It will not be possible to access the UWBs for maintenance during the JUNO operating time. Therefore, the UWBs should be robust enough with a yearly failure rate of less than 0.5%, i.e., less than one failing UWB per year.

2.2.4 Top Tracker

The Top Tracker (TT) in JUNO will be built with the plastic scintillator modules that were decommissioned from the OPERA [141] Target Tracker [142] as OPERA reached the end of its lifetime [143]. The walls were originally fabricated for locating the lead/emulsion brick where the τ^- decays had occurred following a neutrino interaction. The plastic scintillator has many advantages such as fast rise and decay times, high optical transmission, and durability [144], making it a qualified material for the TT. The modules present a long term stability and reliability tested in OPERA, so transplanting the modules to JUNO makes it possible to design the TT based on a mature technology. An ageing monitoring of these walls has been started since 2015 in Italy, and has been continued after the walls were shipped to China. So far, no noticeable ageing of the scintillator strips is reported.

The design of the plastic scintillator strip walls in the TT, referred to as the TT wall in this thesis, remains unchanged from the original one used in OPERA.

The elementary component of TT walls are the 6.86 m long, 10.6 mm thick, 26.3 mm wide scintillator strips, read from both sides using Wave Length Shifting (WLS) fibres. Figure 2.15(a) shows a scintillator strip with its WLS fibre, and a crossing particle that produces "blue" scintillation photons, later wavelength shifted to "green" by the WLS

(a) **(b)**
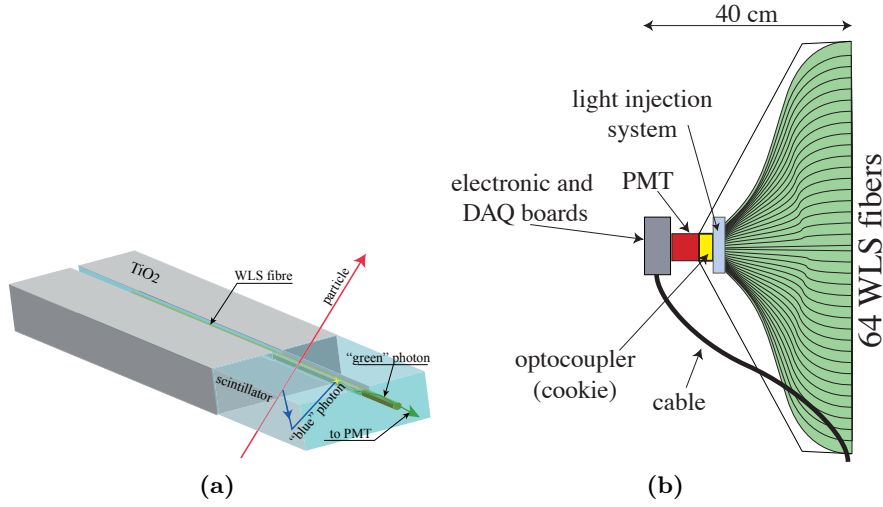
Figure 2.15 – (a) Scintillator strip, and the WLS fibre for light readout. (b) Schematic view of an end-cap of a TT module. Figures are taken from [142].
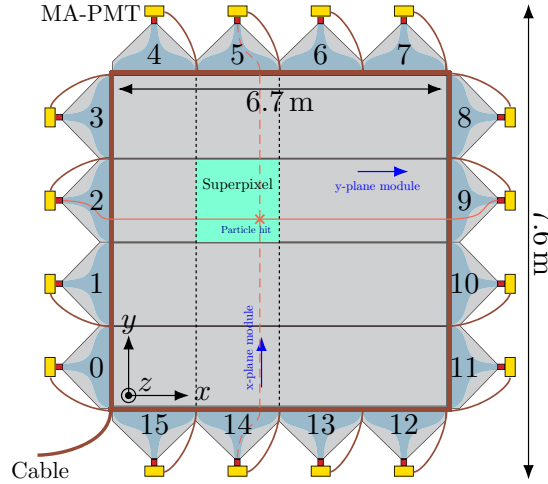
Figure 2.16 – Schematic view of a TT wall from the top.

fibre for the PMT readout. The TiO_2 coating is applied for better light collection.

A module is then built of 64 strips readout by WLS fibres coupled to two 64-channel multi-anode PMTs[6] (MA-PMTs). The 64 strips in the module are fixed by an aluminium cover wrapping the entire module. Figure 2.15(b) shows an end-cap of a TT module, through which all fibres on one side of the module are directly routed to the MA-PMT. The TT front-end electronics will be placed right after the MA-PMTs.

Four modules are arranged in parallel to form a TT plane. A TT wall, illustrated by Figure 2.16, is composed of two planes that are overlapped perpendicularly, such that a 3-dimensional (3D) track information can be reconstructed for a passing particle. The sensitive area of a TT wall is therefore $6.7 \times 6.7 \, \text{m}^2$, not including the end-caps. With the end-caps, the dimension of a TT wall is extended to $7.6 \times 7.6 \, \text{m}^2$. In JUNO, the upper plane is termed y-plane and the lower is x-plane, as they measure the y and the x coordinates of a TT hit in JUNO reference frame, respectively. The overlapped region of two modules belonging to different planes is called a "superpixel". When a particle

---

[6]Model number: Hamamatsu H8804MOD-1

Figure 2.17 – Schematic view of the top tracker. The red line is a passing atmospheric muon, which leaves three 3D points in TT. At the top left corner, the TT profile on the x-z plane is also shown.

passes the TT wall at a superpixel, the 4 related MA-PMTs (2 from x-plane module and 2 from y-plane module) could have signals. It is worth mentioning that, due to the attenuation inside the fibres, it is not always possible to readout the scintillation light on both sides. The MA-PMTs of a TT wall are identified by their IDs from 0 to 15, as labelled in Figure 2.16.

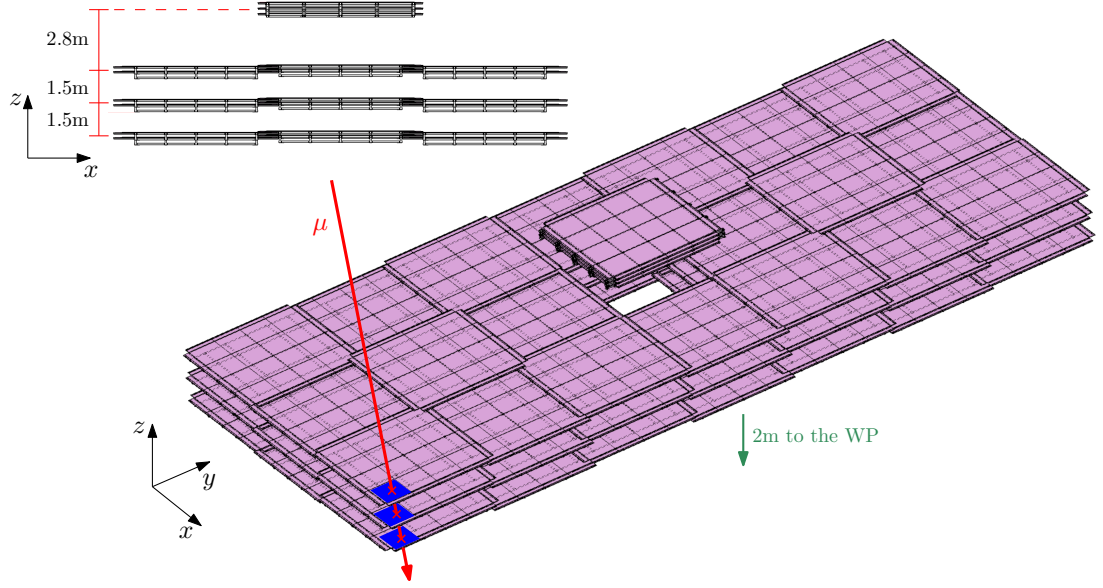The TT has 63 TT walls, and it is designed to be a 3-layer muon tracker, as shown in Figure 2.17, for the reason that a meaningful muon tracking needs at least 3 3-dimensional points (3D points). Each TT layer is a 3×7 grid with 21 TT walls horizontally placed. The 3 TT walls at the centre are lifted above the CD chimney. These walls above the chimney cover the entire gap of the chimney, such that muons entering the CD vertically through the chimney can be tagged. The neighbouring walls in the same layer will have a 15 cm overlap of their sensitive regions, such that the inactive area of one TT wall can always be recovered by the active areas of the others. The vertical distance between two layers is fixed to 1.5 m, and the walls above the chimney are placed 2.8 m above the top layer, while the walls themselves are only separated by 23 cm. The height from the Water Pool (WP) to the bottom layer is about 2 m.

OPERA had developed a functional readout electronics for the auto-triggered readout. However, due to the natural radioactivity level in the JUNO cavern, which is about 60 times higher than the one in the Gran Sasso Underground Laboratory, where the OPERA detector was located, the estimated radioactive rate per MA-PMT is larger than 50 kHz, leading to nearly 100% dead time of the TT readout. In order to suppress the undesired radioactive background, the TT readout electronics must be redesigned. In particular, an efficient trigger strategy is compulsory for the new system. The actual consideration of the trigger strategy is based on a two-level trigger. The design of the TT trigger system is the main subject of Chapter 5, where more details will be discussed.

Besides serving as a muon tracker, thanks to its tracking precision, the TT should be able to perform measurements for the studies on the cosmogenic isotopes, and help to tag the spallation neutrons that are produced in the surrounding rock and induce
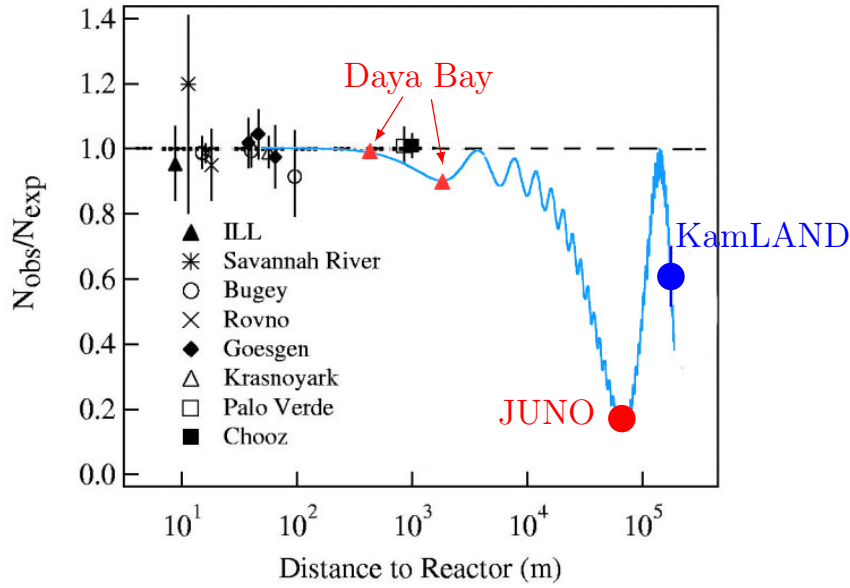
Figure 2.18 – Summary of past reactor antineutrino experiments' results, as ratio of observed to expected count rate vesus the baseline. The predicted $\bar{\nu}_e$ survival probability is also shown (blue line). The plot is taken from [145].

the IBD background. All these TT applications will be detailed in Chapter 6.

2.3 Neutrino mass hierarchy determination

Equation (1.59) points out that antineutrino oscillations are sensitive to the νMH by differentiating the NH and the IH with the sign of the phase ϕ in the oscillating term. Figure 2.18 shows the ratios of observed over non-oscillating expected events as a function of the baseline for various experiments. The theoretical prediction assuming that the νMH is normal, obtained from the oscillation theory, i.e., Equation (1.59), is also shown on the plot. From this prediction, we see that the antineutrino count rate is maximally suppressed at the distance of $\sim 50\,\text{km}$ due to the solar oscillation parameters. At such a baseline, the detector will have the best sensitivity to study the νMH. As a matter of fact, in order to determine the νMH, the JUNO baselines to Taishan and Yangjiang NPPs are both optimised to $53\,\text{km}$, located in the valley of the profile.

Due to neutrino oscillations, $\bar{\nu}_e$ disappears in the JUNO detector, and the measured energy spectrum becomes one of the two spectra depicted by Figure 2.19, depending on the true νMH. The large suppression from the no oscillation spectrum is caused by the solar neutrino oscillation parameters θ_{12} and Δm_{21}^2, while the small ripple mainly stems from θ_{13} and $\Delta m_{31/32}^2$. This configuration allows us to access the phase shift ϕ tied to the νMH, which can be identified on the plot as the difference between two curves.

2.3.1 Inverse beta decay background

In JUNO, there are five major IBD backgrounds: the accidental background, the background from cosmogenic isotopes ^{9}Li and ^{8}He, the spallation fast neutron background, the α-^{13}C interaction background, and the geo-neutrino background.
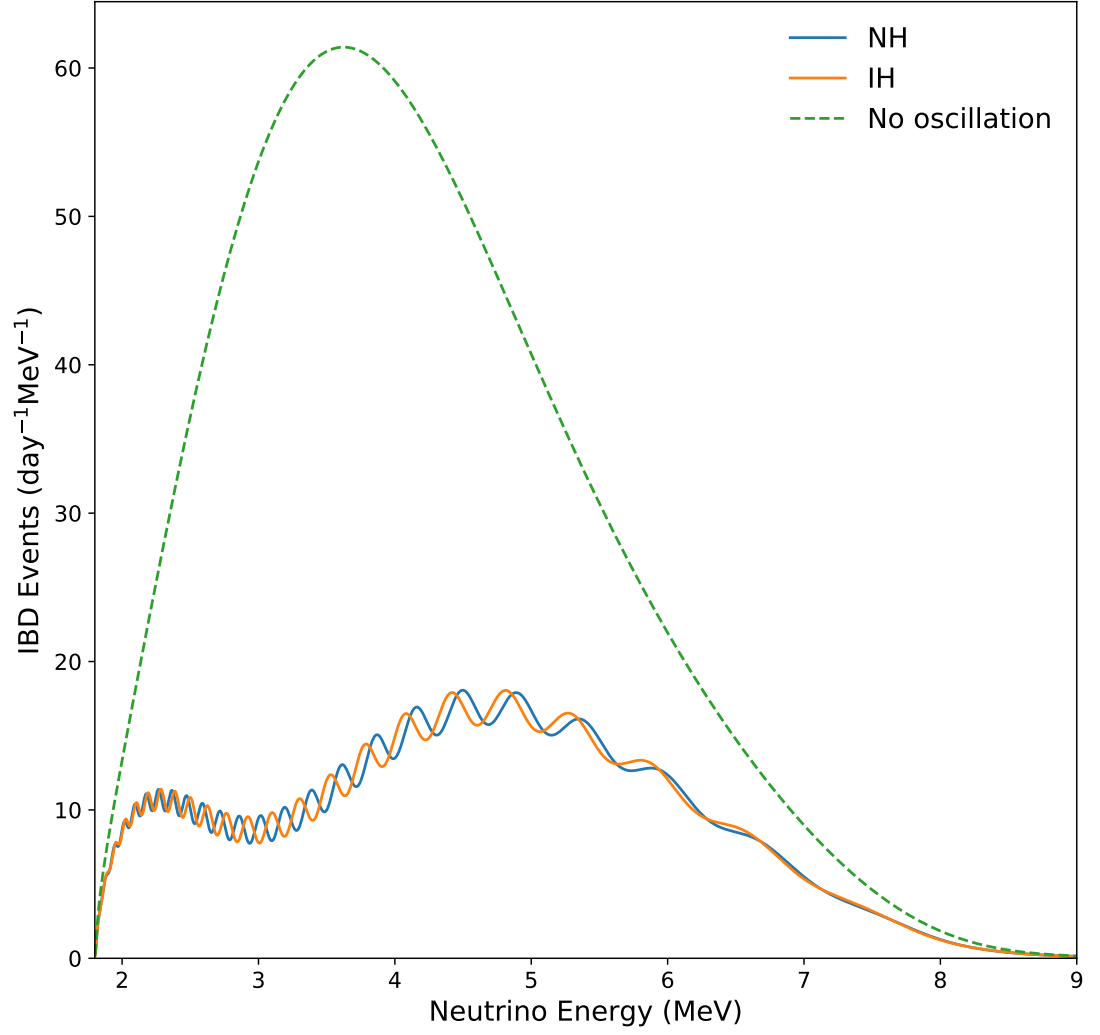
Figure 2.19 – JUNO $\bar{\nu}_e$ energy spectra of NH and IH with oscillation parameters in [14], normalised to one JUNO active day.

Accidental background

As previously mentioned in Section 2.1.2, the IBD detection technique will be a search of prompt-delayed coincidences in the CD. However, it is always possible that some random physics processes happen to be within the IBD time window, which is about 1 ms, and result in a fake IBD. The most probable process contributing to the accidental background is the decay of natural radioactive isotopes. The radioactivity-radioactivity coincidences then form the most important IBD accidental background, giving ∼410 fake IBD counts per day. It exists other possible accidental coincidences that may be observed in JUNO, such as the coincidences between radioactive decays and cosmogenic isotopes, and the coincidences between radioactive decays and spallation neutrons. The accidental coincidence rates can be further suppressed by requiring a space correlation between the prompt and the delayed signals. By limiting the maximal distance between the two signal vertices below 1.5 m, the accidental background drops to 1.1 counts per day, including the contributions of coincidences of pure radioactivity, and between radioactivity and cosmogenic isotopes. Regarding the last type of coincidence, most spallation neutrons in the CD need less than 1.5 ms to be captured, therefore, a veto of the whole LS volume for 1.5 ms following the arrival of atmospheric muons is expected to be efficient for removing the neutron-like signals, resulting in a negligible background rate.

We expect that both rates of radioactivity and of the neutron-like events from muon spallation can be precisely monitored by JUNO, so the uncertainty of accidental background rate can be controlled within 1%. Furthermore, the energy spectrum shape measurement can introduce a systematic uncertainty, which is termed "shape uncertainty". For this uncertainty, we assume that the counts in different bins are not correlated, such that the spectrum shape is transformed. Thanks to a large statistics of prompt-like signals, the energy spectrum of accidental background can be very well measured and thus the shape uncertainty will be negligible.

^{9}Li/^{8}He background

Apart from the accidental background, it exists some physics processes generating the correlated IBD-like signals in the interesting energy range, and they form also backgrounds of the IBD detection. The $\beta^- n$ decay of the cosmogenic isotopes ^{9}Li and ^{8}He is one of these processes.

When these isotopes decay, the electrons will first produce prompt signals in the CD, and the neutrons will be captured later to produce correlated delayed signals. Therefore, the methods used in accidental background veto are not sufficient for rejecting the ^{9}Li and ^{8}He background. Previous measurement [146] reveals that the production rates of the isotopes are roughly an exponential distribution of the lateral distance between the isotopes and the parent muon trajectory. Based on this fact, the most effective approach to reject ^{9}Li/^{8}He background is to veto a sufficient detector volume along all muon trajectories for a relatively long time, as illustrated by Figure 2.20.

In the guideline configuration, the veto time is 1.2 s, being several times of the isotopes' half-lives, and the radius of the veto volume is 3 m. As long as muons in the CD are reconstructed, the muon veto will be applied to reject most background events from the ^{9}Li/^{8}He decays. If muons are badly reconstructed, the whole CD will be vetoed for 1.2 s to avoid the ^{9}Li/^{8}He contamination.

Given the muon flux in the JUNO cavern is 0.0037 Hz/m^2, we estimate 84 background events per day caused by the $\beta^- n$ decays. After applying the cuts for the
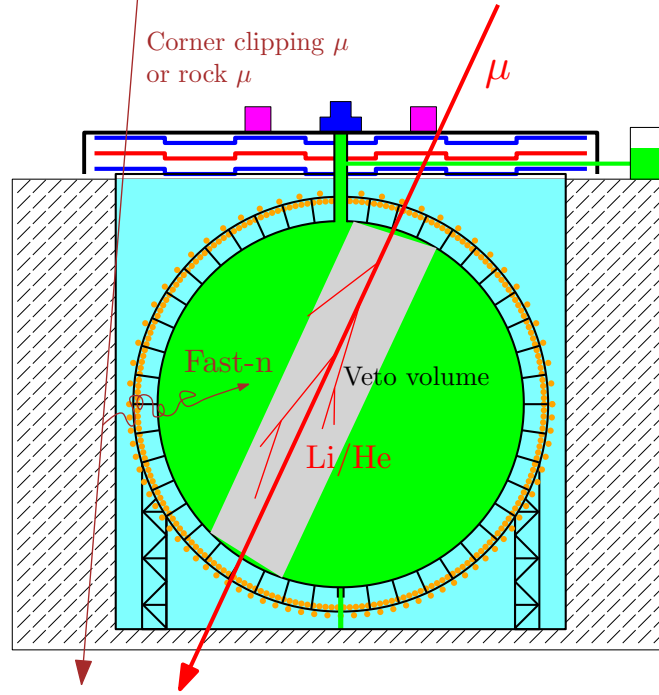
Figure 2.20 – Atmospheric muons producing ^{9}Li/^{8}He isotopes or fast neutrons. When a muon is tracked in the CD, a veto volume along the trajectory will be established.

accidental background, the rate is reduced to 71 per day. Assuming 99% of muon tracks can be reconstructed, the probability that a background event can survive after the muon veto is expected to be only 2.3%. Therefore, just 1.6 ^{9}Li/^{8}He $\beta^- n$ decays per day can really be the IBD background.

Since the ^{9}Li/^{8}He background rate depends on the muon veto, its uncertainties come mainly from the muon reconstruction uncertainty and the vertex resolution of IBD candidates. According to the Monte-Carlo simulations and the experience from the previous experiment [76, 125], the rate uncertainty of the ^{9}Li/^{8}He background is conservatively set to 20%, and the shape uncertainty is taken as 10%.

Fast neutron background

A fast neutron event is a spallation neutron with a sufficient kinetic energy, scattering off a proton and then being captured in the CD. Such a process produces a correlated prompt-delayed coincidence, mimicking the IBD signature, therefore, it is also an IBD background. Like other spallation neutrons that take part in the accidental background, a fast neutron is usually not too troublesome, as long as we apply a veto of the whole CD lasting 1.5 ms after tagging a muon. However, the muons that only pass the surrounding rock of the Water Pool, as well as the corner clipping muons with very short track in the Water Cherenkov Detector, are not able to be tagged, as shown in Figure 2.20. In this case, the TT can help to detect partially these missing muons, and thanks to the TT measurement, we will have a better knowledge of the fast neutron rate in JUNO. The current estimation of the fast neutron rate in JUNO based on the MC is less than 0.1 events per day.

For using the estimated rate of fast neutron background obtained from simulation in the mass hierarchy analysis, the rate uncertainty is conservatively estimated to be 100%. Its energy spectrum is considered to be a flat distribution. The fast neutron events

tagged by the TT can actually provide good information about the energy spectrum, so the shape uncertainty is conservatively estimated to be 20% in the νMH analysis.

$^{13}\mathrm{C}(\alpha, \mathrm{n})^{16}\mathrm{O}$ background

In JUNO, correlated background signals can come from $^{13}\mathrm{C}(\alpha, \mathrm{n})^{16}\mathrm{O}$ interaction. When an α particle emitted from U or Th decay chains, it can react with the $^{13}\mathrm{C}$ in the LS, producing a neutron and a $^{16}\mathrm{O}$ nucleus. The prompt signal is then from neutron elastic scattering on proton or inelastic scattering on $^{12}\mathrm{C}$, and the delayed signal is neutron capture after it is thermalised. If $^{16}\mathrm{O}$ is in the excited state, it emits a γ or a conversion electron by de-excitation, which also contributes to the prompt signal. Lacking a good detection technique, the treatment of this background is to subtract its spectrum calculated *a priori* statistically from the measured IBD spectra [147]. The $^{13}\mathrm{C}(\alpha, \mathrm{n})^{16}\mathrm{O}$ rate in JUNO is calculated based on our knowledge of natural radioactivity concentrations, and is of about 0.05 events per day.

The cross-section of $^{13}\mathrm{C}(\alpha, \mathrm{n})^{16}\mathrm{O}$ has $\sim$20% uncertainty for an α particle with energy below 10 MeV [147]. Therefore, the rate uncertainty of this background depends on how precisely the rate of α particle can be measured in JUNO. In the νMH analysis, both the rate uncertainty and the shape uncertainty are set to 50% for being conservative.

Geo-neutrino background

The geo-neutrinos coming from U and Th inside the Earth crust and mantle form a background of the reactor antineutrino detection. Since the geo-neutrinos produce IBD signals, they are not distinguishable from the reactor $\bar{\nu}_e$. The background can only be removed from the reactor $\bar{\nu}_e$ sample statistically. Based on the estimation of geo-neutrino flux, JUNO is expected to have 1.1 geo-neutrino IBD events per day.

The predictions of crust and mantle geo-neutrino fluxes are assumed to have rate uncertainties of 18% and 100%, respectively [148, 149]. Based on this, the rate uncertainty of geo-neutrino background is set to 30% in the νMH analysis. On the other hand, the β-decay spectra of Th and U are well known from the nuclear physics, so the shape uncertainty can be set to 5% even in the most conservative scenario.

2.3.2 Inverse beta decay signal selection

To reduce contamination of the aforementioned backgrounds in the IBD sample, JUNO set some criteria for IBD event selection:

- fiducial volume cut $r < 17$ m;

- the prompt energy cut $0.7\,\mathrm{MeV} < E_\mathrm{p} < 12\,\mathrm{MeV}$ (Energy cut);

- the delayed energy cut $1.9\,\mathrm{MeV} < E_\mathrm{d} < 2.5\,\mathrm{MeV}$ (Energy cut);

- time interval between the prompt and delayed signal $\Delta T < 1.0\,\mathrm{ms}$ (Time cut);

- the prompt-delayed distance cut $R_\mathrm{p-d} < 1.5\,\mathrm{m}$ (Vertex cut);

- Muon veto criteria:

  - for muon tagged by Water Pool, veto the whole LS volume for 1.5 ms;

  - for good tracked muon in central detector and water Cherenkov detector, veto the detector volume within $R_{d2\mu} < 3\,\mathrm{m}$ and $T_{d2\mu} < 1.2\,\mathrm{s}$;

Table 2.3 – The efficiencies of reactor antineutrino selection cuts, and the signal and background rates. Rates are normalised to per day. The relative rate uncertainties and shape uncertainties of the backgrounds obtained from background studies are appended.

Selection	IBD efficiency	IBD	Geo-νs	Accidental	^{9}Li/^{8}He	Fast n	(α, n)
		83	1.5	$\sim 5.7 \times 10^4$	84		
Fiducial volume	91.8%	76	1.4		77		
Energy cut	97.8%			410			
Time cut	99.1%	73	1.3		71	0.1	0.05
Vertex cut	98.7%			1.1			
Muon veto	83%	60	1.1	0.9	1.6		
Combined	73%	60		3.8			
Rate uncertainty			30%	1%	20%	100%	50%
Shape uncertainty			5%	negligible	10%	20%	50%

– for the tagged, non-trackable muons in central detector, veto the whole LS volume for $1.2\,$s.

These criteria are optimised according to both JUNO MC simulation and results of other neutrino experiments, of which KamLAND and Daya Bay have the most important inputs. By applying these cuts sequentially as in the list, Table 2.3 summarises the estimated signal and background rates. The relative rate uncertainties and shape uncertainties obtained from the background studies are also shown.

Figure 2.21 shows the reactor antineutrino energy spectrum from the Monte-Carlo simulations with 3% energy resolution, and the contributions from the backgrounds within the IBD relevant energy range. From the plot, we have found that, in the energy range $E < 3.5\,$MeV, the geo-neutrinos and accidental backgrounds are dominant backgrounds, and in the range $E > 3.5\,$MeV, the dominant background is the ^{9}Li/^{8}He. Since the νMH determination is more sensitive in the range $E > 3.5\,$MeV, we can conclude that ^{9}Li/^{8}He is the most important background in JUNO, and needs to be treated more carefully.

2.3.3 Neutrino mass hierarchy sensitivity

To quantify the sensitivity of νMH determination, we can first construct a χ^2 function by the least-squares method

$$\chi^2(\text{NH or IH}) = \sum_{i=1}^{N_{\text{bin}}} \frac{[M_i - T_i(1 + \sum_k \alpha_{ik}\epsilon_k)]^2}{M_i} + \sum_k \frac{\epsilon_k^2}{\sigma_k^2}, \qquad (2.5)$$

In the equation, M_i is the measured number of events in the i-th energy bin; T_i is the expected number of events with reactor $\bar{\nu}_e$ oscillation effects, of which the νMH is either the NH or the IH; σ_k is the systematic uncertainty; ϵ_k is the corresponding pull parameter; and α_{ik} is the fraction of IBD event contribution of the k-th pull parameter to the i-th energy bin. The considered systematic uncertainties include the correlated (absolute) reactor uncertainty (2%), the uncorrelated (relative) reactor uncertainty (0.8%),
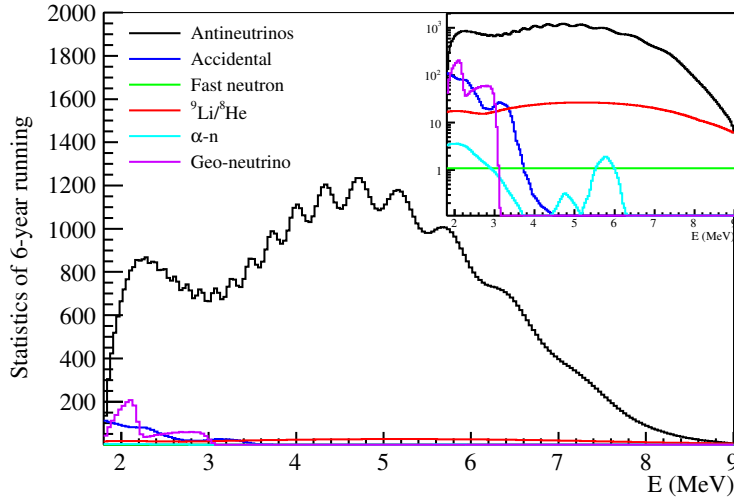
Figure 2.21 – Spectra for the reactor antineutrino signals and the backgrounds in JUNO with 3% energy resolution and 6-year running statistics. The abscissa E is the $\bar{\nu}_e$ energy. The small plot at the top right corner of the main plot is the same but with a logarithmic ordinate.

the spectrum shape uncertainty (1%) and the detector-related uncertainty (1%). 200 equal-size bins are distributed for the incoming neutrino energy ranging from 1.8 MeV to 8 MeV.

The best fit with the χ^2 method for each νMH shall give the minimum of Equation (2.5). The νMH discriminator $\Delta\chi^2_{\text{MH}}$ can therefore be defined by

$$\Delta\chi^2_{\text{MH}} = |\chi^2_{\text{min}}(\text{NH}) - \chi^2_{\text{min}}(\text{IH})|. \tag{2.6}$$

In [150–153], the νMH sensitivity at $n\sigma$ has been proven to be determined by the $\Delta\chi^2_{\text{MH}}$, where $n = \sqrt{\Delta\chi^2_{\text{MH}}}$. Consequently, JUNO has optimised the baselines to both major reactors in order to maximise $\Delta\chi^2_{\text{MH}}$, as shown in Figure 2.22. Here, $\Delta\chi^2_{\text{MH}}$ is calculated without considering yet the systematic uncertainties. The plots in the figure
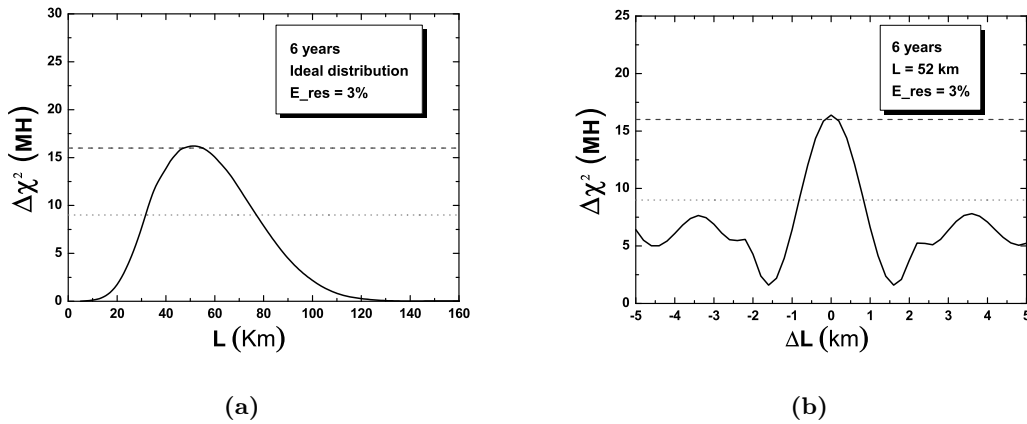

(a)

(b)

Figure 2.22 – The νMH discriminator $\Delta\chi^2_{\text{MH}}$ as the function of (a) the baseline with one reactor, and (b) the baseline difference of two reactors. The energy resolution and the running time are fixed to 3% and 6 years, respectively [118].
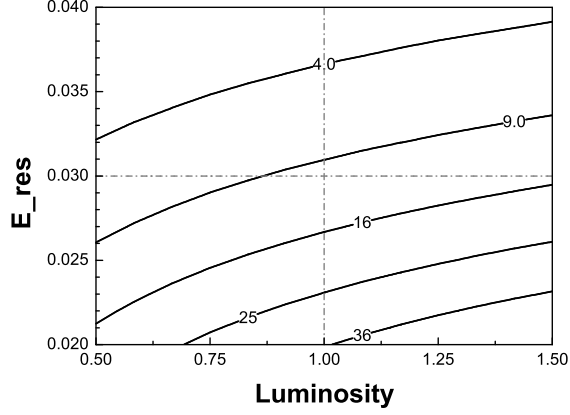
Figure 2.23 – Iso-$\Delta\chi^2_{\text{MH}}$ contour plot as the function of event statistics (luminosity) and the energy resolution, where the vertical dash-dotted line (luminosity=1) stands for the statistics of 6-year running.

reveal that, if we want to achieve the best possible νMH sensitivity, the baselines to both Taishan and Yangjiang reactors must be about 50 km. Moreover, to ensure a sensitivity better than 3σ (equivalently, $\Delta\chi^2_{\text{MH}} > 9$), the difference between any 2 cores must be less than 500 m. The ideal placement leads to a maximal $\Delta\chi^2_{\text{MH}} \approx 16$, with 3% energy resolution for 6-year running. Following this conclusion, the JUNO has chosen its site at 53 km baselines to both reactors.

Besides the statistical approach for sensitivity estimation ($\Delta\chi^2_{\text{MH}} \approx 16$), it is also important to take into account other influences on the final JUNO sensitivity. Firstly, the real locations of Yangjiang and Taishan cores give the baselines slightly differed from the optimal, resulting in a degradation of $\Delta\chi^2_{\text{MH}}$ by 3. Secondly, we need to consider that $\bar{\nu}_e$ from other NPPs in the region, such as Daya Bay NPP and Huizhou NPP, will also be detected in JUNO, and this decreases the discriminator by 1.7. Thirdly, as a reactor $\bar{\nu}_e$ experiment, JUNO relies on a good knowledge of the reactor $\bar{\nu}_e$ spectra, and particularly the shape uncertainty. By assuming 1% of reactor shape uncertainty, $\Delta\chi^2_{\text{MH}}$ will be degraded by 1. Finally, the systematic uncertainties from background estimation (Table 2.3) will further reduce the discriminator, of which the rate uncertainty reduces 0.4, and the shape uncertainty reduces 0.1. In total, we obtain that the discriminator $\Delta\chi^2_{\text{MH}} \approx 9.6$, or equivalently our νMH sensitivity is 3.1σ.

The desired 3σ sensitivity also sets a constraint on the energy resolution of the JUNO detector. JUNO can detect about 60 IBD events per day, giving a total statistics of $\sim 10^5$ in 6 years. Figure 2.23 shows an iso-$\Delta\chi^2_{\text{MH}}$ contour plot as the function of event statistics (luminosity) and the energy resolution, where the statistics is normalised by 10^5 events. If we want to achieve a 3σ sensitivity in 6 years, the plot shows that the energy resolution must be better than 3.1%. The plot also answers why the energy resolution is so critical for JUNO: if the energy resolution is worsened to 3.3%, the JUNO sensitivity can barely reach 3σ even for a 9-year running.

2.4 Other physics in JUNO

JUNO will not only undertake the νMH determination with the reactor $\bar{\nu}_e$, but also has a rich neutrino physics program. It will be used for precision measurements of mixing parameters, various studies on atmospheric neutrinos, geoneutrinos, supernova neutrinos, and contribute to multi-messenger astrophysics.

2.4.1 Precision measurement of mixing parameters

As shown in Figure 2.19, the JUNO $\bar{\nu}_e$ spectrum gives access to the oscillation parameters $\theta_{12}, \theta_{13}, \Delta m_{21}^2$ and Δm_{31}^2. Many established experiments have measured these parameters, as we have shown in Section 1.4, but no one is going to achieve a sub-percent precision with the current apparatuses. Thanks to the large statistics and the unprecedented energy resolution, JUNO will be able to measure three parameters with a sub-percent precision: $\theta_{12}, \Delta m_{21}^2$ and Δm_{31}^2. By taking into account all effects from the previously mentioned systematic uncertainties, the JUNO nominal setup can have a precision of 0.67% for θ_{12} measurement, 0.59% for Δm_{21}^2 measurement, and 0.44% for Δm_{31}^2 measurement.

The precision measurement of θ_{12}, Δm_{21}^2, and Δm_{31}^2 at sub-percent level is important for understanding many interesting physics. One example is that the precisely measured parameters can be used to test the unitarity of the PMNS matrix and reach a CKM-like precision. More applications include the mass sum rule test if $\Delta m_{13}^2 + \Delta m_{21}^2 + \Delta m_{32}^2 = 0$, and the discrimination for models of neutrino masses and mixing.

2.4.2 Non-reactor neutrino physics

JUNO is able to study atmospheric neutrinos with low energy detection threshold and excellent energy resolution. The atmospheric neutrinos above $100\,\mathrm{MeV}$ in the detector interact with nuclei (^{12}C/proton) in the LS through CC and NC interactions [154]. We can identify the original flavour of the neutrinos by the event geometries, and possibly by the time spectra, as suggested in [154]. Therefore, a νMH determination via matter effect of atmospheric neutrinos as a complementary measurement to the reactor $\bar{\nu}_e$ νMH determination is achievable in JUNO. The sensitivity is estimated to be up to 2σ for 10-year running [155].

Although geo-neutrinos are treated as a major background of reactor $\bar{\nu}_e$ detection, JUNO can be used to study the geo-neutrinos thanks to its large target volume. The expected rate of geo-neutrinos is about 400 events per year, making JUNO the largest geo-neutrino sample in less than one year running [149]. With such a high statistics, JUNO should be able to separate the contributions of Th and U in geo-neutrino flux, and the ratio Th/U can be valuable inputs for Earth sciences, such as explaining the power source of the geodynamo.

In a core-collapse supernova (CCSN) explosion, more than 99% of its gravitational binding energy is released as neutrinos [156]. Decoding the information carried by the neutrinos can help us to better understand the physics in CCSN. The neutrino burst from the next nearby CCSN can be characterised easily and the signal lasts about $10\,\mathrm{s}$ [157]. JUNO is sensitive to the neutrino burst detection through various channels: IBD, CC/NC interaction on ^{12}C, elastic scattering of neutrinos on electrons, and elastic scattering of neutrinos on protons. With large target volume, low energy detection threshold, and good energy resolution, JUNO will be one of the best SN neutrino de-

tectors with impressive SN neutrino statistics: for a typical galactic distance of $10\,\mathrm{kpc}$ and typical SN parameters, more than 7000 IBD events is estimated to be registered, of which 5000 are detected via IBD, and the rest is from the other detection channels [158]. Due to the high statistics and short signal duration, the background of SN neutrino should be very small. Furthermore, the neutrino signal should be detected a few hours before the optical discovery [157]. By providing the real-time signals of SN neutrino, JUNO will also take part in SuperNova Early Warning System (SNEWS) [159] in combination with other neutrino detectors, gravitational-wave detectors, and observatories in various electromagnetic channels.

Finally, JUNO has more physics potentials to be exploited, for example, the diffuse supernova neutrino background (DSNB), solar neutrino physics, etc.

2.5   Summary

In this chapter, we introduced the JUNO detector and the physics that will be explored in JUNO. Since this thesis is more related to reactor $\bar{\nu}_e$ detection, the introduction naturally focused more on it. To some extent, this chapter tried to explain the νMH sensitivity at 3σ for the JUNO nominal setup, and showed that it requires the JUNO energy resolution to be better than 3%. Although the resolution can be reached in JUNO, the sensitivity budget is still very tight, and all systematic uncertainties must be well controlled, including the background uncertainties. How to suppress the muon-induced background (cosmogenic isotopes, fast neutrons) and reduce its uncertainties will be the key to success for the experiment.

Chapter 3

Performance study on Occulting Light Concentrators

JUNO requires a high photocathode coverage to ensure a photoelectron yield better than 1200 p.e./MeV. The current design has a coverage of 78%, which is maximised under the constraints of the detector geometry. Although the coverage is sufficient for our targeted photoelectron yield, it is still interesting for us to look for a solution that can increase the coverage beyond the geometrical limits.

One of the possible solutions is to use non-imaging light concentrators (LCs) [160] on the LPMTs, which take light incident on a wider entrance aperture and direct it by reflection from a curved surface onto the PMT photocathodes. The LC is a well known device in particle and astroparticle physics, and they have been applied to a type of neutrino experiments which are designed to have a large sensitive volume and detect neutrinos via light emission, such as SNO/SNO+ [98, 161], Borexino [162], and CTF [162, 163]. JUNO is certainly in this category. Figure 3.1 shows the photos of the LCs used in SNO/SNO+ and Borexino. The main goal of the LCs in these experiments has always been to maximise the collected light by increasing the effective photocathode coverage.

<div align="center">(a)   (b)</div>
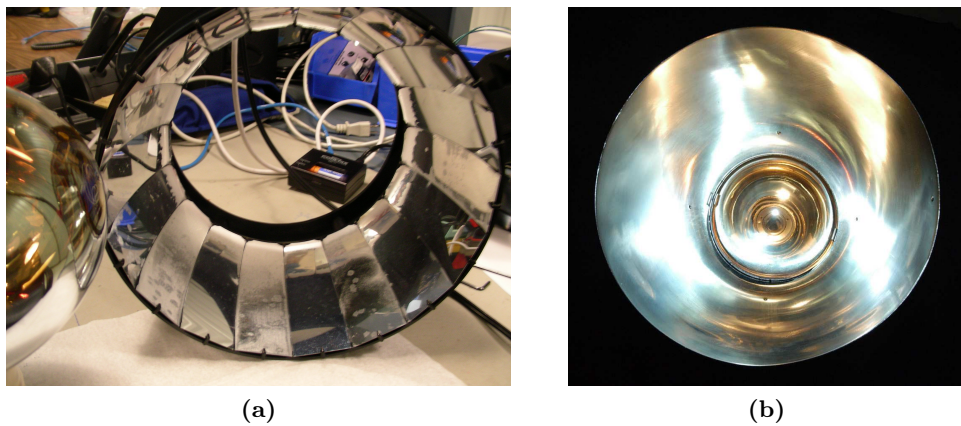
Figure 3.1 – Photos of (a) a SNO/SNO+ LC [164], and (b) a Borexino LC mounted on the PMT [162]. Both LCs are designed for 8" PMTs.

LPMTs in JUNO have a diameter of 20 inches, and with the current technology, the LPMT photocathode will have worse photon detection efficiency at the edge than at the centre. Since the LC can reflect light onto a smaller area, it can be used to
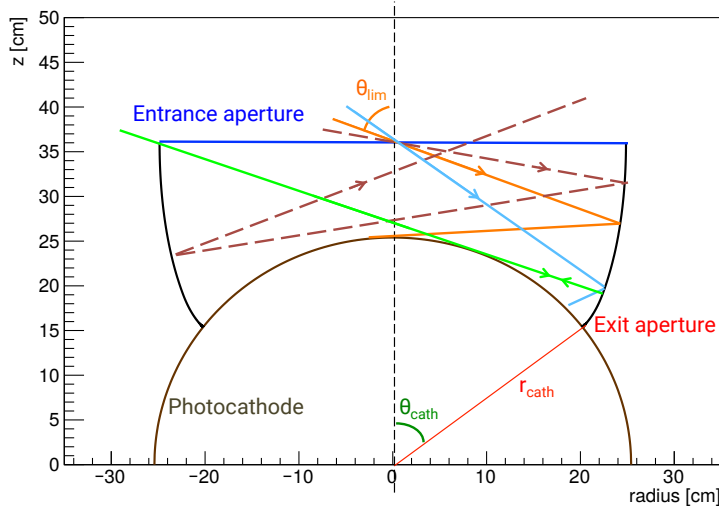
Figure 3.2 – Schematic view of an example OLC design in 2D, and the example rays for cases where the incident angles are $< \theta_{\text{lim}}$ (blue solid line), $= \theta_{\text{lim}}$ (orange solid line), and $> \theta_{\text{lim}}$ (brown dashed line). Green solid line illustrates a ray from the concentrator edge with an incident angle $= \theta_{\text{lim}}$.

improve the LPMT detection efficiency by recovering the light from being absorbed by the worst-performing region. By this means, we expect to increase the total number of photoelectrons (N_{pe}) of the LPMT system. An LC tailored for such a usage is termed Occulting Light Concentrator (OLC).

After a brief introduction of the LC-related optical theory in Section 3.1, this chapter will focus on two OLC designs, the cut OLC and the Crown OLC, which be detailed in Section 3.2 and Section 3.3, respectively. Finally, in Section 3.4, the results of the performance study will be presented together with our conclusions.

3.1 Optical theory of OLC

The OLC is constructed by applying the tangent-ray principle [160]. While the detailed description about how to construct a LC based on the principle can be found in [165], this section will present a few important concepts before starting to develop our new design.

The design principle is optimised for a spherical or ellipsoid photocathode to avoid multiple reflection on the OLC, which can reduce its performance. Therefore, in an OLC, a ray incident at the entrance aperture with an angle equal to θ_{lim} will be reflected to strike the photocathode tangentially, as depicted in Figure 3.2 with the solid ray in orange. If the incident angle is less than θ_{lim}, the ray is transmitted to the photocathode by at most one reflection; otherwise, if the angle is greater than θ_{lim}, the ray is reflected twice on the OLC curved surface and will not be detected by the PMT. Figure 3.2 shows as well the example rays for these two cases: the solid ray in blue illustrates a ray with an angle less than θ_{lim} absorbed by the photocathode after the first reflection, and the dashed line in brown illustrates a ray refused by the OLC after two reflections on its curved surface, as the incident angle is greater than θ_{lim}. In the schematic view, the photocathode is considered to be a hemisphere with a radius r_{cath}. θ_{cath} is the angle between the OLC exit aperture and the symmetry axis of the photocathode. The
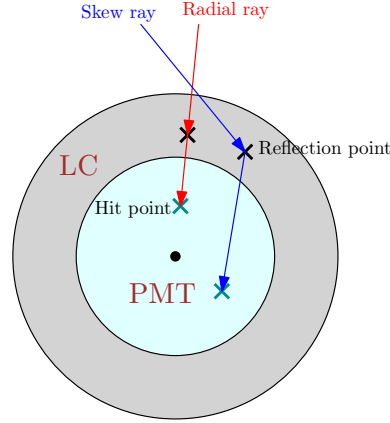
Figure 3.3 – Illustration of radial ray and skew ray in the top view of a PMT with a LC. A radial ray is in the same plane with the PMT central axis, while a skew ray does not belong to the plane that contains the central axis.
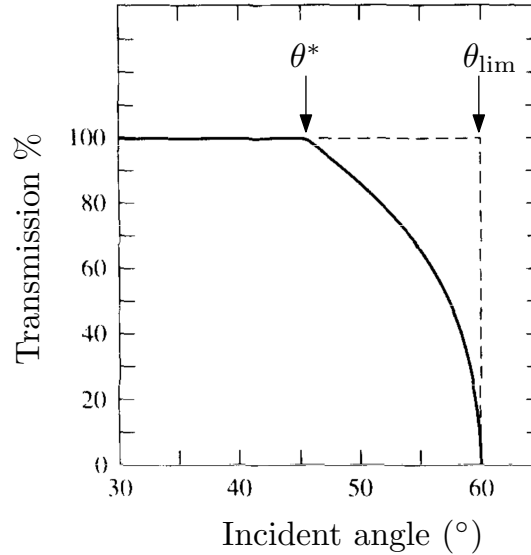

Figure 3.4 – Typical transmission curve for a 3D OLC as a function of light incident angle. The curve is taken from [161], it was calculated according to the SNO LC geometry.

critical angle θ_{lim} is termed the cut-off angle of the OLC.

Based on the 2D design in Figure 3.2, a 3D OLC can be built by rotating the 2D profile around the central axis. In the 3D OLC, it is however impossible to maintain the perfect cut-off angle θ_{lim}, because of skew rays. Skew rays are defined as rays that are not radial to the PMT, as depicted in Figure 3.3. It exists an angle $\theta^* < \theta_{\text{lim}}$ in a 3D OLC, from where light transmission of the OLC starts to fall off, as demonstrated in Figure 3.4 by an example transmission curve.

The relation between the cut-off angle θ_{lim} and the maximal incident angle that keeps 100% light transmission θ^* is given by the formula

$$\theta^* = \arcsin\left(\frac{\sin\theta_{\text{cath}}}{\theta_{\text{cath}}}\sin\theta_{\text{lim}}\right), \tag{3.1}$$

The optics of an OLC limits the angle of view for a PMT, so we need to optimise the OLC parameters according to the detector geometry. Figure 3.5 shows a simplified
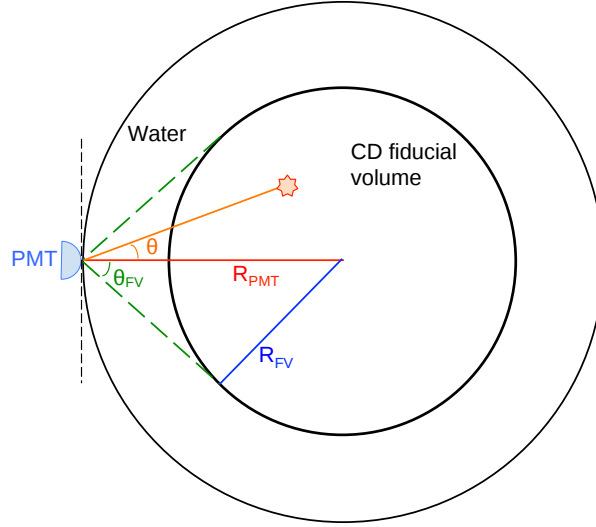
59

Figure 3.5 – The simplified optical geometry of a LPMT in the JUNO detector. θ_{FV} corresponds to the maximal incident angle of light from the CD fiducial volume.

optical geometry of a LPMT in the JUNO detector, from which a maximal incident angle of light from the Central Detector (CD) fiducial volume θ_{FV} can be determined by the CD fiducial volume radius R_{FV} and the distance from a LPMT to the CD centre R_{PMT}. In JUNO, $R_{FV} = 17.2\,\text{m}$ and $R_{PMT} = 19.5\,\text{m}$, θ_{FV} is thus equal to 61.9°. By using 17.2 m radius instead of 17.7 m, we apply an optical fiducial volume cut on the CD. The OLC θ_{lim} must be greater than θ_{FV}, otherwise the LPMT will partially reject the light from the CD fiducial volume, and cause a loss of N_{pe}. An optimisation on the light transmission can be achieved by requiring $\theta^* = \theta_{FV}$, such that the light from the CD fiducial volume is 100% detected by the photocathode.

3.2 Cut OLC design

The detection efficiency (DE) of a PMT is defined as the product of its quantum efficiency (QE) and its collection efficiency (CE) [166]. The quantum efficiency is the ratio between emitted N_{pe} from the photocathode and the number of incident photons [166], and it is usually not dependent on the photon hit position on the photocathode. The collection efficiency is defined as N_{pe} that reach the first dynode divided by N_{pe} produced from the photocathode, which is dependent on the photon hit position on the photocathode.

By measuring a few sample LPMTs, an empirical curve describing the LPMT collection efficiency profile is established, and shown in Figure 3.6. Since the LPMT shape is an ellipsoid, and the collection efficiency changes radially, the hit position ρ is then defined as a radius equal to the distance from the PMT centre to the hit position. We have found that the profile is almost flat up to a radius of 24 cm, where the collection efficiency is about 7% lower than at the PMT centre.

Given that the quantum efficiency is homogeneous across the photocathode, the detection efficiency is therefore much reduced at the edge due to the collection efficiency profile. The dependence of the PMT detection efficiency on the hit position induces dispersive effects in the LPMT system, leading to a reduced light collection and a worsened energy resolution [167]. Placing OLCs on LPMTs can mitigate the impact by reflecting all light to the central area ($\rho < 24\,\text{cm}$) of the photocathode, where the
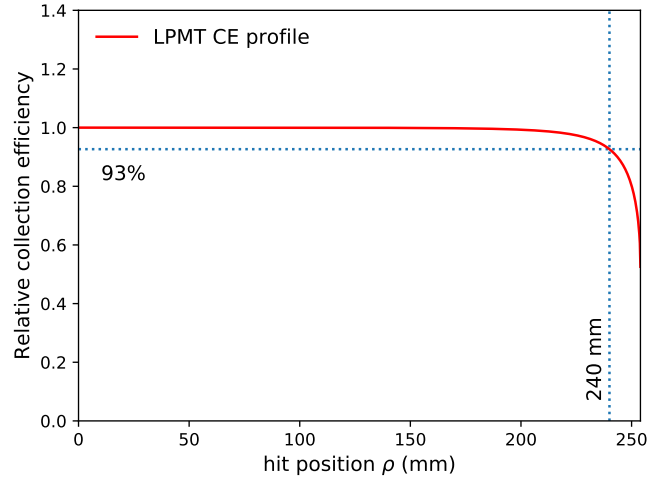
Figure 3.6 – The empirical collection efficiency profile of the LPMT obtained by fitting the measured results of LPMT samples [167]. The collection efficiency at the PMT centre ($\rho = 0$) is equal to 1, and at $\rho = 240\,\mathrm{mm}$, the collection efficiency is about 93%.
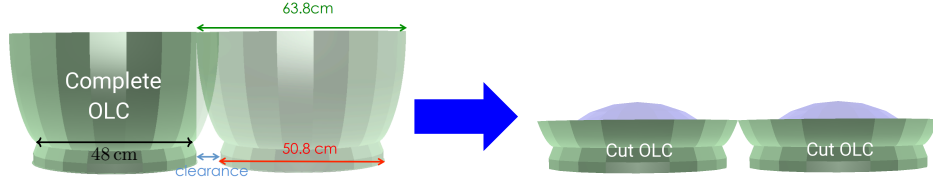

Figure 3.7 – A complete OLC with an exit aperture of 24 cm radius needs to be mowed, such that the Cut OLC can fit the LPMT geometry.

detection efficiency is maximal.

Consequently, the OLC exit aperture radius is fixed to $\rho = 24\,\mathrm{cm}$ to cut off the worst-performing photocathode region. For a complete OLC, the entrance aperture radius then needs to be as wide as 32 cm. However, the LPMT clearance being only 25 mm between LPMT equators, the OLC will not be able to fit the geometry. So the OLC height has to be cut, as illustrated in Figure 3.7. The Cut OLC is then installable for the LPMT clearance, but the field of view is also enlarged so the light outside the CD fiducial volume can enter the LPMT photocathode.

3.3 Crown OLC design

The limitation of Cut OLC is that it cannot provide a solution for 100% geometrical coverage of the detector, as shown in Figure 3.8. As a method to increase the upper limit of coverage to 100%, a new design of OLC is proposed. In the new design, instead of mowing the complete OLCs to avoid overlapping, we simply remove the overlapping parts. At the same time, the emplacements for 3 inch PMTs are also taken into account. Figure 3.9 illustrates how the design is obtained from overlapping complete OLCs. By covering entirely the spaces between LPMTs with the reflective curved surfaces, this approach allows to reach an almost total geometrical coverage without violating the OLC tangent-ray principle. The resultant shape of the OLC is shown in Figure 3.10, and the OLC is termed "Crown OLC" after its shape. It must be noticed that the 100%
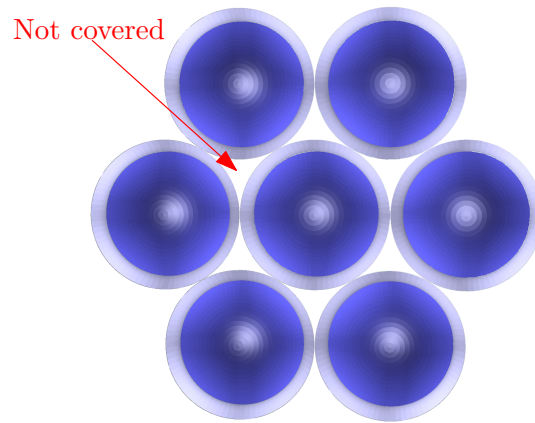
Figure 3.8 − Due to the circular entrance aperture, Cut OLC cannot cover all space between LPMTs.
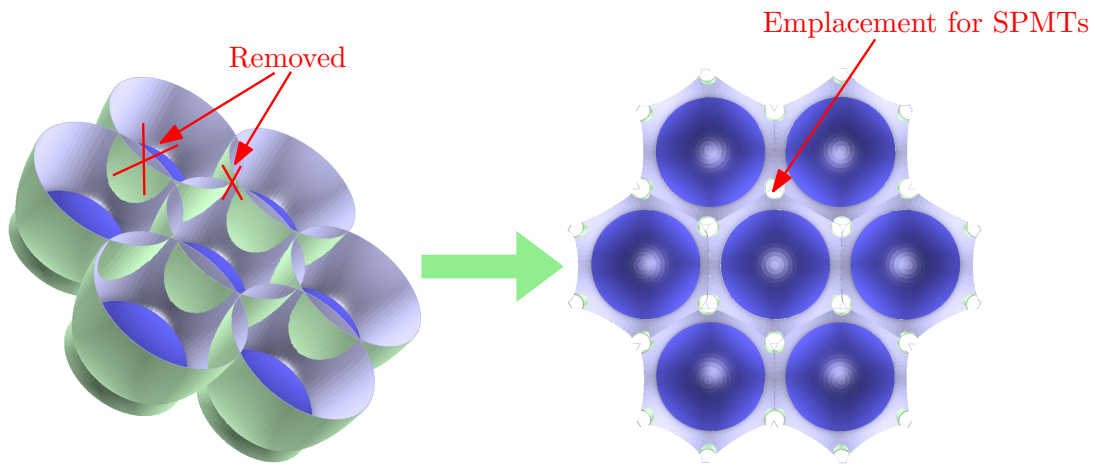
Figure 3.9 − In the new design, geometrical overlap of complete OLCs can be avoided by removing the overlapping parts. The spaces are also left for the SPMT emplacement.

(a)   (b)

Figure 3.10 − (a) A 3D view of an indivial Crown OLC, and (b) the 3D view of a group of LPMTs equipped with Crown OLCs.
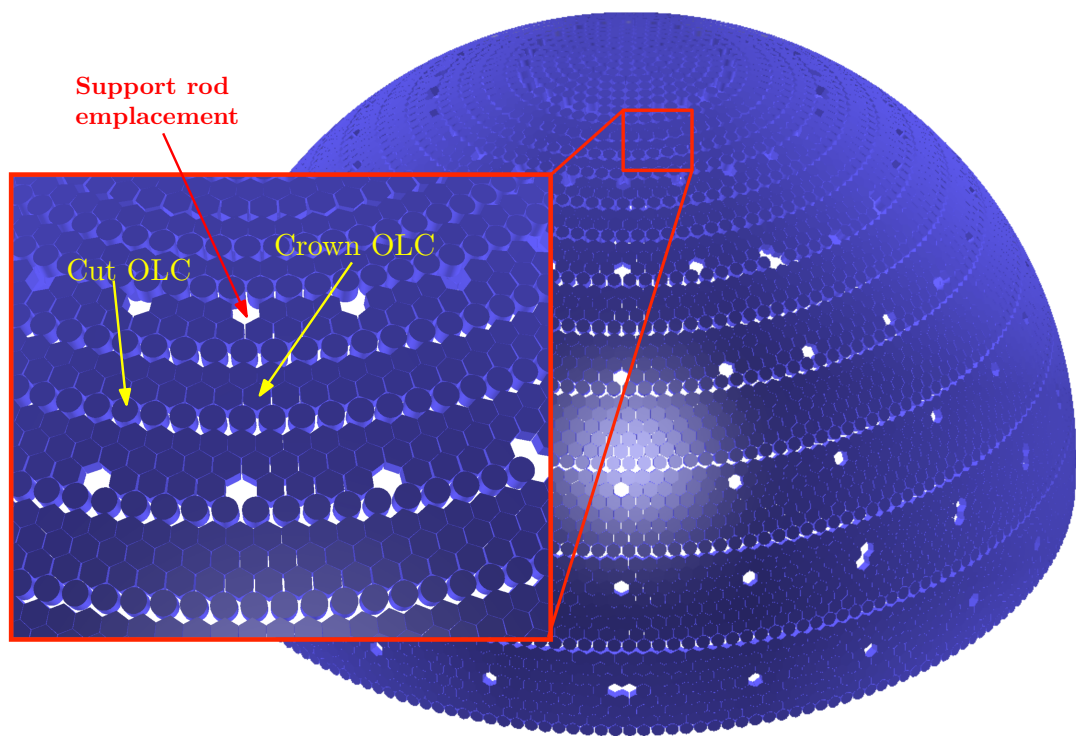
Figure 3.11 − In a spherical detector, Cut OLCs and Crown OLCs are mixed to achieve the a realisable patching of the detector, increasing the final coverage.

coverage with Crown OLCs can only be realised in a perfect hexagonal symmetrical geometry. In the case of a spherical detector, it is not possible to cover the sphere with only Crown OLCs. As illustrated in Figure 3.11, we propose a compromise consisting of 20% of Cut OLCs and 80% of Crown OLCs. In addition, some places are occupied by the support rods of the CD truss, therefore no LPMT can be installed there, which can be seen as holes in Figure 3.11.

3.4 Performances of Cut OLC and Crown OLC

The evaluation of the benefit derived by the implementation of OLC, including Cut OLC and Crown OLC, is performed with a Monte Carlo code based on the GEANT4 toolkit [168]. The JUNO geometry is simplified to a sphere of 17.2 m radius, containing the liquid scintillator and surrounded by a shell of water buffer of 2 m thickness. The LPMTs are settled on a support sphere of 19.3 m radius.

The MC code is independent of the JUNO official MC, however, the optical properties of the detector materials and the photocathode shape are set to be the same as in the official MC. The assumed OLC reflectivity is 90% based on the previous experience in [161], where the dielectric-coated aluminium surface can reach a reflectivity of 93% at 500 nm. The external lateral surface of SPMTs is assumed to be totally absorbent.

The MC studies use electrons of 1 MeV simulated uniformly in the CD volume. In order to generalise the geometry for other clearances greater than 25 mm, and test the effect of different clearances, a simple approach that we have adopted is to enlarge the radius of the sphere supporting the LPMTs to a value that corresponds to the desired clearance. In this way, the code does not have to reduce the number of LPMTs and rearrange the PMT positioning. When the clearance is increased, the OLC height will also be raised to the maximum, such that the neighbour OLCs always touch each other.

3.4.1 OLCs with clearance between LPMTs

As previously mentioned in Section 3.1, a typical OLC can be optimised for a spherical LS-based detector by $\theta^* = \theta_{FV}$. However, according to the study in [167], it is not clear that, in a detector with high photocathode coverage, such as JUNO, the OLC designed with such an optimisation can always have better performance than the OLC designed with $\theta_{lim} = \theta_{FV}$. Due to the high coverage, the clearance usually allows only Cut OLCs to be installed. In this case, a Cut OLC optimised by $\theta_{lim} = \theta_{FV}$ will be taller than the one optimised by $\theta^* = \theta_{FV}$, therefore, more photons are collected by the former, but the latter has smaller dispersive effects on the light collection. To study the difference between two types of OLC designs, we have simulated both with 25 mm clearance.

The N_{pe} distribution of the LPMT system as a function of the event vertex radius, which is defined as the distance from the detector centre to the position of the energy deposit, is shown in Figure 3.12, for the 2 aforementioned OLC designs, and using different OLC design requirements, regarding which angle, θ^* or θ_{lim}, to be set to θ_{FV}. For reference, the N_{pe} for the detector without OLCs is also exhibited in the same figure.

Without OLC, the average N_{pe} observed in an event ($\langle N_{pe} \rangle$) is 1768 p.e.. The two Crown OLC options studied also have $\langle N_{pe} \rangle = 1768$ pe. The two Cut OLC options give again the same performance in terms of $\langle N_{pe} \rangle$, which is equal to 1770 p.e.. From the profiles, we have noticed that, although the OLCs do not help to increase $\langle N_{pe} \rangle$, they have positive effects on the detector uniformity. By increasing the light collection
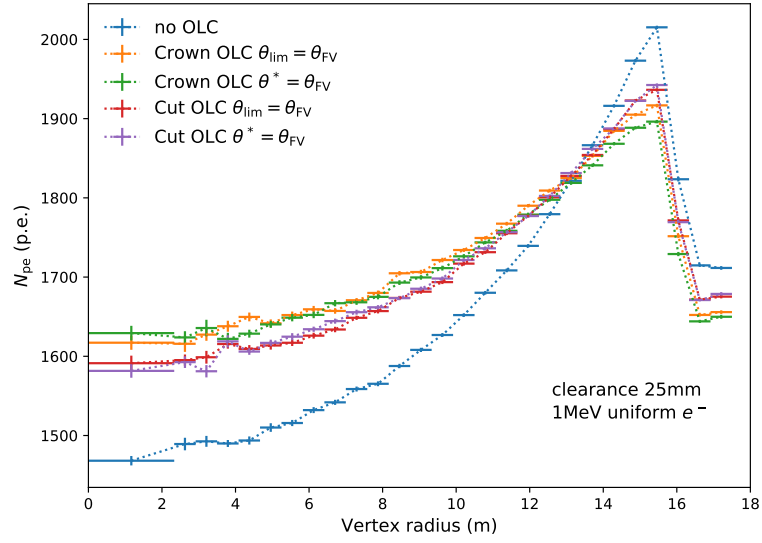
Figure 3.12 – N_{pe} distribution as a function of the vertex radius from the detector centre for different OLC configurations. The LPMT clearance is set to 25 mm.

close to the CD centre (< 13 m) and decreasing the light collection toward the Acrylic Sphere (> 13 m), OLCs make the N_{pe} distribution flatter than the raw LPMTs, which reduces dispersive effects on the light collection. This is particularly interesting if the energy resolution of the system is required to be very precise and thus all errors must be smallest possible.

Based on the simulation results, we have three conclusions for employing OLCs with a clearance as small as 25 mm: first, the OLC design requirement does not change the performance; second, the OLCs do not provide a higher $\langle N_{\text{pe}} \rangle$ than the raw LPMTs; and last, the effects on the detector uniformity are practically identical for both Crown OLC and Cut OLC.

3.4.2 OLCs with larger clearances between PMTs

So far, we have only studied the case where the clearance is 25 mm. By enlarging the radius of LPMT support sphere to 1967 cm and to 2059 cm, we obtain the clearances of 35 mm and 60 mm, respectively.

The N_{pe} distributions in Figure 3.13(a) are obtained with a clearance of 35 mm. $\langle N_{\text{pe}} \rangle$ of configurations with only raw LPMTs, Crown OLCs, and Cut OLCs are 1698 p.e., 1741 p.e., 1764 p.e., respectively. With 35 mm clearance, OLCs start to provide better light collection than raw LPMTs, though the improvement is not large, 3% for Crown OLCs and 4% for Cut OLCs compared to the raw LPMTs. The profile with Crown OLCs shows the best detector uniformity among three.

The N_{pe} distributions in Figure 3.13(b), are obtained with a clearance of 60 mm. $\langle N_{\text{pe}} \rangle$ of configurations with only raw LPMTs, Crown OLCs, and Cut OLCs are 1532 p.e., 1737 p.e., 1706 p.e., respectively. Here, we have found that the OLCs improve significantly the light collection. Compared to the raw LPMTs, we have 13% and 11% more detected photons. Similar to results of smaller clearances, Crown OLC is always helpful for a better detector uniformity, moreover, with this clearance, it exceeds finally Cut OLC in $\langle N_{\text{pe}} \rangle$.

For a larger clearance, it is clearer that Crown OLC improves the uniformity in the
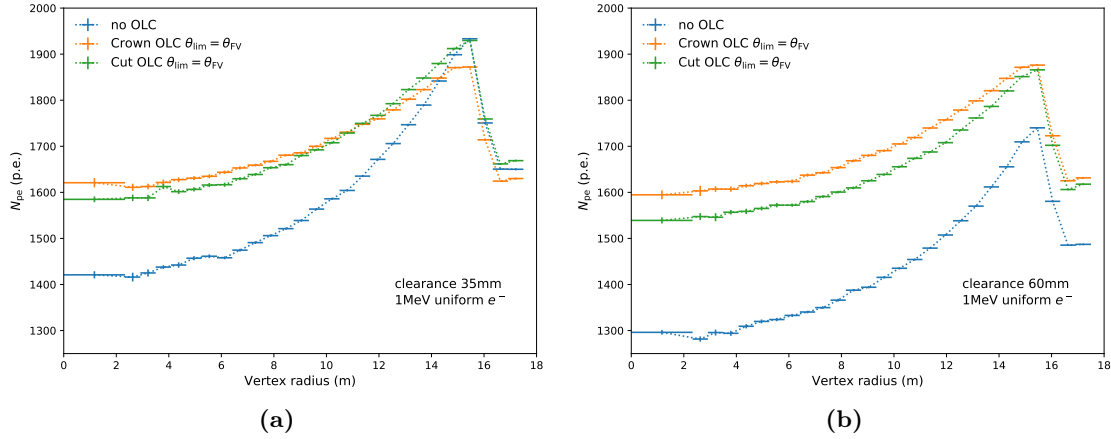
65

(a)

(b)

Figure 3.13 − N_{pe} distribution as a function of the vertex radius from the detector centre for different OLC configurations. The LPMT clearance in (a) is set to 35 mm, and in (b) is 60 mm.

(a)

(b)
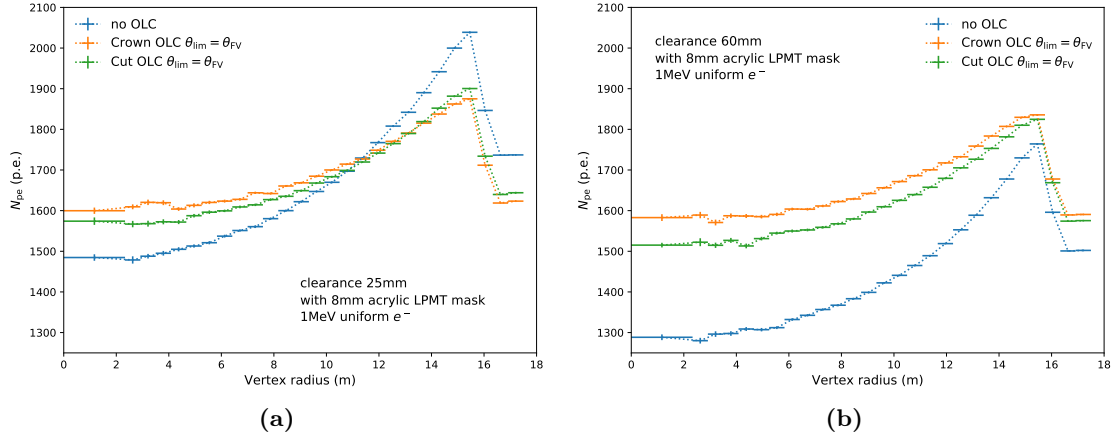
Figure 3.14 − N_{pe} distribution as a function of the vertex radius from the detector centre for the different OLC configurations with acrylic masks. The LPMT clearance in (a) is set to 25 mm, and in (b) is 60 mm.

light collection better than Cut OLC, and the advantage of employing Crown OLC for a larger N_{pe} is more evident. When the clearance is small, since the photons escaping from a Cut OLC are mostly collected by its neighbour LPMTs, the light gain of Crown OLC is not so evident with respect to Cut OLC.

3.4.3 Combine OLCs and PMT protection masks

In fact, as described in Section 2.2.2, LPMTs are protected by acrylic masks from possible shockwave after a PMT implosion. Even though efforts have been made to reduce the reflection and to increase the transmission, the acrylic masks nevertheless modify the optics, and may reduce the effects of OLC. To study the impact of these masks, we have altered the simulation by adding acrylic masks of 8 mm thickness on top of LPMTs, with a 2 mm gap between the masks and the LPMT photocathodes. The N_{pe} distributions are shown in Figures 3.14(a) and 3.14(b) for 25 mm and 60 mm clearances, respectively.

In the case of 25 mm clearance, the curves in Figure 3.14(a) have similar relations

as those in Figure 3.12, namely the OLCs improve the detector uniformity. However, the OLCs reduce the average N_{pe} that the system can collect. Compared to without OLCs, the average N_{pe} is decreased by 3% with either Crown OLC or Cut OLC.

Besides the effects on detector uniformity, the OLCs applied on the LPMTs having masks and with a clearance of 60 mm, do not have the same performance when compared with the configuration where no mask exists. For the simulations shown in Figure 3.14(b), the configuration LPMT+mask collects 1545 p.e. per event in average, whereas the configuration with Crown OLC collects 1700 p.e. per event, corresponding to an increase of 10%, and the configuration with Cut OLC collects 1670 p.e. per event, corresponding to an increase of 8%. In Section 3.4.2, we have studied the performances without protection masks, and we have seen that Crown OLC increases by 13% and Cut OLC increases by 11% the light collection.

We consider that the OLC performance degradation is due to the fact that the mask and the gap take away 0.7 cm from the OLC original height, resulting in shorter OLCs.

Our conclusion is that the improvement of the light collection by employing OLCs is less significant when the masks are taken into account, which suggests to use OLCs in case of large clearance only.

3.5 Summary

In this chapter, we tried to understand whether there is a benefit for employing OLCs in JUNO. MC simulations have been done with both Cut OLC and Crown OLC, as well as for different clearances, such that we can draw conclusions beyond the JUNO geometry. In conclusion, we have found that, employing OLCs to push the coverage to be higher than 75% does not seem to have very significant effects on the amount of collected light, as the clearance in JUNO is small. But in a spherical detector that has a larger clearance, OLCs would still be interesting devices for achieving a higher coverage without increasing the number of PMTs, which makes the whole project more cost-effective. Regarding the Crown OLC, although it is always helpful for a better detector uniformity, its advantage in light collection over Cut OLC emerges only if the clearance is sufficiently large. Even in such a case, it must be noticed that, from the mechanical point of view, the construction and the installation of Crown OLCs are much more complex than Cut OLCs. Finally, if we take into account the necessary acrylic masks of LPMTs, the OLC must be shortened for the mask insertion, which weakens the OLC performance. From our simulation, employing the OLCs in JUNO is expected to decrease the average N_{pe}. As a consequence, to ensure the functionality of the OLC, the effects due to acrylic masks should be seriously considered.

Let us note that, due to this unclear advantage, and to construction timing constraints, the JUNO collaboration finally decided not to use any OLC in the baseline design of the experiment.

Chapter 4

Performance study on SPMT distribution and cabling scheme

In the Central Detector (CD), it exists $\sim$37 000 possible emplacements for SPMT installation. But the number of SPMTs had to be reduced to $\sim$25 000, due to the fact that there is not enough space for SPMT installation under the CD truss beams. This results in a SPMT distribution that is not uniform, as if the CD reticulate structure "shadows" some SPMTs. Therefore, there is a necessity to investigate the detection performance of this non-uniform SPMT distribution, which will be done in Section 4.1.

While the number and distribution of the SPMTs have been fixed in the JUNO design, the cabling scheme for connecting SPMTs to the corresponding Under Water Boxes (UWBs) is not yet decided. Intuitively, one can choose to connect each SPMT to its nearest UWB, and minimise the total cable length, to which the cost is proportional. This configuration might not be the optimal one if there is a failing UWB. In this case, since the failing UWB is connected to its nearest SPMTs, all dead SPMTs are clustered, forming a "blind spot" with sharp edges in the SPMT system. This blind spot introduces again unwanted non-uniformity to the SPMT distribution. A possible optimisation for this problem is to interlace the "service zones" of the UWBs, such that, if any UWB fails, it will just reduce the local SPMT density in the corresponding service zone instead. Of course, this solution does not come for free, as we need to extend the cable lengths, which increases the cost of the system. In Section 4.2, we will study the detection performances of different schemes in case of a UWB failure.

The SPMT system is fully implemented in the JUNO official MC [169], which is developed based on GEANT4. Therefore, all simulations in this chapter are performed with the official MC.

4.1   Non-uniform SPMT distribution

In the JUNO installation, both LPMTs and SPMTs will be firstly mounted on a panel, with SPMTs inserted between LPMTs as shown in Figure 2.13. Then, PMT panels will be inserted into the CD truss, with no space available under the beams for installing more SPMTs. After installation, the SPMT positions will correspond to the layout depicted in Figure 4.1.

In fact, the CD truss divides the sphere into 22 windows in longitudinal direction and 30 windows in latitudinal direction. Figure 4.2 shows a Mercator projection of the central positions of the SPMTs, which better visualises the structure. In this projection, the longitudinal and latitudinal "gaps" between windows due to the CD truss beams can

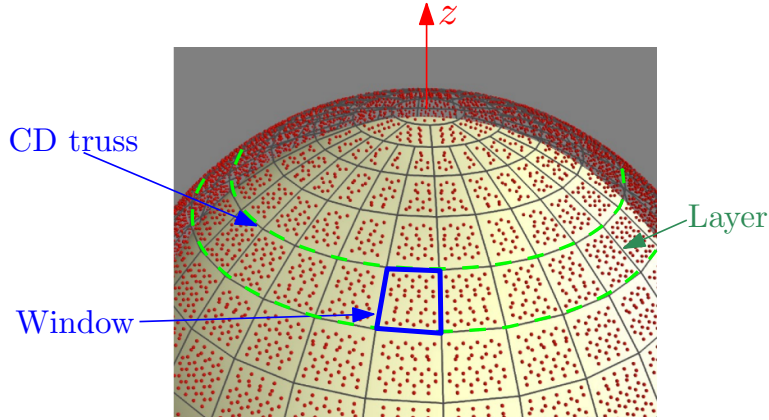**Figure 4.1** – Illustration of the SPMT distribution in JUNO. Red dots represent SPMTs, the grey net represents the CD truss beams (not to scale), and a zone framed by CD truss beams is a window (in blue). All windows at the same latitude are in the same layer.
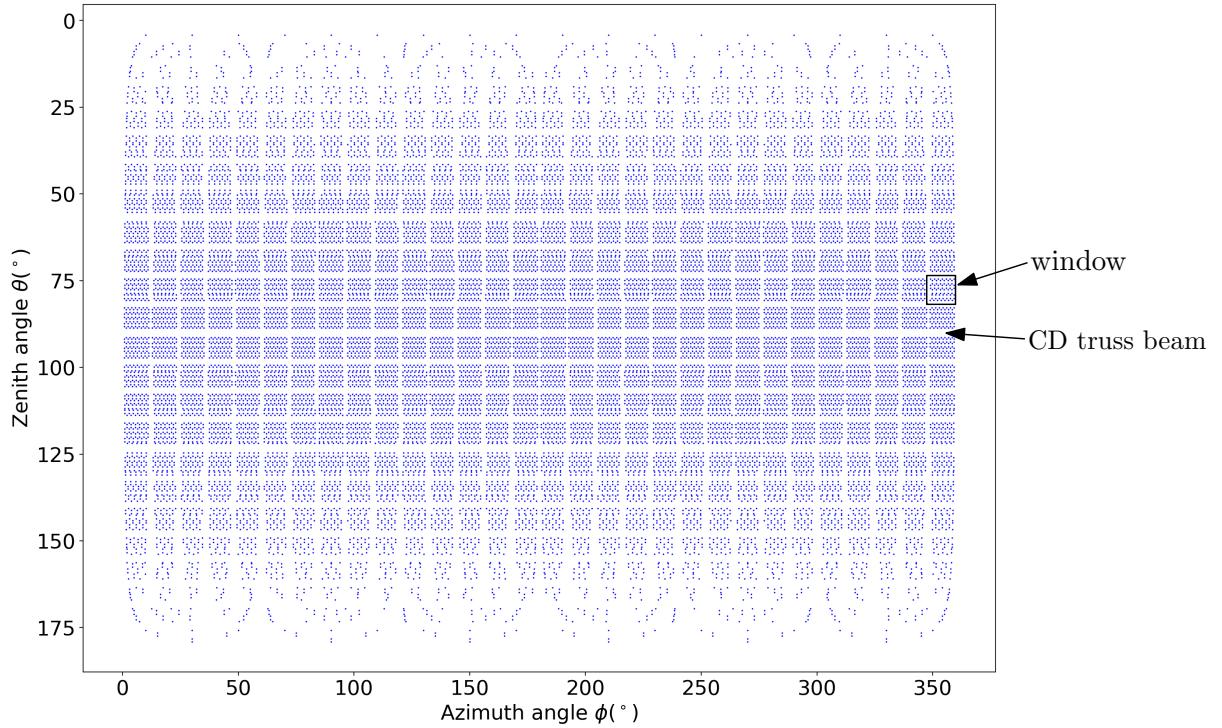

Figure 4.2 – The SPMT distribution of ∼25 000 SPMTs, each dot represents the central position of one SPMT. When $\theta = 0°$, the position is at north pole of the CD.

be identified. It is worth pointing out that, at the north and south poles, the density of SPMTs seems reduced whereas this is just due to the projection.

Such a design leaves two problems for light detection: first, it reduces the SPMT number from $\sim$37 000 to $\sim$25 000, and the second, it makes the SPMT distribution non-uniform. The first problem will lead to an unavoidable degradation of both light collection and energy resolution, but the effect of the second is less clear, and it will be studied in this section

4.1.1 Evaluation by removing different numbers of SPMTs

We firstly simulate different configurations, where the SPMTs under the truss are only partially removed. Five configurations are considered, including the real distribution:

- full SPMT installation, 36572 SPMTs are all enabled ($\sim$37k);

- removal of 25% SPMTs under the beams, the total number of enabled SPMTs is 33688 ($\sim$34k);

- removal of 33% SPMTs under the beams, the total number of enabled SPMTs is 32684 ($\sim$33k);

- removal of 50% SPMTs under the beams, the total number of enabled SPMTs is 30736 ($\sim$31k);

- real installation, the total number of enabled SPMTs is 24952 ($\sim$25k).

A ^{60}Co calibration source placed along the z-axis from 0 m to 17 m at every meter is used to generate the MC sample. At each point, $9 \cdot 10^5$ ^{60}Co decays have been simulated, with each decay giving two γ with energies of 1.1732 MeV and 1.3325 MeV. For each configuration and each source position, the distribution of N_{pe} is fitted with a Gaussian distribution, whereby the mean light collection ($\langle N_{\mathrm{pe}} \rangle$) and the Gaussian standard deviation σ are extracted. We show the distributions and the fits of 37k-SPMT and 25k-SPMT configurations at 0 and 17 m in Figure 4.3. In Figure 4.4(a), we show $\langle N_{\mathrm{pe}} \rangle$ of all configurations at each source position on the z-axis. The first conclusion that can be reached from the plot is that, for any given source position, $\langle N_{\mathrm{pe}} \rangle$ is clearly reduced for the current design with respect to the configurations where more SPMTs are enabled. Let $\langle N_{\mathrm{pe}} \rangle_\forall$ denote the average N_{pe} generated by all events. The results in Table 4.1 reveal that $\langle N_{\mathrm{pe}} \rangle_\forall$ is roughly proportional to the number of enabled SPMTs in the configuration used.

Table 4.1 $-$ $\langle N_{\mathrm{pe}} \rangle_\forall$ of all ^{60}Co events for different configurations, and the ratios of $\langle N_{\mathrm{pe}} \rangle_\forall$ with respect to the value of the 37k-SPMT configuration. The fraction of enabled SPMTs compared to the 37k-SPMT configuration is also shown for reference.

Configurations	SPMT percentage	$\langle N_{\mathrm{pe}} \rangle_\forall$ (p.e.)	$\langle N_{\mathrm{pe}} \rangle_\forall$ ratio
37k	100%	108.8	100%
34k	92.1%	98.8	90.8%
33k	89.4%	96.1	88.4%
31k	84.0%	88.9	81.7%
25k	68.2%	71.3	65.6%

(a) 25k-SPMT configuration at 0 m

(b) 25k-SPMT configuration at 17 m

(c) 37k-SPMT configuration at 0 m
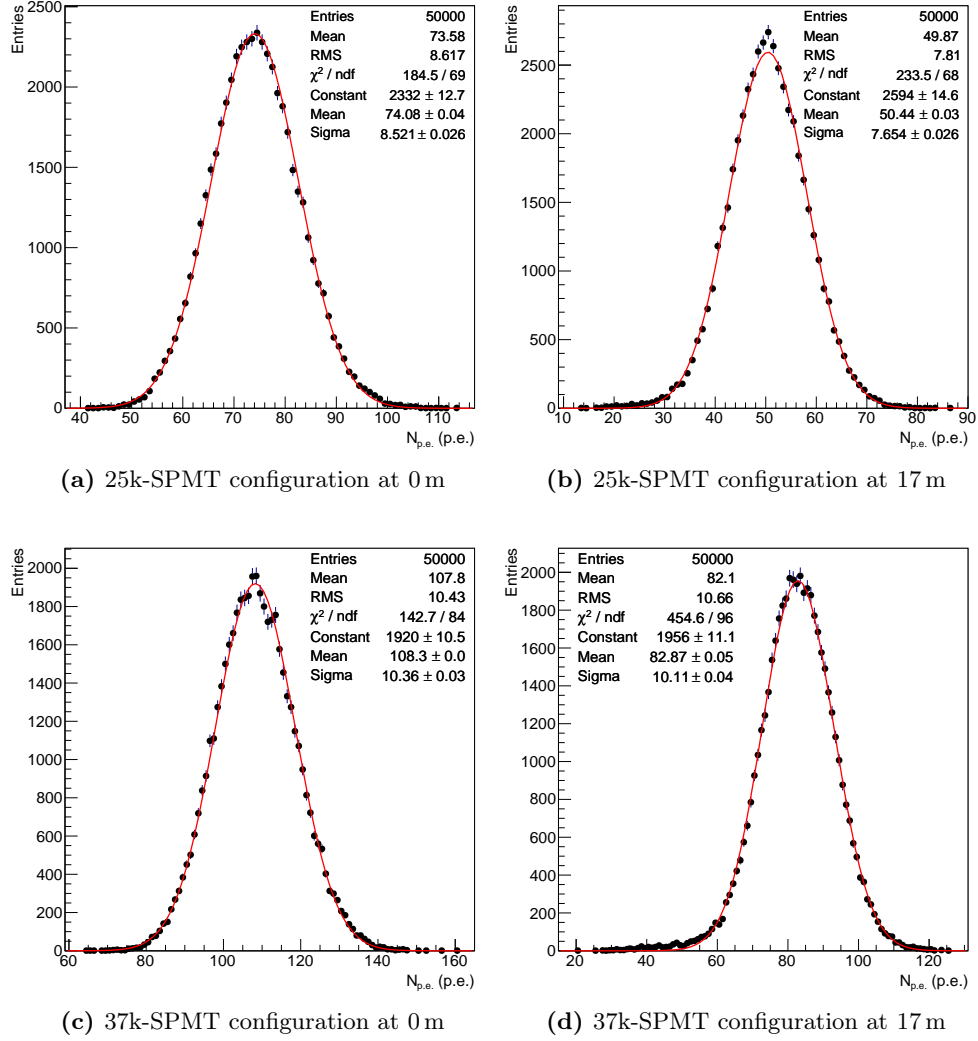

(d) 37k-SPMT configuration at 17 m

Figure 4.3 – Distributions and Gaussian fits of 25k configuration at (a) 0 m and (b) 17 m, and of 37k configuration at (c) 0 m and (d) 17 m.
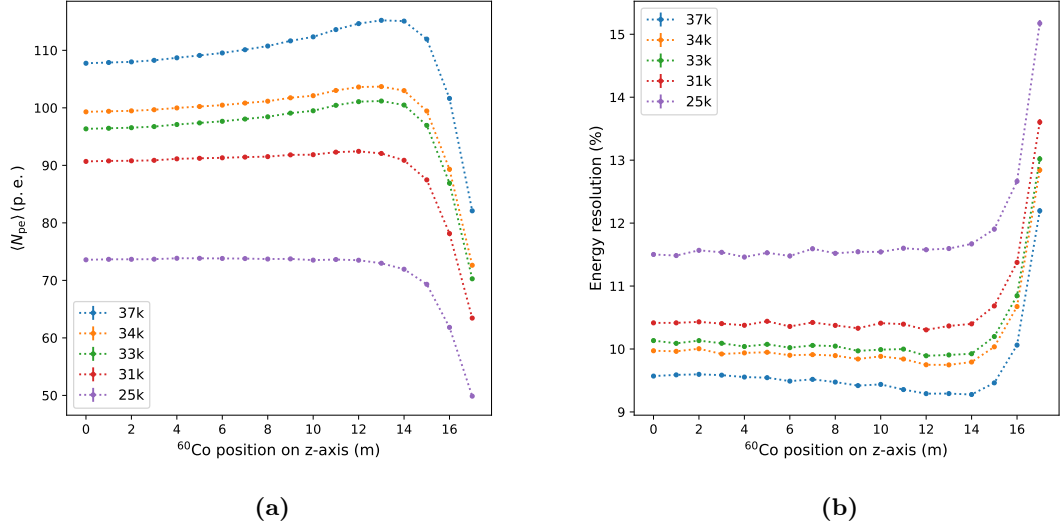
Figure 4.4 – (a) $\langle N_{pe} \rangle$ of 5 configurations as a function of the positions of the ^{60}Co source. (b) The corresponding energy resolutions as a function of the source position. The error bars in (b) are obtained from Gaussian fits.

At the same time, we can notice that the reduction of $\langle N_{pe} \rangle$ is dependent on the source position. Usually, due to the light absorption and scattering in the LS, $\langle N_{pe} \rangle$ is slightly enhanced for events at larger radii up to about 14 m. This is considered as a non-uniformity of the detector response to the energy deposits, and it is most visibly demonstrated by the curve of 37k-SPMT configuration. However, the non-uniform distribution alters the detector non-uniformity by reducing more $\langle N_{pe} \rangle$ at the edge. For example, by comparing the curves of 37k-SPMT and 25k-SPMT, we observe that the difference is increasing from small radii to large radii of the CD, so the curve of 25k-PMT is almost flat from the CD centre to 14 m.

For each point in Figure 4.4(a), we calculate the energy resolution, which is defined as $\sigma/\langle N_{pe} \rangle$. Figure 4.4(b) shows the corresponding energy resolutions of all configurations. The plot suggests that the energy resolution of the SPMT system in this simulation is driven by the photon statistics of each configuration. The 25k-SPMT configuration has therefore the worst energy resolution at any distance.

Actually, what we have simulated so far is equivalent to a source calibration along the CD central axis, and the curves shown are what we expect to be measured by the calibration. However, it is also important to estimate the global effects of the non-uniform SPMT distribution on the light detection for all axes and radii within the CD.

In the next step, we will study the impact of non-uniform distribution with 1 MeV electrons uniformly distributed in the CD, such that the evaluation of the SPMT distribution is not limited to the z-axis. Figure 4.5 shows $\langle N_{pe} \rangle$ along the CD ball radius for different configurations. The curves are obtained with the same method as those in Figure 4.4(a). $\langle N_{pe} \rangle$ of different configurations obtained by using the uniform electron sample have the same shape, therefore the detector non-uniformity is not changed by the configuration this time. Consequently, we observe that $\langle N_{pe} \rangle_\forall$ is strictly proportional to the number of enabled SPMTs in the configuration used, as shown in Table 4.2.
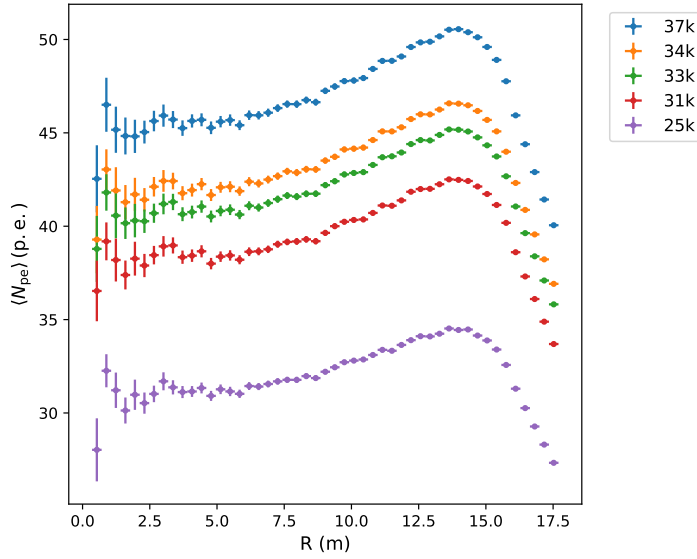
Figure 4.5 – $\langle N_{pe} \rangle$ along the CD ball radius for different configurations, obtained from a uniform electron sample of $1\,\mathrm{MeV}$.

Table 4.2 – $\langle N_{pe} \rangle_\forall$ of all electron events for different configurations, and the ratios of $\langle N_{pe} \rangle_\forall$ with respect to the value of the 37k-SPMT configuration. The fraction of enabled SPMTs compared to the 37k-SPMT configuration is also shown for reference.

Configurations	SPMT percentage	$\langle N_{pe} \rangle_\forall$ (p.e.)	$\langle N_{pe} \rangle_\forall$ ratio
37k	100%	47.1	100%
34k	92.1%	43.4	92.2%
33k	89.4%	42.1	89.4%
31k	84.0%	39.6	84.2%
25k	68.2%	32.2	68.3%

The simulation results suggest that, the main effect of removing the SPMTs under the CD truss beams is merely a reduction of N_{pe} proportional to the number of removed SPMTs. For the z-axis, the detector non-uniformity seems to be different for different configurations. This may be attributed to the fact that we remove relatively more SPMTs near the pole than near the equator, but further investigation would be needed to confirm this hypothesis.

4.1.2 Comparison between real distribution and uniform distribution

In this study, we will take a different approach to understand the effect of non-uniform SPMT distribution. Here we will compare directly the performance of light detection obtained with the real distribution and with a uniform distribution. The uniform distribution is obtained by randomly removing the same amount of SPMTs as in the real distribution, in this case, the "gaps" in Figure 4.2 caused by the CD truss beams can still have enabled SPMTs, and the SPMT "density" is homogeneous all over the SPMT system.

In the real distribution, if the event vertex[1] is near a truss beam, we can expect that

---
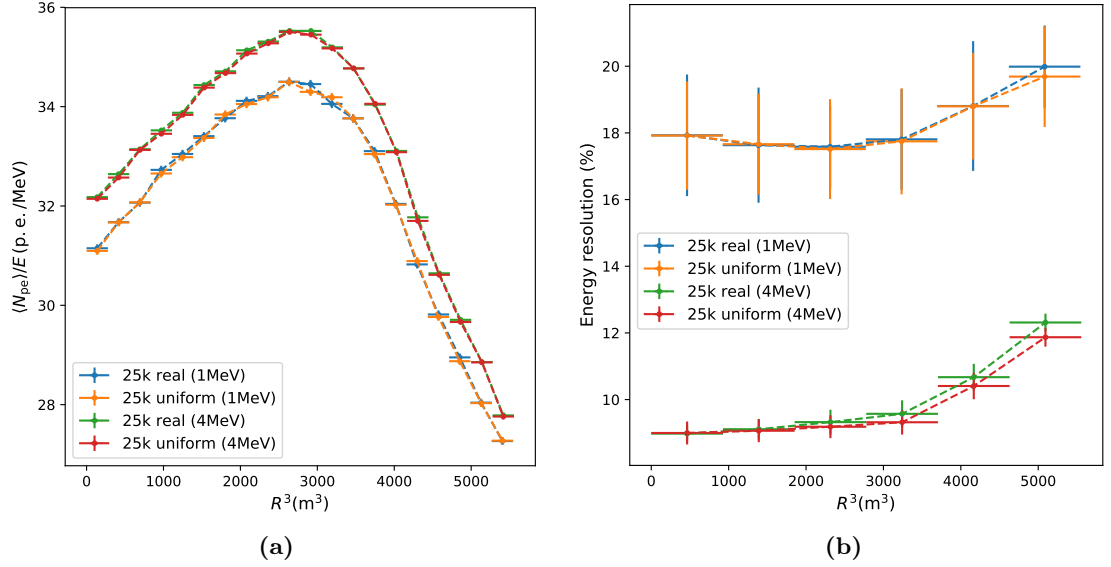
[1]position where the event happens

Figure 4.6 – (a) $\langle N_{pe} \rangle / E$ along the CD ball radius for the real and the uniform SPMT distributions, obtained with electrons at $1\,\mathrm{MeV}$ and $4\,\mathrm{MeV}$. (b) The corresponding energy resolutions for the real and the uniform SPMT distributions.

the SPMT system has a bad light collection for this event; on the contrary, if the vertex is near the centre, the light collection is similar as if the SPMT distribution is uniform. Besides the dependence on the radius, the performance of the real distribution can be different depending on the deposited energy. Therefore, we will use two energy samples of uniform electrons, one of $1\,\mathrm{MeV}$, and the other of $4\,\mathrm{MeV}$.

Figure 4.6(a) shows the $\langle N_{pe} \rangle / E$ as a function of cubic radius for both real and uniform distributions. E denotes the event energy, depending on which sample is used, E can be either $1\,\mathrm{MeV}$ or $4\,\mathrm{MeV}$ in this study. The abscissa in cubic radius makes the volume of each bin be similar for the uniformly distributed electron events. Due to the detector non-linearity, the curve of $4\,\mathrm{MeV}$ electrons is not identical with the one of $1\,\mathrm{MeV}$ electrons, but the shapes of both are very similar. The curves corresponding to different SPMT distributions for the same energy are actually identical, so no obvious dependency of $\langle N_{pe} \rangle$ on the SPMT distribution is observed.

We show also the corresponding resolutions in Figure 4.6(b). The different levels of energy resolution for $1\,\mathrm{MeV}$ and $4\,\mathrm{MeV}$ are explained by the simple fact that $4\,\mathrm{MeV}$ electrons produce 4 times more photons in the CD than $1\,\mathrm{MeV}$ electrons. We observe that, for both energies, the energy resolution has a slight improvement at large radii for the uniform distribution, however, given the size of error bars, the non-uniform distribution cannot be considered to have a significant impact on the energy resolution.

4.2 Cabling scheme and UWB failure

As we have seen in Chapter 2, the electronics of the SPMTs are stored in the Under Water Boxes (UWBs). Though these boxes are designed to be robust, the SPMT system still may experience UWB failures. The design requires that the failure rate should be smaller than 0.5% of UWBs per year, which corresponds to 1 UWB per year in average. The JUNO operating time is foreseen to be at least 20 years, then at most 10% of
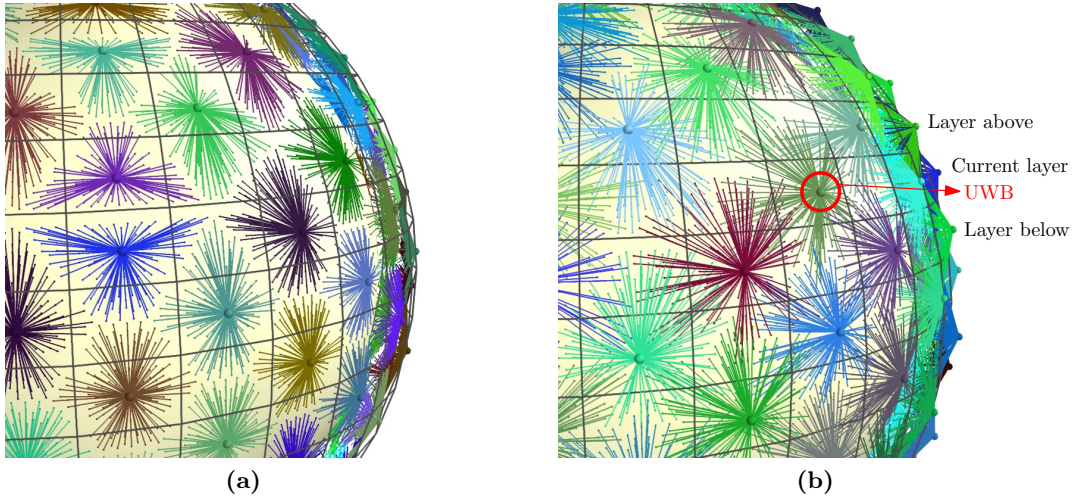
Figure 4.7 – Illustration of (a) the nearest and (b) the overlap cabling schemes.

UWBs are expected to be broken after that time period. In case one UWB is broken, all SPMTs connected to this UWB become inoperative, causing a reduction of light collection and thus a degradation of energy resolution. Furthermore, the blind spots created by the failure can make the SPMT distribution even more non-uniform, of which the effect needs to be studied. At the same time, we expect that, by optimising the cabling scheme of the SPMT system, we may have a lower performance degradation.

We considered for this study two possible cabling schemes, referred to as the "nearest" and the "overlap" schemes.

In Figure 4.7(a), an illustration of the nearest scheme is shown, where different colours represent different UWBs, and the lines are the cables between the UWBs and SPMTs. In such a scheme, one UWB serves the nearest SPMTs, and the total cable length is minimised. Considering that all cables go straight from UWBs to SPMTs, the total cable length of nearest scheme is equal to 52 km, or in average, 2 m for each SPMT link.

The overlap scheme allows a UWB to serve a wider area that is shared with its neighbour UWBs. As shown in Figure 4.7(b), the overlap scheme allows a UWB to pair SPMTs in the current layer, the layer above and the layer below. The overlap scheme increases the total cable length to 74 km, about 40% longer than the nearest scheme. In the overlap scheme, as depicted in Figure 4.8, the algorithm divides the vicinity of a UWB (UWB_1) into six parts and each part is shared with its neighbour UWB (UWB_2). 50% of SPMTs in this region is distributed to UWB_1, while the rest is linked to UWB_2. This assignment does not depend on the SPMT positions.

When one UWB fails, the nearest scheme naturally lets the inoperative SPMTs become a large blind spot with a sharp boundary. The blind spots can be easily noticed in Figure 4.9(a), which shows an example of 10 failing UWBs, with the blue points representing still operative SPMTs. Figure 4.9(b) shows the same UWB failure as in Figure 4.9(a), but with the overlap scheme. In contrast to the nearest scheme, the overlap scheme aids to "dissolve" the large blind spots, and lets the consequence be simply a reduction of SPMT density in the region of the failing UWB. We see that the failing UWB service zones that should have been completely blind are still more or less served by other neighbouring UWBs, although with reduced density.

From these examples, we may have an impression that UWB failure will make the
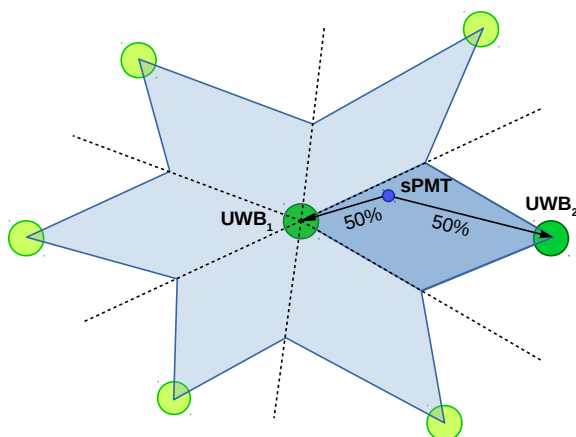
Figure 4.8 – Definition of the overlap scheme: 50% of SPMTs in a region shared by two UWBs (UWB$_1$ and UWB$_2$) will be connected to UWB$_1$, and the other 50% to UWB$_2$.
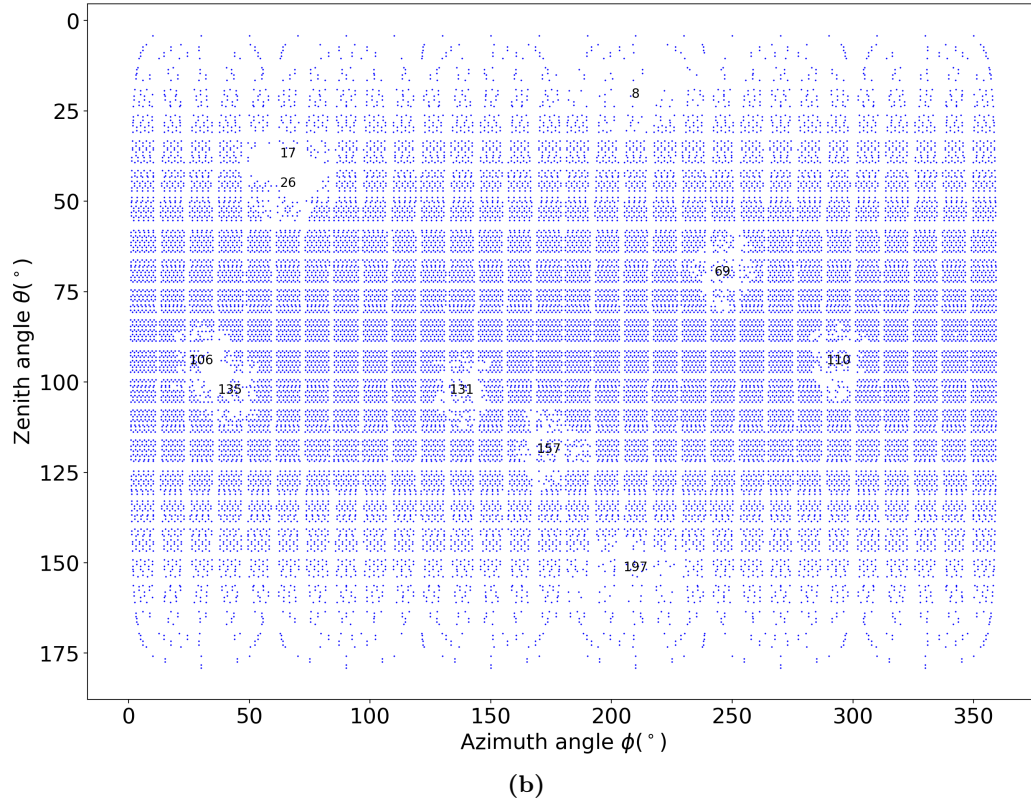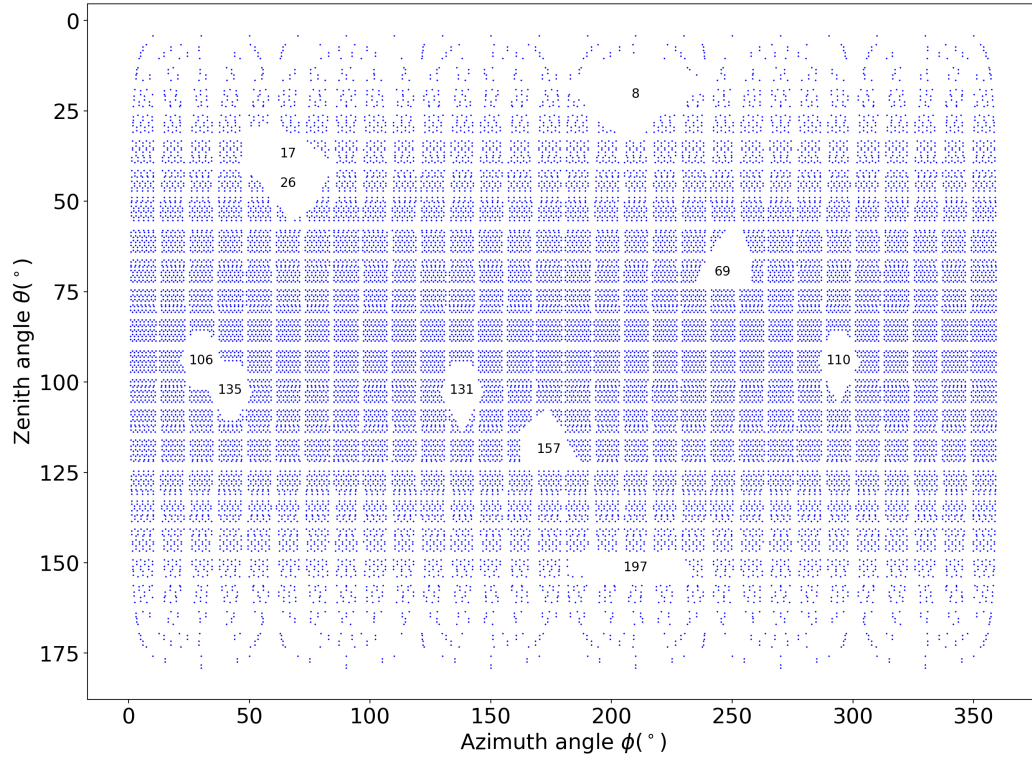
(a)

(b)

Figure 4.9 – 10 UWBs are randomly selected to fail (a) with the nearest scheme, and (b) with the overlap scheme. The UWB IDs of failing UWBs are labelled in the corresponding positions.

SPMT distribution more non-uniform by using the nearest scheme: for an event near the failing UWB, the light collection of this event should be worse as compared to the overlap scheme. However, for the event that is far away from the failing UWB, we should expect that the light collection is similar with both schemes.

To study the improvement that can be brought by the overlap scheme, we simulate UWB failures of 5% (10 failing UWBs) and of 10% (20 failing UWBs) by using a uniform e^- at $1\,\mathrm{MeV}$. For both numbers of UWB loss, 400 simulations have been performed with failing UWBs that are randomly selected. Since the electron sources are uniformly distributed in the CD, we divide the CD into six shells of equal volumes. The shells are $0\,\mathrm{m} < R < 9.7\,\mathrm{m}, 9.7\,\mathrm{m} < R < 12.3\,\mathrm{m}, 12.3\,\mathrm{m} < R < 14.0\,\mathrm{m}, 14.0\,\mathrm{m} < R < 15.5\,\mathrm{m}, 15.5\,\mathrm{m} < R < 16.7\,\mathrm{m}$, and $16.7\,\mathrm{m} < R < 17.7\,\mathrm{m}$.

In each UWB failure simulation, $\langle N_{\mathrm{pe}} \rangle$ of both schemes in all shells are calculated individually. Figure 4.10(a) shows $\langle N_{\mathrm{pe}} \rangle$ of an example failure (5% UWB loss) in each shells with both schemes. The corresponding energy resolutions are also exhibited in Figure 4.10(b).

For 5% UWB loss that is shown in Figure 4.10, no visible difference can be observed between the nearest and overlap schemes. However, by changing the set of failing UWBs, the resultant $\langle N_{\mathrm{pe}} \rangle$ and energy resolution will vary. For 400 different sets of 10 failing UWBs (5% UWB loss), we have obtained the $\langle N_{\mathrm{pe}} \rangle$ and energy resolutions in all shells with both schemes. Figure 4.11 shows the distributions of $\langle N_{\mathrm{pe}} \rangle$, and Figure 4.12 shows the distributions of energy resolution.

Based on these histograms, we draw a conclusion that, for 5% UWB loss and energy deposits of $1\,\mathrm{MeV}$, the two schemes do not have large differences in terms of $\langle N_{\mathrm{pe}} \rangle$, and there is a small improvement of the energy resolution by using the overlap scheme for events at large radii. With the same method, we have obtained the values for 10% UWB loss, and the results for both numbers of UWB loss are then summarised in
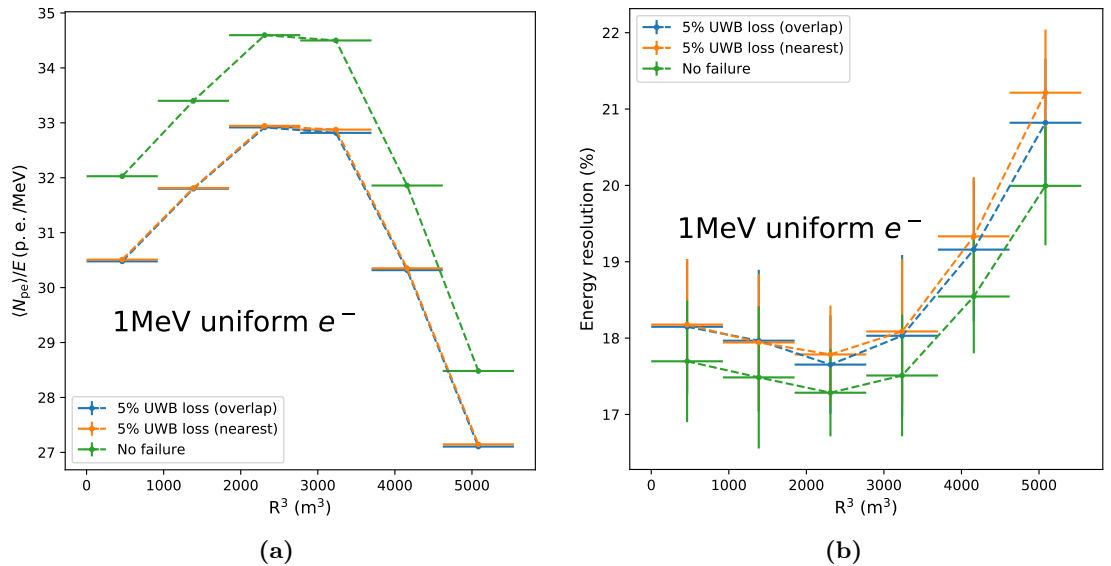
Figure 4.10 − (a) $\langle N_{\mathrm{pe}} \rangle$ in an example that 5% UWB are lost, with both the nearest and the overlap schemes, values are calculated individually in each equal-volume shells. (b) The corresponding energy resolutions of each point in (a). The events are generated with uniform electrons in the CD at a kinetic energy of $1\,\mathrm{MeV}$. The error bars in (a) and (b) are obtained from Gaussian fits.
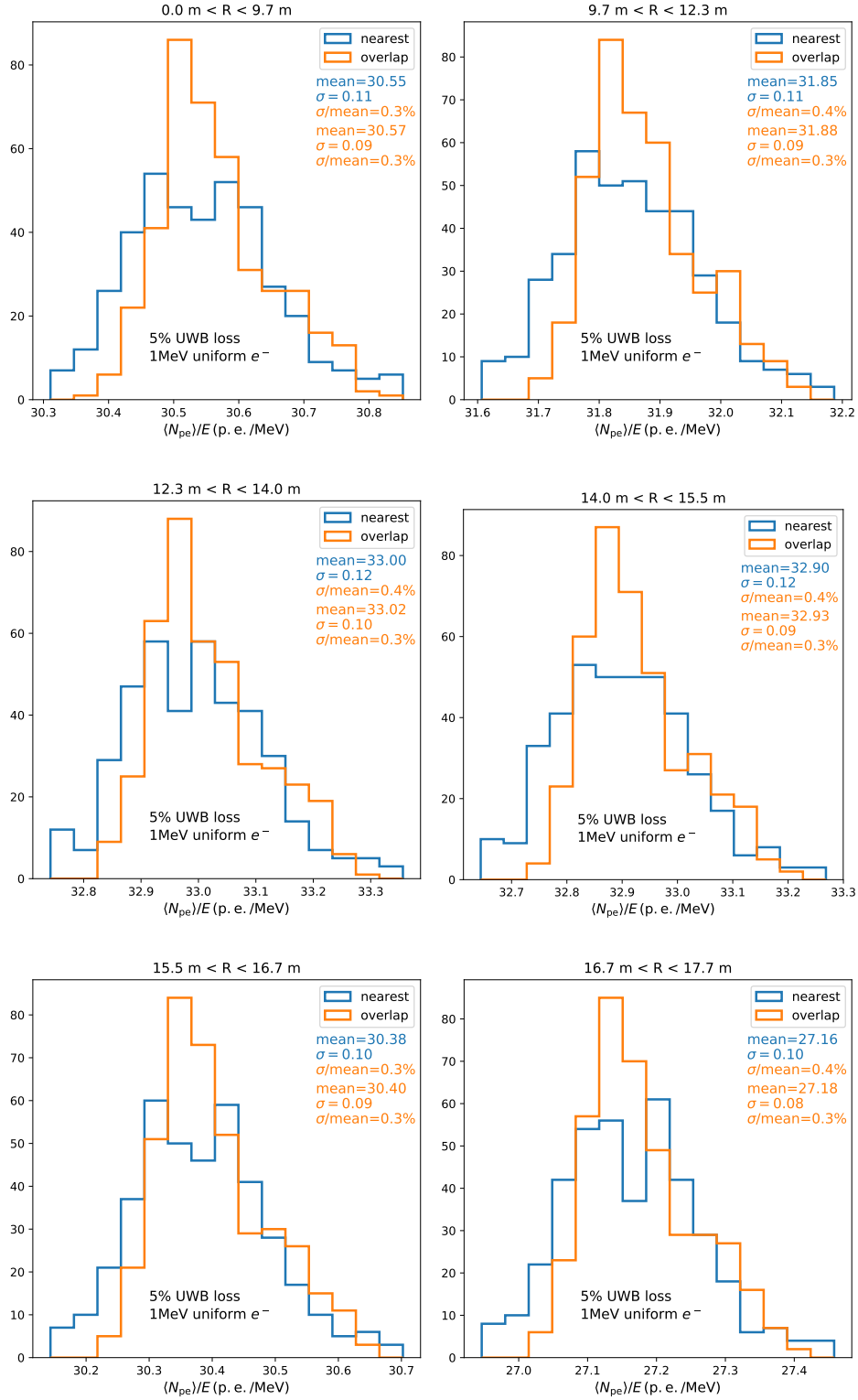
Figure 4.11 − Histograms of $\langle N_{\mathrm{pe}} \rangle$ in all shells with different schemes that are obtained from 400 UWB failure simulations (5% UWB loss).
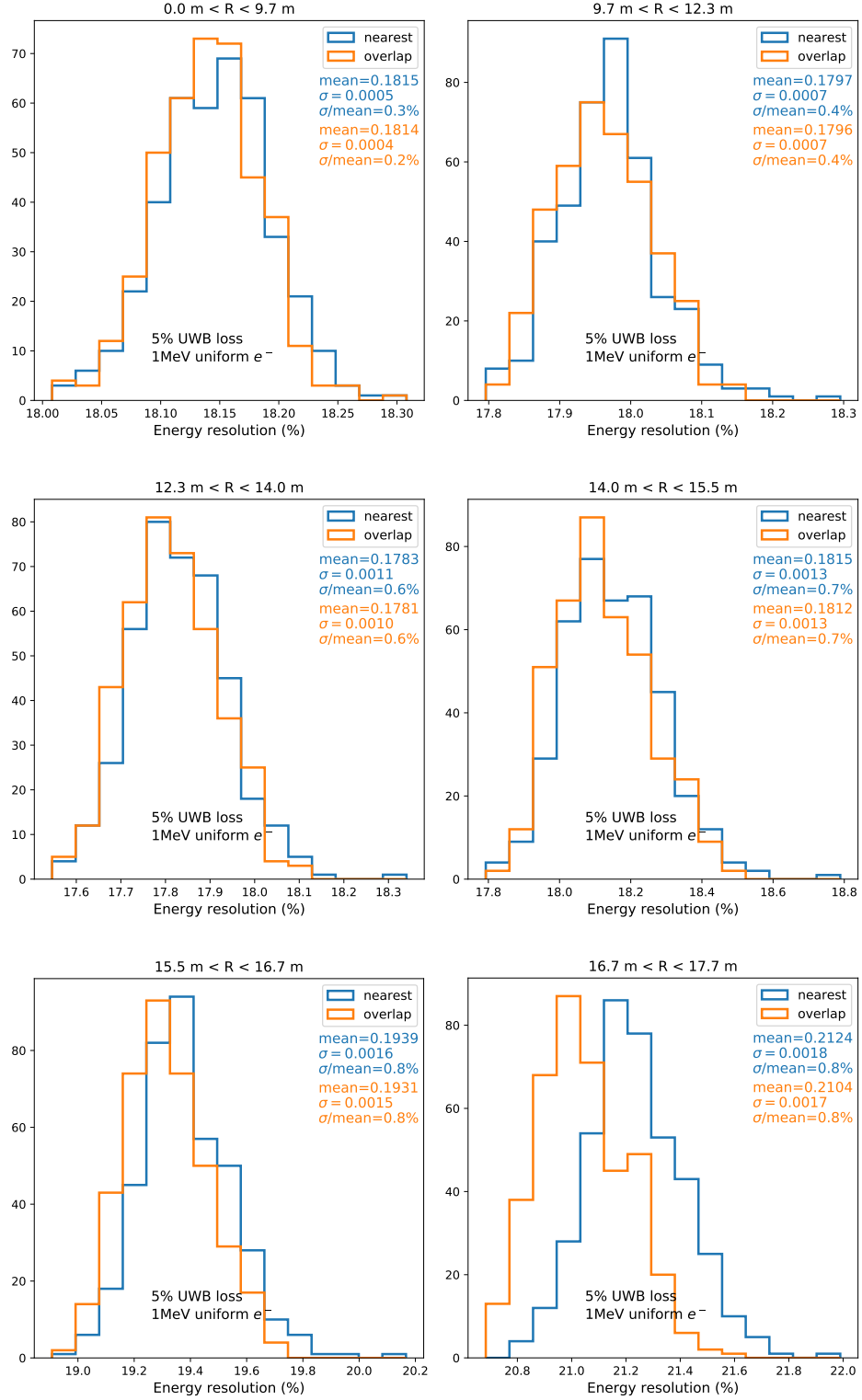
Figure 4.12 − Histograms of energy resolutions in all shells with different schemes that are obtained from 400 UWB failure simulations (5% UWB loss).
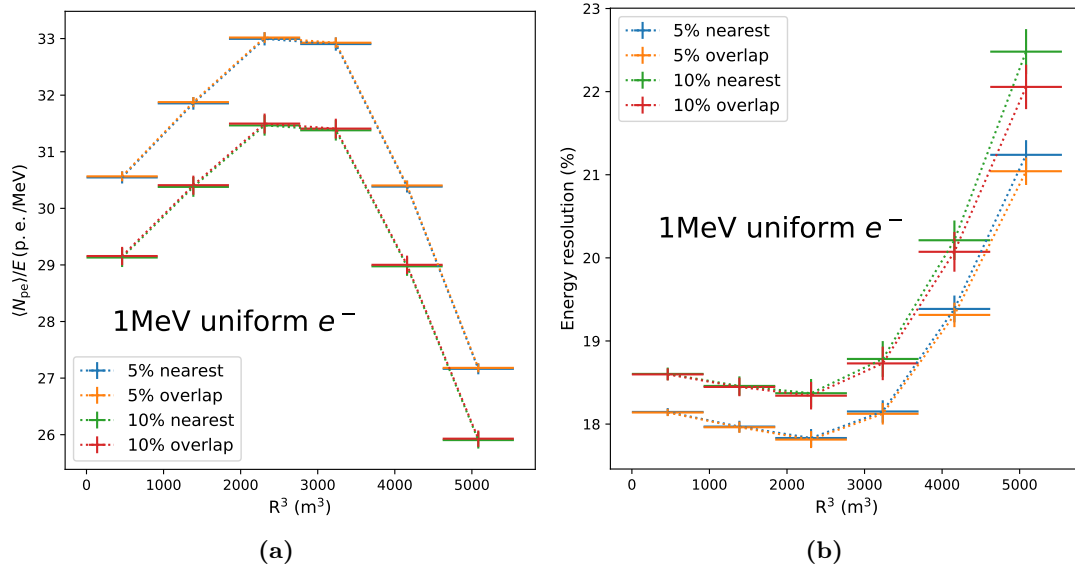
Figure 4.13 − (a) The mean $\langle N_{\mathrm{pe}} \rangle$ and (b) the mean energy resolutions for different radii in the failure simulations, where $1\,\mathrm{MeV}$ uniform electrons are used for both schemes with different UWB loss (5% and 10%).
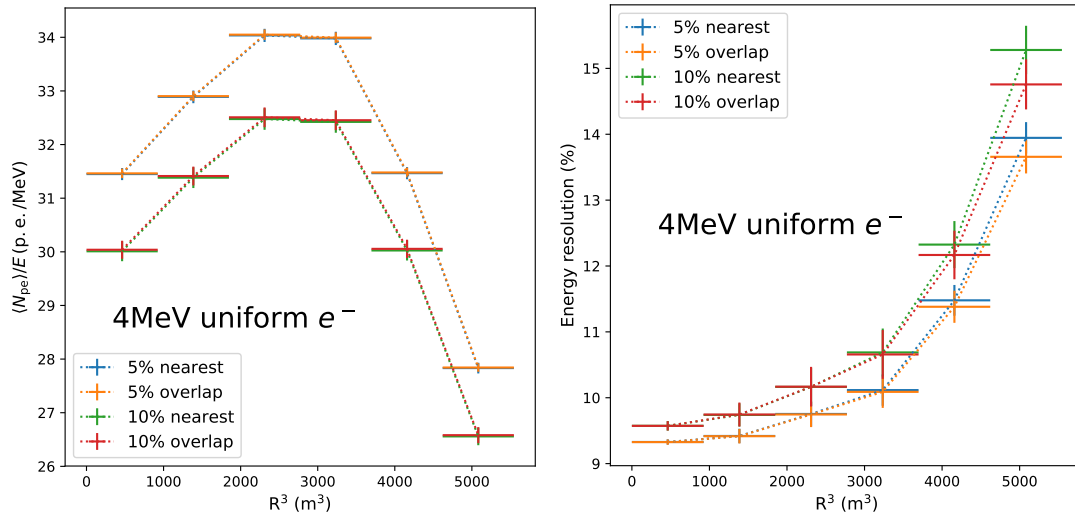
Figure 4.14 − (a) The mean $\langle N_{\mathrm{pe}} \rangle$ and (b) the mean energy resolutions for different radii in the failure simulations, where $4\,\mathrm{MeV}$ uniform electrons are used for both schemes with different UWB loss (5% and 10%).

Figure 4.13. The uncertainties of the 5% UWB loss curves on the plot come from σ of the distributions shown in Figures 4.11 and 4.12, and by using the same method, the uncertainties of 10% curves are also obtained and shown on the plot.

The plots suggest that, for events at 1 MeV, the overlap scheme will not be helpful in recovering the light collection, but it slightly improves the energy resolution by reducing the dispersive effects of the light collection. Besides, the relative improvement on the energy resolution is greater for 10% UWB loss than for 5% UWB loss. On one hand, a better performance of the overlap scheme on energy resolution is confirmed; on the other hand, the improvement is quite limited with respect to the level of the SPMT system energy resolution: the SPMT system resolution is >18% at 1 MeV, while the relative improvement is less than 2%, which is a negligible difference.

The same study has also been carried out by using the events generated from uniform electrons at 4 MeV, and the resultant mean $\langle N_{pe} \rangle$ and mean energy resolution of all 400 UWB failure simulations are shown in Figure 4.14. The same conclusion can be reached from Figure 4.14 as the one from Figure 4.13: the performances of both schemes in the UWB failure are practically the same.

Based on these MC simulation results, we have found that, compared with the nearest scheme, the overlap scheme does not improve the light collection, but in most cases of UWB failure, it can provide a better energy resolution for events at large radii thanks to less significant dispersive effects. In addition, the relative improvement on the energy resolution for events at large radii is greater if more UWBs fail. However, such an improvement is not sufficiently significant to make a clear difference between the two schemes, and the general performances of both are almost identical for an UWB loss of up to 10%. As a consequence, we can conclude that it is not particularly interesting to adopt the overlap scheme.

4.3 Summary

In the chapter, we firstly focus on the performance study of the SPMT distribution, where we have proven that the consequence of removing the SPMTs under the CD truss beams is only a decrease of the light collection proportional to the number of removed SPMTs. A degradation of the energy resolution due to the non-uniform SPMT distribution is not observed.

A MC study is also carried out, aiming at comparing the light detection performances with the nearest and the overlap cabling schemes in case of an UWB loss of up to 10%. Based on the simulation results from random UWB failures, we have pointed out that, both schemes have very similar performances in terms of the light collection and the energy resolution. In other words, the overlap scheme will not be helpful in reducing the damage to the light detection performance of the SPMT system for such cases.

Although we had estimated that the dispersive effects should be observed, the simulation reveals that the non-uniformity in the SPMT distribution has actually no impact on the light detection performance. From our understanding, this can be explained by the water buffer of 2 m thickness around the CD, which ensures that the distances between event vertices and the SPMTs are always sufficiently large. Consequently, light will be collected by SPMTs in a relatively larger region than the one where no SPMT is available, making the dispersive effects negligible.

Chapter 5

Optimisation of the Top Tracker trigger algorithm

In Section 2.3.1, we have explained that the key of the cosmogenic isotope background suppression is to reconstruct muon tracks with sufficient precision. The main task of the Top Tracker (TT) is to provide JUNO with high precision muon tracking information. However, the radioactivity level in the JUNO cavern is high, and the radioactive background events in the TT cause an overload of its readout electronics, if the readout trigger threshold is set to its minimal value of $1/3$ p.e.. To suppress the background, the readout will be triggered only if signals are validated by a 2-level trigger. This chapter will focus on the optimisation of the trigger algorithms for both levels.

The implementation of the algorithms is constrained by the hardware, so we will first introduce the readout electronics in Section 5.1. Then, in Section 5.2, we will detail the TT simulation. The Level1 and Level2 trigger algorithms under test are explained thoroughly in Section 5.3 and Section 5.5, respectively. In between, we show in Section 5.4 the feasibility of the FPGA realisation for the L1 trigger algorithms. Section 5.6 and Section 5.7 explain the muon reconstruction method and how we simulate the muon reconstruction with triggers. Finally in Section 5.8, performances of different trigger configurations will be compared and studied.

For simplicity, in the following, we will refer to the Top Tracker multi-anode PMT as "PMT".

5.1   Readout electronics

When a muons crosses a TT strip and deposits energy, scintillation photons are generated. The light subsequently propagate in the WLS fibres towards both ends, where two PMTs are responsible to collect the photons, and convert them into a pulse of which electric charge is number of photoelectrons (N_{pe}). The charges then need to be digitalised by an Analog-to-Digital Converter (ADC). To suppress the radioactive background, these signals will be validated by Level1 (L1) and Level2 (L2) triggers. Only validated signals will be accepted by the data acquisition system (DAQ).

The schematic design of the TT readout electronics is illustrated by Figure 5.1. It consists of 64 individual channels per PMT (64512 channels in total), 16 Front-End Boards (FEBs) per wall (1008 FEBs in total), 16 Readout Boards (ROBs) per wall (1008 ROBs in total), one Concentrator Board (CB) per wall (63 CBs in total), one L2 trigger. We will describe the main function of each component in the next part.
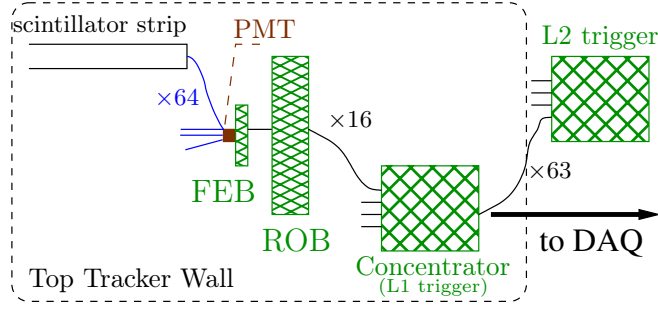
Figure 5.1 – Schematic design of the TT readout electronics.

5.1.1 MAROC3, Front-End Board, and Readout Board

The MAROC3 is an application-specific integrated circuit (ASIC) from the MAROC ASICs family, developed by OMEGA. The MAROC ASICs family is dedicated to the readout of 64-channel PMTs. Its main roles are to correct the gain spread of PMT channels thanks to an individual variable gain preamplifier and to discriminate the input signals in order to produce 64 trigger outputs [170]. In the TT readout system, the MAROC3 is carried by the FEB, and the digitalised MAROC3 signals are sent to the CB via a ROB. Figure 5.2 is a picture showing a ROB connected to the FEB, which carries a MAROC3.
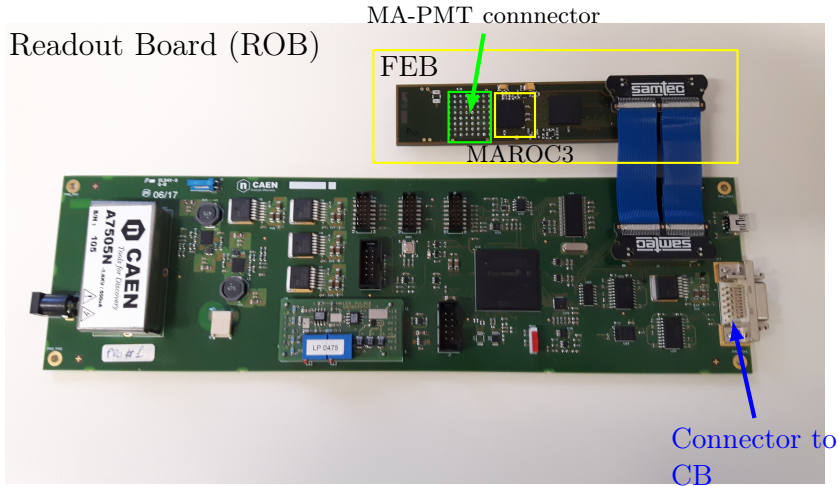
Figure 5.2 – Photo of a ROB connected to a FEB. From the shown version of the ROB, the connector to the CB will be changed by 2 RJ-45 connectors.

As the first processing device of PMT pulses, the MAROC3 delivers multiplexed analog charge output, whose amplitudes are proportional to the input pulse charges. At the same time, the MAROC3 can generate individual trigger outputs for all channels based on a configurable threshold. The individual trigger outputs are subsequently serialised by the FEB FPGA and sent to the ROB. In addition to that, it exists a FAST-OR output, which is a global OR of the trigger outputs for all 64 channels.

The MAROC3 starts the readout for all 64 channels when a signal is over-threshold. During the processing, no new charge readout is possible, so the processing time can be considered as the dead time of one MAROC3. To interrupt the processing of one MAROC3, one must send a reset signal (RESET), by this means, it ceases the current charge readout and resets the state to be ready for new signals in about 10 ns.

Figure 5.3 − Illustration of a CB connected to 16 FEB+ROB.

In the system, there are 2 ADCs available for the PMT charge readout: the MAROC3 built-in Wilkinson ADC [171] and an external Flash ADC (FADC) on the ROB. Due to the different technologies, the charge readout times are different: the 8-bit Wilkinson ADC takes at maximum 14 μs, while the 12-bit FADC on the ROB takes at maximum 7 μs. The collaboration has not yet decided which ADC should be used, 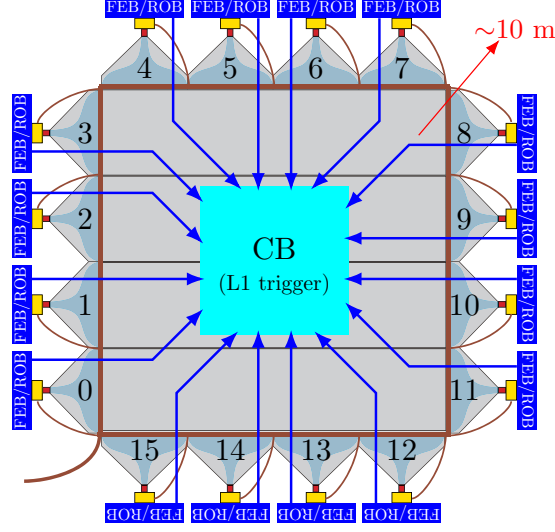and so far, the design keeps the compatibility with both. In this thesis, we consider the conservative 14 μs from the Wilkinson ADC as the charge readout time in the studies presented later.

5.1.2 Concentrator Board

On each TT wall, one Concentrator Board (CB) is connected to all 16 ROBs on the same wall as shown in Figure 5.3. One of main functions of the CB is to serve as the L1 trigger, which checks the coincidence at TT wall level with the minimal requirement that two PMTs on different planes should be triggered, in order to reject hits in the TT that cannot be reconstructed to 3D points that are needed in the track reconstruction.

In the current design, L1 trigger is implemented on a system-on-module (SOM) developed specifically for the TT. ROBs send PMT data to the CB through commercial Ethernet cables with 2 RJ-45 connectors, with a length of about 10 m. Tests show that the signal quality via these cables is good. A photo of the newest version of concentrator is shown in Figure 5.4.

Although MAROC3 sends out the individual trigger outputs, they are not used for the L1 trigger decision. If we want to successfully reduce the dead time, the trigger must react quickly to deliver reset signals before the MAROC3 finishes the charge readout, and reading the individual trigger outputs is too slow for this application.

Figure 5.5 illustrates the timeline of one channel of the PMT in the concentrator processing. The values shown correspond to the following setting: the PMT threshold is set to 1/3 p.e.,[1] with which the MAROC3 trigger efficiency is 100% according to the MAROC3 datasheet [172]; the coincidence time window (TW) has a duration of 200 ns; the transit time of FAST-OR or reset signals between the CB and the FEB is estimated to be 50 ns.

---

[1]Equivalent to a charge of 50 fC, for a PMT functioning at gain 10^6 (900 V) [170]
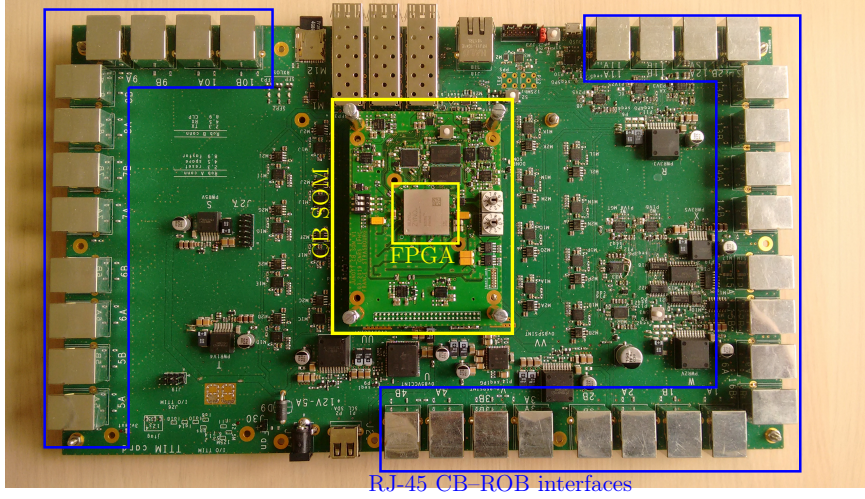
Figure 5.4 – Photo of the most recent Concentrator Board.
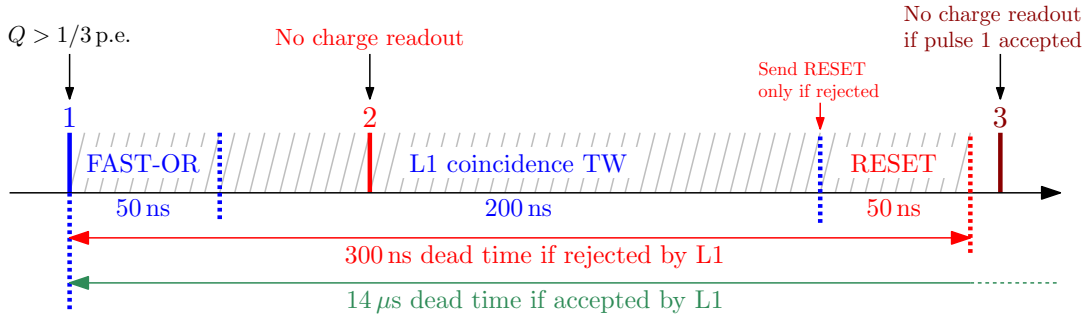
Figure 5.5 – Example of the behaviour of the L1 trigger.

To better explain Figure 5.5, we assume that the PMT has received 3 pulses, labelled with numbers 1, 2, 3. For the pulse 1, MAROC3 outputs a FAST-OR because the channel is triggered at PMT level. When the FAST-OR arrives in the L1 trigger after 50 ns transit, the trigger logic will check if it can be coincident with FAST-ORs from other PMTs within a sliding time window (L1 coincidence time window) of 200 ns. If it is not validated by any other, the L1 trigger will send RESET to the MAROC3. RESET needs 50 ns to arrive in the MAROC3, and therefore the total dead time of the MAROC3 since the arrival of pulse 1 is 300 ns. The dead time is illustrated in Figure 5.5 by a shadowed zone, and the charge of any pulse during this dead time will not be read out by the MAROC3, as the pulse 2 shown in the example. After the reset, the MAROC3 is ready to process new charge readout. In this schematic, a new readout will be started by pulse 3.

If the L1 trigger finds a coincidence, it will produce a valid trigger output for this coincidence, such that the L2 trigger is informed to further check this MAROC3. Assuming no rejection from the L2 trigger, then the dead time will be equal to the total readout time, namely, 14 µs. In this case, any pulse received by MAROC3 during the readout time, for example, the pulse 3, will not be processed for charge readout.

5.1.3 L2 trigger system

Muons are expected to leave well-aligned 3D points in different layers, whereas radio-active events are very unlikely to have such a pattern. Therefore, to further reduce

the TT event rate, the L2 trigger will check if the L1 triggered walls within the L2 coincidence time window are aligned. A typical choice of the L2 time window is 300 ns. If a coincidence is found, the L2 trigger will validate this event. Otherwise, depending on the implementation, the L2 trigger may send RESET to corresponding MAROC3s.

There are two ways to implement the L2 trigger under our consideration. The first option, named "FPGA option", is to use an FPGA-based electronic board. In this case, the L2 trigger is able to reset the MAROC3 within about one microsecond, and the dead time can be further reduced.

The second option, named "CPU option", will require online-processing CPUs for global coincidence validation. In this option, as it is not feasible to have a sufficiently low latency to reset MAROC3s, we plan to wait until CPUs can access all information for each event. The extra informations, for example, individual triggers of all PMT channels, make it more efficient to identify muon events. Because MAROC3s will not be reset, this option can reduce only the TT output data volume to the DAQ, but not the MAROC3 dead time. Compared with the FPGA option, this option needs less efforts in its development.

As no decision has been made at this time by the JUNO collaboration, we assume that the L2 trigger is realised with the FPGA option in our studies, which allows to reset MAROC3s in an invalid L2 coincidence.

5.2   Top Tracker simulation

The simulations for the TT physics are performed by using the framework of the JUNO official MC. We will explain here some details about the TT signal simulation and the event generation.

5.2.1   Top Tracker signals

The TT geometry is implemented in the official MC based on the description in Section 2.2.4.

The number of photoelectrons generated by each energy deposit is calculated directly from the corresponding deposited energy in our simulation. The reason for not having the scintillation simulation is that the TT scintillator properties have been extensively studied by the OPERA collaboration [142]. This also makes the TT simulation lightweight.

To obtain the number of photoelectrons from energy deposits, we use the empirical formula describing the relation between observed number of photoelectrons and deposited energy [142]

$$N_{\text{pe}}(x) = \frac{E}{2.15} \times \left(\alpha_0 e^{-\beta_0 x} + \alpha_1 e^{-\beta_1 x} \right), \tag{5.1}$$

where x is the light propagation distance in Wave Length Shifting (WLS) fibre, E is the deposited energy in the scintillator strip, and α_0, α_1, β_0, β_1 are four empirical coefficients that are defined by the calibration curve of each strip. Figure 5.6 shows an example of a strip calibration done by OPERA by moving the calibration source along the strip from left to right (0 is leftmost). The red curve gives the observed number of photoelectrons for the left-side PMT, and the green curve for the right-side PMT.

In reality, every strip will be recalibrated for JUNO, and the coefficients in Equation (5.1) will be updated to the measured values. However, in the current simulation
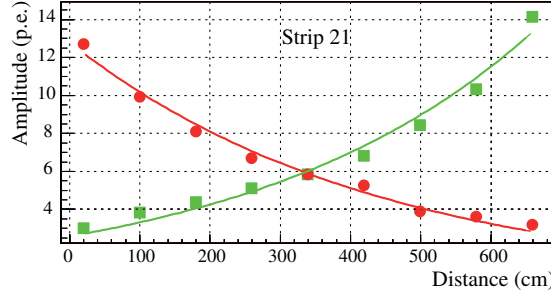
Figure 5.6 – Number of photoelectrons observed by the left-side PMT (red) and the right-side (green) PMT versus the distance from the leftmost in the calibration for OPERA [142].
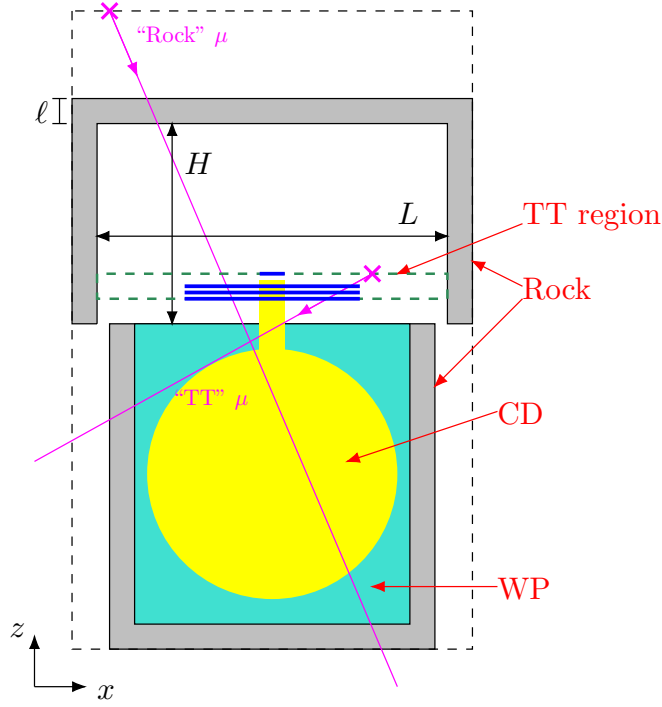
Figure 5.7 – Schematic view of the JUNO cavern implemented in the MC simulation. It is not drawn to scale.

configuration, as an approximation, the mean values of each coefficient are used in the equation, for the WLS fibres that have the same length. The mean values were obtained by doing a Gaussian fit of the measured parameters in OPERA. Finally, to mimic a "measurement", the number of photoelectrons obtained in the simulation is sampled from a Poisson distribution of which the mean value is $N_{\mathrm{pe}}(x)$ determined in Equation (5.1).

Lastly, effects of optical crosstalk between neighbouring PMT channels is also considered in the simulation with the measured crosstalk probabilities taken from OPERA.

5.2.2 Muon generation

The muon generator gives primary muon tracks based on the realistic atmospheric muon flux and energy spectra in the JUNO cavern.

The official MC simplifies the JUNO cavern as shown in Figure 5.7. The surrounding rock of the experimental hall is a square box, whose inner side length (L) is 48 m and

inner height (H) is 18.6 m. The thickness of rock (ℓ) is set to 3 m and the rock density is by default 2.59 g/cm^3. The surrounding rock of the WP is a cylinder tube with the same thickness of rock.

In order to accelerate the computing and add some flexibility, muons are injected in the simulation from the surfaces of a box-like volume, as if muons flew from the same level and intersected with the volume there. The muon rate must be recalculated to maintain the correct muon flux in the cavern. Two options "TT" and "Rock" are provided for the muon injection.

In the option "TT", the muons are generated from the surface of a 48×48×8.4 m^3 virtual box centred at the TT ("TT region" in Figure 5.7). Because muons are injected inside the experimental hall, they will not cross the surrounding rock. The muon rate for this option is 9.8 Hz. By using this option, most muons cross directly the TT. In Figure 5.7, an example track generated in this way is given with label "TT".

In the option "Rock", the muons are generated from the surfaces of a box whose dimension is 54×54×73.5 m^3, namely a box encompassing the entire JUNO setup, including the surrounding rock, as illustrated by the black dashed box in Figure 5.7. The muon rate for this option is 23 Hz. An example muon track generated with "Rock" option is also drawn in Figure 5.7.

Due to the high density of the rock, muons generated with option "Rock" can sometimes induce showers, and the secondary particles fly over a long distance to trigger much more PMT channels than the parent muons do. Figure 5.8 shows a showering muon event.

We have simulated 10^6 muons without option "TT", and the maximal number of triggered channels observed is 300. Therefore, we define a rock showering muon by requiring at least 300 triggered channels. For reference, a non-showering muon has only 12 triggered channels in average. The rate of rock showering muons detected by the TT can also be estimated in the simulation, and it is equal to 4×10^{-5} Hz.

Multiple muons can be produced in one single interaction of cosmic ray in the atmosphere, and the muons that arrive simultaneously in JUNO have to be parallel. Events of this kind are called muon bundles, and we expect that 10% of muon events in JUNO are muon bundles. In a muon bundle, it is possible that more than one muons cross the TT and leave tracks, as the example shown in Figure 5.9, where 3 primary muons pass through the TT.

The rock and the muon bundles make the simulation more realistic, but they increase the time consumption of simulation and unnecessarily complicate our analysis for the TT resolution. For example, muons can be deviated by the rock, which makes the simulation less precise. Moreover, for the studies focusing on the radioactive background suppression, which is the main task of the trigger system, we only simulate radioactive decays, so the muon generation is irrelevant in this case. For most usage in our studies, we simply generated single muons injected with option "TT", as they provide net muon tracks that are preferred to test the performances of different trigger algorithms.

5.2.3   Radioactivity generation

We use a dedicated generator to produce ^{238}U, ^{232}Th, and ^{40}K decay events. Isotopes ^{238}U and ^{232}Th have chain-decay processes, namely they will decay multiple times to reach final states. The intermediate decays are simulated in different events, by this means, the generator takes into account the chains.

The generator lets users decide where the decays should happen. As the radiation is from the surrounding rock, the decay positions should be set uniformly inside the entire

(a)   **(b)**
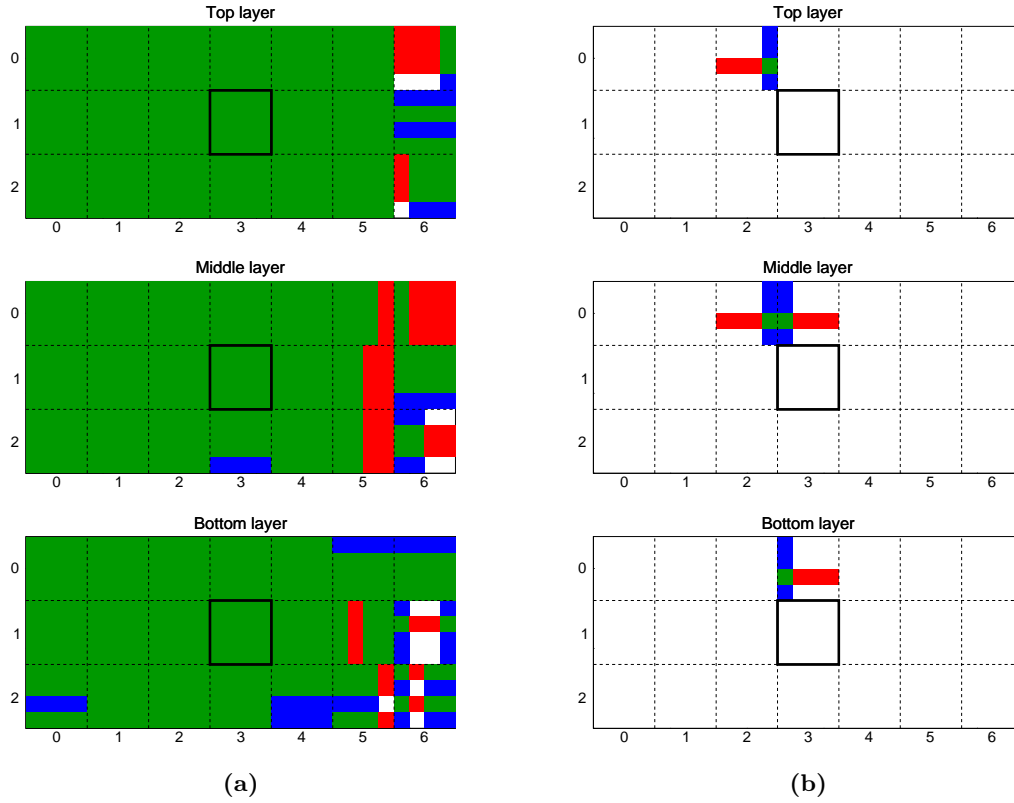
Figure 5.8 – Event displays of (a) total touched modules in a rock showering muon event, compared with (b) the display showing only the modules touched by the primary muon. Blue is for touched modules on y-planes, red is for touched modules on x-planes. When two touched modules in both planes cross, the area is displayed in green. The middle square of each layer shows the wall located above the chimney. We can observe in (a) that almost all channels are touched in the event.
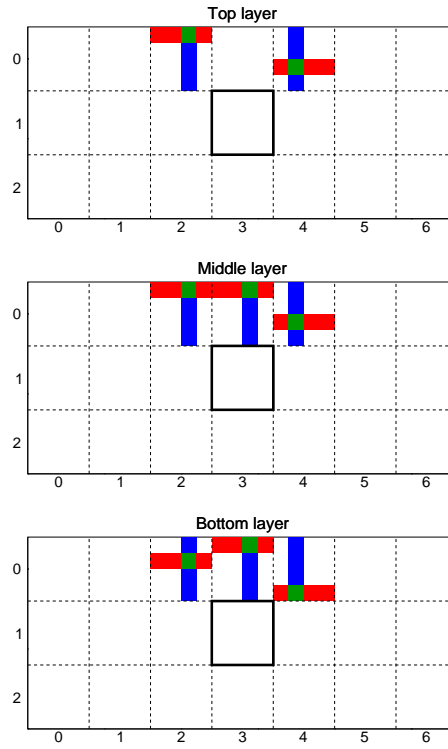
Figure 5.9 – TT event display of total touched modules of a muon bundle. Blue is for touched modules on y-planes, red is for touched modules on x-planes. When two touched modules in both planes cross, the area is displayed in green. The middle square of each layer shows the wall located above the chimney.
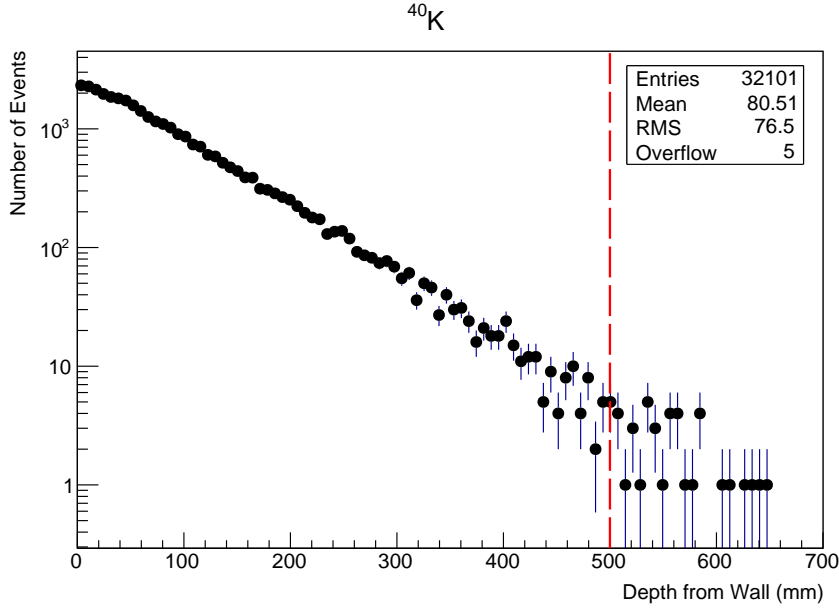
Figure 5.10 – Number of ^{40}K decay events triggering TT PMTs as a function of the depth in the rock where the decays take place.

Table 5.1 – Decay properties of the relevant isotopes, and their decay rates estimated in the TT simulation.

	^{238}U	^{232}Th	^{40}K
Chain length	14	10	1
Activity a (Bq/kg/ppm)	12.4	4.0	258.4
Abundance Y_{NA} (ppm)	9	26	5
Decay rate N (Hz)	7.2×10^8	8.10×10^8	1.22×10^{10}

rock. However, not every decay in the rock can produce signals in the TT. Let ^{40}K be an example, Figure 5.10 shows that the number of ^{40}K decays that trigger TT PMTs as a function of the depth where the decays take place.

The number of decays triggering PMTs reduces exponentially, and only 0.14% of the decays are actually located at a rock depth larger than 50 cm.

Based on this study, we chose to generate only decays shallower than 50 cm of rock depth in the surrounding rock of the experimental hall. As expected, the simulation efficiency is significantly improved.

In the simulation, the decay rate due to the relevant isotopes is calculated with the following formula

$$N = a \times Y_{\mathrm{NA}} \times M, \tag{5.2}$$

where N denotes the decay rate of the isotope, a is the activity of one kilogramme of rock where the abundance of the isotope is 1 parts-per-million (ppm), Y_{NA} is the natural abundance in the JUNO cavern, and $M = 7.8 \times 10^6$ kg is the mass of 50 cm depth top rock. The resulting parameters and rates for the studied parent isotopes are summarised in Table 5.1.

Figure 5.11 – An example XY coincidence where both PMT1 and PMT13 are triggered and send FAST-ORs to the CB.

5.3 L1 trigger algorithms

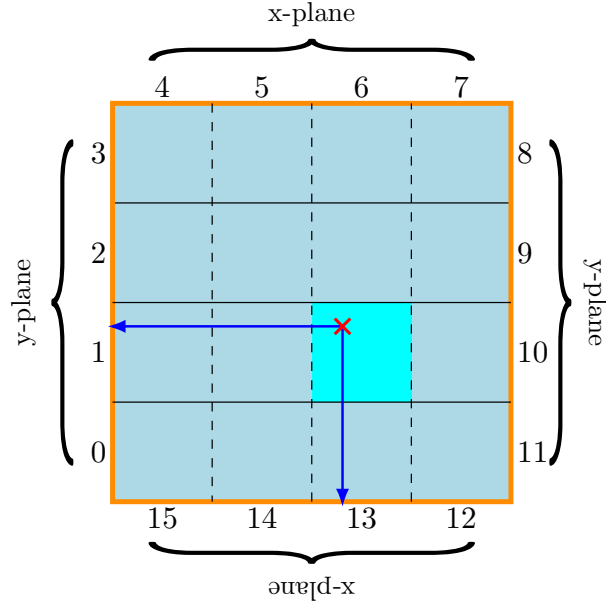The L1 trigger is implemented by the Concentrator Board (CB). Based on the different features of muon and radioactivity signals on a TT wall, the L1 trigger algorithm is designed to favour muon events and disfavour radioactive events. In this section, we will present all considered L1 algorithms that will be used later in the performance studies.

5.3.1 XY coincidence

XY coincidence is the minimal required level of coincidence, as it rejects any PMT coincidence that cannot create a 3D point. Figure 5.11 gives an example where the PMT1 on the y-plane and the PMT13 on the x-plane form a valid XY coincidence. We remind here that, according to Figure 2.16, PMTs 0–3 and 8–11 are on the y-plane, and PMTs 4–7 and 12–15 are on the x-plane. Additionally, since the L1 trigger sees only FAST-ORs, it cannot know exactly which channels are triggered, instead, it can identify a superpixel that contains all 64 channels for each PMT.

By using the JUNO official MC, which does not consider yet the triggers, we checked how many times the radioactive decays can produce energy deposits on both planes of a TT wall. The simulation shows that, radioactivity has a probability of 3% to deposit energy on both planes of a wall, whereas this probability for muons is as high as 96%. Since most radioactivity does not penetrate both planes, we expect that an XY coincidence can reject most hits caused by radioactivity. However, the accidental XY coincidences can still be produced by two different radioactive decays.

5.3.2 XY+ order coincidence

An XY coincidence can be produced by two different decays accidentally. In this case, we expect that the hit positions on two planes are not correlated, which is illustrated in Figure 5.12(a). In order to further reduce the accidental XY coincidences, on top
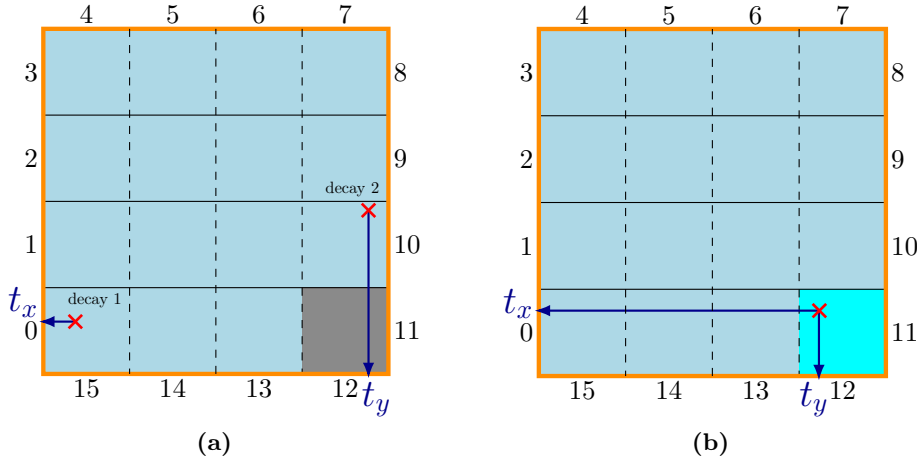
Figure 5.12 – (a) An example accidental XY coincidence. The hits on two planes that trigger PMT0 and PMT12 are given by two different decays. (b) An example correlated XY coincidence. A muon leaves hits on both planes, whose positions and times of scintillation photon production are correlated.

of the XY coincidence requirement, the criterion can be set more stringent with the requirement on the correct arrival times of the FAST-ORs in the CB. Although we do not plan to add a Time-to-Digital Converter (TDC) in the CB for this purpose, the L1 trigger should still be able to verify the correct sequence of FAST-ORs in an XY coincidence, and filter out accidental coincidences arriving in the wrong sequence.

The algorithm checking FAST-OR order is named XY+ordering coincidence (or XYo coincidence, for short). We will explain the algorithm by using the example illustrated in Figure 5.12, where in both (a) and (b) the L1 trigger finds an XY coincidence of PMT0 and PMT12.

In this example, the times t_x and t_y are the arrival times of the FAST-ORs from PMT0 and PMT12 in the CB, respectively. In Figure 5.12(a), two decays are accidentally coincident, so it is possible that they produce signals with $t_x < t_y$, which cannot be explained by a single muon hit. In this case, such an XY coincidence is rejected.

If both PMTs are triggered by a single muon, as depicted in Figure 5.12(b), the FAST-OR from PMT0 should arrive before the one from PMT12, due to the different travel distances of the light, and given the scintillation photons in WLS fibres are produced almost at the same time, t_x must be greater than t_y. In this case, the L1 trigger accepts this XY coincidence.

The correct time order is not always unambiguous. As the L1 trigger can only see information at superpixel level, for the hits in the diagonal superpixels (e.g., the superpixiel connected to PMT1 and PMT6), both orders are possible for a single muon event depending on the hit positions on the planes. For example, given an XY coincidence of PMT1 and PMT6, as shown in Figure 5.13, the arrival times in the CB can be either $t_x \leq t_y$ (hit position A) or $t_x \geq t_y$ (hit position B). Consequently, we want the algorithm to accept both possibilities, i.e. no time-ordered condition should be imposed for PMT coincidences corresponding to diagonal superpixels.

In Figure 5.14, we make a graphical lookup table for the required orders of all possible binary combinations of PMTs by the XYo coincidence. The table consists of 4 large squares, each having 16 small squares. On the left side are the PMTs 0–3, at the top are the PMTs 4–7, on the right side are the PMTs 8–11, and at the bottom are
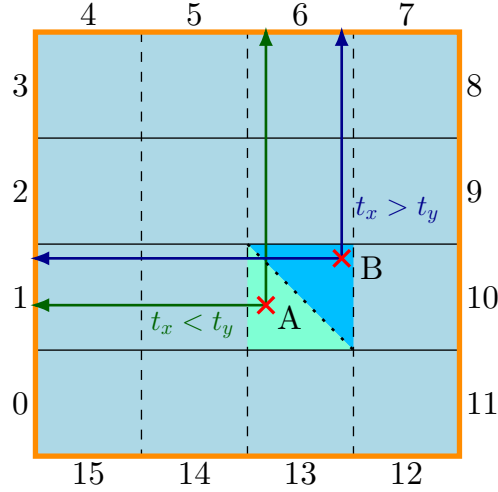
Figure 5.13 – For a muon passage in the diagonal superpixel, the correct time order of FAST-ORs of PMT6 and of PMT1 in the L1 trigger is not unique. If the point of passage of a muon is A, then the correct order is $t_x < t_y$; if it is B, the correct order should be reversed.
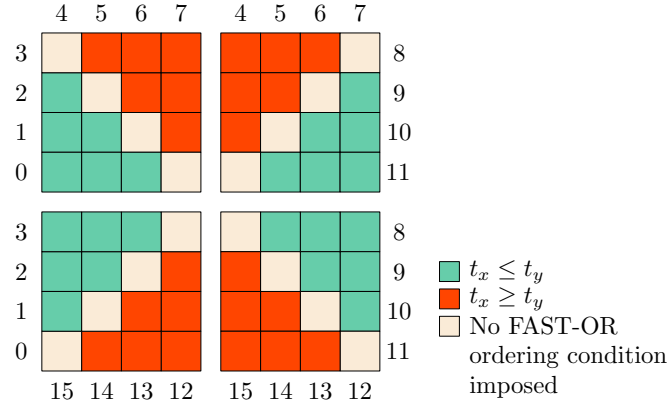
Figure 5.14 – Lookup table for the required orders of all possible binary combination of PMTs by the XYo coincidence. The numbered PMTs at the edges correspond to which pair of PMTs is being tested.

the PMTs 12–15. The upper left large square is the group of all combinations of (left, top). Similarly, the upper right large square is the group of (right, top); the bottom left large square is the group of (left, bottom); the bottom right large square is the group of (right, bottom).

The L1 trigger will test the XYo coincidences according to the table in Figure 5.14. For example, if the L1 trigger receives FAST-ORs from PMT0 and PMT4, in order to validate the coincidence, the time order must be that the FAST-OR of PMT0 arrives before the one of PMT4.

There are 64 possible combinations for an XY coincidence. If we consider the different time orders, as the accidental coincidence might be seen first in x- or in y-plane PMT, there are 128 different possible time-ordered combinations. XYo can exclude 48 of them. Assuming the time order is random for radioactive hits, we expect that XYo helps to reject 48 out of 128 possibilities, giving a reduction of 37.5% in the accidental coincidences of radioactive hits.

5.3.3   XY3, XY⊥, and XY× coincidences

Instead of imposing XYo coincidence, other algorithms based on the PMT multiplicity and the wall geometry can also be helpful for background reduction. They should actually be easier to be realised on the CB than the XYo coincidence, because a discrimination on the time of arrival for PMT signals is not required.

A distinguishing feature of muon signals is the PMT multiplicity on a TT wall. Figure 5.15(a) compares the PMT multiplicity on a TT wall triggered by muons and by radioactivity. The distributions show that, 95% of TT walls triggered by a muon have a coincidence of more than 3 PMTs on the same TT wall, whilst only 2% of triggered walls in a radioactive decay can have the same number of coincident PMTs on a TT wall. Therefore, we consider an algorithm to identify muons from the background by requiring 3 triggered PMTs in coincidence, where 2 of them form an XY coincidence, and the third one can be any other PMT on the same wall. This algorithm is termed "XY3". Compared with the XY coincidence, which is a 2-fold coincidence, XY3 reduces the accidental coincidence rate by requiring 3-fold coincidence. However, the simulation also shows that we will lose about 2% of TT walls triggered with XY coincidence by a muon.

Figure 5.15(b) shows the distributions of number of triggered PMTs on the same module for muons and radioactive decays. We observe that about 90% of modules triggered by a muon have 2-sided PMT signals, while only about 45% of modules triggered by radioactive decays do the same thing. This feature allows us to exclude more background by requiring a two-sided coincidence on top of the XY coincidence, while preserving the muon efficiency compared with XY3. Such a coincidence is termed XY⊥ coincidence, and the 3 validated PMTs should form a T-shape, crossing at one superpixel.

Lastly, we can even go further by requiring a coincidence where the 4 validated PMTs must form a cross, namely two-sided coincidences are required on both TT planes. This algorithm is labelled as XY×. It further reduces the probability that a correlated
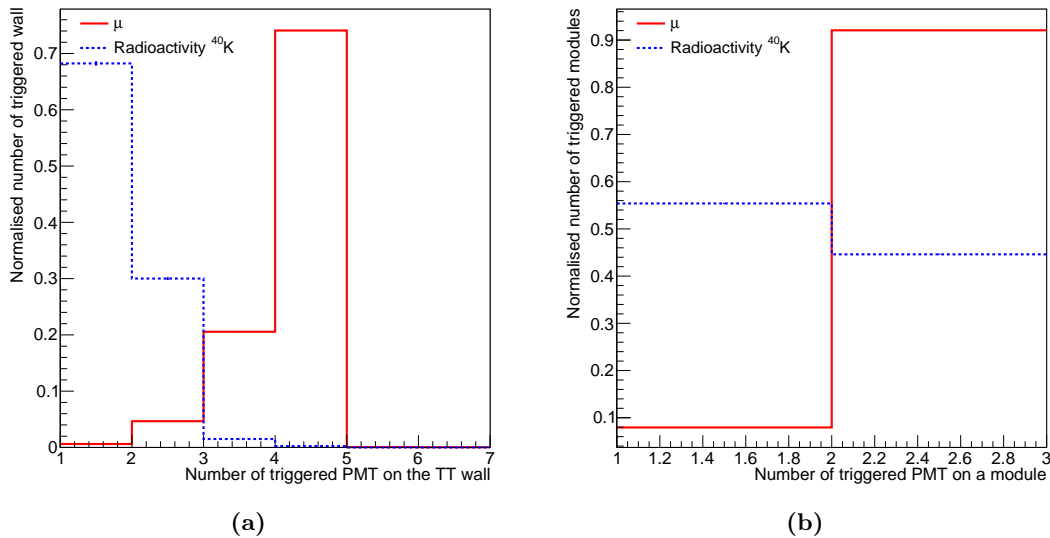

(a)   (b)

Figure 5.15 – (a) Distributions of numbers of triggered PMTs on the same TT wall, and (b) distributions of numbers of triggered PMTs on the same module, in muon events and radioactive decay events, respectively. The distributions are normalised to 1.

coincidence is found in a TT wall touched by radiation to 0.2%, but it also leads to a loss of 23% of true muon triggers with respect to the XY coincidence.

In fact, it is worth pointing out that, the three algorithms have a relation as XY3 ⊃ XY⊥ ⊃ XY×. That is to say, coincidences that meet stricter conditions are also accepted by the algorithms with less strict conditions.

Figure 5.16(a) shows an example XY3 coincidence. In this example, the L1 trigger validates the coincidence of PMT6+PMT9+PMT14, of which PMT9+PMT14 and PMT6+PMT9 are XY coincidences. Figure 5.16(b) shows an example XY⊥ coincidence. In this case, the L1 trigger validates the coincidence of PMT5+PMT9+PMT14. Figure 5.16(c) shows an example XY× coincidence. The L1 trigger will validate the coincidence of PMT2+PMT5+PMT9+PMT14.

5.4 Test bench for XYo coincidence

Given that all the above proposed algorithms will have to be implemented on the Concentrator Board (CB) FPGA, they need to run efficiently such that MAROC3s can be reset as fast as possible. To ensure that this can be done as required in this FPGA, we have decided to implement a test bench for the XYo algorithm, which should be the most complicated one amidst those described above.

The most recent version of the CB is equipped with a `Zynq Ultrascale+` FPGA. However, this study was done before the release of the new CB, so we did not use the same FPGA model. The FPGA used here is a `Zynq 7030` carried by a commercial `PicoZed` board, which is mounted on a `PicoZed FMC Carrier V2` as its development board. This model has nevertheless a similar number of resource as the new model.

An FPGA is an integrated circuit that can be programmed in the field after manufacture, thanks to the large amount of configurable interconnection wires and logic blocks. The core component of a configurable logic blocks (CLB) is the lookup table (LUT), which takes a few inputs and outputs the result of any given function with these inputs. Therefore, the designer is able to program both wiring and CLBs to tailor the functionality of the chip. Today FPGAs are widely used in the particle detectors, as they can satisfy the increasing requirements on timing precision, speed of decision, fast prototyping, and high flexibility. For this reason, we have chosen to implement most functionalities on the CB FPGA, including the L1 trigger logic, time-stamping, high speed data transmission, and slow controls.

The XYo is the only L1 algorithm in Section 5.3 that requires correct time orders of the FAST-ORs arriving in the CB. A time sequential implementation is nevertheless not optimal for the FPGA architecture, and we do not plan to implement real Time-to-Digital Converters (TDCs) on the CB FPGA. So it is also crucial to verify if it exists a solution compatible with the FPGA architecture. Moreover, since the resources in an FPGA are limited, it is important to know if the implementation of the L1 trigger algorithm may cause a shortage of resources.

5.4.1 FPGA design for XYo L1 trigger

Based on the XYo algorithm described in Section 5.3.2, the FPGA must manage different PMT timelines in parallel, such that it is possible to check any coincidence for all PMT permutations within a 200 ns time window, and reset each triggered MAROC3 in time if the corresponding PMTs are rejected. Figure 5.17 shows examples how the FPGA should execute the XYo coincidence validation with PMT0 and PMT12.
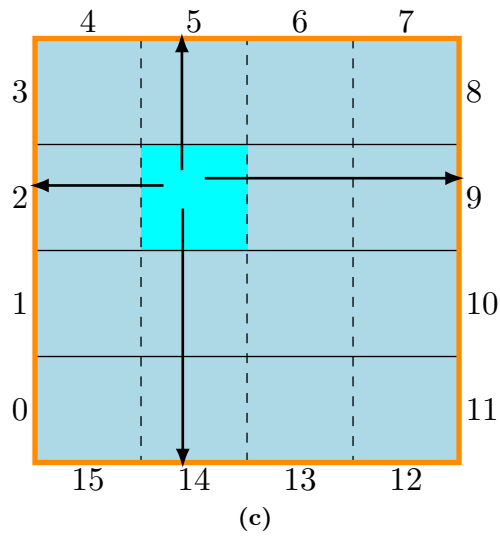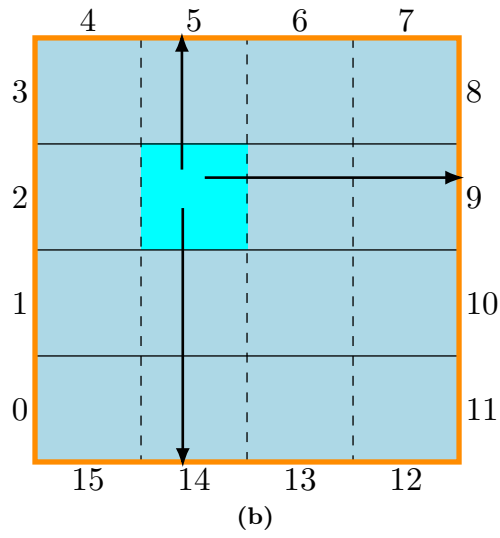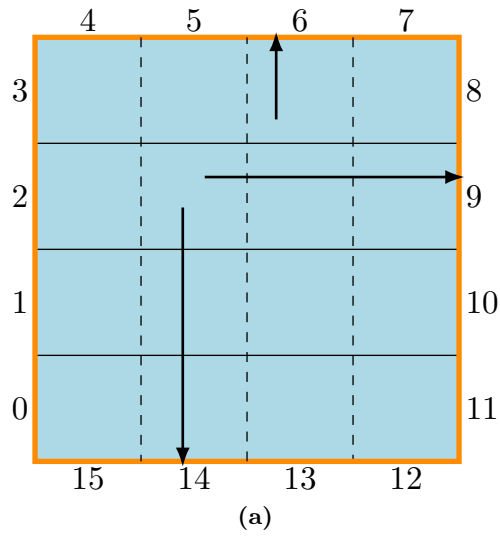
Figure 5.16 − Example of minimal L1 coincidences passing the requirements for (a) XY3, (b) XY⊥, and (c) XY×.
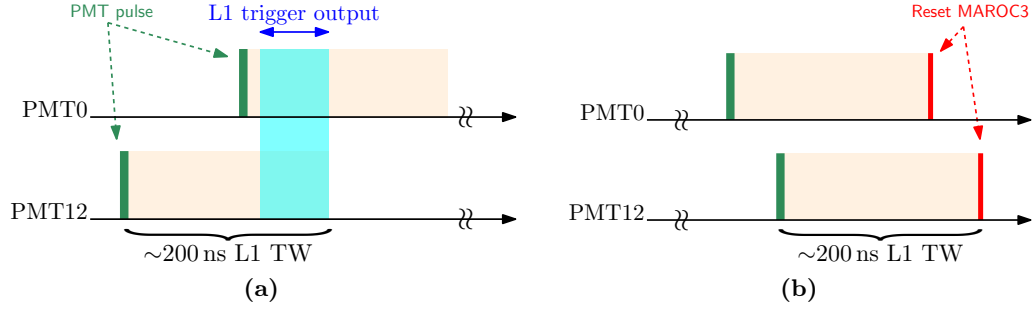
Figure 5.17 − Two coincidences between PMT0 and PMT12 for XYo validation. (a) shows a valid event that is accepted, and (b) a bad time order that is rejected.
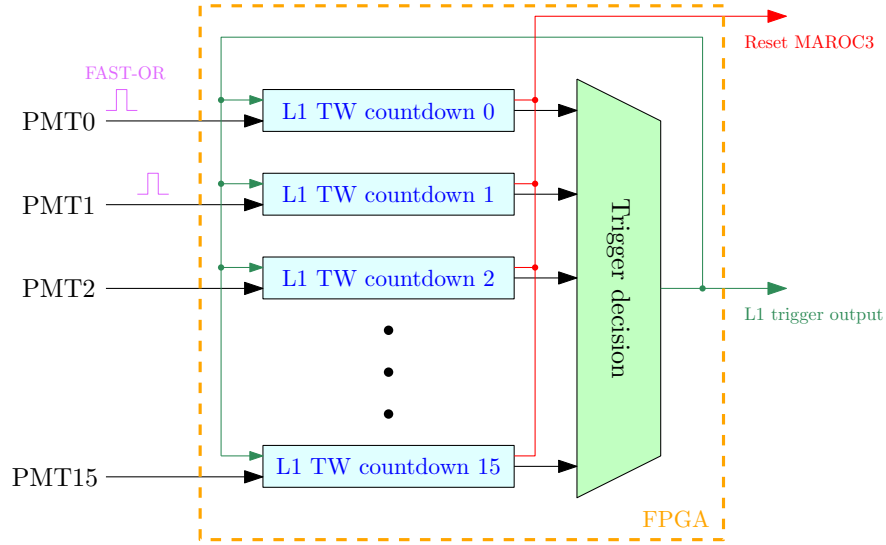
Figure 5.18 − Block diagram of the FPGA design for the XYo L1 trigger implementation.

The coincidence in Figure 5.17(a) is given by a muon hit that has been shown in Figure 5.12(b). Since the time order is correct, after receiving the FAST-OR from PMT0, the FPGA raises the L1 trigger output at the next clock cycle, and maintains it until the end of the time window opened by the PMT12.

The coincidence in Figure 5.17(b) is given by the accidental XY coincidence from decays as shown in Figure 5.12(a). This time the time order is wrong, so no L1 trigger signal will be output. Because the FPGA should wait for potential coincidences with any PMT, the time windows of PMT0 and PMT12 should remain open. Assuming that no other PMT is triggered, the FPGA will send RESET to each MAROC3 of the PMTs after their time window closes.

The FPGA firmware is designed to take 16 inputs that mimic FAST-ORs. If any XYo coincidence is validated, the test bench will raise the L1 trigger output. It consists of 16 individual "L1 TW countdown" modules for each PMT, and a trigger decision module where the XYo algorithm is implemented to check the time order. The block diagram of the test bench is depicted in Figure 5.18.

For each PMT, the FAST-OR starts the countdown, and the started countdown modules output the counts by a 8-bit bus to the trigger decision module internally. The trigger decision then compares the counts and makes a decision whether the PMTs form an XYo coincidence. If the time order is not validated, the decision module will do

nothing. Without the L1 trigger output from the trigger decision module, the started countdown modules will continue the countdown until it reaches 0, and then reset the corresponding MAROC3s. If the XYo coincidence is found, the decision module will output a valid signal showing that the event is triggered. This output will be feedbacked to countdown modules to acknowledge them that the coincidence has been validated. In this case, the state of valid coincidence will be registered in the countdown modules, such that the MAROC3s of the corresponding PMTs will not be reset when their own time windows are closed.

5.4.2 Implementation on a test bench

Figure 5.19 shows the test bench, consisting the FPGA and its development board, a mezzanine card for Input/Output (I/O) of the FPGA, a pulse generator, and an oscilloscope for L1 trigger output observation. In order to make a simplest possible test bench for our modules for XYo trigger algorithm, only two-PMT coincidences are considered.

We used a single pulse generator to simulate the FAST-OR signals of the two PMTs. The pulse from the generator is internally split into two pulses with a configurable relative delay up to 333 ns, with smallest step being 0.83 ns. Subsequently, the split signals are output from the FPGA and loopbacked via two ports INPUT_0 and INPUT_1. A multiplexer implemented on the FPGA can be used to select two PMTs as PMTs under test. For example, we can select PMT0 and PMT4 as the PMTs under test, and their FAST-OR signals are from INPUT_0 and INPUT_1, respectively. By this means, we are able to simulate all possible binary combinations of all channels. The FPGA design is driven by a 100 MHz clock.

On the oscilloscope, we checked the L1 trigger output to verify whether the design works properly. Figure 5.20 shows the waveform of accepted or rejected PMT0 and PMT4 trigger. The L1 trigger output is also shown and remains flat for the rejected event, while being raised for the accepted. It must be noticed that in Figure 5.20(a), the L1 trigger output shown on the oscilloscope is delayed by 3 clock cycles, i.e. 30 ns, from the internal L1 trigger signal, due to the test bench configuration. Figure 5.21 shows the same waveform as in Figure 5.20(a) for a larger time scale that contains multiple pulse periods. As we expect, the logic is working in all periods with identical behaviour.

Due to the fact that the FPGA I/O mezzanine card does not have available ports for outputting MAROC3 reset signals, they remain internal signals and thus cannot be connected directly to an oscilloscope. The reset signals are only visible with the ILA[2]. A captured waveform is shown in Figure 5.22 for a PMT0-PMT4 coincidence that is rejected due to the wrong time order. We can see from the waveform that resets are raised after the time windows of PMT4 and PMT0 are closed.

A few tests have been done to confirm the FPGA logic of XYo validation. We scanned different delay times between two signals (PMT0+PMT4) from 0 to 300 ns with step of 16.6 ns, which is short enough for our FPGA running at 100 MHz. The valid L1 trigger output is generated until the delay reaches 200 ns where the time window is supposed to be closed. Beyond that, the L1 trigger output is not raised. We also changed the inputs to different channel numbers, in order to check if the algorithm works also for other PMT combinations. The combinations in Figure 5.14 belonging to the upper left square, have been tested with a relative delay of 170 ns. For all these combinations, only when the delay is set in the correct order, the coincidence of the

---

[2]Integrated Logic Analyzer, developed by Xilinx
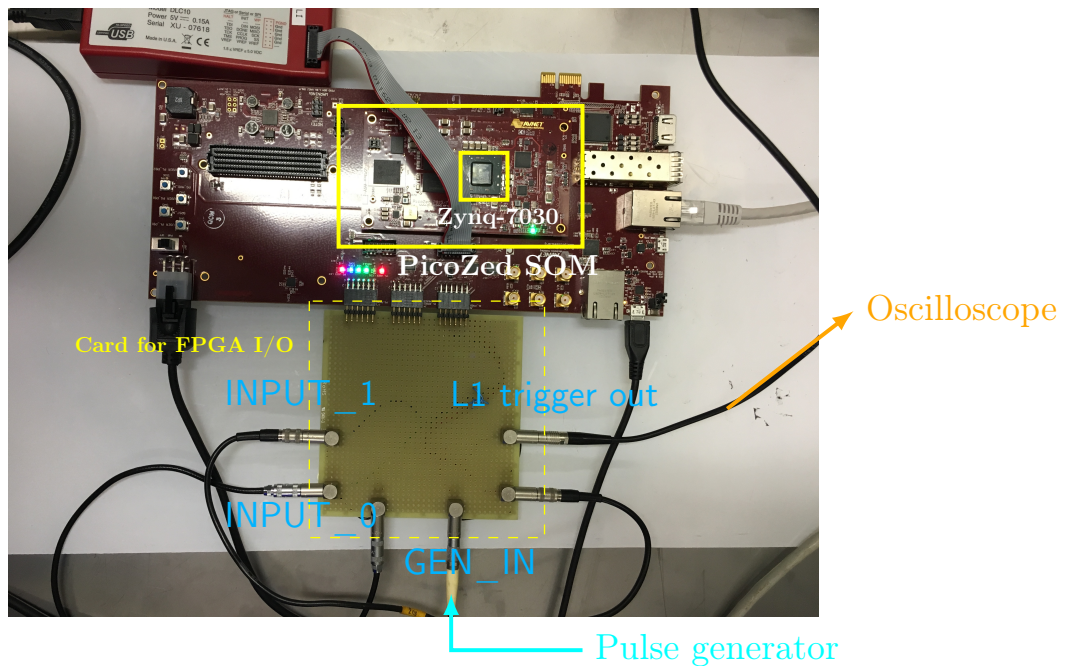
Figure 5.19 − Photo of the test bench. A mezzanine board provides one input for pulse generator, and then the FPGA splits and delays the pulses. The pulses are output and loopbacked to the FPGA for mimicking the FAST-OR signals. The L1 trigger output is connected to an oscilloscope for observation.
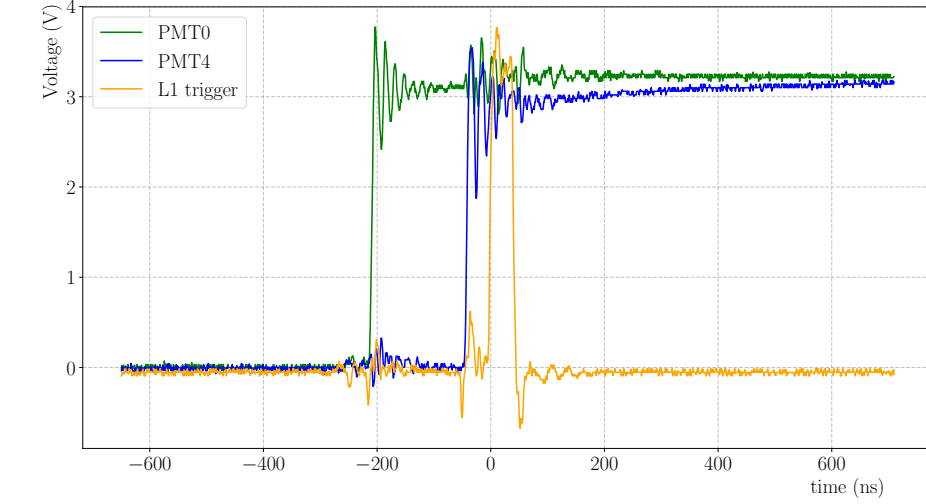
(a)
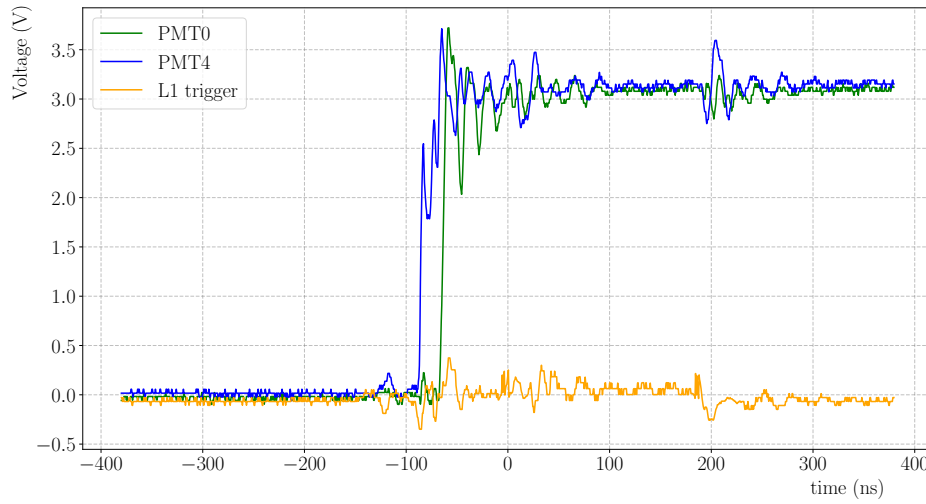
(b)

Figure 5.20 – The test waveforms of PMT0 (green) and PMT4 (blue) for the simulations of (a) XYo coincidence where PMT0 FAST-OR arrives 170 ns before PMT4, and (b) false time order where PMT0 FAST-OR arrives 20 ns after PMT4. The waveform of the L1 trigger output (yellow) is also shown.
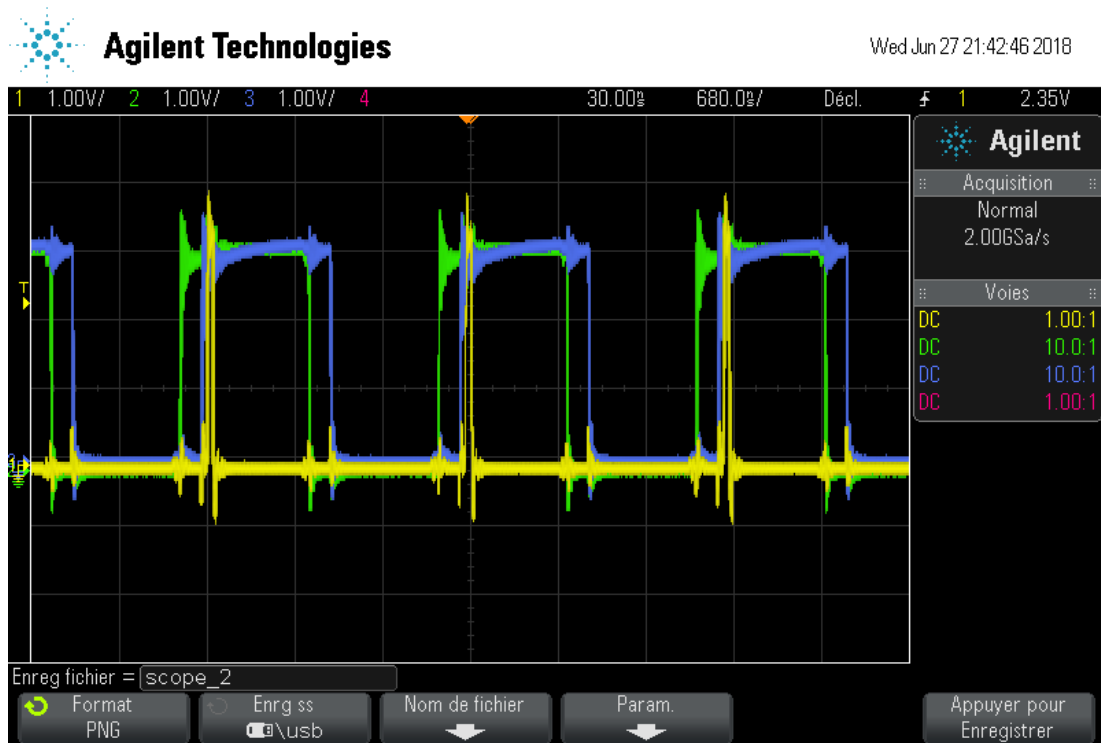
Figure 5.21 – The same waveform as in Figure 5.20(a), green is the PMT0, blue in the PMT4, and yellow is the L1 trigger output. The time scale is enlarged so that multiple pulse periods are shown on the same screen. One division of the voltage is $1\,V$, and one division of the time is $680\,ns$.
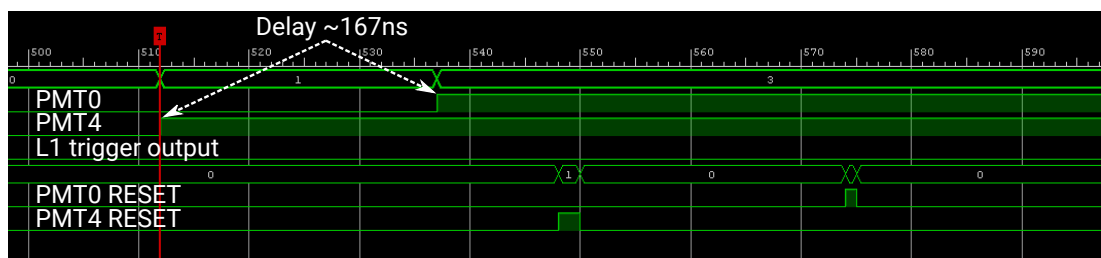
Figure 5.22 – Waveform of a rejected XY coincidence that is captured with ILA.

combination is validated by the FPGA. With all test results, we confirm that the FPGA logic of XYo validation works as it is designed.

Additionally, the synthesis tool gives a summary of the resources required by the design. Including the supporting logic, the whole design takes 3% of CLBs in the FPGA, so we estimate that an implementation of XYo L1 trigger should not cause any shortage of resources on the CB FPGA.

In conclusion, this study shows that we can implement the XYo L1 trigger logic through the FPGA-featured parallelism. The tested design satisfies both the algorithm timing requirement and the CB resource requirement. Given that the XYo is the most complicated one amidst all L1 trigger algorithms that are considered in Section 5.3, we do not foresee any issue with the implementation of other algorithms on the CB FPGA.

5.5   L2 trigger algorithms

The L2 trigger is able to reject more events that are unlikely to be generated by muons by looking at the full detector. In the current consideration, we studied three different L2 trigger algorithms.

In the first algorithm, we keep only the events with more than two triggered layers. We name this algorithm 2-layer coincidence (2L). The condition of 2L coincidence ensures that the accepted events can always give a reconstructed track defined by at least two 3D points with different z positions.

Since a good muon track should be reconstructed with at least three 3D points that are aligned, the L2 trigger algorithm can therefore be designed to select only events that contain good muon tracks. This algorithm is called "Align", and it requires that a validated event must have at least 3 triggered walls on different layers, and these walls must be aligned. For its implementation, we consider to use a lookup table, which takes 3 wall IDs as input arguments and outputs the result if these 3 walls are aligned or not. The lookup table can be calculated in advance and stored in the FPGA which runs the L2 trigger.

Although the "Align" algorithm should give the best veto efficiency, the online alignment checking results in a longer latency to reset MAROC3s of non-accepted PMTs. From the simulation, we have noticed that 97% of the muon events that trigger more than 3 TT walls are actually valid events under the "Align" condition. So we propose a third algorithm, namely the 3-wall coincidence (3W), in order to avoid the online alignment checking.

5.6   Muon track reconstruction

After a TT event is built by the DAQ, a reconstruction algorithm will try to fit PMT triggered channels offline and obtain the best fit muon tracks.

The first step before fitting is to filter the optical crosstalk between different PMT channels. This work is done by looking for the channel of each PMT that has the maximal number of photoelectrons (N_{pe}) and assuming it to be the main channel. We will identify and remove the crosstalk channels by checking if any of the 8 channels around this main channel has a N_{pe} less than 30% of the main channel's. Otherwise, if the channel's N_{pe} is larger than 3 p.e., it will still be kept. By this means, the crosstalk channels are removed in a conservative way.

The second step is to build 3D points from triggered PMT channels. The 3D points will be used later in the linear fit. For each triggered wall, the triggered channels on

x-direction will be merged into x-coordinates by averaging the positions of a span of 30 TT strips, and the same merging is done for the triggered channels on y-direction for y-coordinates. The z-coordinate of the triggered wall will be taken as the middle between the x- and y-plane.

The last step is the 3-dimensional linear fitting of the muon track. The reconstruction routine starts with n 3D points out of all found 3D points in the TT, where n is initialised to the total number of triggered walls in the event, e.g., if there are 3 triggered walls, then $n = 3$. If the points selected for fitting are all in different walls, the algorithm will then try to fit them by using `TMinuit2` [173]. A muon track in the 3D space can be defined by the equation

$$\boldsymbol{x}(t) = \boldsymbol{x_0} + t\boldsymbol{r}, \tag{5.3}$$

where $\boldsymbol{x} = (x, y, z)$ denotes points on the line mapped by the variable t, $\boldsymbol{x_0} = (x_0, y_0, z_0)$ is one specific point on the line, and $\boldsymbol{r} = (\delta x, \delta y, \delta z)$ is the direction. Analogue to the 2D case, the 3D χ^2 is defined as

$$\begin{aligned}
\chi^2 &= \sum_{i=0}^{n-1} \frac{d_i^2}{\sigma_i^2} \\
&= \sum_{i=0}^{n-1} \frac{\|(\boldsymbol{x_i} - \boldsymbol{x_0}) \times \boldsymbol{r}\|^2}{\|\boldsymbol{r}\|^2 \sigma_i^2},
\end{aligned} \tag{5.4}$$

where n is the number of 3D points used in the fitting, d_i is the minimal distance from the point $\boldsymbol{x_i}$ to the line, and σ_i is the uncertainty. σ_i is fixed to $13\,\mathrm{mm}$, which is the half width of a TT scintillator strip. Because muons that cross different TT layers must not be horizontal, we fix δz in the algorithm to -1. z_0 is set to the middle of the TT. Therefore, only 4 free parameters x_0, y_0, δx, and δy are left to be determined by the algorithm.

The algorithm minimises the χ^2 for all permutations of the found 3D points. If more than 3 points are used in the fit, the reconstructed track with the minimal χ^2 among all permutations is accepted only if its χ^2 is smaller than 3. If none of the permutation gives a χ^2 lower than 3, in this case, we decrement the number of 3D points used in the fitting by 1, namely $(n-1)$ 3D points will be used, and redo the previous execution until all tracks are successfully reconstructed. If no track can give acceptable χ^2 with $(n-1)$ points, the same procedure will be applied until we end up with only three 3D points being used for the reconstruction. If finally no track can be reconstructed with three 3D points, the algorithm will enlarge the χ^2 acceptance up to 10 for accepting tracks having three 3D point. After this, if there is still no successful reconstruction, the algorithm will stop and jump to the next event.

Since this reconstruction method is not designed for rock showering muons, we set the maximal number of 3D-points to 80. If more than 80 points are found in one event, we skip such an event as it is considered as muon-induced shower. In the simulation, the rate that an event has more than 80 points is estimated to be smaller than $10^{-4}\,\mathrm{Hz}$.

Figure 5.23 shows one example of successfully reconstructed muon, where 3 3D points are used for this reconstruction and the $\chi^2 = 0.5$.

In order to study the accuracy of the reconstruction algorithm, a metric is defined as the distance between the true and the reconstructed muon tracks at the level of the Water Pool (WP) bottom, since it gives the largest possible error that can be measured in the JUNO geometry. Such a distance is called "distance true-reco". Another metric is
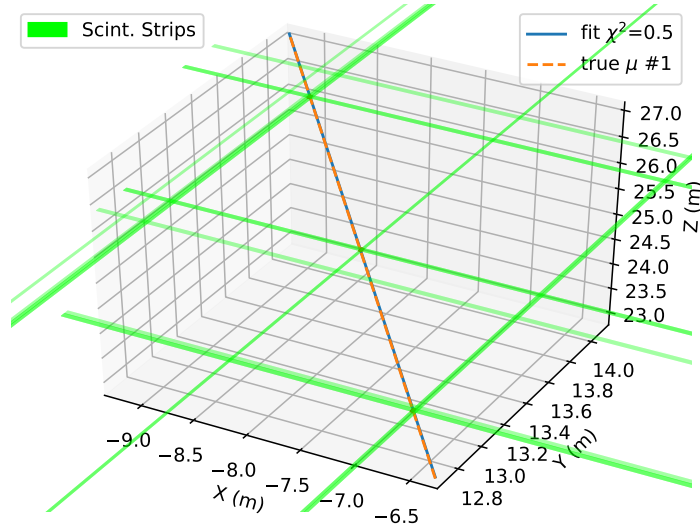
Figure 5.23 – An example of the sucessful muon reconstruction. Blue solid line is the reconstructed muon track, and the orange dashed line is the true muon track. The cyan bands illustrate the triggered TT scintillator strips.
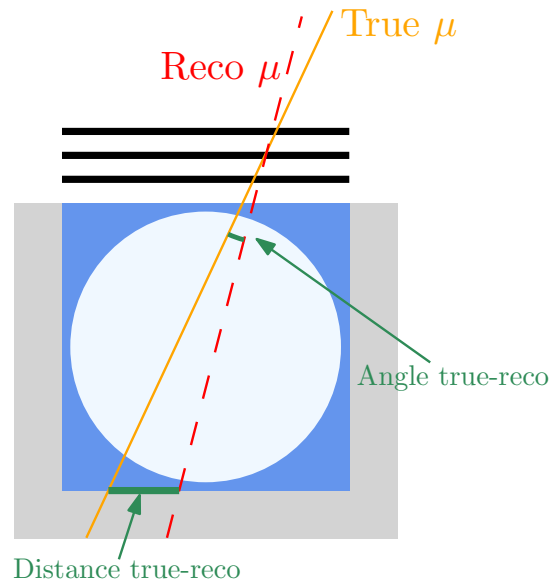

Figure 5.24 – Illustration of the definitions of "distance true-reco" and "angle true-reco".
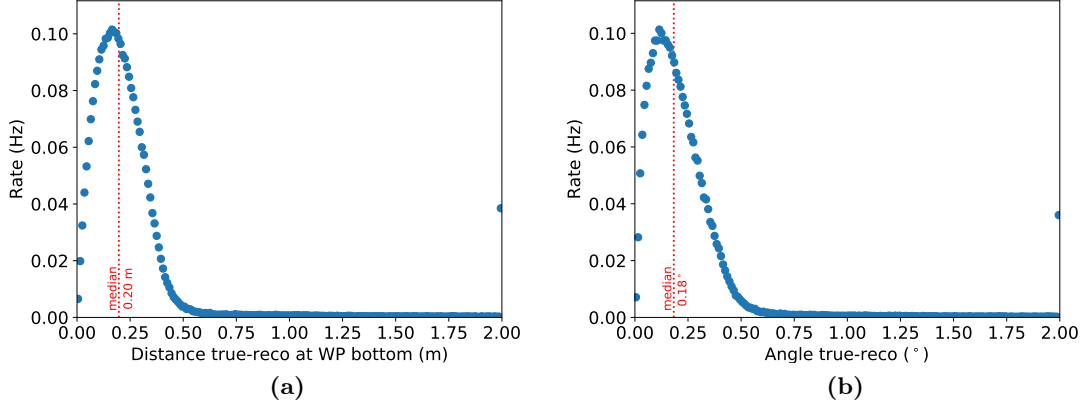
Figure 5.25 − Distributions of (a) distance true-reco at WP bottom and of (b) angle true-reco, obtained from pure muon events. All reconstructions that have a distance true-reco or an angle true-reco larger than 2 m and 2° are put into the overflow bin.

the angle between the true muon track and the reconstructed one, which is called "angle true-reco". An illustration of the definitions of both distance true-reco and angle true-reco is shown in Figure 5.24. From the schematic, we can see that these two metrics are actually correlated. In Figure 5.25, we show the distribution of distance true-reco and of angle true-reco. From these distributions, we calculate the median distance true-reco to be 0.20 m, and the median angular resolution to be 0.18°.

The reconstructed muon rate is 2.97 Hz, given that the rate of muons that cross 3 layers is 3.02 Hz, the reconstruction efficiency obtained with pure muon events is estimated to be 98%. In addition, we have found that 2% of tracks have a distance true-reco larger than 1.5 m.

5.7 Event mixing and trigger simulation

TT energy deposits due to atmospheric muons and different isotopes are simulated separately in the official MC, and we must mix them to obtain realistic TT events. Event mixing is important for estimating accidental coincidences generated by decays. Additionally, the L1 and L2 triggers should be considered in the simulation. As the official MC implements neither event mixing nor TT triggers, the "SCD" software was developed as a necessary tool for the studies in this thesis, of which results will be unveiled in Section 5.8. So far, SCD is made to work outside the scope of official MC. Once the study of trigger algorithms is finalised, the relevant functionality of SCD will be merged into the official MC.

We separated two main simulation chains as "TT radioactivity simulation" and "TT muon simulation". Figure 5.26 shows how they are implemented. Except for SCD itself, the other simulation steps are always realised with the official JUNO software.

For the TT radioactive background studies, we always use the TT radioactivity simulation. 10^9 decays have been simulated with the official MC for each of the three isotopes (U/Th/K). The isotope data is subsequently input into SCD for event mixing. In the U/TH/K decay samples, since they are simulated independently, the time $t = 0$ is always the moment when a decay happens. From this starting time, different t for hits caused by this decay are registered. So the task of the event mixing is to assign a

Figure 5.26 – Implementation of TT radioactivity simulation and TT muon simulation.

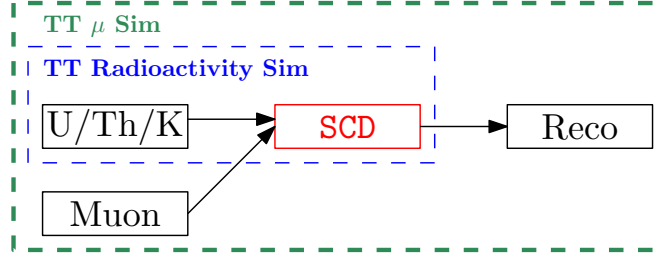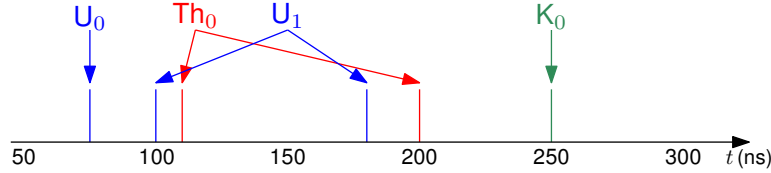**Figure 5.27** – An example timeline of energy deposits (TT hits) after the event mixing, where two U-decays, one Th-decay, and one K-decay are mixed. Each spike represents one TT hit.

starting time offset to each decay and its corresponding hits. The starting time offset is calculated for every decay event such that the decay time distributions are uniform with the same decay rate as in Table 5.1. Figure 5.27 shows an example timeline after the event mixing, with the purpose of illustrating the procedure. By mixing the decay events, all TT hits can be found on a common timeline, which simplifies the simulation of the TT triggers. For the decay samples that we use, the simulated number of decays corresponds to a real simulated livetime of 82 ms after the event mixing.

For the studies on the reconstructed muon rate and the reconstruction accuracy, the TT muon simulation is a must. However, the event mixing between muons and isotopes has an intrinsic difficulty: the real muon rate is smaller than the decay rate by 10 orders of magnitude. To overcome this difficulty, we insert muons with a much higher frequency, at equal time interval. As a consequence, we will have to afterwards re-weight these events properly to retrieve the muon event rates.

For all TT muon simulations in this thesis, 10^5 muons have been simulated, which is equivalent to a simulated livetime of 2.8 h. In SCD, the muons are mixed with isotope decays at the rate of one per 15 μs. Even with muons separated by 15 μs, we would still need 1.5 s of radioactivity simulation for this livetime. While it is not easy to produce so much radioactive decays, we reused the sample of 82 ms for the mixing with muons.

In addition to the event mixing, SCD simulates the L1 and L2 triggers, and outputs the digitalised PMT signals. Unlike the official MC, the crosstalk between PMT channels is not simulated in SCD, because it is not related to the trigger algorithms that are based on FAST-ORs. By default, L1 simulation uses the timeline shown in Figure 5.5, i.e. the PMT threshold is 1/3 p.e., the L1 time window length 200 ns, the L1 transit time 50 ns, and the MAROC3 RESET transit time 50 ns. Regarding the L2 trigger, the time window is 300 ns, and the transit time between the L2 trigger and the L1 trigger is 200 ns.

In case we want to study only the L1 trigger, instead of restructuring the program, we simply let L2 trigger accept all L1 trigger outputs in the given L2 coincidence time window. In other words, the L2 is always there, but practically it is disabled, as it will never reject PMT FAST-ORs and reset MAROC3s. In the following, this mode of the L2 trigger is referred to as "L2All".

Finally, the `SCD` output is processed by the official MC for muon track reconstruction.

5.8 Performance of the Top Tracker triggers

The main task of TT triggers is to reduce the background rate caused by the natural radioactivity in the cavern. At the same time, we would expect that good algorithms result in a good muon reconstruction efficiency, and do not impair the reconstruction accuracy. The studies on the performances of different L1 and L2 trigger configurations will focus on these points.

The TT has a two-level trigger, therefore, a trigger configuration is defined by the combination of the L1 trigger algorithm and the L2 trigger algorithm. To distinguish different trigger configurations in the study, we use a nomenclature for which all configurations are named A+B, where A is the L1 trigger algorithm and B is the L2 trigger algorithm. For example, a configuration using XY for L1 and 2L for L2, is labelled as XY+2L. The possible choices for the L1 algorithms are XY, XYo, XY3, XY⊥, and XY×. The possible choices for the L2 algorithms are 2L, 3W, Align, and L2All. In total, we have 20 different configurations to be studied. These algorithms have been described in extensive detail in Section 5.3 and Section 5.5.

5.8.1 Background rate reduction

Due to the high radioactivity level in the JUNO cavern, almost all PMT FAST-ORs sent to the CB are induced by radioactive decays. Figure 5.28 shows the distribution of the rate of FAST-ORs sent to the CB without taking into account the dead time.

The rates are grouped as 4 distributions: the bottom layer, the middle layer, the top layer, and the walls that are installed above the chimney. The radiation is emitted from the surrounding rock, and the top layer is not shielded, so it receives the highest average rate. The middle layer is shielded by the top layer, so its average rate is lower than the top layer one. The bottom layer is the farthest from the rock, and shielded by the top and the middle layers, so its average rate is the lowest among all three layers. Though the walls above the chimney are the closest to the rock on the ceiling, they are far away from the rock of the sides. So its average rate is higher than the bottom and the middle layer ones, but lower than the top layer rate.
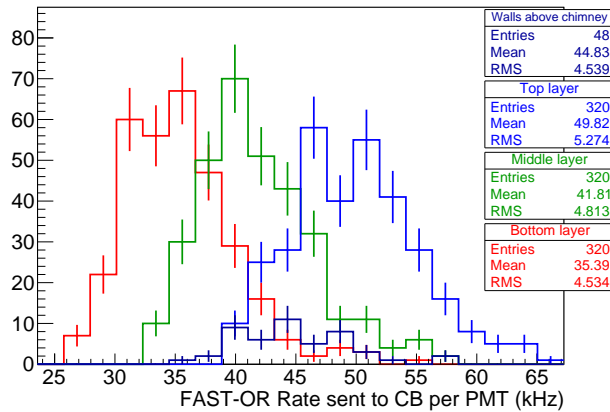
Figure 5.28 – The distribution of FAST-OR rate sent to CB per PMT without taking into account the MAROC3 charge readout dead time.

Walls above chimney	
Entries	48
Mean	5.619
Std Dev	0.7897
Top layer	
Entries	320
Mean	6.395
Std Dev	0.7518
Middle layer	
Entries	320
Mean	5.002
Std Dev	0.7251
Bottom layer	
Entries	320
Mean	4.061
Std Dev	0.6643
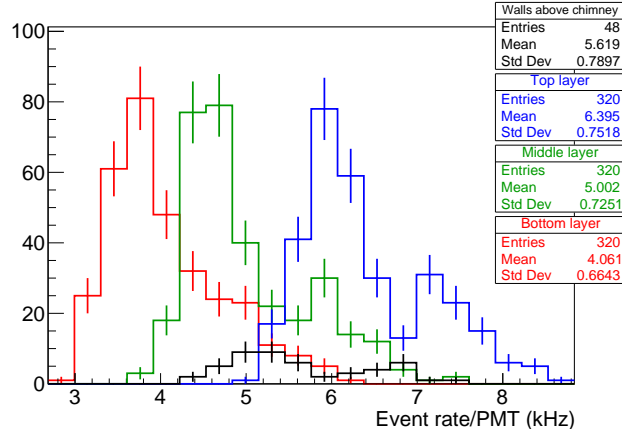
Figure 5.29 – Distributions of event rates on different PMTs of the trigger configuration XY+L2All.
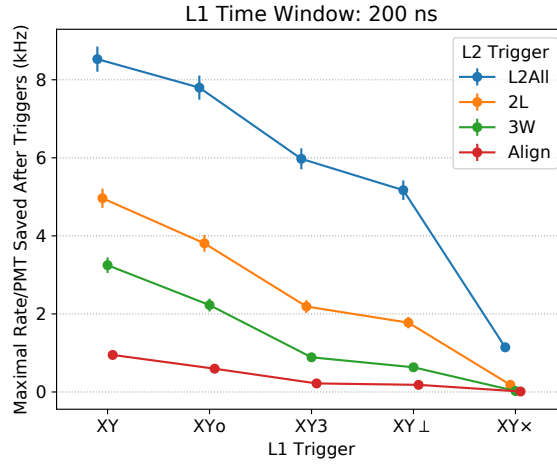
Figure 5.30 – Maximal event rates per PMT of different trigger configurations.

The maximal FAST-OR rate per PMT is given by PMTs on the top layer, and it about 65 kHz. Due to the 14 µs dead time for a MAROC3 to complete the charge readout of one PMT pulse, as shown in Figure 5.5, such a rate will cause a large dead time in MAROC3s, and thus muon hits are very likely to be missed. Moreover, most hits registered are simply due to radioactivity, which may cause fake muon tracks and reduce the reconstruction accuracy.

Even the minimal trigger configuration XY+L2All will help to reduce the background event rate. Figure 5.29 shows the background event rates on different PMTs for this configuration. The maximal event rate per PMT of XY+L2All is 8.5 ± 0.3 kHz. Compared to the configuration without any trigger, XY+L2All therefore reduces the maximal event rate per PMT by a factor of 4.

The same kind of analysis is performed for all possible trigger configurations and the resultant maximal event rates are shown in Figure 5.30. We notice from the plot that, when the configuration has more stringent conditions, the maximal event rate at PMT level will be reduced.

Lastly, we show the event rate of the whole TT with different trigger configurations in Figure 5.31. For the whole TT, the background event rate is at the level of MHz if
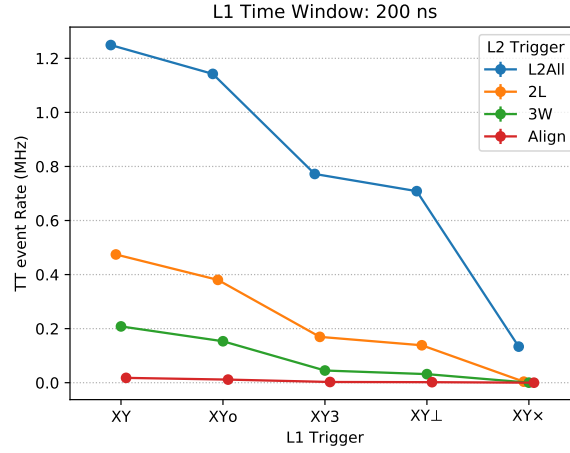
Figure 5.31 − Event rates of the whole TT with different trigger configurations.
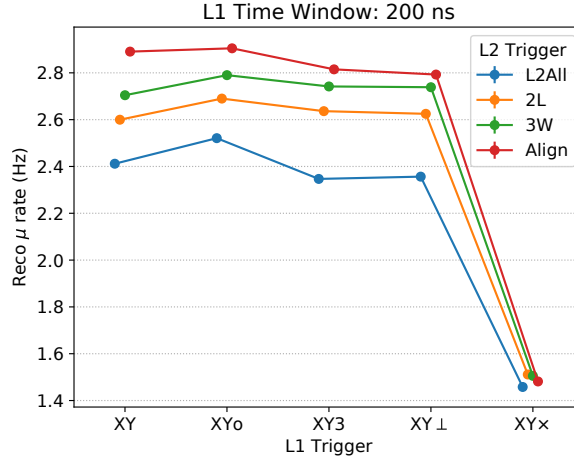
Figure 5.32 − The TT reconstructed muon rate of different trigger configurations.

only minimal trigger configuration XY+L2All is applied. For any L1 trigger algorithms, if we choose the strictest L2 algorithm "Align", the event rate can be reduced by at least two orders of magnitude with respect to the rate of "L2All".

5.8.2 Muon reconstruction efficiency

Assuming L1 and L2 triggers do not exist, we estimate the reconstructed muon event rate to be 0.78 Hz. Given the rate of muons that should be detected by the TT is about 3.02 Hz, the TT without trigger has a muon reconstruction efficiency of 26%. The low efficiency is attributed to the dead time. By reducing the background event rates, the triggers will help to recover the muon reconstruction efficiency. The results corresponding to different trigger configurations are shown in Figure 5.32.

We have found from Figure 5.32, except for the XY×, the other L1 algorithms have very close rates if the L2 algorithm is the same. Furthermore, the reconstructed muon rate increases as the L2 algorithm gets stricter and is almost independent of the applied L1 algorithm. This can be explained by the fact that, although L1 triggers help in reducing event rates and PMT dead time at the wall level, it is less efficient than
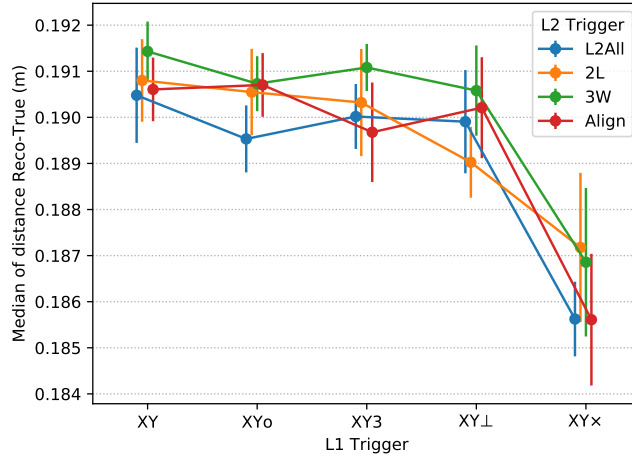
Figure 5.33 − Medians of distance true-reco obtained with different trigger configurations.

the L2 trigger for picking true muon events, since the muon events are more different from the radioactivity background for a global pattern. The XY+Align and XYo+Align configurations give the highest reconstruction muon rate at about 2.9 Hz. Given that the rate of muons crossing 3 TT layers is 3.0 Hz, this reconstruction muon rate is equivalent to a reconstruction efficiency of 97%. In case that the L1 trigger algorithm is XY3 or XY⊥, the efficiency will be slightly reduced to 93%.

When the L1 algorithm is set to be XY×, the rates are nearly identical regardless of different L2 algorithms. In fact, XY× is a very strict algorithm at the wall level, so muon events are not much contaminated with radioactivity hits. In this case, the L2 trigger cannot help to remove more radioactivity hits from the event, and it explains why the L2 algorithms do not change the reconstructed muon rate. Apparently, XY× rejects also a significant fraction of muon hits, resulting in a reconstructed muon rate much lower than for any other trigger configurations.

5.8.3 Muon reconstruction accuracy

In addition to maximising the muon detection efficiency, it is also important to check if the trigger configurations would have an impact on the reconstruction accuracy. All TT events obtained with different trigger configurations are reconstructed, and the median distance true-reco of different configurations is calculated in the same way as the one shown in Figure 5.25(a). Figure 5.33 shows the median distances true-reco for all configurations. By considering the statistical uncertainty of the median resolutions, all configurations have a similar median resolution of about 19 cm, or equivalently a median angular resolution of 0.20° given in the same simulation. Compared with Figure 5.25, the accuracy with triggers is at the same level as if only pure muon events are used for the reconstruction. Therefore, the 2-level trigger has no impact on the reconstruction accuracy.

5.9 Summary

As all L1 triggers must be implemented on the Concentrator Board (CB) FPGA, it is necessary to make sure that all L1 trigger algorithms that we considered are actually compatible with the hardware. A test bench was therefore designed to demonstrate the

functionality of XYo trigger logic on the CB FPGA. The XYo trigger was implemented successfully, and since it is the most complicated L1 trigger algorithm, we foresee no difficulty for the implementation of the others.

Following this, we have studied the performances of different trigger configurations by using MC simulations. The results show firstly that the triggers can reduce the background event rate, and the resultant background rate is always lower for configurations with stricter coincidence requirements. But it is not always true that "the stricter, the better". When we studied the muon reconstruction efficiency. the strictest L1 algorithm XY× was shown to have poor efficiency. In this study, we have found that the reconstruction efficiency is more sensitive to the L2 trigger algorithm than to the L1 trigger algorithm with the exception of the very strict XY× coincidence. With the L2 trigger algorithm "Align", the reconstruction efficiency is estimated to go as high as 97%. Regarding the reconstruction accuracy, we have shown that all trigger configurations have very similar performances, with a median distance true-reco of 19 cm, or equivalently a median angular resolution of 0.20°. Lastly, by comparing this accuracy with the one shown in Section 5.6, where only pure muon events are involved, we prove that the L1 and L2 triggers do not worsen the TT muon tracking precision.

By summarising the results from these studies, we propose that the optimised configuration can be XY⊥+Align. As shown in Figure 5.34, it reduces largely the background by more than 3 orders of magnitude. This level of background makes it much easier to finalise the readout system design with a capacity to handle the data streaming. It is worth noticing that, after performing the offline reconstruction, no surviving background of XY⊥+Align is found successfully reconstructed in our sample, and in the figure, the upper limit at 90% of confidence level is shown. Besides, the XY⊥+Align configuration will not be difficult to be implemented on the FPGA-based hardware. From the results of previous studies, we expect that this configuration lets the TT have a muon reconstruction efficiency of about 93% and a median angular resolution of 0.20°. In the figure, the rates obtained with pure muon events are also shown to reveal that the selections barely decrease the true muon event rates.
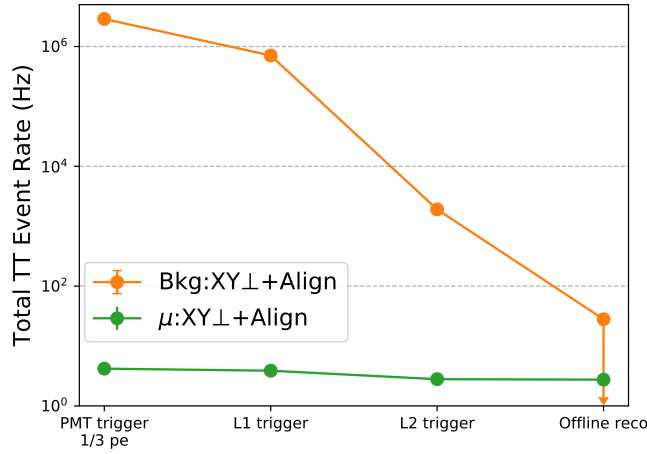
Figure 5.34 – The total TT event rates in each step of background suppression for the configuration XY⊥+Align obtained with radioactive background events (orange). The steps include the PMT trigger, L1 trigger, L2 trigger, and the offline reconstruction. For reference, the rates obtained with pure muon events are also shown for each step (green). The rate given after the offline reconstruction for radioactive background events is the upper limit at 90% confidence level.

Chapter 6

Muon-induced background study with the Top Tracker

The muon spallation process is an interaction between a high energy muon and a nucleus via an exchange of a virtual photon, which can produce neutrons and pions. A Feynman diagram describing this interaction is shown in Figure 6.1.
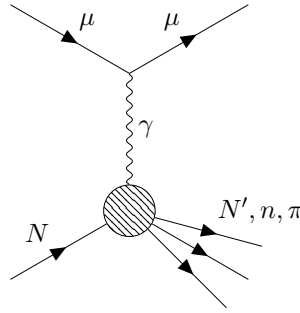
Figure 6.1 – Feynman diagram of the muon spallation process, N denotes a nucleus.

JUNO will be built underground such that most atmospheric muons cannot reach the detector. Nevertheless, a few hertz of atmospheric muons carrying the high average energy of $\sim 200\,\mathrm{GeV}$ can still enter the detector and cause muon spallation on nuclei. Due to its abundance in the liquid scintillator (LS), the reactant nucleus is usually ^{12}C. The spallation neutrons and the cosmogenic radioisotopes produced in such processes form then backgrounds of the JUNO inverse beta decay (IBD) detection. Since both backgrounds are induced by muons, they are also referred to as muon-induced background.

To reject the cosmogenic isotope background as explained in Section 2.3.1, a veto volume must be set along the muon tracks, so achieving efficient muon reconstruction becomes a key question. For an easier understanding of this question, we first classify the muons according to the part of the detector that they pass through: the muons crossing the Central Detector (CD) are called "CD muons", the muons passing only through the Water Pool (WP) with a track length greater than 0.5 m are called "WP muons". The muons crossing the WP but with a track length less than 0.5 m are named "corner clipping muons". The corner clipping muons are not detectable by the Water Cherenkov Detector (WCD), due to the short tracks producing insufficient Cherenkov photons. Any other muons not in the aforementioned categories are named "rock muons", and like the corner clipping muons, they are not detectable by neither the CD nor the
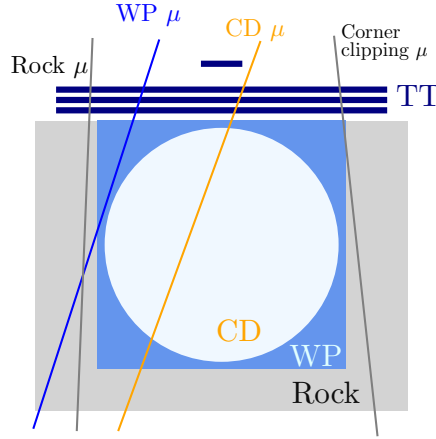
Figure 6.2 – Schematic picture of example muon tracks in all categories: CD muon, WP muon, corner clipping muon, and rock muon.

Table 6.1 – Summary of contributions of muons in each category to the muon-induced background in JUNO.

	CD	WP	Corner clipping or Rock
Cosmogenic	Main producer	little contribution	no contribution
Fast neutron	little contribution	little contribution	Main producer

WCD. A schematic picture is shown in Figure 6.2 to give an example muon track for each category.

Depending on the muon category, they have different contributions to the muon-induced background. Before going into details, Table 6.1 summaries these contributions.

For most of the CD muons, the CD itself is already a good muon tracker. But for stopping muons, the track reconstruction is more difficult [174]. At the same time, the Top Tracker (TT) can detect a large fraction of CD muons with a more precise track reconstruction, including stopping muons. The amount of muons that can be detected by the TT depends on the selection criteria. As for Chapter 5, we require at least 3 triggered TT layers to consider that a muon event is detected. The CD muons are the dominant producers of cosmogenic isotope background. When a CD muon is detected, according to the muon veto criteria in Section 2.3.2, all events within 1.5 ms after the detection will be rejected. Most spallation neutrons should be thermalised and captured in the veto time window, therefore, almost no spallation neutron will contribute to the background after the veto.

WP muons can produce also cosmogenic isotopes and thus induce background. For the WP muons, the CD cannot help for their track reconstruction. The WP muons can be tagged by the WCD, but the spatial resolution in the WCD is estimated to be about 0.5 m, which is not sufficient to be used for the muon reconstruction. Even though the WP muons induce much less background than CD muons, this background is not negligible. As Figure 6.3 shows, the TT partially covers the WP, therefore, it can be used to track WP muons and to measure the residual background in the CD after applying the fiducial volume cut. Same as CD muons, WP muons do not induce spallation neutron background because the time veto of the whole LS volume will be applied every time a WP muon is tagged by the WCD.

Because the muon tracks are far away from the CD, the corner clipping muons and

the rock muons will not contribute to the cosmogenic isotope background. However, as the corner clipping and the rock muons cannot be detected by the CD or the WCD, the time veto of the whole LS volume is not applicable. Without this veto, the spallation neutrons with sufficient energy, i.e., fast neutrons, can enter the CD and generate IBD background events.

The TT covers partially the top rock, as illustrated in Figure 6.3, and the regions covering the surrounding rock have a sensitive area of $68\,\mathrm{m}^2$, about 7% of the total TT sensitive area. Consequently, the TT is the only detector in JUNO that can tag and measure the fast neutron events induced by the corner clipping or the rock muons. Given that the MC prediction for the fast neutrons produced by these "invisible" muons is not considered reliable, the measurement performed by the TT will provide the unique experimental data for JUNO to reduce this systematic uncertainty.

We will first focus on the contribution from the TT to suppress the cosmogenic isotope background in Section 6.1. After this, we will show in Section 6.2 that it is possible to perform a measurement of cosmogenic isotope lateral distance profile with the muon direction information exclusively measured by the TT. Finally, in Section 6.3, the fast neutron background is studied in order to estimate its rate in JUNO and the TT performance for its measurement.

6.1 Muon tracking for cosmogenic isotopes

In Chapter 2, we have introduced that ^{9}Li ($T_{1/2} = 178\,\mathrm{ms}$, $Q = 13.6\,\mathrm{MeV}$) and ^{8}He ($T_{1/2} = 119\,\mathrm{ms}$, $Q = 10.7\,\mathrm{MeV}$) are the cosmogenic isotopes forming an important IBD background. In fact, many more isotopes than ^{9}Li and ^{8}He are produced by such a mechanism in the LS. Table 6.2 summaries the radioactive properties (Q values, branching ratios, half-lives) of all cosmogenic isotopes that can be produced in the CD, and their estimated production rates. Most cosmogenic isotopes are not directly relevant to the IBD background, only those marked in red in Table 6.2 are potentially IBD background sources because they have a $\beta^- n$ decay mode. Among the relevant isotopes, ^{9}Li and ^{8}He have the largest estimated rates in the CD and the longest half-lives. Their Q values also allow them to emit electrons with energies that are inside the prompt energy selection range. All these features make ^{9}Li/^{8}He the most dangerous background for the IBD detection in JUNO, and we will only consider these cosmogenic isotopes in the following discussion.

The simplest way to reduce the background from cosmogenic isotopes is to do a time veto on the whole LS volume after a muon crosses the CD. Based on the measurements in KamLAND [146], we calculated that a veto time of $1.2\,\mathrm{s}$ can reject 99% of total isotopes produced by the muon. However, this veto will cause a nearly 100% dead time of the CD, given that the muon rate is estimated to be about $4\,\mathrm{Hz}$. Fortunately, the vertices of cosmogenic isotope background events are strongly correlated to the parent muon tracks. KamLAND [146] and Borexino [176] results suggest that the lateral distance from the background events to muon tracks should follow approximately an exponential distribution. A veto volume with $3\,\mathrm{m}$ around the parent muon track seems to be a good choice to reject most background as described in Section 2.3.1. This approach does not decrease too much the CD's active time-volume. Only the badly reconstructed tracks will requires a whole LS veto with a duration of $1.2\,\mathrm{s}$. The resultant IBD efficiency is estimated to be 83%.

To study the TT contribution to the ^{9}Li/^{8}He background suppression, we will use a MC sample generated by the JUNO official MC , with a livetime corresponding to

Table 6.2 – The Q values, branching ratios of major decay modes, and half-lives $T_{1/2}$ of the cosmogenic isotopes that can be found in the CD. The estimated rates of the isotopes are from JUNO's MC study [118]. The decay modes and Q values are from TUNL Nuclear Data Group [175].

Isotopes	Q (MeV)	$T_{1/2}$	Rate (per day)
^{3}H	0.0186 (β^-)	12.31 year	1.14×10^4
^{6}He	3.508 (β^-)	0.807 s	544
^{7}Be	Q_{EC}=0.862 (10.4% γ, $E_\gamma = 0.478$)	53.22 day	5438
^{8}He	10.66 ($\beta^-\gamma : 84\%$), 8.63 ($\beta^-n : 16\%$)	0.119 s	11
^{8}Li	16.0 (β^-)	0.839 s	938
^{8}B	16.6 (β^+)	0.770 s	225
^{9}Li	13.6 ($\beta^- : 49\%$), 11.94 ($\beta^-n : 51\%$)	0.178 s	94
^{9}C	15.47 ($\beta^+p : 61.6\%, \beta^+\alpha : 38.4\%$)	0.126 s	31
^{10}Be	0.556 (β^-)	1.51e6 year	1419
^{10}C	2.626 ($\beta^+\gamma$)	19.29 s	482
^{11}Li	20.55 ($\beta^-n : 83\%, \beta^-2n : 4.1\%$)	0.00875 s	0.06
^{11}Be	11.51 ($\beta^-\gamma : 96.9\%$), 2.85 ($\beta^-\alpha : 3.1\%$)	13.76 s	24
^{11}C	0.960 (β^+)	20.36 min	1.62×10^4
^{12}Be	11.708 ($\beta^-\gamma$, $\beta^-n : 0.5\%$)	0.0215 s	0.45
^{12}B	13.37 ($\beta^-\gamma$)	0.0202 s	966
^{12}N	16.316 ($\beta^+\gamma$)	0.0110 s	17
^{13}B	13.437 ($\beta^-\gamma$)	0.0174 s	12
^{13}N	1.198 (β^+)	9.965 min	19
^{14}B	20.644 ($\beta^-\gamma$, $\beta^-n : 6.1\%$)	0.0126 s	0.021
^{14}C	0.156 (β^-)	5730 year	132
^{15}C	9.772 (β^-)	2.449 s	0.6
^{16}C	8.010 ($\beta^-n : 99\%$)	0.747 s	0.012
^{16}N	10.42 ($\beta^-\gamma$)	7.130 s	13
^{17}N	8.680 ($\beta^-\gamma : 5\%$), 4.536 ($\beta^-n : 95\%$)	4.173 s	0.42
^{18}N	13.896 ($\beta^-\gamma : 93\%$), 5.851 ($\beta^-n : 7\%$)	0.620 s	0.009
neutron			155 000

497 running days. A precise modelling of the cosmogenic isotope production is very difficult and beyond the scope of this thesis. We simply normalised ^{9}Li and ^{8}He yields per muon in the official MC to the measured yields in KamLAND [146], and obtained the ^{9}Li and the ^{8}He production rates in JUNO. Finally, the ^{9}Li and the ^{8}He production rates in the CD are estimated to be 179.9 ± 0.9 and 69 ± 1 per day, respectively. Only the limited number of events in the MC is considered to calculate the errors.

From Table 6.2, ^{8}He decays to neutron-unstable excited states of ^{8}Li with a 16% branching ratio, and ^{9}Li decays to neutron-unstable excited states of ^{9}Be with a 51% branching ratio. With these branching ratios, we estimate that the IBD background rate in JUNO from ^{9}Li is 91.7 ± 0.5 per day, and from ^{8}He is 11.0 ± 0.2 per day. Summing these 2 numbers, we estimate a background rate of 102.8 ± 0.6 ^{9}Li/^{8}He events per day. This result is consistent with the rates estimated in previous studies for JUNO that used different approaches and simulation tools [118, 177].

6.1.1 Geometrical effects of muon reconstruction accuracy

The muon veto volume is a cylinder with a fixed radius along the muon track, with radius set to 3 m. Figure 6.4 shows the lateral distance profile obtained from the simulation. For IBD background events, the isotope production vertices found with a lateral distance greater than 3 m from the real muon tracks correspond to 1.1% of the total number of isotopes found in the CD. But in reality, we do not have access to the true muon tracks, only to our reconstructed tracks using the information of the TT and the CD.

To give a first estimation of the degradation due to the muon reconstruction, we simulate the reconstructed tracks by tilting and shifting the true tracks in a toy MC. Figure 6.5 illustrates how a true muon track is transformed after reconstruction. The new track is tilted by an angle α and shifted by a distance D from the original track. By using α and D, the new track is defined always on the same plane as the original one. To make the new track free in a 3D space, we choose random azimuth angles for α and for D turning the new track around the true muon track.

This study is aimed to reveal a general relation between the reconstruction accuracy and the ^{9}Li/^{8}He residual rate after the muon veto, so the smearing is done for all muon tracks. Since most muon tracks relevant to the ^{9}Li/^{8}He background are reconstructed by the CD, this smearing is based on results from CD muon tracking studies in [131], where we consider that the tilt angle α and the shift distance D follow roughly Gaussian distributions $\mathcal{N}(\langle\alpha\rangle, \langle\alpha\rangle/2)$ and $\mathcal{N}(\langle D\rangle, \langle D\rangle/2)$, with $\langle\alpha\rangle$ and $\langle D\rangle$ being the mean angular resolution and the mean resolution of the lateral distance. The values of $\langle\alpha\rangle$ and $\langle D\rangle$ are chosen in the $0° < \langle\alpha\rangle < 9°$ and $0\,\mathrm{m} < \langle D\rangle < 0.6\,\mathrm{m}$ ranges.

After the transformation, the lateral distance profile shown in Figure 6.4 will be recalculated and the percentage of ^{9}Li/^{8}He with a lateral distance greater than 3 m will also be changed. In Figure 6.6, we show the percentage of ^{9}Li/^{8}He that is produced with a lateral distance to the parent muon tracks larger than 3 m, as a function of $\langle\alpha\rangle$. The value $\langle D\rangle$ used is represented in the colour scale. The plot shows that, by only taking into account the geometrical effects, the degradation of the veto efficiency remains at the level of 1% for an angular resolution below 3°. But this number increases very rapidly for higher values of the angular bias. This confirms that a better reconstruction accuracy is helpful for further reducing the residual ^{9}Li/^{8}He background events. The plot also shows that a larger shift distance always leads to a worse efficiency for any given $\langle\alpha\rangle$, although this effect is not dominant.

This residual background rate can affect the final νMH sensitivity. By performing νMH fits with different ^{9}Li/^{8}He background event rate, we show in Figure 6.7 that
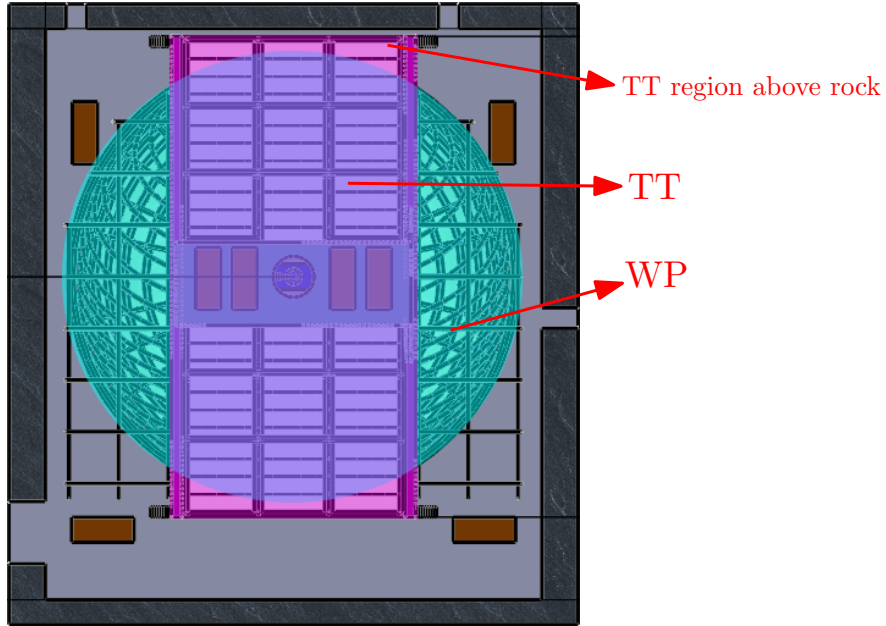
Figure 6.3 – Top view of the TT (magenta) and the WP (cyan).
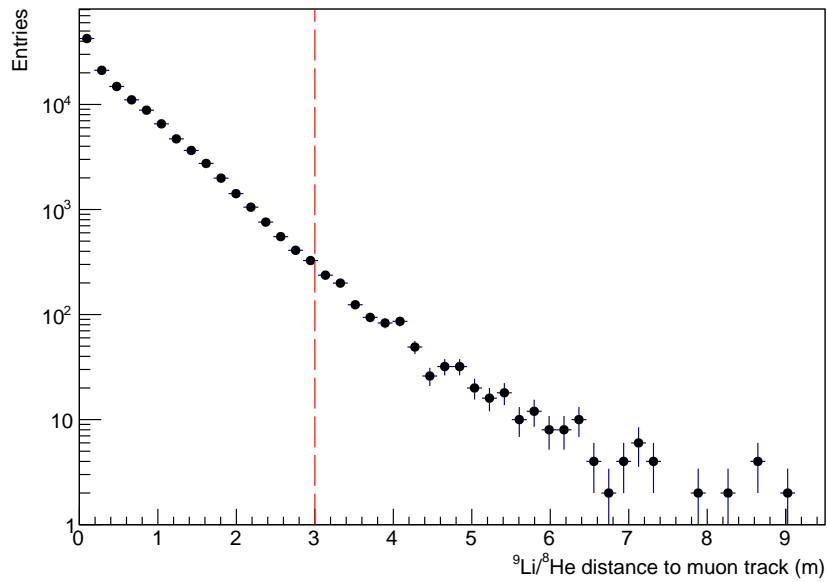
Figure 6.4 – Lateral distance profile of the ^{9}Li/^{8}He vertices obtained from the simulation using JUNO official MC. The vertical red dashed line represents the radius of muon veto volume at $3\,\mathrm{m}$.
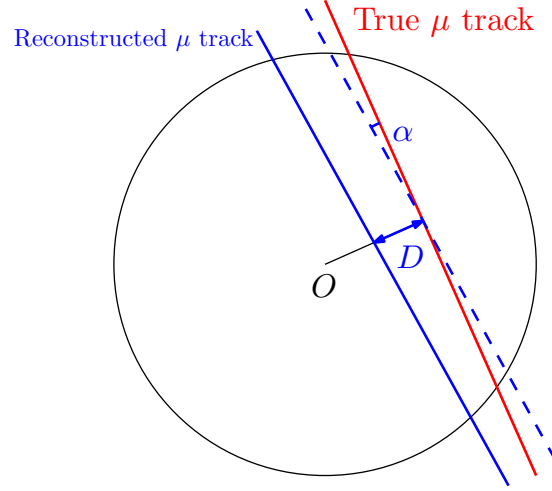
Figure 6.5 – 2D schematic view of the transformation from "true muon track" to "reconstructed muon track" used in our toy MC.
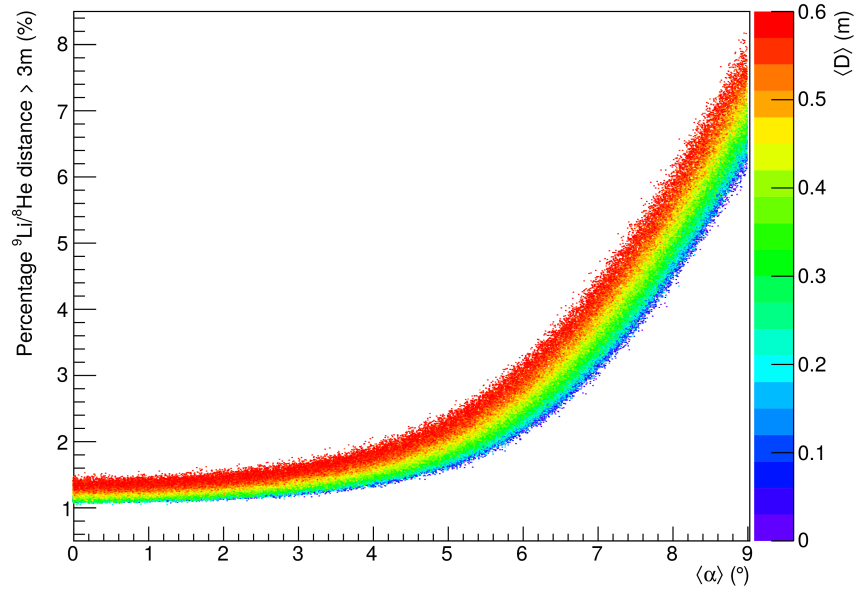
Figure 6.6 – Percentage of ^{9}Li/^{8}He of which the production vertices are found with a lateral distance larger than 3 m, as a function of $\langle \alpha \rangle$. The colour shows the value of $\langle D \rangle$ used in each calculation.
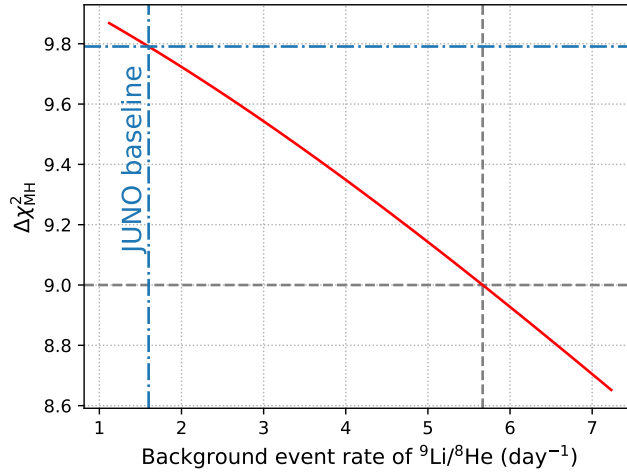
Figure 6.7 – νMH sensitivity $\Delta\chi^2_{\mathrm{MH}}$ as a function of ^{9}Li/^{8}He background event rate. The horizontal grey dashed line marks the νMH sensitivity at 3σ, and the grey vertical line marks the corresponding ^{9}Li/^{8}He background rate, which is 5.7 per day. The blue vertical and horizontal dashed lines represent the JUNO baseline estimation of the ^{9}Li/^{8}He background rate [118], and the corresponding νMH sensitivity, respectively.

$\Delta\chi^2_{\mathrm{MH}}$ drops as the background rate increases. It shows also that, if JUNO has more than 5.7 ^{9}Li/^{8}He background events per day remaining after all cuts, the sensitivity will be below 3σ for 6-year of data.

6.1.2 Cosmogenic isotope background induced by CD muons

From our simulation, we estimated the CD muon rate to be 4.6 Hz. 34% of the total number of CD muons are detected by the TT, which is equivalent to a rate of 1.5 Hz.

A CD muon reconstruction method currently being developed reports a median angular resolution of 1.6° [131]. The CD may also have difficulties to reconstruct muon tracks in complicated situations, such as for stopping muons or the muons that induce showers in the CD.

In any case, the tracking information from the TT is important for the CD muon reconstruction. Firstly, the muons tracked by the TT will be used as a calibration source for the CD. Moreover, the angular resolution of the CD muon tracking deteriorates significantly when the muon incident is at large radius, due to the short tracks. For the same reason, the detection efficiency is also much reduced at the CD edge. As the TT has a different geometry, it can help to recover partially this lost accuracy and efficiency. Finally, the TT helps for the reconstruction of complicated muon tracks, including stopping muons and CD showering muons. Especially, the precise reconstruction of CD showering muons is extremely important for the background veto, as the majority of ^{9}Li/^{8}He are produced by them [146].

From our simulation, the background event rate for ^{9}Li by CD muons is estimated to be 91.1 ± 0.4 per day, and for ^{8}He 10.9 ± 0.2 per day. Among them, the TT can tag 30.1 ± 0.2 ^{9}Li per day, and 3.6 ± 0.1 ^{8}He per day. This result means that 33% of the total ^{9}Li/^{8}He produced by the CD muons can be rejected with the TT muon tracking.

We can compare this ratio obtained in our simulation with the ratio estimated with the empirical formula written as

$$R_{\mathrm{Li/He}} \propto \langle E_\mu \rangle^{0.74} \cdot L_\mu \cdot R_\mu \cdot f_{\mathrm{n-Cap}}, \qquad (6.1)$$
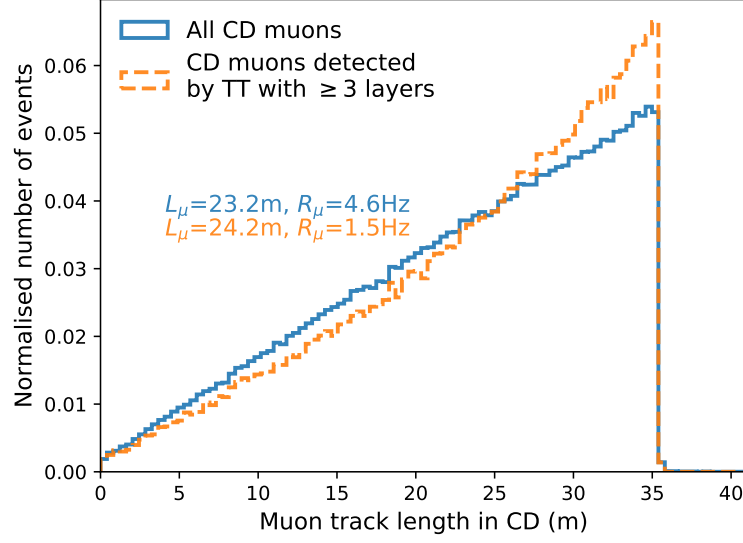
Figure 6.8 – Distributions of all CD muons and of the CD muons that are detected by the TT. Both distributions shown are normalised to have the integral equal to 1.

where $\langle E_\mu \rangle$ is the muon average energy, L_μ is the average track length in the CD, R_μ is the muon rate in the CD, and $f_{\mathrm{n-Cap}}$ is the neutron capture ratio, which is assumed to be 1 in JUNO. This formula with an exponent 0.74 [178–180] has been commonly used within the JUNO collaboration for the estimation of the background rate due to the cosmogenic isotopes.

In the simulation, the average CD muon energy is $250\,\mathrm{GeV}$, and the average energy of CD muons that are detected by the TT is slightly lower, $231\,\mathrm{GeV}$. Because of the TT geometry, the TT tends to detect more muons that pass the CD vertically. Therefore, the average track length of TT detected CD muons is slightly longer than the average of all CD muons, as shown in Figure 6.8. The average track length is $23.2\,\mathrm{m}$ for all CD muons, and $24.2\,\mathrm{m}$ for TT detected CD muons. By using the empirical formula (6.1), we obtain a ratio $R_{\mathrm{TT+CD}}/R_{\mathrm{CD}}$ equal to 32%, which is similar to the simulation result of 33%.

6.1.3 Cosmogenic isotope background induced by WP muons

The rate of WP muons is $5.5\,\mathrm{Hz}$, and the one of TT detected WP muons is $1.3\,\mathrm{Hz}$, namely 24% of total WP muons are also detected by the TT.

The simulation shows that the WP muons generate 0.65 ± 0.03 ^{9}Li background events per day, and 0.047 ± 0.004 ^{8}He background events per day. In total, the WP muon-induced ^{9}Li/^{8}He background rate is of 0.7 per day. As shown in Figure 6.9, most vertices are found at the edge of the CD, therefore, the fiducial volume cut at $17\,\mathrm{m}$ removes most background events. 0.2 background events per day survive this cut, corresponding to 27% of the total WP muon-induced ^{9}Li/^{8}He background rate.

As the TT covers partially the WP, it is possible that the TT detects the WP muons that induce fake IBD events in the CD. From the simulation, we estimate that, the TT can tag in average 0.03 ^{9}Li/^{8}He background events from WP muons in the fiducial volume per day, i.e., 15% of total WP muon-induced background events in the fiducial volume. However, given that the IBD-like event rate is 63.8 per day, this measurement can be difficult due to the accidental coincidence between a TT detected muon and a
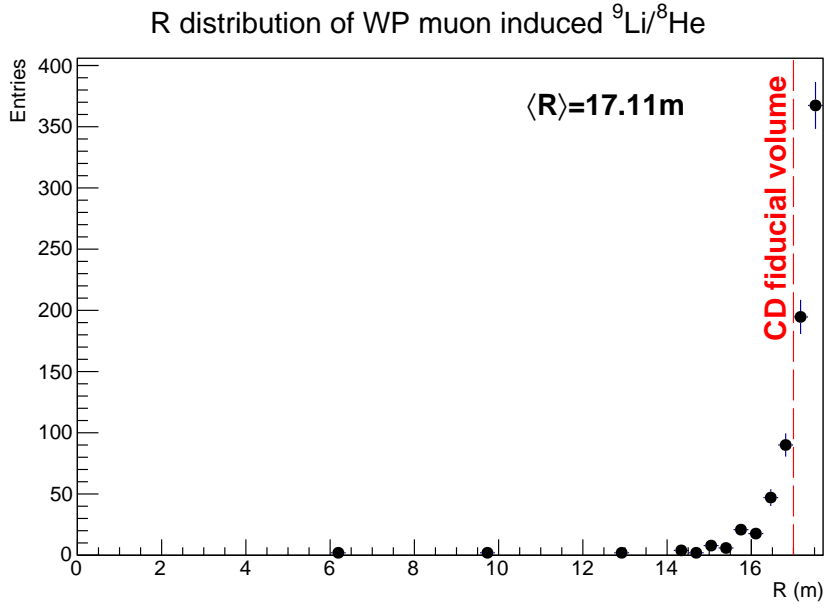
Figure 6.9 – Distribution of ^{9}Li/^{8}He vertex radius R for WP muons. The left side of the red dashed line presents the fiducial volume of 17 m radius.

Table 6.3 – ^{9}Li/^{8}He background rate in the fiducial volume for all CD/WP muons and for CD/WP muons that are detected by the TT. Rates are given in events per day. Errors are statistical only.

	CD muons	WP muons	total
All	90.9 ± 0.6	0.19 ± 0.02	91.1 ± 0.6
TT detected	28.2 ± 0.3	0.03 ± 0.01	28.2 ± 0.3
Percentage of TT detected	31%	16%	31%

real IBD event.

Table 6.3 summarises the estimated ^{9}Li/^{8}He background rate for all CD/WP muons and for CD/WP muons that are detected by the TT, after applying the fiducial volume cut at 17 m. The TT muon detection efficiency is set to 93%, corresponding to our study in Chapter 5.

6.2 Measurement of cosmogenic isotope lateral distance profile

Besides improving the muon tracking for a better ^{9}Li/^{8}He background suppression, the TT can also perform a ^{9}Li/^{8}He measurement by combining the TT tracking information and vertices measured in the CD for the produced isotopes. As the TT muon reconstruction has very good accuracy with an angular resolution of 0.2°, we expect that such a measurement can provide a precise lateral distance profile of ^{9}Li/^{8}He events. This improved lateral distance profile can contribute to a better precision for the estimation of the remaining ^{9}Li/^{8}He background outside the veto volume.

In order to perform the measurement with only the TT tracking information, we consider that all muons in an event must be detected by the TT. Events of this kind are

called "TT muon events". The simulation shows that, 23.4 ± 0.2 ^{9}Li/^{8}He background events per day are found in TT muon events, and thus can be studied with the tracking information measured only by the TT. Among them, 20.9 ± 0.2 per day are inside the fiducial volume, which is equivalent to 23% of total ^{9}Li/^{8}He background events in the fiducial volume. It must be noticed that, due to the selection criteria of TT muon events, we cannot tag as many ^{9}Li/^{8}He events as the rate shown in Table 6.3. However, the statistics of a measurement with only TT muon events should still be sufficient to determine the lateral distance profile within a reasonable measurement time.

First, we wanted to evaluate if the lateral distance profile obtained from TT muon events is biased from the true profile or not. Figure 6.10(a) shows a simulation of both the true profile and the one obtained from TT muon events only. The ratio between two profiles is then exhibited in Figure 6.10(b), where the fit of a flat distribution confirms that the two profiles have the same shape.

After this check, starting from the MC true profile, we smear the muon tracks according to the reconstructed sample that is obtained with the TT described in Section 5.8.3. The ^{9}Li/^{8}He vertices are also smeared by using a spatial resolution of $10\,\mathrm{cm}$ to simulate the CD vertex reconstruction. Finally, a muon detection efficiency of 93% that is constant everywhere on the TT is considered. The resultant profile is shown in Figure 6.11(a). From the ratio between the two distributions depicted in Figure 6.11(b), we see that the smeared distribution, i.e., "TT measured" distribution, does not exactly reproduce the true distribution for short distances ($< 300\,\mathrm{mm}$), due to the uncertainties of the vertex reconstruction and the muon reconstruction. However, for distances larger than $300\,\mathrm{mm}$, the ratio is well described by a constant nearly at 1. This means that both distributions have again approximately the same shape. Based on the measured distribution, we will be able to directly estimate a survival probability of ^{9}Li/^{8}He background events after the muon veto, i.e. the ratio of the integral of the TT measured distribution (dots) in Figure 6.11(a) for a lateral distance larger than $3\,\mathrm{m}$, to the integral of the same distribution (dots) over the entire range. Its value is equal to $(1.6 \pm 0.2)\,\%$. By adding 1% of the events due to the cosmogenic isotopes decaying after the $1.2\,\mathrm{s}$ veto time window, the residual rate with the TT tracking precision is estimated to be 3%.

Similarly, we smeared also the MC true lateral distance profile of CD muons with the reconstruction accuracy and the muon detection efficiency given by [131], in order to simulate a lateral distance profile measured by the CD. The resultant profile after smearing is shown in Figure 6.12(a), and the ratio between the two distributions is shown in Figure 6.12(b). A fit with a constant value of the ratio is done for distances larger than $700\,\mathrm{mm}$. Compared with the profile measured by the TT, the TT clearly improves the rate measurement thanks to the better reconstruction accuracy. If the muon veto relies completely on the CD muon reconstruction, the survival probability of ^{9}Li/^{8}He background events is estimated to be $(5.0 \pm 0.1)\,\%$ from this simulation. Again, to include the isotopes decaying after the veto time, the final residual rate is estimated to be 6%.

It is worth mentioning that, compared to Figure 6.6, the residual rate for the CD tracking precision ($\langle \alpha \rangle = 1.6°$) is increased from $\sim 1.5\%$ to 5%. An investigation shows that such an increase is mostly attributed to the CD muon detection efficiency that we have considered in the latter.

So far, what we have considered is the measurements with muon tracking carried out independently by only one detector. In reality, the cosmogenic background rate in JUNO will be studied with all muons detected in JUNO, namely, a combination of the samples detected by the TT and by the CD. A combined residual rate can be
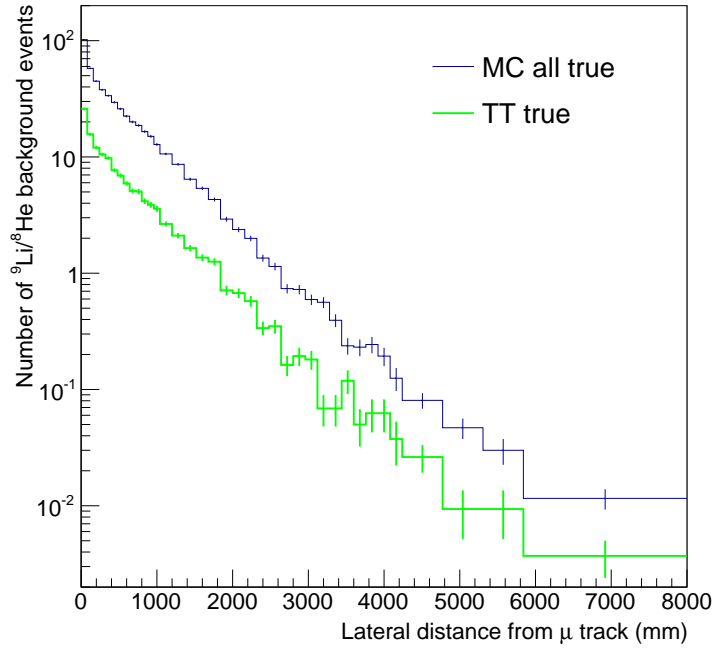
(a)
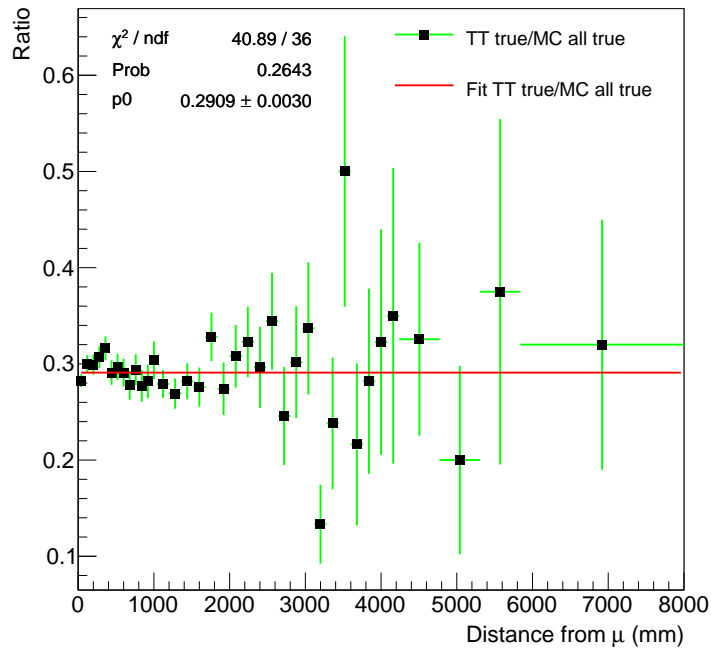
(b)

Figure 6.10 – (a) Lateral distance profiles of all events ("MC all true") and of only TT muon events ("TT true"), obtained from the simulation. Only ^{9}Li/^{8}He inside the fiducial volume at 17 m are selected. (b) The ratio between the two profiles. The red line is the fit with a constant value of the "TT true"/"MC all true".
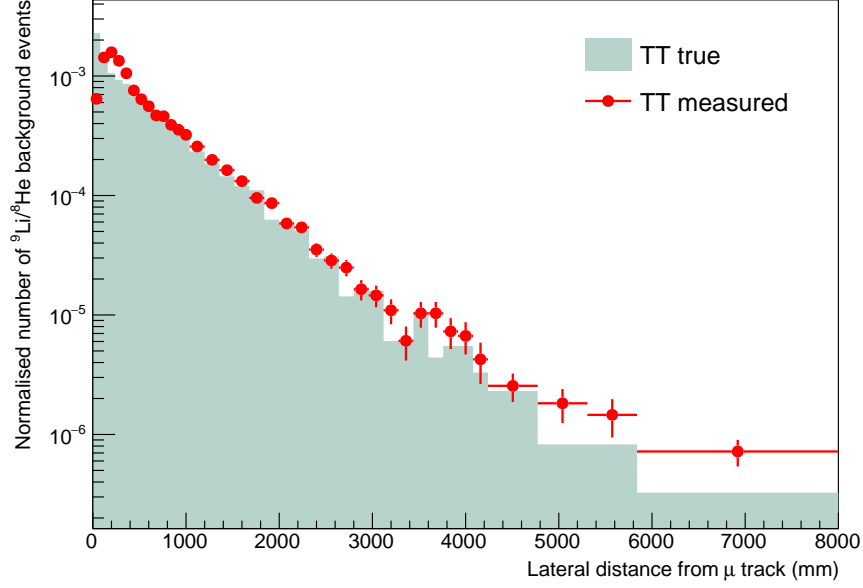
(a)
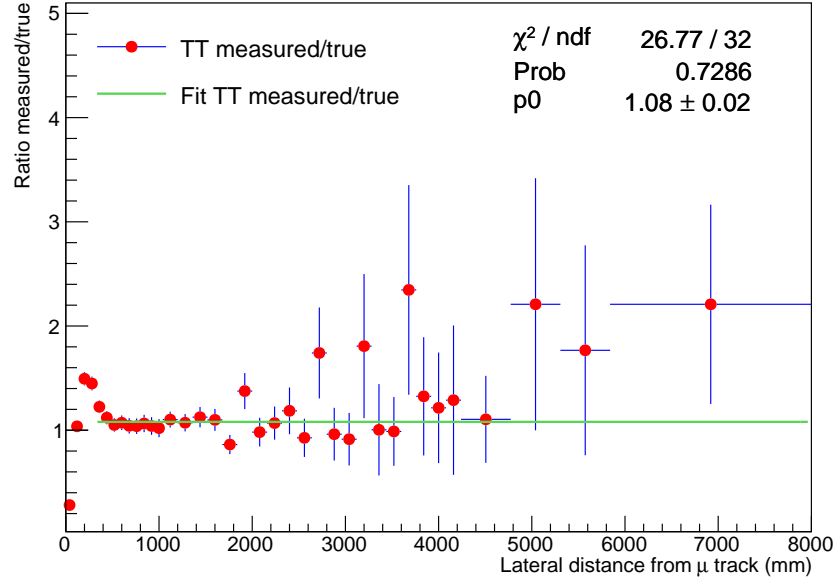
(b)

Figure 6.11 – (a) "Measured" lateral distance profile of ^{9}Li/^{8}He for TT muon events, obtained by smearing the muon tracks with the TT reconstruction accuracy (red points), and the MC true profile of TT muon events (green fill). Only ^{9}Li/^{8}He inside the fiducial volume at $17\,$m are selected. (b) Ratios between the TT measured and the TT true distributions, and the fit for distance larger than $300\,$mm. For large distance, the bins are resized to have more statistics.
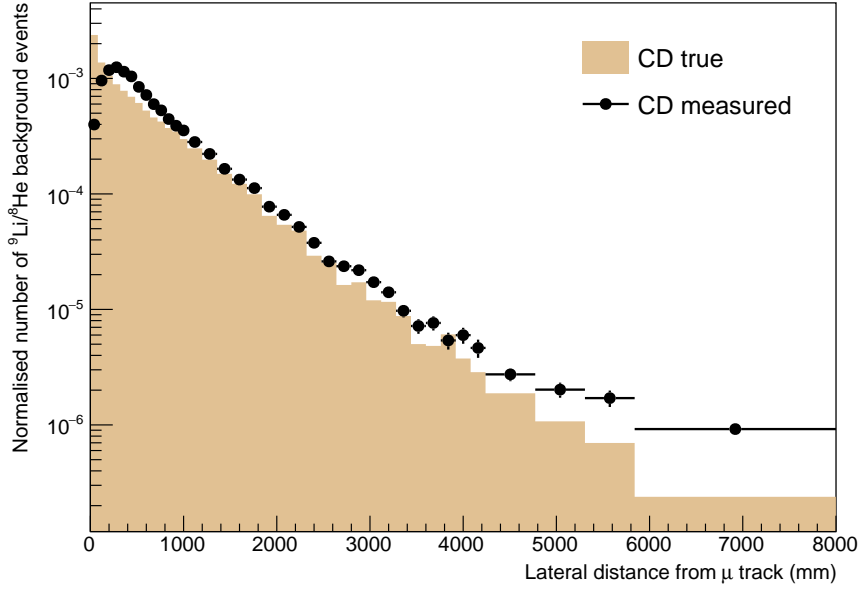
(a)
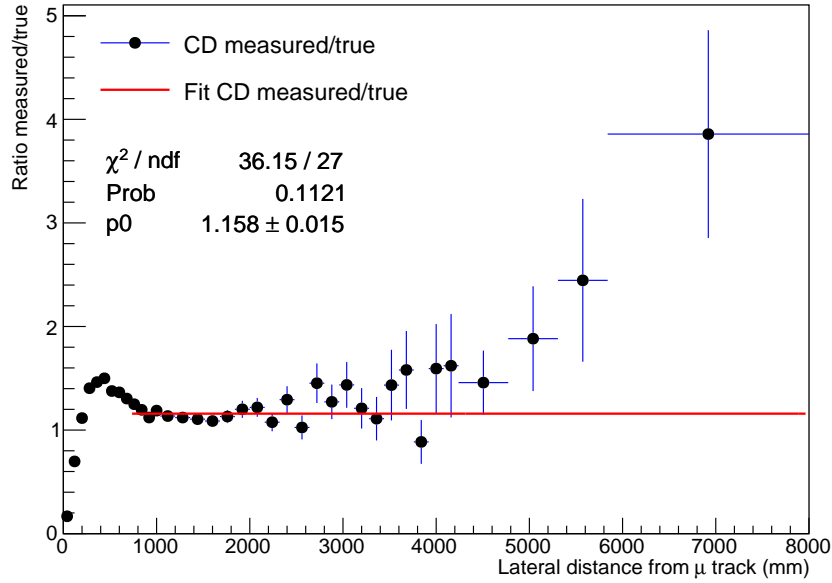
(b)

Figure 6.12 – (a) "Measured" lateral distance profile of ^{9}Li/^{8}He by the CD for CD muons (black points), and the MC true profile of all CD muons (brown fill). Only ^{9}Li/^{8}He inside the fiducial volume at 17 m are selected. (b) Ratios between the CD measured and the CD true distributions, and the fit for distance larger than 700 mm. For large distance, the bins are resized to have more statistics.

approximately estimated by this formula

$$R_{\text{Comb.}} = pR_{\text{TT}} + (1 - p)R_{\text{CD}}, \tag{6.2}$$

where p is the percentage of the cosmogenic events tagged by the TT, R_{TT} and R_{CD} are residual rates corresponding to the TT tracking precision and the CD tracking precision, respectively. From the simulation results, we know that $R_{\text{TT}} = 3\%$ and $R_{\text{CD}} = 6\%$. The studies in Section 6.1 give $p = 0.31$, so the combined residual rate is estimated to be 5%.

In Equation 6.2, the interplay between the TT and the CD is ignored, because it has effects only for muon bundles. At the same time, a study of the final residual rate can be even more comprehensive, if the Monte-Carlo simulation including the time and energy spectra of ^{9}Li/^{8}He decay, and a combined analysis of the TT and CD raw data, is performed. This has not yet been worked out within the collaboration, and may become an interesting subject for further investigation.

Finally, given that the cosmogenic rate is 91 events per day, the combined residual rate gives a background rate of 4.6 counts per day, which is still good enough for a mass hierarchy sensitivity better than 3σ by referring to Figure 6.7.

6.3 Measurement of fast neutron

To study the fast neutron events, we use a sample generated by the JUNO official MC corresponding to 1516 days of data. Generating fast neutron events needs a large amount of simulated muons and thus becomes very time-consuming. Therefore, our sample contains only the rock and corner clipping muons whereby the production was accelerated.

We processed the simulation in a way similar to the real detector, all hit information within a 300 ns time window are combined into one CD event, which can be either a prompt signal or a delayed signal of an IBD event. After building the events, a fast neutron event is selected if no other signal is found during a 1 ms time window before its prompt signal and after its delayed signal, and if the time difference between the prompt and delayed signals is less than 1 ms. The timeline of a selected fast neutron event is shown in Figure 6.13. A minimal energy cut is applied by requiring all events to have a visible energy larger than 0.7 MeV.

After the selection, we have 391 fast neutron events left in the sample, or equivalently a rate of 0.26 fast neutron events per day, produced by rock and corner clipping muons. In fact, not all fast neutron events should be considered as IBD background. In order to be an IBD background event in JUNO, the prompt energy must be lower than 12 MeV. This condition reduces the sample size to 49, i.e., 0.03 events per day. This level of sample statistics will not be sufficient for studying the fast neutrons with this simulation when also requiring TT information. Therefore, we decided not to apply the
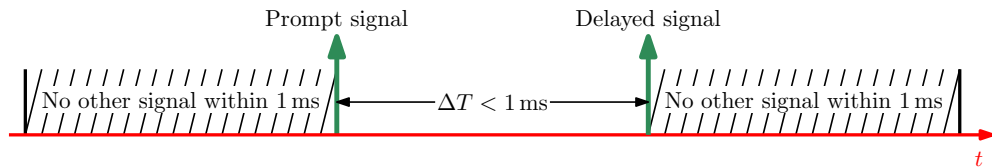
Figure 6.13 − Timeline of a selected fast neutron event.
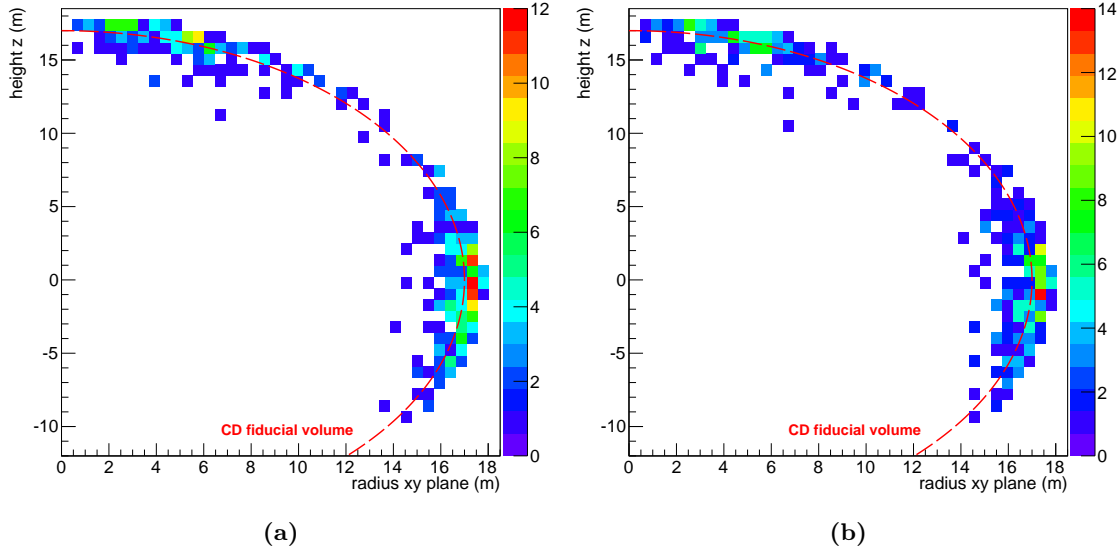
Figure 6.14 – Distributions of (a) prompt signal and (b) delayed signal vertices of fast neutron events. The fiducial volume at 17 m is labelled with the red dashed line. Colours in the plots represent the number of events.

IBD energy cut to have more available TT detected events. To consider only the IBD background, a scale factor of $\frac{49}{391} \approx 0.125$ needs to be applied in the calculation.

Since the fast neutrons are produced outside the CD, most fast neutron events are accumulated at the edge of the CD. Figure 6.14 shows the vertex distribution of the prompt and delayed signals of the selected fast neutron events. The plots show clearly that, the vertices are populated on top and at the equator of the CD. This result was expected, as the water buffer is ∼4 m thick in these regions, being the shallowest around the CD.

By applying a fiducial volume cut at 17 m radius, the number of fast neutron events is reduced to 122, or 0.08 events per day. The TT can detect the parent muons of 14 of these fast neutrons, which amounts to 11.5% of the total fast neutrons. The rate of TT tagged fast neutron event is then estimated to be 0.009 events per day.

The measurement of the fast neutron events is therefore possible by a coincidence between a muon that is only detected by the TT and going into the rock, and the prompt signal of an IBD-like event in the CD. In the simulation, all prompt signals of fast neutron events occur within 300 ns after the muons, as depicted in Figure 6.15. So it should be enough that the coincidence time window is ∼300 ns wide. The rate of rock and corner clipping muons detected by the TT is calculated in the simulation to be 0.3 Hz. Putting together the numbers, we estimate that an accidental coincidence rate between such a muon and an IBD-like event not caused by fast neutrons is about $\mathcal{O}(10^{-5})$ per day, being two orders of magnitude less than the rate of TT tagged fast neutron events.

This result shows that, it is possible to use the TT to measure the fast neutron event rate, whereby its uncertainty can be much reduced in contrast to the situation where no experimental information is available. For example, if in one year, the TT tags 4 fast neutron events, the count of total fast neutron events in the fiducial volume can be estimated to be 35 per year, or 0.095 per day, with a relative rate uncertainty of 50%, which is already better than the ad-hoc 100% that would be used if the rate were
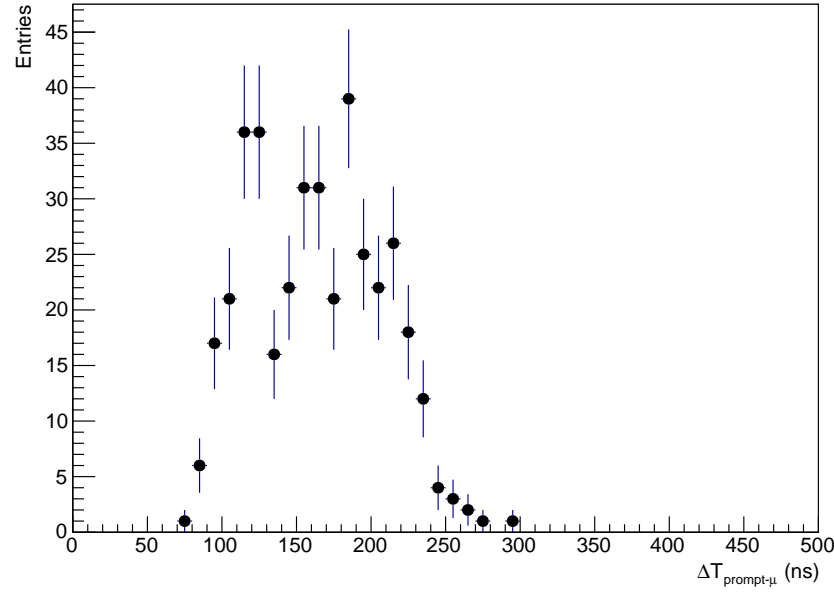
Figure 6.15 – Distribution of the time of fast neutron prompt signals since the parent muon is detected by the TT.

predicted only by MC simulation.

6.4   Summary

In this chapter, we have shown that the TT can contribute to the physics in JUNO by different means. Firstly, the TT muon tracking can have important contribution to the ^{9}Li/^{8}He background suppression thanks to its precision. Secondly, the TT is able to perform an efficient and unbiased ^{9}Li/^{8}He lateral distance profile measurement with only the muon tracking information provided by the TT, and the result is proven to be better than the one obtained by using only the CD muon tracking. Finally, as the only detector in JUNO that is sensitive to certain fast neutron events produced by the rock muons or the corner clipping muons, we have estimated that the TT can tag about 12% of the total fast neutron events in the CD, by requiring a coincidence between a muon that is exclusively detected by the TT and an IBD-like prompt signal in the CD within a 300 ns coincidence time window. The TT fast neutron measurement is important for reducing the corresponding systematic uncertainty for JUNO.

Conclusions

The neutrino mass hierarchy (νMH) is profoundly connected to many problems in neutrino physics, as for example, their Dirac or Majorana nature, or a possible CP-violation in the leptonic sector.

The νMH determination is one of the most challenging measurements in today's physics. The intrinsic difficulty stems from the fact that the measurement used to determine the νMH must take into account the 3-flavour oscillation effects, in which the difference between the NH and the IH is rather subtle.

JUNO is designed to be a high energy resolution neutrino detector that is able to determine the νMH with more than 3σ sensitivity. In order to achieve the design sensitivity, JUNO must have high photoelectron yield of the order of 1200 p.e./MeV and well controlled IBD backgrounds, especially the background that is induced by the atmospheric muons. Many instrumental studies in the JUNO collaboration have been done to ensure that the design is optimised for these two objectives. As part of these studies, this thesis presented my contribution to the design of LPMT Occulting Light Concentrator (OLC), the optimisation on the SPMT system, and the Top Tracker (TT) trigger algorithms.

The energy resolution can be improved by increasing the photon statistics, so it is worth testing any possibility to gain more light in JUNO. We have noticed that the limitation of the photocathode coverage is actually due to the geometrical constraints from the CD and the LPMTs. As a tool to overcome the geometrical limitation and to occult the worst performing part of the LPMT photocathode, we tested two new designs, the Cut OLC and the Crown OLC, both tailored for the LPMT clearance and the LPMT collection efficiency profile. In this study, we compared the light collection performances of raw LPMTs, Cut OLCs, and Crown OLCs. This comparison shows that employing OLCs to push the coverage to be higher than 75% does not seem to have very significant effects on the amount of collected light, as the clearance between JUNO LPMTs is small. Given that the fabrication and the installation of OLCs will overcomplicate the LPMT assembly, JUNO should have no particular interest in the OLCs. On the other hand, as we have proven in MC simulations, if a spherical detector has a large clearance between PMTs, OLCs can still be interesting devices for enhancing the overall light collection performance of the detector, without investing more budget in PMTs. By comparing the performances between Cut OLCs and Crown OLCs, we conclude that both have comparable results on improving the light collection. Crown OLCs can be more effective if the PMT clearance is larger. Finally, the study also suggests that, the OLCs may become less effective if the LPMT protection masks are used.

Although the LPMT system is the main calorimetric system in JUNO, the SPMT system helps to further reduce the systematic uncertainty. In the current consideration, there will be no SPMTs under the Central Detector (CD) truss beams, forming a non-

uniform SPMT distribution. We have studied this distribution with MC simulations, and shown that the non-uniformity of the SPMT spatial distribution has no impact on its light collection. At the same time, we also considered that the failure of Under Water Boxes (UWBs) can also create blind spots on the sphere of the detector. Like the removal of SPMTs under the CD truss beams, the blind spots increase the non-uniformity of the SPMT distribution and thus introduce dispersive effects to the light collection. A different cabling scheme called "overlap" is proposed to replace the "nearest" scheme, in order to mitigate such a degradation. By performing MC simulations on different random failure tests, we have concluded that both schemes have the same level of degradation in case of UWB failure. From our understanding, the small impact of the non-uniformity is due to the 2 m thick water buffer located around the CD. This buffer makes the distance between event vertices and the SPMTs sufficiently large, so light produced from an event vertex will always be collected by still operative SPMTs.

Besides the studies on the CD-related systems, this thesis has contributed to the TT trigger algorithm. Due to the relatively high natural radioactivity level in the JUNO cavern, the TT encounters a large radioactive background which causes too much dead time and significantly reduces the muon detection efficiency. A two-level trigger is therefore employed to suppress this background, whereby the muon detection efficiency can be recovered. In our studies, different configurations of L1 and L2 triggers have been considered. For the L1 trigger algorithms, we have shown that their implementations are completely compatible with Concentrator Board (CB) FPGA, by demonstrating the most complicated algorithm, XYo, through a test bench. We have tested all trigger configurations with MC simulations, and the results reveal that they are effective to reduce the background. Thanks to the smaller dead time, the muon detection efficiency is largely recovered. For most configurations, this effect is more significant when the coincidence conditions become more stringent. We have also verified that the choice of a trigger configuration does not have any impact on the muon reconstruction accuracy, as they all achieve a median angular resolution of 0.20°. Finally, we conclude that, with the optimised algorithm, XY⊥+Align, the radioactive background is suppressed by three orders of magnitude, and the muon detection efficiency of the TT is estimated to be 93%.

After all the aforementioned contributions to the JUNO instrumentation, in the last chapter we focus on the physics to which the TT can serve. As the first and the most important application in JUNO, the TT contributes to the cosmogenic isotope background veto with its good tracking precision. We showed that about 30% of CD muons are expected to be measured by the TT, therefore, the corresponding background events can be rejected with less residue. The second application of the TT is to perform a measurement of ^{9}Li/^{8}He lateral distance profile, with the muon direction information coming exclusively from the TT muon tracking. Thanks to the TT precision, this measurement should give a good approximation of the true distribution in the whole JUNO detector. Lastly, we have shown that, for fast neutron events that are produced by the rock muons or the corner clipping muons, the TT can be used to measure them by requiring a 300 ns coincidence between such a muon and an IBD-like prompt signal in the CD. With this measurement, we will put constraints on the uncertainty of the fast neutron rate estimation, which leads to a decrease of the total JUNO systematic uncertainty.

JUNO is planned to start its first data taking by the end of 2021. According to the project schedule, most hardware related work for the LPMT system, the SPMT system, and the TT has been settled. However, we still need to utilise efficiently the

remaining time to complete the optimisation. In particular, as the TT will be installed last, we expect to have more progress by then. Although in this thesis, the TT readout electronics, including the 2-level trigger system, has been studied with realistic simulations, the best way to fully test it is still to use a TT prototype that takes data from real atmospheric muons. We have started to set up such a device at IPHC, Strasbourg, in which the latest TT electronics is employed. This muon telescope will have 4 layers, with each layer being 1/4 of a TT wall. We expect also that the data taken by this telescope will be used to improve our TT simulation.

Regarding the muon-induced background, this thesis has made some pioneer work on its detection with the TT, which can be a starting point for developing the future TT data analysis dedicated to the muon veto. In the next step, we will integrate the detailed energy and time information of ^{9}Li/^{8}He decays in the MC. Additionally, a fast neutron sample containing events produced by all muons will be generated. Both are very challenging tasks, but thanks to this improvement, we should be able to give a more precise estimation of the background rates induced by atmospheric muons. An improved simulation also allows us to develop algorithms for the CD to directly discriminate the background ^{9}Li/^{8}He events.

Glossary

2L 2-layer coincidence, a L2 trigger algorithm requiring a coincidence of L1 trigger outputs from at least 2 different TT layers. 106

3D point a 3-dimensional point reconstructed in the TT reconstruction algorithm from the hit information. 45, 106

3W 3-wall coincidence, a L2 trigger algorithm requiring a coincidence of L1 trigger outputs from at least 3 different TT walls. 106

AC acrylic cover or acrylic mask. They are used to protect the LPMT from shockwave. 40

ADC Analog-to-Digital Converter. 85

Align a L2 trigger algorithm requiring a coincidence of L1 trigger outputs from at least 3 aligned TT walls. 106

angle true-reco the angle between the true muon track and the muon track reconstructed by the TT. 109

AS acrylic sphere built to contain $20\,\mathrm{kton}$ LS of JUNO. 34

ASIC application-specific integrated circuit. 86

cabling scheme the way that SPMTs are linked to the corresponding UWBs. 69

CB Concentrator Board, the hardware responsible for the L1 trigger implementation. 85

CC charged-current interaction. 7

CD JUNO Central Detector. 34

CD muon a muon that crosses the CD. 117

CD truss see stainless steel truss. 34

CE collection efficiency, the probability that photoelectrons will land on the effective area of the first dynode. 60

CKM Cabibbo–Kobayashi–Maskawa. 13

corner clipping muon a muon that crosses the WP but leaves a track length less than $0.5\,\mathrm{m}$. It is considered to be not detectable by the WP. 117

cut-off angle see $\theta_{\lim}$. 59

DAQ data acquisition system. 40

DE detection efficiency, the ratio of the detected photoelectrons to incident photons. 39

delayed signal the signal given by the recoiled neutron produced in an IBD reaction, it is detected after the corresponding prompt signal. 33

distance true-reco the distance between the intersection points of the true muon track and the muon track reconstructed by the TT at the Water Pool bottom level. 107

EMF Earth's magnetic field. 36

EW electroweak theory. 6

FADC Flash ADC, a type of ADC that is usually faster than other types commonly seen. 87

FAST-OR a global OR of all discriminator outputs of 64 channels of MAROC3. 86

FEB Front-End Board, carrier of MAROC3. 85

FPGA Field-Programmable Gate Array. 85

GSW Glashow-Salam-Weinberg. 6

HV high voltage. 42

IBD inverse beta decay. 32

IH inverted hierarchy. 15

ILA Integrated Logic Analyzer, a logic analyzer core developed by Xilinx, and it can be used to monitor the internal signals of a design. 102

L1 Level1 or Level1 trigger, implemented in the Concentrator Board on a TT wall. 85

L2 Level2 or Level2 trigger, to validate the TT global coincidence of L1 trigger outputs. 85

L2All a L2 trigger mode in `SCD` accepting any L1 trigger outputs in the given coincidence time window. 110

LC light concentrator. 57

LHC Large Hardon Collider. 4

LPMT Large PMT, namely the 20"-PMT used in JUNO. 1, 39

LS liquid scintillator. 34

MA-PMT 64-channel multi-anode PMT, used in the TT for scintillation photon detection. 44

MAROC3 a chip used in the TT for the charge readout. 86

MC Monte-Carlo. 18, 21

MCP Micro-Channel-Plates. 39

MSW Mikheyev–Smirnov–Wolfenstein. 15

muon bundle a muon event in which multiple muons arrive simultaneously in JUNO and their tracks are parallel. 91

NC neutral-current interaction. 8

NH normal hierarchy. 15

NPP nuclear power plant. 31

N_{pe} number of photoelectrons. 38

ν**MH** neutrino mass hierarchy. 15

OLC Occulting Light Concentrator, used to improve the PMT detection efficiency. 58

OMEGA manufacturer of MAROC3, OMEGA-Centre de Microélectronique, École Polytechnique, Route de Saclay, 91128 Palaiseau, France. 86

OPERA Oscillation Project with Emulsion-tRacking Apparatus, a past neutrino experiment in the Laboratori Nazionali del Gran Sasso (LNGS) in Gran Sasso. The JUNO TT modules are taken directly from OPERA Target Tracker. 43

p.e. photoelectron or photoelectrons. 34

photon-counting an energy reconstruction method that can be applied for the SPMT system, which counts only the number of triggered SPMTs instead of doing the charge measurement. 41

PicoZed a commercial system-on-module that carries a Zynq 7030 FPGA, used in the XYo test bench. 99

PicoZed FMC Carrier V2 a commercial development board that is compatible with the PicoZed, it is used as the XYo test bench. 99

PMNS Pontecorvo-Maki-Nakagawa-Sakata. 13

PMT photomultiplier tube. In Chapter 5, see MA-PMT. 1

ppm parts-per-million, 10^{-6}. 94

prompt signal the signal given by the positron produced in an IBD reaction, it is detected first in the detector. 33

QCD quantum chromodynamics. 6

QE quantum efficiency, the ratio of output electrons to incident photons. 60

QED quantum electrodynamics. 5

RESET reset signal of MAROC3, which can interrupt the current charge readout. 86

RJ-45 a jack type commonly used for Ethernet. 87

ROB Readout Board. 85

rock muon a muon that does not cross any sensitive volume of the JUNO detector. 117

SCD a program used to implement event mixing and simulate TT triggers. 109

SM Standard Model. 3

SNU solar neutrino unit. 18

SOM system-on-module, usually is an electronic card carrying an FPGA or a micro-controller. 87

SPMT Small PMT, namely the 3"-PMT used in JUNO. 2, 41

SPMT distribution spatial distribution of SPMT emplacements. 69

SSM Standard Solar Models. 17

stainless steel truss structure supporting the JUNO CD acrylic sphere. 34

superpixel a region in the TT that is defined by intersecting a x-plane module and a y-plane module. 44

TDC Time-to-Digital Converter. 96

θ_{FV} the maximal incident angle of a ray emitted from the detector fiducial volume to a PMT. 60

θ_{lim} the OLC cut-off angle on the incident angle of the incoming ray. 59

θ^* the maximal incident angle of the incoming ray that ensures a 100% transmission for an ideal 3D OLC. 59

TOF time-of-flight. 40

TT JUNO Top Tracker. 35

TT muon event a muon event in JUNO, of which all muons are detected by the TT. 127

TT muon simulation a simulation chain using `SCD` to mix muon and radioactive events. 109

TT radioactivity simulation a simulation chain using `SCD` to mix only radioactive events. 109

TTS transit time spread. 40

TW time window. 87

UWB Under Water Box is a box installed in the JUNO WP in order to store the SPMT readout electronics. 2, 42

VEV vacuum expectation value. 9

WCD JUNO Water Cherenkov Detector. 36

Wilkinson ADC a type of ADC that is based on the comparison of an input voltage with that produced by a charging capacitor, invented by D. H. Wilkinson in 1950. 87

Winston cone a non-imaging light collector with a reflective inner surface, invented by the physicist R. Winston. 1

WLS Wave Length Shifting. 43

WP JUNO Water Pool. It is also the target volume of the JUNO WCD. 36

WP muon a muon that does not cross the TT, and leaves a track length larger than $0.5\,\mathrm{m}$ in the WP. 117

XY a L1 trigger algorithm requiring a coincidence of FAST-ORs from x- and y-plane modules. 95

XY⊥ a L1 trigger algorithm requiring a coincidence of 3 FAST-ORs giving a T-shape on a TT wall. 98

XY× a L1 trigger algorithm requiring a coincidence of 4 FAST-ORs giving a cross on a TT wall. 98

XY+ordering a L1 trigger algorithm requiring a coincidence of FAST-ORs from x- and y-plane modules that respect the correct time ordering. 96

XY3 a L1 trigger algorithm requiring a coincidence of 3 FAST-ORs, of which 2 form an XY coincidence. 98

XYo see XY+ordering. 96

Zynq 7030 the FPGA model used in the XYo test bench. 99

Zynq Ultrascale+ the FPGA model used in the Concentrator Board. 99

Bibliography

[1] E. Vitagliano, *et al.*, JCAP **2017**, 010 (2017).

[2] G. Bellini, *et al.*, Prog. Part. Nucl. Phys. **73**, 1 (2013).

[3] A. C. Hayes and P. Vogel, Ann. Rev. Nucl. Part. Sci. **66**, 219 (2016).

[4] W. Pauli, Phys. Today **31N9**, 27 (1978).

[5] F. Reines and C. L. Cowan, Phys. Rev. **92**, 830 (1953).

[6] Y. Fukuda *et al.* (Super-Kamiokande), Phys. Rev. Lett. **81**, 1562 (1998).

[7] Q. R. Ahmad *et al.* (SNO), Phys. Rev. Lett. **87**, 071301 (2001).

[8] S. Schael *et al.*, Phys. Rept. **427**, 257 (2006).

[9] G. Danby, *et al.*, Phys. Rev. Lett. **9**, 36 (1962).

[10] K. Kodama *et al.* (DONUT), Phys. Lett. **B504**, 218 (2001).

[11] F. Capozzi, *et al.*, Phys. Rev. **D95**, 096014 (2017).

[12] G. Aad, *et al.*, Phys. Lett. **B716**, 1 (2012).

[13] S. Chatrchyan, *et al.*, Phys. Lett. **B716**, 30 (2012).

[14] M. Tanabashi, *et al.* (Particle Data Group), Phys. Rev. **D98**, 030001 (2018).

[15] S. Capelli and P. D. Bari, Nucl. Phys. Proc. Suppl. **237-238**, 347 (2013).

[16] R. Bouchendira, *et al.*, Phys. Rev. Lett. **106**, 080801 (2011).

[17] M. E. Peskin and D. V. Schroeder, *An Introduction to Quantum Field Theory* (Addison-Wesley, Reading, USA, 1995).

[18] T. D. Lee and C. N. Yang, Phys. Rev. **104**, 254 (1956).

[19] C. S. Wu, *et al.*, Phys. Rev. **105**, 1413 (1957).

[20] M. Goldhaber, *et al.*, Phys. Rev. **109**, 1015 (1958).

[21] F. Englert and R. Brout, Phys. Rev. Lett. **13**, 321 (1964).

[22] P. W. Higgs, Phys. Lett. **12**, 132 (1964).

[23] G. S. Guralnik, *et al.*, Phys. Rev. Lett. **13**, 585 (1964).

[24] N. Cabibbo, Phys. Rev. Lett. **10**, 531 (1963).

[25] M. Kobayashi and T. Maskawa, Prog. Theor. Phys. **49**, 652 (1973).

[26] Z. Maki, *et al.*, Prog. Theor. Phys. **28**, 870 (1962).

[27] R. N. Mohapatra and G. Senjanović, Phys. Rev. **D23**, 165 (1981).

[28] B. Pontecorvo, Sov. Phys. JETP **6**, 429 (1957).

[29] B. Pontecorvo, Sov. Phys. JETP **26**, 984 (1968).

[30] V. Gribov and B. Pontecorvo, Phys. Lett. **B28**, 493 (1969).

[31] C. Giganti, *et al.*, Prog. Part. Nucl. Phys. **98**, 1 (2018).

[32] S. P. Mikheyev and A. Y. Smirnov, Nuovo Cim. **C9**, 17 (1986).

[33] L. Wolfenstein, Phys. Rev. **D17**, 2369 (1978).

[34] L. Wolfenstein, Phys. Rev. **D20**, 2634 (1979).

[35] Y.-F. Li, *et al.*, Chin. Phys. **C40**, 091001 (2016).

[36] Y.-F. Li, *et al.*, Phys. Rev. **D88**, 013008 (2013).

[37] X. Qian, *et al.*, Phys. Rev. **D87**, 033005 (2013).

[38] H. Minakata, *et al.*, Phys. Rev. **D76**, 079901 (2007).

[39] H. Nunokawa, *et al.*, Phys. Rev. **D72**, 013009 (2005).

[40] A. de Gouvêa, *et al.*, Phys. Rev. **D71**, 113009 (2005).

[41] R. Davis, Jr., *et al.*, Phys. Rev. Lett. **20**, 1205 (1968).

[42] J. N. Bahcall, Nucl. Phys. Proc. Suppl. **77**, 64 (1999).

[43] R. Davis, Int. J. Mod. Phys. **A18**, 3089 (2003).

[44] J. N. Abdurashitov *et al.* (SAGE), Phys. Rev. **C60**, 055801 (1999).

[45] P. Anselmann *et al.* (GALLEX), Phys. Lett. **B314**, 445 (1993).

[46] K. S. Hirata, *et al.*, Phys. Rev. Lett. **65**, 1301 (1990).

[47] Y. Fukuda *et al.* (Super-Kamiokande), Phys. Rev. Lett. **81**, 1158 (1998), [Erratum: Phys. Rev. Lett. **81**, 4279 (1998)].

[48] J. Boger *et al.* (SNO), Nucl. Instrum. Meth. **A449**, 172 (2000).

[49] J. N. Bahcall and R. Davis, Science **191**, 264 (1976).

[50] Q. R. Ahmad *et al.* (SNO), Phys. Rev. Lett. **89**, 011301 (2002).

[51] J. N. Bahcall, *et al.*, Astrophys. J. **555**, 990 (2001).

[52] K. Eguchi *et al.* (KamLAND), Phys. Rev. Lett. **90**, 021802 (2003).

[53] A. Gando *et al.* (KamLAND), Phys. Rev. **D83**, 052002 (2011).

[54] A. Gando *et al.* (KamLAND), Phys. Rev. **D88**, 033001 (2013).

[55] I. Esteban, *et al.*, JHEP **01**, 106 (2019).

[56] C. Achar, *et al.*, Phys. Lett. **18**, 196 (1965).

[57] F. Reines, *et al.*, Phys. Rev. Lett. **15**, 429 (1965).

[58] T. J. Haines, *et al.*, Phys. Rev. Lett. **57**, 1986 (1986).

[59] M. Nakahata *et al.* (Kamiokande), J. Phys. Soc. Jap. **55**, 3786 (1986).

[60] R. Becker-Szendy, *et al.*, Phys. Rev. **D46**, 3720 (1992).

[61] K. Hirata, *et al.*, Phys. Lett. **B280**, 146 (1992).

[62] M. Aglietta, *et al.* (NUSEK), EPL **8**, 611 (1989).

[63] C. Berger, *et al.*, Phys. Lett. **B227**, 489 (1989).

[64] S. Hatakeyama, *et al.*, Phys. Rev. Lett. **81**, 2016 (1998).

[65] K. Abe *et al.* (T2K), Nucl. Instrum. Meth. **A659**, 106 (2011).

[66] R. Patterson (NOνA), Nucl. Phys. Proc. Suppl. **235-236**, 151 (2013).

[67] Y. Fukuda, *et al.*, Phys. Lett. **B433**, 9 (1998).

[68] M. G. Aartsen *et al.*, Nucl. Phys. **B908**, 161 (2016).

[69] K. Abe *et al.* (Super-Kamiokande), Phys. Rev. **D97**, 072001 (2018).

[70] IceCube Collaboration, *Measurement of atmospheric neutrino oscillations with three years of data from the full sky*, IceCube Neutrino Observatory, Dataset (2018).

[71] M. A. Acero, *et al.* (NOνA), Phys. Rev. Lett. **123**, 151803 (2019).

[72] L. Pickering (T2K), *Status of T2K*, 20th International Workshop on Next generation Nucleon Decay and Neutrino Detectors, Medellín, Colombia (2019).

[73] M. Apollonio *et al.* (CHOOZ), Phys. Lett. **B466**, 415 (1999).

[74] F. Boehm *et al.*, Phys. Rev. Lett. **84**, 3764 (2000).

[75] Y. Abe *et al.* (Double Chooz), Phys. Rev. Lett. **108**, 131801 (2012).

[76] F. P. An *et al.* (Daya Bay), Phys. Rev. Lett. **108**, 171803 (2012).

[77] J. K. Ahn *et al.* (RENO), Phys. Rev. Lett. **108**, 191802 (2012).

[78] X. Qian and J.-C. Peng, Rept. Prog. Phys. **82**, 036201 (2019).

[79] M. H. Ahn *et al.* (K2K), Phys. Rev. Lett. **93**, 051801 (2004).

[80] K. Abe *et al.* (T2K), Phys. Rev. Lett. **107**, 041801 (2011).

[81] P. Adamson *et al.* (MINOS), Phys. Rev. Lett. **107**, 181802 (2011).

[82] K. Abe *et al.* (T2K), Phys. Rev. **D96**, 092006 (2017), [Erratum: Phys. Rev. **D98**, no.1, 019902 (2018)].

Bibliography

[83] K. Abe, *et al.* (T2K), Phys. Rev. Lett. **118**, 151801 (2017).

[84] K. Abe *et al.* (Hyper-Kamiokande), PTEP **2015**, 053C02 (2015).

[85] A. Y. Smirnov, Phys. Scripta **T121**, 57 (2005).

[86] R. B. Patterson, Ann. Rev. Nucl. Part. Sci. **65**, 177 (2015).

[87] A. Tonazzo (DUNE), SciPost Phys. Proc. **1**, 43 (2019).

[88] K. Abe *et al.* (Hyper-Kamiokande), PTEP **2018**, 063C01 (2018).

[89] M. G. Aartsen *et al.* (IceCube), J. Phys. **G44**, 054006 (2017).

[90] S. Adrián-Martínez, *et al.*, J. Phys. **G43**, 084001 (2016).

[91] A. Ghosh, *et al.*, JHEP **04**, 009 (2013).

[92] S. M. Bilenky and C. Giunti, Mod. Phys. Lett. **A27**, 1230015 (2012).

[93] W. H. Furry, Phys. Rev. **56**, 1184 (1939).

[94] A. Gando *et al.* (KamLAND-Zen), Phys. Rev. Lett. **117**, 082503 (2016), [Addendum: Phys. Rev. Lett. **117**, no.10, 109903 (2016)].

[95] J. B. Albert *et al.* (EXO), Phys. Rev. Lett. **120**, 072701 (2018).

[96] J. B. Albert, *et al.* (nEXO), Phys. Rev. **C97**, 065503 (2018).

[97] J. Martín-Albo *et al.* (NEXT), JHEP **05**, 159 (2016).

[98] S. Andringa *et al.* (SNO+), Adv. High Energy Phys. **2016**, 6194250 (2016).

[99] M. and Agostini, *et al.* (GERDA), Nature **544**, 47 (2017).

[100] R. Arnold, *et al.*, Eur. Phys. J. **C70**, 927 (2010).

[101] A. Barabash, *et al.*, Nucl. Instrum. Meth. **A868**, 98 (2017).

[102] L. Cardani, SciPost Phys. Proc. , 24 (2019).

[103] G. Benato, Eur. Phys. J. **C75**, 563 (2015).

[104] F. Vissani, JHEP **06**, 022 (1999).

[105] P. Huber, Phys. Rev. **C84**, 024617 (2011).

[106] T. A. Mueller *et al.*, Phys. Rev. **C83**, 054615 (2011).

[107] G. Mention, *et al.*, Phys. Rev. **D83**, 073006 (2011).

[108] F. P. An, *et al.*, Chin. Phys. **C41**, 013002 (2017).

[109] A. C. Hayes, *et al.*, Phys. Rev. Lett. **112**, 202501 (2014).

[110] Y. Abe, *et al.* (Double Chooz), JHEP **2014**, 86 (2014).

[111] J. H. Choi *et al.* (RENO), Phys. Rev. Lett. **116**, 211801 (2016).

[112] Y. J. Ko *et al.* (NEOS), Phys. Rev. Lett. **118**, 121802 (2017).

[113] J. Kopp, *et al.*, JHEP **05**, 050 (2013).

[114] V. Lobashev, *et al.*, Phys. Lett. **B460**, 227 (1999).

[115] C. Weinheimer, *et al.*, Phys. Lett. **B460**, 219 (1999), [Erratum: Phys. Lett. **B464**, 352 (1999)].

[116] L. Bornschein, Nucl. Phys. **A752**, 14 (2005).

[117] K. N. Abazajian *et al.*, Astropart. Phys. **63**, 66 (2015).

[118] F. An, *et al.*, J. Phys. **G43**, 030401 (2016).

[119] S.-B. Kim, *et al.*, Adv. High Energy Phys. **2013**, 453816 (2013).

[120] P. Vogel and J. Engel, Phys. Rev. **D39**, 3378 (1989).

[121] L. Zhan, *et al.*, Phys. Rev. **D78**, 111103 (2008).

[122] V. Kopeikin, *et al.*, Phys. Atom. Nucl. **67**, 1892 (2004).

[123] G. Mention, *Étude des sensibilité et bruits de fond de l'expérience Double Chooz pour la recherche du paramètre de mélange leptonique θ_{13}*, Ph.D. thesis, Université Claude Bernard - Lyon I (2005).

[124] F. P. An, *et al.* (Daya Bay), Phys. Rev. **D93**, 072011 (2016).

[125] F. P. An, *et al.* (Daya Bay), Phys. Rev. **D95**, 072006 (2017).

[126] P. Vogel and J. F. Beacom, Phys. Rev. **D60**, 053003 (1999).

[127] H. R. Band *et al.*, JINST **7**, P06004 (2012).

[128] M. Krohn, *et al.*, JINST **7**, T08001 (2012).

[129] Y. Guo, *et al.* (JUNO), in *APS Meeting Abstracts* (2018) p. G08.004.

[130] K. Zhang, *et al.*, Radiat. Detect. Technol. Methods **2**, 13 (2018).

[131] C. Genster, *et al.*, JINST **13**, T03003 (2018).

[132] X. Zhou, *et al.*, Rev. Sci. Instrum. **86**, 073310 (2015).

[133] H. T. J. Steiger (JUNO), *Prospects, Design and Status of JUNO*, 8th International Conference on New Frontiers in Physics, Kolymvari, Greece (2019).

[134] R. Brown and D. Cockerill, Nucl. Instrum. Meth. **A666**, 47 (2012).

[135] J. Crespo-Anadón, Nucl. Part. Phys. Proc. **265-266**, 99 (2015).

[136] D. Franco *et al.* (Borexino), J. Phys. Conf. Ser. **136**, 042006 (2008).

[137] C. Yanagisawa and T. Kato, *Report on the Super-Kamiokande Accident*, `http://www-sk.icrr.u-tokyo.ac.jp/cause-committee/1st/report-nov22e.pdf` (2001).

[138] G. Gong, *et al.*, in *Proc. of International Conference on Accelerator and Large Experimental Physics Control Systems (ICALEPCS'15), Melbourne, Australia, 17-23 October 2015*, International Conference on Accelerator and Large Experimental Physics Control Systems No. 15 (JACoW, Geneva, Switzerland, 2015) pp. 1107–1110.

[139] M. He (JUNO), Radiat. Detect. Technol. Methods **1**, 21 (2017).

[140] M. Grassi, *JUNO Stereo-Calorimetry System JUNO*, 14th Pisa Meeting on Advanced Detectors: Frontier Detectors for Frontier Physics, Livorno, Italy (2018).

[141] R. Acquafredda *et al.*, JINST **4**, P04018 (2009).

[142] T. Adam, *et al.*, Nucl. Instrum. Meth. **A577**, 523 (2007).

[143] N. Agafonova, *et al.* (OPERA), Phys. Rev. Lett. **120**, 211801 (2018).

[144] C. H. Lee, *et al.*, Nuclear Engineering and Technology **49**, 592 (2017).

[145] G. Ranucci (JUNO), J. Phys. Conf. Ser. **1056**, 012048 (2018).

[146] S. Abe, *et al.* (KamLAND), Phys. Rev. **C81**, 025807 (2010).

[147] J. Zhao, *et al.*, Chin. Phys. **C38**, 116201 (2014).

[148] V. Strati, *et al.*, Progress in Earth and Planetary Science **2**, 5 (2015).

[149] R. Han, *et al.*, Chin. Phys. **C40**, 033003 (2016).

[150] M. Blennow, *et al.*, JHEP **03**, 028 (2014).

[151] X. Qian, *et al.*, Phys. Rev. **D86**, 113011 (2012).

[152] S.-F. Ge, *et al.*, JHEP **05**, 131 (2013).

[153] E. Ciuffoli, *et al.*, JHEP **01**, 095 (2014).

[154] Settanta, Giulio, *et al.*, EPJ Web Conf. **209**, 01011 (2019).

[155] W. Guo (JUNO), J. Phys. Conf. Ser. **888**, 012205 (2017).

[156] A. Mirizzi, *et al.*, Riv. Nuovo Cim. **39**, 1 (2016).

[157] M. Aglietta, *et al.*, Nuovo Cim. **C13**, 365 (1990).

[158] G. Salamanna, *et al.* (JUNO), PoS **ICHEP2016**, 1239 (2017).

[159] P. Antonioli *et al.*, New J. Phys. **6**, 114 (2004).

[160] W. T. Welford and R. Winston, *The optics of nonimaging concentrators—Light and solar energy* (New York: Academic Press, 1978).

[161] G. Doucas, *et al.*, Nucl. Instrum. Meth. **A370**, 579 (1996).

[162] L. Oberauer, *et al.*, Nucl. Instrum. Meth. **A530**, 453 (2004).

[163] M. G. Giammarchi, Nucl. Phys. Proc. Suppl. **35**, 433 (1994).

[164] K. Kamdin, Phys. Procedia **61**, 719 (2015).

[165] M. Moorhead (SNO), *Reflectors in Cherenkov Detectors*, Ph.D. thesis, Oxford University (1992).

[166] *Photomultiplier tubes, Basics and Applications*, Hamamatsu Photonics, 3rd ed. (2007).

[167] M. B. Avanzini, *et al.*, J. Phys. Conf. Ser. **888**, 012055 (2017).

[168] S. Agostinelli, *et al.*, Nucl. Instrum. Meth. **A506**, 250 (2003).

[169] T. Lin, *et al.*, J. Phys. Conf. Ser. **898**, 042029 (2017).

[170] S. Blin, *et al.*, in *IEEE Nucl. Sci. Symp. Conf. Rec.* (2010) pp. 1690–1693.

[171] D. H. Wilkinson, Math. Proc. Cambridge Phil. Soc. **46**, 508–518 (1950).

[172] P. Barrillon *et al.*, *64-channel Front-End readout chip*, MAROC3 datasheet, `http://omega.in2p3.fr`.

[173] R. Brun and F. Rademakers, Nucl. Instrum. Meth. **A389**, 81 (1997).

[174] B. Wonsak, *et al.*, JINST **13**, P07005 (2018).

[175] Triangular Universities Nuclear Laboratory (TUNL), the Nuclear Data Evaluation Group: `http://www.tunl.duke.edu/nucldata/`.

[176] G. Bellini *et al.* (Borexino), JCAP **1308**, 049 (2013).

[177] M. Grassi, *et al.*, JHEP **09**, 049 (2014).

[178] Y.-F. Wang, *et al.*, Phys. Rev. **D64**, 013012 (2001).

[179] F. P. An, *et al.* (Daya Bay), Phys. Rev. **D97**, 052009 (2018).

[180] H. de Kerret *et al.* (Double Chooz), JHEP **11**, 053 (2018).

Synthèse en français

Les neutrinos sont des fermions décrits par le « modèle standard », qui ne subissent que les interactions « faibles », qui sont quatre ordres de grandeur moins intenses que les interactions électromagnétiques. Il existe trois saveurs de neutrino correspondant à chaque saveur leptonique : neutrino électronique ν_e, neutrino muonique ν_μ, et neutrino tauique ν_τ. En 1998, l'expérience Super-Kamiokande a mis en évidence pour la première fois le phénomène d'oscillation des neutrinos. Grâce à cette cette observation, nous savons que les neutrinos possèdent trois états propres de masse ν_1, ν_2, et ν_3, dont les masses sont notées : m_1, m_2 et m_3. L'oscillation des neutrinos est modélisée par trois angles d'oscillation (θ_{12},θ_{13},θ_{23}), une phase traduisant la violation de la symétrie CP (δ_{CP}), ainsi que trois différences de masse au carré ($\Delta m_{ij}^2 = m_i^2 - m_j^2$), dont seulement deux ($\Delta m_{21}^2$,$\Delta m_{31}^2$) sont indépendantes. Ces paramètres ont été mesurés par différentes expériences étudiant les neutrinos provenant du Soleil, de l'atmosphère, de réacteurs nucléaires et d'accélérateurs de particules. Par contre, aucune expérience n'a pu à ce jour déterminer le signe de Δm_{31}^2, qui détermine la hiérarchie de masse entre deux possibilités : la hiérarchie dite « normale », dans laquelle $m_1 < m_2 < m_3$, et hiérarchie « inversée », correspondant à $m_3 < m_1 < m_2$.

L'expérience Jiangmen Underground Neutrino Observatory (JUNO) se donne pour objet la détermination de la hiérarchie de masse avec une sensibilité de trois écarts standards en six ans. Pour atteindre cet objectif, JUNO a besoin d'une résolution en énergie meilleure que 3% à 1 MeV, d'une incertitude systématique inférieure à 1%, et d'un faible bruit de fond par rapport aux signaux donnés par les antineutrinos de réacteurs que cette expérience détectera.

Le détecteur central de JUNO est constitué de 20 kilotonnes de scintillateur liquide, dont la détection de lumière est assurée par 18 000 photomultiplicateurs de 20 pouces et 25 000 de 3 pouces, fournissant une couverture de photocathode élevée (78%). Ce système de double-calométrie est novateur : d'un côté, les grands photomultiplicateurs possèdent un rendement photoélectronique d'environ 1200 photoélectrons par MeV pour minimiser l'incertitude stochastique du système ; d'un autre côté, le système de petits photomultiplicateurs améliore la performance en linéarité et en uniformité du détecteur pour que JUNO puisse posséder une incertitude systématique inférieure à 1%. Une telle configuration dotera JUNO d'une résolution en énergie sans précédent, qui sera meilleure que 3% à 1 MeV.

Malgré les 700 m d'épaisseur de roche protégeant le détecteur du rayonnement cosmique, les muons atmosphériques peuvent induire un bruit de fond non négligeable par rapport au signal attendu pour la détermination de la hiérarchie de masse. Ce bruit de fond induit provient de deux composantes : le bruit de fond « cosmogénique » et les « neutrons rapides ». Les muons peuvent créer des isotopes radioactifs (^{9}Li et ^{8}He) par le phénomène de spallation. Ces isotopes se désintègrent en cascade ($\beta^- n$) en émettant un électron, puis un neutron. Ce type de désintégration produit exactement le même

signal dans JUNO que l'interaction par courant chargé d'un antineutrino. Pour éliminer la plupart des signaux causés par ces isotopes cosmogéniques, nous devons rejeter tous les événements survenant dans un cylindre d'un rayon de 3 m tout au long de la trajectoire d'un muon atmosphérique pendant 1,2 s.

La bonne efficacité de veto de cette stratégie s'appuie sur la précision de la trajectographie des muons. Dans JUNO, un détecteur appelé « Top Tracker » est utilisé pour améliorer cette précision. Il s'agit d'un trajectographe de scintillateur plastique à 3 couches couvrant environ 60% de la surface au-dessus du détecteur central, ayant pour rôle de fournir des trajectoires précisément reconstruites. Des simulations de ce dispositif montrent qu'un tiers des muons entrant dans le détecteur central peuvent être reconstruits par ce trajectographe, et que ces trajectoires reconstruites pourront être utilisées comme source de calibration pour le détecteur central. Les autres muons seront détectés par le détecteur central ainsi étalonné. En combinant les résultats obtenus pour le trajectographe et le détecteur central, JUNO pourra supprimer plus de 98% de ces événements parasites liés aux isotopes cosmogéniques.

En ce qui concerne les neutrons rapides, ceux d'entre eux qui sont engendrés par un muon détecté (soit dans le détecteur central, soit dans le détecteur Tcherenkov à eau qui l'entoure) seront rejetés facilement. En conséquence, seuls les neutrons rapides qui sont produits dans la roche par les muons ne traversant ni le détecteur central ni le détecteur Tcherenkov peuvent constituer un bruit de fond. Grâce au trajectographe, qui couvre partiellement la roche entourant le détecteur Tcherenkov, certains de ces événements pourront être identifiés.

Cette thèse présente mes travaux d'optimisation des systèmes constitués par les petits et les grands photomultiplicateurs, mes études sur le système de déclenchement du trajectographe, ainsi que mon étude des bruits de fond cosmogénique et de neutrons rapides, pour cette expérience actuellement en cours de construction dont les prises de données commenceront en 2021.

1 Étude de la performance des « concentrateurs occultants de lumière »

La première voie permettant d'améliorer la résolution en énergie du détecteur, est de diminuer l'incertitude stochastique en augmentant le rendement photoélectronique du détecteur. La stratégie adoptée pour cela par la collaboration JUNO est de maximiser le nombre de photomultiplicateurs de 20 pouces installés, afin d'avoir un rendement supérieur à 1200 p.e./MeV. Ce choix conduit à un espacement géométrique de 25 mm entre deux grands photomultiplicateurs. De plus, ces tubes, très fragiles, doivent être protégés par des masques d'acrylique destinés à éviter une implosion en chaîne, ce qui réduit encore cet espacement à 3 mm.

L'augmentation du nombre de grands photomultiplicateurs étant impossible, la seule méthode pour pousser la couverture effective de photocathode au-delà de cette limite imposée par la géométrie est d'utiliser des « concentrateurs de lumière », également connus sous le nom du « cônes de Winston », placés au dessus des photomultiplicateurs. Ces concentrateurs sont par ailleurs capables d'améliorer l'efficacité de détection des tubes en réfléchissant les photons vers la zone centrale des photocathodes, où l'efficacité de collection est maximale. Pour cette dernière raison, ce dispositif est dénommé « Occulting Light Concentrator » (ou concentrateurs occultants) dans cette thèse.

L'espacement entre deux grands photomultiplicateurs étant insuffisant pour installer des concentrateurs de lumière complets, deux géométries sont possibles, selon que l'on

choisit de réduire le diamètre global des cônes (cônes coupés) ou que l'on préfère ne retirer que les parties qui se superposent (cônes en couronne). Cette dernière configuration permet en théorie d'atteindre une couverture maximale, bien que sa fabrication soit largement plus compliquée que celle des cônes coupés.

Les résultats de nos simulations montrent qu'avec un espacement de 25 mm, l'augmentation du rendement photoélectronique avec des concentrateurs de lumière est négligeable, quelle que soit la configuration choisie pour la forme des cônes. En revanche, l'utilisation de concentrateurs occultants améliore l'uniformité de collection de lumière, c'est-à-dire que le nombre de photoélectrons détectés par le système est moins dépendant de la position où l'événement se produit. Nous avons aussi choisi de tester l'effet des concentrateurs de lumière dans le cas où les espacements entre les photomultiplicateurs sont plus larges que dans JUNO. La simulation prouve que dans ce cas-là, les concentrateurs permettent de collecter plus de photoélectrons qu'avec les tubes photomultiplicateurs nus. La conclusion de cette étude est que, bien que certainement avantageux en général pour le rendement photoélectronique d'une expérience, et bien qu'ils permettent une amélioration de l'uniformité de détection, les concentrateurs de lumière occultants ne sont pas adaptés à la géométrie choisie pour l'expérience JUNO. Du fait du planning très contraint de construction du détecteur, et du manque de temps pour envisager d'autres configurations, la collaboration a finalement choisi d'utiliser les photomultiplicateurs sans concentrateurs de lumière.

2 Étude de la performance du système de photomultiplicateurs de 3 pouces

Le nombre d'emplacements existant entre les photomultiplicateurs de 20 pouces est ~37 000. Cependant, tous ces emplacements ne sont pas propices à l'installation de photomultiplicateurs de 3 pouces. En effet, certains d'entre eux sont situés en regard d'éléments de la structure de support de l'ensemble des photomultiplicateurs du détecteur central, ce qui rend l'installation d'un petit photomultiplicateur difficile, voire impossible. Du fait de ces contraintes mécaniques, la collaboration a décidé que les photomultiplicateurs de 3 pouces ne seront pas installés sous cette structure de support du détecteur central. Cette décision réduit le nombre de petits photomultiplicateurs utilisables de ~37 000 à ~25 000, et conduit simultanément à une distribution spatiale non-uniforme de ces petits tubes. Cette distribution non-uniforme peut potentiellement dégrader l'uniformité de la réponse du système, parce que la collection de photons de scintillation dépend de la position de l'événement. En effet, si les photons sont émis par un événement très proche d'une zone aveugle, la plupart de ces photons ne seront pas collectés.

Une autre possibilité qui peut dégrader l'uniformité du système est issue de la défaillance potentielle des boîtes de connections immergées (« Under Water Boxes ») durant les vingt années d'exploitation du détecteur JUNO. Ces boîtiers étanches sont utilisés pour placer l'électronique de lecture du système, chaque boîtier desservant 128 petits photomultiplicateurs. Aucune maintenance n'étant prévue, si l'électronique d'un boîtier tombe en panne, les 128 photomultiplicateurs desservis par ce boîtier seront définitivement déconnectés du système et laisseront place à une zone aveugle sur la sphère du détecteur. En fonction du schéma de câblage, la distribution des petits photomultiplicateurs déconnectés est différente et l'impact sur la performance du système peut éventuellement être réduit par un schéma de câblage plus astucieux que la simple proximité des tubes par rapport au boîtier. Dans ce but, nous avons étudié une configuration

où les zones desservies par chaque boîtier se recouvrent afin de répartir les photomultiplicateurs manquants plutôt que de créer une zone totalement morte au contour franc en cas de panne.

Pour répondre aux deux questions évoquées ci-dessus, nous avons effectué des simulations et évalué les impacts de la distribution non-uniforme des petits photomultiplicateurs et du choix du schéma de câblage des boîtiers immergés.

Cinq configurations comportant différents nombres de petits photomultiplicateurs retirés du système sont utilisées dans les simulations : $\sim$37 000 (installation complète), $\sim$34 000, $\sim$33 000, $\sim$31 000, et $\sim$25 000 (installation réelle). Les résultats obtenus avec une source d'étalonnage de ^{60}Co le long l'axe vertical central et avec les électrons d'1 MeV uniformément distribués dans le détecteur central ont été étudiés. De $\sim$37 000 à $\sim$25 000, nous observons que le nombre de photoélectrons est proportionnel au nombre de photomultiplicateurs installés. Quant à la résolution, elle empire, principalement à cause du plus faible nombre de photons collectés. En revanche, aucune dégradation de la résolution due à la non-uniformité de la distribution des photomultiplicateurs n'est constatée. Ce dernier point est confirmé par une comparaison directe entre la distribution réelle (non-uniforme) de photomultiplicateurs et une distribution uniforme obtenue en retirant 12 000 tubes au hasard dans le système.

Afin de savoir quel est le schéma de câblage optimal en cas de défaillance d'un boîtier électronique immergé, les défaillances de 5% et 10% de boîtiers ont été simulées, dans les deux configurations de câblage. Il existe dans le détecteur central de JUNO une distance minimale d'au moins 2 m entre la limite du volume de scintillateur utile et les photomultiplicateurs. De ce fait, aucun événement ayant lieu dans le volume fiduciel ne peut être plus proche que cette distance d'une zone aveugle, et les photons produits peuvent alors être collectés par les zones actives les plus proches. Ceci atténue notablement l'impact de la distribution non-uniforme des photomultiplicateurs sur les performances calorimétriques du système. Les résultats de nos simulations confirment ce point et montrent que le schéma où les zones desservies se recouvrent n'aide pas à améliorer la résolution en énergie. Ce dernier schéma demandant un câblage plus coûteux, nous concluons que le schéma optimal est le plus simple des deux, dans lequel chaque photomultiplicateur est connecté au boîtier le plus proche.

3 Optimisation des algorithmes de déclenchement du trajectographe à muons

Pour atteindre l'objectif de déterminer la hiérarchie de masse des neutrinos à trois écarts standards en six années de prises de données, l'expérience JUNO devra posséder non seulement une excellente résolution en énergie, mais aussi un faible bruit de fond. Il faut préciser que cette détermination sera effectuée par des ajustements du spectre en énergie mesurée des antineutrinos par des courbes théoriques correspondant aux deux hiérarchies. Dans cette procédure, un bruit de fond trop important peut conduire à une incertitude statistique sur le spectre mesuré, suffisante pour réduire la sensibilité et la rendre inférieure à 3σ. Les études des différents bruits de fond montrent que la composante « cosmogénique » induite par les muons atmosphériques est la composante la plus importante dans JUNO. Pour faire face à ce bruit de fond, une stratégie de veto, le « muon veto » est mise en place. Cette stratégie consiste à rejeter pendant 1,2 s, tous les événements survenant dans un volume cylindrique centré sur la trajectoire bien reconstruite du muon. Avec cette stratégie, nous estimons que seuls 1,6 événements, sur 84 par jour induits par les muons atmosphériques, survivent et contaminent les

événements provenant de l'interaction des antineutrinos.

Le trajectographe à muons (« Top Tracker ») sera installé au dessus de la piscine que constitue le détecteur Tcherenkov à eau, et sera utilisé comme détecteur de veto permettant de détecter les trajectoires des muons avec une précision meilleure que celle des autres détecteurs de JUNO. Ce trajectographe consiste en des lattes de scintillateur plastique, dont 64 sont juxtaposés pour fabriquer un module. Les signaux sont extraits des deux extrémités par deux photomultiplicateurs à anodes multiples de 64 canaux. Chacun des 63 « murs » de ce trajectographe est fabriqué en plaçant côte-à-côte 4 modules dans une direction, superposés avec 4 autres modules orientés dans la direction perpendiculaire. Ces détecteurs proviennent de l'expérience OPERA, où ils ont été utilisés comme cible active dans le tunnel du Gran Sasso (en Italie) pendant plus de 13 ans. Les murs ainsi constitués sont disposés en 3 couches, chaque couche comportant une grille de 3×7 murs. La granularité de ce détecteur est de $2,6\,\text{cm} \times 2,6\,\text{cm} \times 1\,\text{cm}$, déterminée par les dimensions des lattes. De par sa couverture géométrique incomplète, l'ensemble de ce trajectographe sera capable de détecter environ 30% des muons atmosphériques qui pénètrent dans le détecteur central de JUNO. D'une part, ces muons bien caractérisés seront utilisés pour le détecteur central comme échantillon d'étalonnage, afin d'améliorer la précision de sa trajectographie. D'autre part, ces trajectoires bien reconstruites pourront servir directement au trajectographe à muons lui-même pour en garantir une bonne efficacité de veto, et la mesurer.

Bien que les murs constituant le trajectographe soient identiques à ceux utilisés dans l'expérience OPERA, leur électronique de lecture doit être entièrement refaite pour JUNO, et un système de déclenchement à deux niveaux doit notamment être ajouté dans la chaîne de lecture. La raison pour cette évolution de l'électronique tient au fait que le niveau de la radioactivité naturelle dans la caverne de JUNO s'avère être 50 fois plus élevé que dans le site du Gran Sasso. En effet, les désintégrations des radioisotopes (essentiellement ^{238}U, ^{232}Th, et ^{40}K) émettent des rayonnements γ qui peuvent produire, dans les scintillateurs, des signaux identiques à ceux produits par les muons. Du fait de la radioactivité ambiante élevée, les simulations montrent que la fréquence des signaux provenant de la radioactivité dans le trajectographe atteindra $65\,\text{kHz}$, ce qui saturera l'électronique de lecture, chaque coup entraînant un temps mort de $14\,\mu\text{s}$. Pour éviter cette saturation de la chaîne d'acquisition de données, un système de déclenchement sera nécessaire pour rejeter en temps réel les coups dus à la radioactivité. Ce système de déclenchement consistera en un déclenchement de niveau 1, qui sera implémenté sur la carte concentratrice de signaux au niveau de chaque mur, et un déclenchement de niveau 2. La tâche du déclenchement de premier niveau est de vérifier si une coïncidence entre les canaux touchés dans un mur est valide ou pas, selon l'algorithme choisi. Par exemple, l'algorithme le plus simple consiste à vérifier si une coïncidence comporte au moins un canal touché dans une direction, et au moins un autre dans la direction perpendiculaire. Ce type de coïncidence dans un mur donné permet de repérer un point de passage en trois dimensions. La tâche du système de déclenchement de niveau 2 est similaire, c'est-à-dire qu'il vérifie la coïncidence entre plusieurs murs dont le déclenchement a été validé par le système de niveau 1. Dans cette thèse, nous considérons 5 différents algorithmes de niveau 1 discriminant les signaux de muons de ceux dus à la radioactivité par l'utilisation de la géométrie et des temps d'arrivée des signaux. Trois différents algorithmes de niveau 2, réduisant encore la fréquence du bruit de fond de radioactivité, sont également étudiés. Dans le cas où une coïncidence est rejetée par le système de déclenchement, les circuits électroniques de lecture impliqués dans cette coïncidence seront remis à zéro pour interrompre la conversion et la lecture des signaux analogiques,

ce qui permet de réduire considérablement le temps mort du système d'acquisition des données. Afin d'être sûrs que nous pourrons implémenter l'algorithme choisi dans les cartes électroniques, un test de compatibilité d'une carte avec l'algorithme le plus complexe a été réalisé, et a montré que tous les algorithmes envisagés seront compatibles avec le matériel choisi.

Dans les simulations, toutes les combinaisons possibles des algorithmes de niveau 1 et de niveau 2 ont été testées. Les résultats montrent que le système de déclenchement est très efficace pour rejeter les signaux dus à la radioactivité, réduisant ainsi leur fréquence de trois ordres de grandeur. Grâce à cette discrimination des signaux, le système de lecture pourra enregistrer les signaux dus aux muons avec une efficacité de 97%. De plus, nous avons pu montrer que les différentes configurations de déclenchement n'affecteront pas la résolution angulaire de la mesure des trajectoires, qui est estimée à 0,2°.

4 Étude du bruit de fond induit par muons avec le trajectographe à muons

Les muons atmosphériques peuvent engendrer deux types de bruits de fond dans JUNO. Le premier type provient des désintégrations des radioisotopes qui sont produits quand un muon énergétique déclenche une spallation d'un noyau de ^{12}C dans le scintillateur liquide du détecteur central. Parmi les noyaux créés, les productions de ^9Li et ^8He possèdent les rendements les plus élevés. Selon des études menées précédemment par d'autres expériences, la désintégration de ces isotopes conduit à des événements de bruit de fond possédant une distribution exponentielle en fonction de la distance du point de production à la trajectoire du muon parent. Bien que la forme de cette distribution soit approximativement connue, une mesure plus précise que celle existant dans la littérature permettrait d'effectuer une estimation de meilleure précision du taux résiduel de $^9Li/^8He$ dans JUNO. Nous proposons dans cette thèse d'utiliser la bonne précision de détermination des trajectoires par le trajectographe à muons, pour étudier ce bruit de fond cosmogénique. Notre étude montre en effet que la distribution mesurée par le trajectographe à muons est totalement représentative de la distribution originelle de tous les événements liés aux isotopes $^9Li/^8He$ produits dans le détecteur central. Une comparaison avec la même distribution, mesurée par le détecteur central, montre la que meilleure précision obtenue avec le trajectographe réduit significativement la distorsion sur la mesure, bien que la précision finie de la reconstruction par celui-ci soit prise en compte. Une analyse combinée des données prises par les deux détecteurs donnera un taux résiduel de $^9Li/^8He$ de 4,6 événements par jour, plus important que ce qui avait été initialement déterminé par la collaboration. Néanmoins, ce taux est encore acceptable pour la détermination de la hiérarchie de masse, pour laquelle une mesure à trois écarts standards nécessite un taux inférieur à 5,7 événements par jour.

Le deuxième type de bruit de fond provient des neutrons rapides, également produits dans les processus de spallation. La plupart de ces neutrons peuvent être rejetés en imposant un veto de 1,5 ms à compter du passage du muon parent. Cette stratégie impose par contre de détecter le muon parent dans le détecteur Tcherenkov à eau, ou dans le détecteur central. Pour les muons passant hors du volume de ces détecteurs, aucune stratégie de veto ne peut être mise en œuvre. Les neutrons rapides produits par des muons passant dans la roche de la caverne peuvent alors entrer dans le détecteur central et subir une collision avec un proton, créant ainsi un signal prompt, avant sa capture par l'hydrogène, qui produit un signal retardé.

Le trajectographe à muons possède 7% de sa superficie située au-dessus de la roche entourant le détecteur Tcherenkov à eau. Cette zone sensible, permet de détecter les muons qui ne passent dans aucun des deux autres détecteurs. Nous montrons ainsi que 8% des événements dus aux neutrons rapides peuvent être détectés par le trajectographe, grâce à la coïncidence entre un potentiel muon parent et un événement ressemblant à la détection d'un antineutrino. Cette mesure, que seul le trajectographe permettra d'effectuer, pourra être utilisée pour contraindre l'erreur systématique sur l'estimation du taux de neutrons rapides.

5   Conclusions

Une excellente résolution en énergie, meilleure que 3% à 1 MeV, et une réduction des bruits de fond, notamment celui engendré par les muons cosmiques, seront les deux clés du succès de l'expérience JUNO pour la détermination de la hiérarchie de masse des neutrinos.

Cette thèse a pour objet l'amélioration et l'optimisation des systèmes essentiels de JUNO, que constituent les ensembles de petits et de gros photomultiplicateurs pour la résolution en énergie, et le trajectographe supérieur pour la lutte contre le bruit de fond causé par les muons atmosphériques. Du fait de la petite distance laissée libre entre les capots de protection des gros photomultiplicateurs, nous montrons que l'utilisation de concentrateurs de lumière n'augmente pas le rendement photoélectronique, malgré une amélioration visible de l'uniformité du détecteur. Dans le même temps, nous montrons que la distribution non-uniforme des petits photomultiplicateurs, ou le choix d'un schéma de câblage simplifié avec les boîtes de liaison immergées, n'entraînera aucune dégradation des performances du système.

En ce qui concerne le trajectographe à muons, nous avons conçu et étudié les différents algorithmes de déclenchement que nous pourrons mettre en œuvre pour discriminer les signaux dus à la radioactivité ambiante dans la caverne. Nous montrons qu'avec notre algorithme optimal, le taux de bruit de fond dû à la radioactivité est divisé par mille, alors que l'efficacité de détection des muons augmente à 97%. Grâce à sa bonne précision de reconstruction, le trajectographe peut améliorer l'efficacité du veto des muons atmosphériques et être utilisé dans les études des bruits de fond dus aux isotopes cosmogéniques. Enfin, ce même trajectographe permettra la mesure du taux d'événements engendrés par les neutrons rapides prenant naissance dans la roche, qui ne sont pas détectables avec les autres systèmes existant dans l'expérience JUNO.

Titre : Vers la détermination de la hiérarchie de masse des neutrinos avec l'expérience JUNO

Mots clés : physique des particules, JUNO, hiérarchie de masse des neutrinos, isotopes cosmogéniques, système de déclenchement, tube photomultiplicateur

Résumé :
L'expérience JUNO est une expérience basée sur un détecteur à scintillateur liquide ayant pour objectif principal de déterminer la hiérarchie de masse des neutrinos. JUNO atteindra une sensibilité de trois écarts standards en 6 ans, avec une résolution en énergie sans précédent, meilleure que 3% à 1 MeV. Le détecteur central de JUNO est un détecteur à scintillateur liquide de 20 kilotonnes, construit avec une couverture de photocathode élevée (78%) et une bonne transparence. La couverture de photocathode est assurée par 18 000 photomultiplicateurs de 20 pouces et 25 000 de 3 pouces, ce qui permet d'atteindre un rendement d'environ 1200 photoélectrons par MeV. Malgré les 700 m d'épaisseur de roche protégeant le détecteur des rayonnements cosmiques, le bruit de fond induit par les muons atmosphériques est toujours considéré comme non négligeable par rapport au signal attendu pour la détermination de la hiérarchie de masse. Pour faire face à ce bruit de fond, un détecteur appelé « Top Tracker » permet d'améliorer la détection de ces muons. Cette thèse concerne les travaux d'optimisation pour cette expérience actuellement en cours de construction, et dont les prises de données commenceront en 2021.

Pour les photomultiplicateurs de 20 pouces, deux nouvelles géométries de concentrateurs de lumière sont étudiées afin de vérifier leurs performances pour augmenter le rendement photoélectronique et donc la résolution en énergie de JUNO. La distribution spatiale et le schéma de câblage des photomultiplicateurs de 3 pouces font aussi l'objet d'études pour assurer une performance optimale du système.

Cette thèse aborde ensuite la conception du système de déclenchement du Top Tracker. En effet, ce détecteur doit posséder un tel système pour rejeter les signaux produits par la radioactivité naturelle dans la caverne. Les résultats montrent qu'un système à 2 niveaux doté d'algorithmes optimisés est efficace pour la suppression de ces signaux et qu'il est ainsi possible d'obtenir une efficacité de détection des muons de 93%. Une discussion sur la contribution du Top Tracker à la suppression et à la mesure du bruit de fond induit par les muons atmosphériques est également incluse.

Title : On the way to the determination of the neutrino mass hierarchy with JUNO

Keywords : particle physics, JUNO, neutrino mass hierarchy, cosmogenic isotopes, trigger system, photomultiplier tube

Abstract :
The JUNO experiment is a multi-purpose liquid scintillator neutrino experiment with the main objective of determining the neutrino mass hierarchy (νMH) with a significance better than 3σ. To achieve this goal, it is crucial that JUNO has an unprecedented energy resolution of 3% at 1 MeV. Therefore, the JUNO Central Detector (CD) will be built with 20 000 ton high transparency liquid scintillator and high photomultiplier tube (PMT) photocathode coverage of 78%, which is provided by 18 000 20"-PMTs (LPMTs) and 25 000 3"-PMTs (SPMTs). At the same time, the background induced by atmospheric muons should be vetoed by using reconstructed muon tracks. The Top Tracker (TT) is a muon tracker installed on top of the CD for precise muon tracking.

This thesis details firstly the optimisation of the LPMT and the SPMT systems, which are directly related to the antineutrino calorimetry. New designs of light concentrator tailored for the JUNO LPMT are studied in order to verify their performance on increasing the JUNO photoelectron yield. By comparing different configurations, the relation between the SPMT system performance and the non-uniform distribution of the SPMT emplacements is studied, and the scheme used for cabling between SPMTs and their Under Water Boxes (UWBs) is studied to ensure a minimal performance degradation in case of UWB failure.

Afterwards, this thesis reports on the design and optimisation of the TT trigger algorithms. Due to the background induced by natural radioactivity in the JUNO cavern, the TT cannot work correctly without a trigger system. The results show that a 2-level trigger with the optimised trigger algorithm is effective for the background suppression and thus a muon detection efficiency of 93% can be achieved.

A discussion about the TT contribution to the suppression and the measurement of the atmospheric muon-induced background, is also included.